

Eirik Holm Fyhn

# Exotic Vortex Structures in Diffusive Superconducting Systems

Master's thesis in MTFYMA

Supervisor: Jacob Linder

June 2019

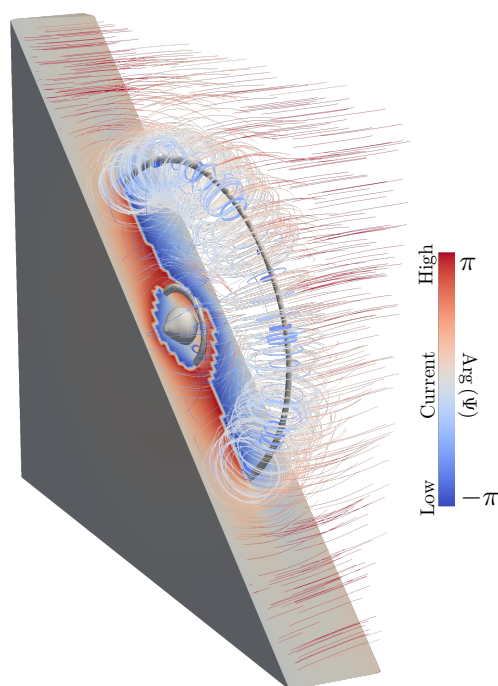


Illustration of controllable superconducting vortex loops



Eirik Holm Fyhn

# Exotic Vortex Structures in Diffusive Superconducting Systems

Master's thesis in MTFYMA  
Supervisor: Jacob Linder  
June 2019

Norwegian University of Science and Technology  
Faculty of Natural Sciences  
Department of Physics





*This thesis in theoretical condensed matter physics is submitted as the conclusion of my studies in the 10 semester integrated master program in Applied Physics and Mathematics at the Norwegian University of Science and Technology (NTNU), and amounts to 30 ECTS-credits. The work started in January 2019 and the thesis was submitted in June 2019. I want to thank my supervisor, Jacob Linder, who has provided guidance, insight and inspiration. I look forward to continue our collaboration. I also want to thank Vetle Risinggård and Morten Amundsen for helpful discussions.*



---

# ABSTRACT

When otherwise non-superconducting materials are placed in close proximity to a superconductor, superconducting correlations can leak through their shared boundary. This phenomenon is known as the proximity effect and when two materials are placed adjacent to each other in this way it can lead to new physics not seen in either material on their own. The study of these heterogenic mesoscopic structures offer great opportunities for fundamental as well as applied research in various fields in physics, including quantum computation, spintronics, interferometry and superconductivity. Still, much remains unknown and many problems remains unsolved. This thesis tackles two such problems. The first is regarding the formation of superconducting vortices in pure triplet-spin odd-frequency superconducting condensates and the latter is about the formation of vortex loops in superconducting systems.

Quantized vortices can form when ordinary superconductors are exposed to a magnetic field. This is a basic characteristic of superconductivity, but little is known about if and how vortices appear in odd-frequency superconductors. Odd-frequency superconductivity has never been observed to arise spontaneously in a material, but purely odd-frequency superconducting correlations do in fact occur in diffusive fully-polarized ferromagnets when they are placed in proximity to conventional superconductors. In this thesis I study such systems and find that superconducting vortices can also form in purely odd-frequency triplet-spin superconducting condensates. I find that, compared to vortices in normal proximity systems, the vortices in half-metals exhibit extra dynamics. This finding can possibly be used to determine interfacial magnetization angles which are difficult to find directly.

In certain situations these quantized vortices are believed to form closed loops. These superconducting vortex loops have so far avoided experimental detection despite being the focus of much theoretical work. In the second part of this thesis I propose a system which host controllable superconducting vortex loops. Because the size of the loops in this system can be controlled and be made arbitrary large, they can be tuned so as to hit the surface. This makes them directly detectable through the method of scanning tunneling microscopy, a method which has already been used successfully to observe superconducting vortices. The findings in this thesis also suggest that vortex loops in systems which are less obviously controllable but more easy to create experimentally can be controlled in a similar fashion.

The findings presented in this thesis has yielded two submissions to the journal *Physical Review Letters*. Preprints are attached in the appendix.

---

---

# SAMMENDRAG

Selv vanligvis ikke-superledende materialer kan oppføre seg superledende dersom de blir plassert inntil en superleder. Dette fenomenet kalles *the proximity effect* på engelsk, og når to materialer plasseres inntil hverandre på denne måten kan det oppstå ny fysikk som ikke finnes i materialene hver for seg. Studien av slike heterogene mesoskopiske strukturer tilbyr gode muligheter, både for grunnleggende og anvendt forskning innen mange ulike felt innen fysikk, slik som kvantedata-maskiner, spintronikk, interferometri og superledning. Likevel er det fortsatt mye som ukjent, og mange problemer er fortsatt uløste. Denne oppgaven tar for seg to slike problemer. Den første handler om dannelsen av superledende vortekser i superledende kondensater som er odd-frekvens og triplett-spinn. Den andre dreier seg om dannelsen av lukkede vorteksløkker i superledende systemer.

Kvantiserte vortekser kan dannes når vanlige superledere eksponeres for et magnetfelt. Dette er et grunnleggende kjennetegn ved superledning, men likevel er lite kjent om hvis og hvordan vortekser kan oppstå i odd-frekvens superledere. Oddfrekvens superledning har aldri blitt observert å oppstå i et materiale spontant, men rene odd-frekvente superledende korrelasjoner kan oppstå i diffusive fullpolariserte ferromagneter dersom de plasseres i nærheten av konvensjonelle superledere. I denne oppgaven studerer jeg slike systemer og finner at superledende vortekser også kan danne seg i rene odd-frekvens triplett-spinn superledende kondensater. Jeg finner at vorteksene i halvmetaller har ekstra dynamikk sammenlignet med vorteksene i normale proksimitetssystemer. Denne dynamikken kan brukes til å avgjøre magnetiseringsvinkler ved grensesjikt som ellers kan være vanskelig å måle.

I visse tilfeller antas det at kvantiserte vortkeser kan danne lukkede løkker. Disse superledende vorteksløkkene har vært fokus i mye teoretisk arbeid, men hittil har man ikke klart å detektere dem eksperimentelt. I den andre delen av denne oppgaven studerer jeg et system som jeg viser at gir vorteksløkker med størrelser som enkelt kan kontrolleres. Disse vorteks-løkkene kan gjøres vilkårlig store, og kan dermed justeres så de treffer overflaten. Dette betyr at de kan bli observert direkte, ettersom skanning-tunnelering-mikroskop allerede har blitt brukt til å se superledende vortekser på overflaten av proksimitetssystemer. Resultatene i denne oppgaven antyder også at man kan kontrollere vortekssløkker i andre systemer som er det ikke er like åpenbart at man kan kontrollere, men som det er enklere å lage eksperimentelt.

Funnene som presenteres i denne oppgaven har gitt to innsendinger til tidsskriftet *Physical Review Letters*. Disse ligger vedlagt.

---



---

# CONTENTS

<b>Abstract</b>	<b>iii</b>
<b>Sammendrag</b>	<b>iv</b>
<b>1 Introduction</b>	<b>1</b>
1.1 Structure . . . . .	2
1.2 Conventions . . . . .	2
<b>2 Methodology</b>	<b>5</b>
2.1 Green's functions . . . . .	5
2.2 Quasiclassical Theory . . . . .	6
2.2.1 Derivation of the Usadel Equation . . . . .	7
2.2.2 Parametrization . . . . .	15
2.2.3 Bulk BCS Solution . . . . .	15
2.2.4 Strongly Polarized Ferromagnets . . . . .	16
2.3 Observables . . . . .	16
2.3.1 Local Density of States . . . . .	17
2.3.2 Current . . . . .	19
2.4 Cooper Pair Correlation Function . . . . .	21
2.5 Numerics . . . . .	22
2.5.1 Weak Formulation of Differential Equations . . . . .	22
2.5.2 The Finite Element Method . . . . .	23
2.5.3 The Newton-Rhapson Method . . . . .	24
2.5.4 Differentiation . . . . .	26
2.5.5 Integration . . . . .	28
2.5.6 The Final Program . . . . .	32
<b>3 Superconducting Vortices in Half-Metals</b>	<b>33</b>
3.1 System . . . . .	34
3.1.1 Gauge Field . . . . .	35
3.2 Boundary conditions . . . . .	35
3.3 Order Parameter . . . . .	36
3.4 Analytics . . . . .	37
3.4.1 Analytic Solution in the Superconductors . . . . .	37
3.4.2 Ricatti-Parametrized Equations . . . . .	38
3.4.3 Analytic Solution . . . . .	39
3.5 Numerics . . . . .	40
3.5.1 Local Density of States . . . . .	40
3.5.2 Supercurrent . . . . .	44
3.5.3 Cooper Pair Correlation Function . . . . .	45
3.5.4 Vortex Position . . . . .	47

---

<b>4</b>	<b>Controllable Vortex Loops</b>	<b>51</b>
4.1	System . . . . .	52
4.1.1	Gauge field . . . . .	52
4.2	Boundary Conditions . . . . .	54
4.3	Analytics . . . . .	54
4.3.1	Analytical Solution in the Superconductors . . . . .	54
4.3.2	Ricatti-Parametrized Equations . . . . .	55
4.3.3	Analytical Solution . . . . .	55
4.3.4	Vortex Loop Radii . . . . .	56
4.4	Numerics . . . . .	57
4.4.1	Supercurrent and Local Density of States . . . . .	57
4.4.2	Cooper Pair Correlation Function . . . . .	59
4.5	Possible Model Improvements . . . . .	64
4.6	Experimental Realization . . . . .	66
<b>5</b>	<b>Conclusion and Outlook</b>	<b>69</b>
	<b>Bibliography</b>	<b>71</b>
<b>A</b>	<b>Paper I</b>	<b>79</b>
<b>B</b>	<b>Paper II</b>	<b>85</b>
<b>C</b>	<b>Computer Program</b>	<b>91</b>

---

# INTRODUCTION

“ *The interface is the device* ”

HERBERT KROEMER, 2000

One important realization which has been essential to much of the technological progress in the last 50 years is that combining materials with different properties allows for novel phenomena not seen in the materials separately. This is the key idea behind the transistor, a device for which the importance can hardly be overstated. It is not the P-doped or N-doped semiconductors themselves which are important in a transistor, but rather the interface, where the interplay between the different structures creates a depletion layer. This led Nobel Laureate Herbert Kroemer to coin the famous phrase introducing this chapter.

Although Kroemer was referring to semiconductors, the same remains true for other materials. Combining materials with different types of quantum order are showing promise for new applications and a deeper understanding of how the universe works on the length scales of atoms. For example, combining semiconductors and superconductors are exciting interest in the field of quantum computers [1, 2] for being a promising platform for realizing the anyons needed for topological quantum computers [3]. Another example is systems combining ferromagnetism and superconductivity, where it is possible to generate Cooper pairs that are, in contrast to conventional Cooper pairs, spin-polarized. The interplay between ferromagnetism and superconductivity has become the basis for the field of superconducting spintronics [4], which has as one of its goals to enable new types of devices utilizing spin-polarized supercurrents [5].

*Cooper pair* is the name given to a pair of correlated electrons as described by the famous BCS-theory [6]. Although these correlations originate in superconductors, they can leak through interfaces to other materials. This leakage of Cooper pairs results in signs of weak superconductivity being observed in the neighboring material; a phenomenon known as the *proximity effect*. The microscopic origin of this effect is known as Andreev reflection [7, 8]. Such proximity systems provide a versatile and rich way of exploring new fundamental physics. One example of this is in heterogenic structures with superconductors and fully polarized (half-metallic) diffusive ferromagnets. Interestingly, the proximity of a conventional superconductor induces Cooper pair correlations even in a half-metallic ferromagnets. The astonishing part about this statement is that the spin-singlet Cooper pairs which occur in conventional superconductors are impossible in half-metals. The Cooper pairs in half-metals must be spin-triplets because only one spin band is conducting. Moreover, if the half-metal is diffusive, the Pauli exclusion principle states that a temporal interchange of the correlated electrons must give a minus sign to the overall wave function. When the superconducting condensate is correlated in this unusual manner in time it is known as *odd-frequency* superconductivity [9]. For the proximity effect to occur in a half-metal, there must be a mechanism at the interface which converts the spin-singlet Cooper pairs in the superconductor to fully polarized spin-triplets which are odd in time.

While fully polarized odd-frequency superconducting states are not known to arise spontaneously in a material, it can be induced in a half-metal (H) when placed in proximity to a

conventional superconductor (S). A possible way to study this exotic state of matter is therefore provided by SH-heterostructures. One hitherto unsolved problem regarding odd-frequency superconductivity is whether superconducting quantum vortices can occur. This problem is addressed in this thesis and in the accompanying paper which has been submitted to Physical Review Letters (see appendix A).

Vortices are a type of topological defect, also known as a topological excitation. Topology is the study of properties which are preserved under continuous deformation, and topological defects have the defining property of being homotopically distinct from a uniform or trivial solution, meaning that there is no continuous mapping which can transform a topological defect into a uniform field. Many key properties are defined by topological defects. Dislocations in solids are important for the hardness of solids, domain walls in ferroics are important for their electric and magnetic properties and holds promise for nanoelectronics and spintronics applications [10, 11] and cosmological defects such as cosmic strings, textures, domain walls and monopoles are important for understanding the evolution of the early universe [12].

The topological defects in superconductors are superconducting vortices, which are lines of quantized magnetic flux. These lines have non-superconducting cores and a phase-winding of an integer multiple of  $2\pi$  in the superconducting order parameter, leading to circulating supercurrents [13]. In addition to being interesting from a fundamental physics point of view, understanding the behaviour of vortices is useful on a practical level. Their motion is a source of non-zero electrical resistance [14], so being able to create structures which discourage vortex formation or vortex movement is important for high performance superconductors. More recently it has been proposed that superconducting vortices can be used as a means for long-range spin transport [15] because their topological nature makes them stable against perturbations.

One natural question regarding superconducting vortices is whether they can form closed loops. It is allowed topologically, and theoretically they have been predicted to form around strong magnetic inclusions inside superconductors [16] and through vortex cutting and recombination [17, 18]. Nevertheless, no observation of vortex loops in superconducting systems has been found to date. This is possibly because they are typically small in conventional superconductors, about the size of the superconducting coherence length, and difficult to stabilize for an extended period of time [19]. In the second part of this thesis we will see how controllable and easily detectable vortex loops can be created in a SNS-junction with an inhomogeneous magnetic field. This work too resulted in a submission to Physical Review Letters which is also attached here. See appendix B.

## 1.1 Structure

Chapter 2 introduces the quasiclassical theory and numerical methods needed for both the analytics and numerics presented in chapters 3 and 4. Chapter 3 treats SHS-junctions with applied magnetic fields. A linearized version of the resulting equations are solved analytically and the full non-linear equations are solved numerically. Chapter 4 gives a similar treatment to a SNS-junction with an additional wire which gives rise to controllable vortex loops. The papers which resulted from these chapters are given in appendices A and B, respectively. Finally, some concluding remarks is given in chapter 5.

## 1.2 Conventions

Natural units will be used throughout the work presented here, meaning that  $c = \hbar = k_B = 1$ , where  $c$  is the speed of light,  $\hbar$  is the reduced Planck constant and  $k_B$  is the Boltzmann constant. In addition,  $e = -|e|$  is the electron charge. The imaginary unit is  $i$  and complex conjugation is denoted  $(a + ib)^* \equiv a - ib$ . The real part of a complex number is denoted by  $\Re$ , and the imaginary part is denoted by  $\Im$ . That is, if  $z = a + ib$ , then  $\Re\{z\} = a$  and  $\Im\{z\} = b$ .



The Pauli matrices are the traceless  $2 \times 2$  Hermitian matrices, namely

$$\sigma_1 = \begin{pmatrix} 0 & 1 \\ 1 & 0 \end{pmatrix}, \quad \sigma_2 = \begin{pmatrix} 0 & -i \\ i & 0 \end{pmatrix}, \quad \sigma_3 = \begin{pmatrix} 1 & 0 \\ 0 & -1 \end{pmatrix}, \quad (1.1)$$

and we will also use the  $4 \times 4$  version of the third Pauli matrix,

$$\hat{\rho}_3 = \begin{pmatrix} 1 & 0 & 0 & 0 \\ 0 & 1 & 0 & 0 \\ 0 & 0 & -1 & 0 \\ 0 & 0 & 0 & -1 \end{pmatrix}. \quad (1.2)$$

In this work we will operate with square matrices of size 2, 4 and 8, and for notational convenience we will use the following convention to interpret equations involving multiple types of matrices. When two matrices of different sizes are combined in a binary operation, the dimensionality of the matrix with the smaller dimension is extended through the tensor product of an appropriate identity matrix. For instance, if  $A$  is a scalar,  $B$  is a  $2 \times 2$  matrix and  $C$  is a  $4 \times 4$  matrix, then

$$A + BC = \begin{pmatrix} A & 0 & 0 & 0 \\ 0 & A & 0 & 0 \\ 0 & 0 & A & 0 \\ 0 & 0 & 0 & A \end{pmatrix} + \begin{pmatrix} B_{11} & B_{12} & 0 & 0 \\ B_{21} & B_{22} & 0 & 0 \\ 0 & 0 & B_{11} & B_{12} \\ 0 & 0 & B_{21} & B_{22} \end{pmatrix} \begin{pmatrix} C_{11} & C_{12} & C_{13} & C_{14} \\ C_{21} & C_{22} & C_{23} & C_{24} \\ C_{31} & C_{32} & C_{33} & C_{34} \\ C_{41} & C_{42} & C_{43} & C_{44} \end{pmatrix}. \quad (1.3)$$

Note that with this convention there is no difference between scalars and  $1 \times 1$  matrices.

In order to distinguish matrices of different sizes, hats ( $\hat{A}$ ) indicate that the matrix is  $4 \times 4$  and checks ( $\check{A}$ ) indicate that the matrix is  $8 \times 8$ . Bold letters is used for vectors ( $\mathbf{u}$ ). The elements of vectors can itself be matrices.

The commutation between two quantities  $A$  and  $B$  is written

$$[A, B] \equiv AB - BA, \quad (1.4)$$

and anticommutation is written

$$\{A, B\} \equiv AB + BA, \quad (1.5)$$

where  $\equiv$  is to be read “is equivalent to”. The symbol  $:=$  is used to mean “is defined as”. The transpose of a matrix  $A$  is written  $A^\top$  and the adjoint, or Hermitian conjugate, is written  $A^\dagger \equiv (A^\top)^*$ .

The absolute value or modulus of a real or complex number  $a$  is  $|a| \equiv \sqrt{a^*a}$  and when applied to vectors it is interpreted as the  $l^2$ -norm,

$$|\mathbf{u}| \equiv \sqrt{\sum_i |u_i|^2}, \quad (1.6)$$

where the sum runs over the elements of  $\mathbf{u} = (u_1, \dots, u_i, \dots, u_n)^\top$ . Integration limits are, unless otherwise specified, the entire domain over which the variables being integrated over are defined. For instance, integration over  $t$  are always from  $-\infty$  to  $\infty$  if other integration limits are not given.

Finally,

$$\theta(x) := \begin{cases} 0 & \text{if } x < 0, \\ \frac{1}{2} & \text{if } x = 0, \\ 1 & \text{if } x > 0, \end{cases} \quad (1.7)$$

is the Heaviside step function,  $\delta$  is the delta distribution, defined by

$$\delta(f) \equiv \int \delta(x)f(x) dx = f(0) \quad (1.8)$$

for all functions  $f$ , and  $\mathbf{e}_u$  is the unit vector in the direction of  $\mathbf{u}$ . Note that the distributional derivative of the Heaviside step function is the delta distribution,

$$\theta'(f) \equiv \int \theta'(x)f(x) \, dx = - \int \theta(x)f'(x) \, dx = - \int_0^\infty f'(x) \, dx = f(0) = \delta(f). \quad (1.9)$$

“ Although a variety of theoretical techniques have been used to describe proximity-coupled systems, the quasiclassical theory of superconductivity has proved to be a remarkably powerful tool in understanding the microscopic basis for the remarkable effects observed in these systems. ”

VENKAT CHANDRASEKHAR, 2004

The framework used to investigate the physical systems used in this work is the quasiclassical Green’s function approach. In this chapter I first summarize the relevant theory and how it can be used to investigate proximity systems. The relevant equations will not be solvable in the general case, and so when it comes to analytical solutions we must content ourselves with approximate solutions only valid in certain limits. To show that features such as vortices which are present in the approximate solutions also exist in the solutions to the full non-linear equations, I will also solve the equations numerically. This will require a range of numerical algorithms and mathematical theory which will also be introduced in this chapter.

## 2.1 Green’s functions

The use of Green’s functions has become a powerful technique to describe microscopic and mesoscopic systems both in and out of equilibrium. See for instance the textbook by Rammer [20]. Green’s functions are correlation functions, and from them one can extract a range of physical observables such as charge currents, spin currents and local density of states. One method of finding these Green’s functions is known as the equation of motion technique [21]. The idea is to find a closed set of differential equations the Green’s functions must satisfy. Such equations will be given in section 2.2. In this section I define the Green’s function which will be used here.

First, define the Nambu bispinors

$$\psi := \begin{pmatrix} \psi_{\uparrow} \\ \psi_{\downarrow} \\ \psi_{\uparrow}^{\dagger} \\ \psi_{\downarrow}^{\dagger} \end{pmatrix}, \quad \psi^{\dagger} := \left( \psi_{\uparrow}^{\dagger} \quad \psi_{\downarrow}^{\dagger} \quad \psi_{\uparrow} \quad \psi_{\downarrow} \right), \quad (2.1)$$

where the field operators  $\psi_{\sigma}(\mathbf{r}, t)$  and  $\psi_{\sigma}^{\dagger}(\mathbf{r}, t)$  respectively destroys and creates a particle at position  $\mathbf{r}$  and time  $t$ . The retarded, advanced and Keldysh Green’s functions are then respectively defined as

$$\hat{G}^{\text{R}}(\mathbf{r}_1, t_1, \mathbf{r}_2, t_2) := -i\hat{\rho}_3 \left\langle \left\{ \psi(\mathbf{r}_1, t_1), \psi^{\dagger}(\mathbf{r}_2, t_2) \right\} \right\rangle \theta(t_1 - t_2), \quad (2.2a)$$

$$\hat{G}^{\text{A}}(\mathbf{r}_1, t_1, \mathbf{r}_2, t_2) := +i\hat{\rho}_3 \left\langle \left\{ \psi(\mathbf{r}_1, t_1), \psi^{\dagger}(\mathbf{r}_2, t_2) \right\} \right\rangle \theta(t_2 - t_1), \quad (2.2b)$$

$$\hat{G}^{\text{K}}(\mathbf{r}_1, t_1, \mathbf{r}_2, t_2) := -i\hat{\rho}_3 \left\langle \left[ \psi(\mathbf{r}_1, t_1), \psi^{\dagger}(\mathbf{r}_2, t_2) \right] \right\rangle, \quad (2.2c)$$

where  $\theta$  is the Heaviside step function and commutation and anticommutation are defined in Nambu space as

$$[\alpha, \beta] = \alpha\beta - (\beta^\top \alpha^\top)^\top, \quad \{\alpha, \beta\} = \alpha\beta + (\beta^\top \alpha^\top)^\top, \quad (2.3)$$

These  $4 \times 4$  matrices are then combined to give a  $8 \times 8$  matrix of Greens functions,

$$\check{G} = \begin{pmatrix} \hat{G}^R & \hat{G}^K \\ 0 & \hat{G}^A \end{pmatrix}. \quad (2.4)$$

Finally, define the quasiclassical Green's function,

$$\check{g}(\mathbf{R}, T, \mathbf{p}_F, \varepsilon) := \frac{i}{\pi} \int d\xi_p \check{G}(\mathbf{R}, T, \mathbf{p}, \varepsilon), \quad (2.5)$$

where  $\xi_p = |\mathbf{p}|^2/2m - \mu$ ,  $\mu$  is the chemical potential,

$$\check{G}(\mathbf{R}, T, \mathbf{p}, \varepsilon) = \int d^3r dt \check{G}(\mathbf{R}, T, \mathbf{r}, t) e^{i\mathbf{p}\cdot\mathbf{r} - i\varepsilon t}, \quad (2.6)$$

$\mathbf{r} = \mathbf{r}_1 - \mathbf{r}_2$  and  $t = t_1 - t_2$  are the relative coordinates and  $\mathbf{R} = (\mathbf{r}_1 + \mathbf{r}_2)/2$  and  $T = (t_1 + t_2)/2$  are the center of mass coordinates.

## 2.2 Quasiclassical Theory

The underlying assumption needed to treat the system quasiclassically is that the Fermi wavelength is much shorter than all other relevant length scales. If in addition the system is diffusive, meaning that the scattering time is small, the isotropic part of the quasiclassical Green's function dominates and in equilibrium it solves the Usadel equation [20, 22–24],

$$D\bar{\nabla} \cdot (\check{g}\bar{\nabla}\check{g}) + i \left[ \varepsilon\hat{\rho}_3 + \hat{\Delta}, \check{g} \right] = 0. \quad (2.7)$$

Here,  $D$  is a diffusion constant,  $\hat{\Delta} = \text{antidiag}(+\Delta, -\Delta, +\Delta^*, -\Delta^*)$  where  $\Delta$  is the superconducting gap parameter, the covariant derivative is

$$\bar{\nabla}\check{g} \equiv \nabla\check{g} - ie \left[ \hat{\mathbf{A}}, \check{g} \right], \quad \hat{\mathbf{A}} = \mathbf{A}\hat{\rho}_3, \quad (2.8)$$

where  $\mathbf{A}$  is the vector potential, and

$$\check{g} = \begin{pmatrix} \hat{g}^R & \hat{g}^K \\ 0 & \hat{g}^A \end{pmatrix} \quad (2.9)$$

is the spherically symmetric part of the quasiclassical impurity-averaged Green's function, which satisfies the normalization condition

$$\check{g}\check{g} = 1. \quad (2.10)$$

The derivation of eq. (2.7) comes in section 2.2.1.

In equilibrium, the components of the  $8 \times 8$  Green's function in eq. (2.4) are related by the identities [20]

$$\hat{g}^K = (\hat{g}^R - \hat{g}^A) \tanh\left(\frac{\varepsilon\beta}{2}\right) \quad \text{and} \quad \hat{g}^A = -\hat{\rho}_3 \hat{g}^{R\dagger} \hat{\rho}_3, \quad (2.11)$$

which means that it is in general sufficient to solve for the retarded component  $\hat{g}^R$  when the system is in equilibrium. In this thesis I will assume equilibrium.

The quasiclassical formalism is not applicable across boundaries because the associated length scale is too short. Equation (2.7) must therefore be solved in different materials separately, and the solutions must be connected through boundary conditions. These boundary are obtained by solving the full microscopic equations at the boundaries and then connecting them to the quasiclassical Green's functions [25], and can be written

$$G_i L_i \mathbf{e}_n \cdot (\hat{g}_i^R \bar{\nabla} \hat{g}_i^R) = \hat{I}(\hat{g}_i^R, \hat{g}_j^R), \quad (2.12)$$

where  $\mathbf{e}_n$  is the outward-pointing normal vector for region  $i$ ,  $G_i$  is the bulk conductance of material  $i$  and  $L_i$  is the length of material  $i$  in the direction of  $\mathbf{e}_n$ .  $\hat{I}(\hat{g}_i^R, \hat{g}_j^R)$  is the matrix current from material  $i$  to material  $j$ . The form of  $\hat{I}$  will depend on what kind of boundary is being considered and will be different in chapters 3 and 4.

The Usadel equation can be made dimensionless by introducing the Thouless energy,

$$\varepsilon_T = \frac{D}{L^2}, \quad (2.13)$$

where  $L$  some length scale and  $D$  is a diffusion constant.  $\varepsilon_T$  can be interpreted as the time it takes for a diffusive system with diffusivity constant  $D$  to diffuse over the length scale  $L$ . To see why, note that  $\varepsilon_T$  is also the constant which makes the normal diffusion equation dimensionless [26]. Doing the substitutions  $\nabla \rightarrow L\nabla$ ,  $\mathbf{A} \rightarrow L\mathbf{A}$ ,  $\varepsilon \rightarrow \varepsilon/\varepsilon_T$  and  $\Delta \rightarrow \Delta/\varepsilon_T$  renders all the quantities in the Usadel equation dimensionless.

In general, the Usadel equation has to be solved together with the Maxwell equation,

$$\nabla \times \mathbf{B} = \mu_0 \mathbf{j}, \quad (2.14)$$

in a self-consistent manner. However, we are here interested in the case where the junctions are smaller than the Josephson penetration depth

$$\lambda_j = \sqrt{\frac{\hbar}{2\mu_0 e j_c d}}, \quad (2.15)$$

where  $j_c$  is the critical current per unit area and

$$d = L + \lambda_1 + \lambda_2 \quad (2.16)$$

is the effective length of the junction where  $L$  is the length of the junction and  $\lambda_1$  and  $\lambda_2$  are the London penetration depths in the superconductors. In eq. (2.16) it is assumed that the lengths of the superconductors are large compared to their penetration depths. When the junction is small compared to the Josephson penetration depths, we can ignore the screening of the magnetic field by the Josephson currents and the field is equal to the external one [27].

### 2.2.1 Derivation of the Usadel Equation

The starting point of this derivation is the Green's function  $\check{G}$  defined in eq. (2.2) and eq. (2.4). In order to write down an equation of motion for  $\check{G}$ , we will use the fact that in the Heisenberg picture the field operators satisfy the Heisenberg equation [21]

$$\frac{\partial \psi_\sigma}{\partial t} = i[H, \psi_\sigma]. \quad (2.17)$$

Assume that the Hamiltonian can be written as a sum of terms consisting of two field operators,

$$H = \int d^3r \sum_{\sigma\sigma'} \left\{ \psi_\sigma^\dagger(\mathbf{r}) \left[ \frac{\delta_{\sigma\sigma'}}{2m} (-i\nabla_{\mathbf{r}} - e\mathbf{A}(\mathbf{r}))^2 + h_{\sigma\sigma'}(\mathbf{r}) \right] \psi_{\sigma'}(\mathbf{r}) + \frac{1}{2} \left[ \gamma_{\sigma\sigma'}(\mathbf{r}) \psi_\sigma^\dagger(\mathbf{r}) \psi_{\sigma'}^\dagger(\mathbf{r}) + \gamma_{\sigma'\sigma}^*(\mathbf{r}) \psi_\sigma(\mathbf{r}) \psi_{\sigma'}(\mathbf{r}) \right] \right\}. \quad (2.18)$$

Using that the field operators satisfy the anticommutation relations

$$\{\psi_\sigma(\mathbf{r}, t), \psi_{\sigma'}(\mathbf{r}', t)\} = 0, \quad (2.19a)$$

$$\{\psi_\sigma(\mathbf{r}, t), \psi_{\sigma'}^\dagger(\mathbf{r}', t)\} = \delta_{\sigma\sigma'} \delta(\mathbf{r} - \mathbf{r}'), \quad (2.19b)$$

$$\{\psi_{\sigma'}^\dagger(\mathbf{r}, t), \psi_{\sigma'}^\dagger(\mathbf{r}', t)\} = 0, \quad (2.19c)$$

we see that we may choose  $\gamma_{\sigma\sigma'}(\mathbf{r}) = -\gamma_{\sigma'\sigma}(\mathbf{r})$ . Additionally, because  $H$  is Hermitian,  $h_{\sigma\sigma'}(\mathbf{r}) = h_{\sigma'\sigma}^*(\mathbf{r})$ .

To calculate the commutator needed in the Heisenberg equation we first define the part of  $H$  which involve differentiation,

$$H_0 := \int d^3r \sum_\sigma \frac{1}{2m} \psi_\sigma^\dagger(\mathbf{r}) (-i\nabla_{\mathbf{r}} - e\mathbf{A}(\mathbf{r}))^2 \psi_\sigma(\mathbf{r}). \quad (2.20)$$

Using the fact that

$$[AB, C] = A\{B, C\} - \{A, C\}B, \quad (2.21)$$

I get that

$$\begin{aligned} [H_0, \psi_\sigma(\mathbf{r})] &= \frac{1}{2m} \sum_{\sigma'} \int d^3r' \left[ \underbrace{\psi_{\sigma'}^\dagger(\mathbf{r}') \{(-i\nabla_{\mathbf{r}'} - e\mathbf{A}(\mathbf{r}'))^2 \psi_{\sigma'}(\mathbf{r}'), \psi_\sigma(\mathbf{r})\}}_{=0} \right. \\ &\quad \left. - \underbrace{\{\psi_{\sigma'}^\dagger(\mathbf{r}'), \psi_\sigma(\mathbf{r})\}}_{=\delta_{\sigma'\sigma} \delta(\mathbf{r}' - \mathbf{r})} (-i\nabla_{\mathbf{r}'} - e\mathbf{A}(\mathbf{r}'))^2 \psi_{\sigma'}(\mathbf{r}') \right] = -\frac{1}{2m} (-i\nabla_{\mathbf{r}} - e\mathbf{A}(\mathbf{r}))^2 \psi_\sigma(\mathbf{r}), \end{aligned} \quad (2.22)$$

where the first anticommutator is 0 because differentiation with respect to  $\mathbf{r}'$  commutes with  $\psi_\sigma(\mathbf{r})$  and can therefore be pulled outside the anticommutator. From the linearity of the commutator, therefore,

$$\begin{aligned} [H, \psi_\sigma(\mathbf{r})] &= -\frac{1}{2m} (-i\nabla_{\mathbf{r}} - e\mathbf{A}(\mathbf{r}))^2 \psi_\sigma(\mathbf{r}) \\ &\quad + \sum_{\sigma'\sigma''} \int^3 r' \left\{ h_{\sigma'\sigma''}(\mathbf{r}') \left( \underbrace{\psi_{\sigma'}^\dagger(\mathbf{r}') \{\psi_{\sigma''}(\mathbf{r}'), \psi_\sigma(\mathbf{r})\}}_{=0} - \underbrace{\{\psi_{\sigma'}^\dagger(\mathbf{r}'), \psi_\sigma(\mathbf{r})\}}_{=\delta_{\sigma'\sigma} \delta(\mathbf{r}' - \mathbf{r})} \psi_{\sigma''}(\mathbf{r}') \right) \right. \\ &\quad + \frac{1}{2} \left[ \gamma_{\sigma'\sigma''}(\mathbf{r}') \left( \underbrace{\psi_{\sigma'}^\dagger(\mathbf{r}') \{\psi_{\sigma''}^\dagger(\mathbf{r}'), \psi_\sigma(\mathbf{r})\}}_{=\delta_{\sigma''\sigma} \delta(\mathbf{r}' - \mathbf{r})} - \underbrace{\{\psi_{\sigma'}^\dagger(\mathbf{r}'), \psi_\sigma(\mathbf{r})\}}_{=\delta_{\sigma'\sigma} \delta(\mathbf{r}' - \mathbf{r})} \psi_{\sigma''}^\dagger(\mathbf{r}') \right) \right. \\ &\quad \left. \left. \gamma_{\sigma''\sigma'}^*(\mathbf{r}') \left( \underbrace{\psi_{\sigma'}(\mathbf{r}') \{\psi_{\sigma''}(\mathbf{r}'), \psi_\sigma(\mathbf{r})\}}_{=0} - \underbrace{\{\psi_{\sigma'}(\mathbf{r}'), \psi_\sigma(\mathbf{r})\}}_{=0} \psi_{\sigma''}(\mathbf{r}') \right) \right] \right\} = \\ &\quad - \sum_{\sigma'} \left\{ \frac{\delta_{\sigma\sigma'}}{2m} (-i\nabla_{\mathbf{r}} - e\mathbf{A}(\mathbf{r}))^2 \psi_{\sigma'}(\mathbf{r}) + h_{\sigma\sigma'}(\mathbf{r}) \psi_{\sigma'}(\mathbf{r}) - \gamma_{\sigma\sigma'}(\mathbf{r}) \psi_{\sigma'}^\dagger(\mathbf{r}) \right\}. \end{aligned} \quad (2.23)$$

Using the fact that

$$[A, B^\dagger] = (AB^\dagger - B^\dagger A) = (BA^\dagger - A^\dagger B)^\dagger = -([A^\dagger, B])^\dagger, \quad (2.24)$$

and that the Hamiltonian is Hermitian, I get<sup>1</sup>

$$[H, \psi_\sigma^\dagger(\mathbf{r})] = \sum_{\sigma'} \left\{ \frac{\delta_{\sigma\sigma'}}{2m} (-i\nabla_{\mathbf{r}} + e\mathbf{A}(\mathbf{r}))^2 \psi_{\sigma'}^\dagger(\mathbf{r}) + h_{\sigma\sigma'}(\mathbf{r}) \psi_{\sigma'}^\dagger(\mathbf{r}) - \gamma_{\sigma\sigma'}^*(\mathbf{r}) \psi_{\sigma'}(\mathbf{r}) \right\}. \quad (2.25)$$

<sup>1</sup> Another way to achieve this would be to calculate it in the same manner as for  $\psi$  above. If this is the preferred way to proceed one must be careful with the Dirac delta functions arising from the anticommutations. One must use partial integration in order to make them go outside the differentiation.

Defining the matrix

$$\bar{H} := \begin{pmatrix} h_{\uparrow\uparrow} & h_{\uparrow\downarrow} & 0 & -\gamma_{\uparrow\downarrow} \\ h_{\downarrow\uparrow} & h_{\downarrow\downarrow} & -\gamma_{\downarrow\uparrow} & 0 \\ 0 & -\gamma_{\uparrow\downarrow}^* & h_{\uparrow\uparrow} & h_{\uparrow\downarrow} \\ -\gamma_{\downarrow\uparrow}^* & 0 & h_{\downarrow\uparrow} & h_{\downarrow\downarrow} \end{pmatrix} + \frac{1}{2m} \begin{pmatrix} (-i\nabla_{\mathbf{r}} - e\mathbf{A})^2 & 0 & 0 & 0 \\ 0 & (-i\nabla_{\mathbf{r}} - e\mathbf{A})^2 & 0 & 0 \\ 0 & 0 & (-i\nabla_{\mathbf{r}} + e\mathbf{A})^2 & 0 \\ 0 & 0 & 0 & (-i\nabla_{\mathbf{r}} + e\mathbf{A})^2 \end{pmatrix}, \quad (2.26)$$

the time evolution of the bispinors defined in eq. (2.1) may be written

$$i\hat{\rho}_3 \frac{\partial}{\partial t} \psi(\mathbf{r}, t) = \bar{H}(\mathbf{r})\psi(\mathbf{r}, t), \quad i\frac{\partial}{\partial t} \psi^\dagger(\mathbf{r}, t)\hat{\rho}_3 = -\psi^\dagger(\mathbf{r}, t)\bar{H}^\dagger(\mathbf{r}). \quad (2.27)$$

Differentiating the retarded Greens functions (2.2a), using the product rule and the fact that the derivative of the Heaviside step function is the Dirac delta function,<sup>2</sup>

$$\begin{aligned} i\frac{\partial}{\partial t} \hat{\rho}_3 \hat{G}^{\text{R}}(\mathbf{r}, t, \mathbf{r}', t') &= i\frac{\partial}{\partial t} \hat{\rho}_3 \left( -i\theta(t-t') \hat{\rho}_3 \left\langle \left\{ \psi(\mathbf{r}, t), \psi^\dagger(\mathbf{r}', t') \right\} \right\rangle \right) \\ &= \delta(t-t') \left\langle \left\{ \psi(\mathbf{r}, t), \psi^\dagger(\mathbf{r}', t) \right\} \right\rangle - i\theta(t-t') \hat{\rho}_3 \left\langle \left\{ i\frac{\partial}{\partial t} \hat{\rho}_3 \psi(\mathbf{r}, t), \psi^\dagger(\mathbf{r}', t') \right\} \right\rangle \\ &= \delta(t-t') \delta(\mathbf{r} - \mathbf{r}') + \hat{\rho}_3 \bar{H} \hat{\rho}_3 \hat{G}^{\text{R}}(\mathbf{r}, t, \mathbf{r}', t'), \end{aligned} \quad (2.28)$$

where in the last equality the anticommutation relations (2.19) between the field operators at equal times was used. Further, the linearity of the expectation value was used to extract  $\bar{H}$  from the expectation value. The time evolution of the advanced and the Keldysh Green's functions can be evaluated in the same manner, and the time evolution of the full  $8 \times 8$  Green's function matrix reads

$$\left( i\frac{\partial}{\partial t} \hat{\rho}_3 - \check{H} \right) \check{G}(\mathbf{r}, t, \mathbf{r}', t) = \delta(t-t') \delta(\mathbf{r} - \mathbf{r}'), \quad (2.29)$$

where

$$\check{H} = \begin{pmatrix} \hat{\rho}_3 \bar{H} \hat{\rho}_3 & 0 \\ 0 & \hat{\rho}_3 \bar{H} \hat{\rho}_3 \end{pmatrix}. \quad (2.30)$$

Equation (2.29) is known as the Gor'kov's equation [28, 29].

Similarly, one may differentiate the Green's functions with respect to the other time variable,  $t'$ , in which a similar calculation yields<sup>3</sup>

$$\check{G}(\mathbf{r}, t, \mathbf{r}', t') \left( i\frac{\partial}{\partial t'} \hat{\rho}_3 - \hat{\rho}_3 \check{H}(\mathbf{r}') \hat{\rho}_3 \right)^\dagger = \delta(t-t') \delta(\mathbf{r} - \mathbf{r}'), \quad (2.31)$$

where the time differentiation and  $\check{H}$  acts to the left. Subtracting eq. (2.31) from eq. (2.29) gives

$$\left( i\frac{\partial}{\partial t} \hat{\rho}_3 - \check{H}(\mathbf{r}) \right) \check{G}(\mathbf{r}, t, \mathbf{r}', t) - \check{G}(\mathbf{r}, t, \mathbf{r}', t') \left( i\frac{\partial}{\partial t'} \hat{\rho}_3 - \hat{\rho}_3 \check{H}(\mathbf{r}') \hat{\rho}_3 \right)^\dagger = 0. \quad (2.32)$$

<sup>2</sup>While the step function is not differentiable when interpreted as a function, it is differentiable in the distributional sense. The distributional derivative of the step distribution is indeed the Dirac delta distribution [26] See section 1.2.

<sup>3</sup>Note that the  $\hat{\rho}_3$  in the expression for  $\check{H}$  in eq. (2.29) came from the fact that the Hamiltonian was extracted to the left and had to be moved past a  $\hat{\rho}_3$  in eq. (2.28). This does not happen in eq. (2.31) because the Hamiltonian is extracted to the right.

Note that the effect of  $\hat{\rho}_3$  in eq. (2.30) is to change the sign of the upper right and lower left  $2 \times 2$  block of  $\bar{H}$ , and that this is undone by taking the adjoint. Therefore, if we define

$$\check{H}_0 = \begin{pmatrix} \bar{H}_0 & 0 \\ 0 & \bar{H}_0 \end{pmatrix}, \quad (2.33a)$$

$$\check{H}_I := \check{H} - \check{H}_0, \quad (2.33b)$$

where

$$H_0 := \frac{1}{2m} (-i\nabla_{\mathbf{r}} - e\mathbf{A}\hat{\rho}_3)^2, \quad (2.34)$$

we may write eq. (2.35) as

$$\begin{aligned} \left( i \frac{\partial}{\partial t} \hat{\rho}_3 - \check{H}_0(\mathbf{r}) \right) \check{G}(\mathbf{r}, t, \mathbf{r}', t) - \check{G}(\mathbf{r}, t, \mathbf{r}', t') \left( i \frac{\partial}{\partial t} \hat{\rho}_3 - \check{H}_0(\mathbf{r}') \right)^\dagger \\ - \check{H}_I(\mathbf{r}) \check{G}(\mathbf{r}, t, \mathbf{r}', t) + \check{G}(\mathbf{r}, t, \mathbf{r}', t) \check{H}_I(\mathbf{r}') = 0. \end{aligned} \quad (2.35)$$

Next, it will be useful to introduce the notation of the *bullet product*,<sup>4</sup>

$$A \bullet B(\mathbf{r}_1, t_1, \mathbf{r}_2, t_2) = \int d^3r_3 dt_3 A(\mathbf{r}_1, t_1, \mathbf{r}_3, t_3) B(\mathbf{r}_3, t_3, \mathbf{r}_2, t_2) \quad (2.36)$$

Finally, instead of looking at the Green's function for a particular system, we are interested in the *impurity averaged Green's function*. In the self-consistent Born approximation the impurity averaged Green's function can be found by using the self energy [30]

$$\tilde{\Sigma} = \Sigma_{\text{imp}} + \Sigma, \quad (2.37)$$

where  $\Sigma_{\text{imp}}$  is the impurity averaged self energy resulting from the impurity potentials and

$$\Sigma(\mathbf{r}_1, t_1, \mathbf{r}_2, t_2) = \delta(\mathbf{r}_1 - \mathbf{r}_2) \delta(t_1 - t_2) \check{H}_I(\mathbf{r}_1), \quad (2.38)$$

such that the Gor'kov equations can be written

$$\begin{aligned} \left( i \frac{\partial}{\partial t_1} \hat{\rho}_3 - \check{H}_0(\mathbf{r}_1) \right) \check{G}(\mathbf{r}_1, t_1, \mathbf{r}_2, t_2) - \check{G}(\mathbf{r}_1, t_1, \mathbf{r}_2, t_2) \left( i \frac{\partial}{\partial t_2} \hat{\rho}_3 - \check{H}_0(\mathbf{r}_2) \right)^\dagger \\ - (\tilde{\Sigma} \bullet \check{G})(\mathbf{r}_1, t_1, \mathbf{r}_2, t_2) + (\check{G} \bullet \tilde{\Sigma})(\mathbf{r}_1, t_1, \mathbf{r}_2, t_2) = 0. \end{aligned} \quad (2.39)$$

The next step is to go to the Wigner representation, in which we Fourier transform the relative coordinates.

### Wigner Representation

First, define the relative coordinates,

$$t = t_1 - t_2, \quad \mathbf{r} = \mathbf{r}_1 - \mathbf{r}_2, \quad (2.40)$$

and the center of mass coordinates,

$$T = \frac{t_1 + t_2}{2}, \quad \mathbf{R} = \frac{\mathbf{r}_1 + \mathbf{r}_2}{2}. \quad (2.41)$$

<sup>4</sup> In the literature the bullet product is sometimes known as a convolution, although the definition is slightly different from the standard definition of a convolution product. However, if  $A$  and  $B$  depend only on the difference between their two parameters, eq. (2.36) can be rewritten  $\int dx_3 A(x_1 - x_2 - x_3) B(x_3) \equiv (A * B)(x_1 - x_2)$ , where  $*$  is the standard convolution product.



If we denote which variable we differentiate with respect to by a subscript, we can rewrite the differential operators in eq. (2.39) in terms of the relative and center of mass coordinates,

$$\frac{\partial}{\partial t_1} = \frac{\partial}{\partial t} + \frac{1}{2} \frac{\partial}{\partial T} \quad (2.42a)$$

$$\frac{\partial}{\partial t_2} = -\frac{\partial}{\partial t} + \frac{1}{2} \frac{\partial}{\partial T} \quad (2.42b)$$

$$\nabla_{\mathbf{r}_1} = \nabla_{\mathbf{r}} + \frac{1}{2} \nabla_{\mathbf{R}} \quad (2.42c)$$

$$\nabla_{\mathbf{r}_2} = -\nabla_{\mathbf{r}} + \frac{1}{2} \nabla_{\mathbf{R}} \quad (2.42d)$$

$$\nabla_{\mathbf{r}_1}^2 - \nabla_{\mathbf{r}_2}^2 = \left( \nabla_{\mathbf{r}} + \frac{1}{2} \nabla_{\mathbf{R}} \right)^2 - \left( -\nabla_{\mathbf{r}} + \frac{1}{2} \nabla_{\mathbf{R}} \right)^2 = 2 \nabla_{\mathbf{r}} \cdot \nabla_{\mathbf{R}} \quad (2.42e)$$

With this, the part of eq. (2.39) containing  $\check{H}_0$  becomes

$$\begin{aligned} & -\check{H}_0 \left( \mathbf{R} + \frac{1}{2} \mathbf{r} \right) \check{G}(\mathbf{R}, T, \mathbf{r}, t) + \check{G}(\mathbf{R}, T, \mathbf{r}, t) \check{H}_0^\dagger \left( \mathbf{R} - \frac{1}{2} \mathbf{r} \right) \\ &= \frac{1}{m} \nabla_{\mathbf{r}} \cdot \nabla_{\mathbf{R}} \check{G}(\mathbf{R}, T, \mathbf{r}, t) - \frac{i}{2m} \left( \hat{\mathbf{A}} \left( \mathbf{R} + \frac{1}{2} \mathbf{r} \right) \cdot [\nabla_{\mathbf{r}} \check{G}(\mathbf{R}, T, \mathbf{r}, t)] - [\nabla_{\mathbf{r}} \check{G}(\mathbf{R}, T, \mathbf{r}, t)] \cdot \hat{\mathbf{A}} \left( \mathbf{R} - \frac{1}{2} \mathbf{r} \right) \right) \\ & \quad - \frac{i}{4m} \left( \hat{\mathbf{A}} \left( \mathbf{R} + \frac{1}{2} \mathbf{r} \right) \cdot [\nabla_{\mathbf{R}} \check{G}(\mathbf{R}, T, \mathbf{r}, t)] + [\nabla_{\mathbf{R}} \check{G}(\mathbf{R}, T, \mathbf{r}, t)] \cdot \hat{\mathbf{A}} \left( \mathbf{R} - \frac{1}{2} \mathbf{r} \right) \right) \\ & \quad - \frac{i}{2m} \nabla_{\mathbf{r}} \cdot \left( \hat{\mathbf{A}} \left( \mathbf{R} + \frac{1}{2} \mathbf{r} \right) \check{G}(\mathbf{R}, T, \mathbf{r}, t) - \check{G}(\mathbf{R}, T, \mathbf{r}, t) \hat{\mathbf{A}} \left( \mathbf{R} - \frac{1}{2} \mathbf{r} \right) \right) \\ & \quad - \frac{i}{4m} \nabla_{\mathbf{R}} \cdot \left( \hat{\mathbf{A}} \left( \mathbf{R} + \frac{1}{2} \mathbf{r} \right) \check{G}(\mathbf{R}, T, \mathbf{r}, t) + \check{G}(\mathbf{R}, T, \mathbf{r}, t) \hat{\mathbf{A}} \left( \mathbf{R} - \frac{1}{2} \mathbf{r} \right) \right) \\ & \quad - \frac{1}{2m} \left( \hat{\mathbf{A}}^2 \left( \mathbf{R} + \frac{1}{2} \mathbf{r} \right) \check{G}(\mathbf{R}, T, \mathbf{r}, t) - \check{G}(\mathbf{R}, T, \mathbf{r}, t) \hat{\mathbf{A}}^2 \left( \mathbf{R} - \frac{1}{2} \mathbf{r} \right) \right), \quad (2.43) \end{aligned}$$

where  $\hat{\mathbf{A}} = e \hat{\rho}_3 A$ , and the part containing time differentiation becomes

$$\begin{aligned} i \frac{\partial}{\partial t_1} \hat{\rho}_3 \check{G}(\mathbf{R}, T, \mathbf{r}, t) + i \frac{\partial}{\partial t_2} \check{G}(\mathbf{R}, T, \mathbf{r}, t) \hat{\rho}_3 &= \frac{i}{2} \left[ \hat{\rho}_3 \frac{\partial}{\partial T} \check{G}(\mathbf{R}, T, \mathbf{r}, t) + \frac{\partial}{\partial T} \check{G}(\mathbf{R}, T, \mathbf{r}, t) \hat{\rho}_3 \right] \\ & \quad + i \left[ \hat{\rho}_3 \frac{\partial}{\partial t} \check{G}(\mathbf{R}, T, \mathbf{r}, t) - \frac{\partial}{\partial t} \check{G}(\mathbf{R}, T, \mathbf{r}, t) \hat{\rho}_3 \right] \quad (2.44) \end{aligned}$$

To get the Wigner representation, we Fourier transform in the relative coordinates,

$$\mathcal{F}\{A\}(\mathbf{R}, T, \mathbf{p}, \varepsilon) = \int d^3 r dt e^{-i(\mathbf{p} \cdot \mathbf{r} - \varepsilon t)} A(\mathbf{R}, T, \mathbf{r}, t). \quad (2.45)$$

Assuming  $A$  and  $B$  can be Taylor expanded, one can show that the Fourier transform in the relative coordinates of a bullet product is given by [30]

$$\begin{aligned} \mathcal{F}\{A \bullet B\} &\equiv \int d^3 r dt e^{-i(\mathbf{p} \cdot \mathbf{r} - \varepsilon t)} (A \bullet B)(\mathbf{R}, T, \mathbf{r}, t) \\ &= \exp \left( -\frac{i}{2} \partial_T^A \partial_\varepsilon^B + \frac{i}{2} \partial_\varepsilon^A \partial_T^B \right) \exp \left( \frac{i}{2} \nabla_{\mathbf{R}}^A \nabla_{\mathbf{p}}^B - \frac{i}{2} \nabla_{\mathbf{p}}^A \nabla_{\mathbf{R}}^B \right) A(\mathbf{R}, T, \mathbf{p}, \varepsilon) B(\mathbf{R}, T, \mathbf{p}, \varepsilon), \quad (2.46) \end{aligned}$$

where the superscripts denote which function the differential operators acts on. To lowest order in gradients, Fourier transforming a bullet product therefore results in

$$\mathcal{F}\{A \bullet B\} \approx \mathcal{F}\{A(\mathbf{R}, T, \mathbf{r}, t)\} \mathcal{F}\{B(\mathbf{R}, T, \mathbf{r}, t)\} \equiv A(\mathbf{R}, T, \mathbf{p}, \varepsilon) B(\mathbf{R}, T, \mathbf{p}, \varepsilon). \quad (2.47)$$

The explanation for why keeping only the zeroth order in the gradient expansion (2.46) is reasonable will come when we discuss the quasiclassical approximation below. Note that

$$\hat{\mathbf{A}}\left(\mathbf{R} + \frac{1}{2}\mathbf{r}\right) \check{G}(\mathbf{R}, T, \mathbf{r}, t) = \left[ \hat{\mathbf{A}}\left(\mathbf{R} + \frac{1}{2}\mathbf{r}\right) \delta(\mathbf{r})\delta(t) \right] \bullet \check{G}(\mathbf{R}, T, \mathbf{r}, t) \quad (2.48)$$

and

$$\mathcal{F} \left\{ \hat{\mathbf{A}}\left(\mathbf{R} + \frac{1}{2}\mathbf{r}\right) \delta(\mathbf{r})\delta(t) \right\} = \hat{\mathbf{A}}(\mathbf{R}). \quad (2.49)$$

With eq. (2.47) and assuming  $\check{G}$  independent of  $T$ , we may write the Gorkov's equation in the Wigner representation as

$$\begin{aligned} \frac{i}{m}\mathbf{p} \cdot \left( \nabla_{\mathbf{R}}\check{G}(\mathbf{R}, \mathbf{p}, \varepsilon) - i \left[ \hat{\mathbf{A}}(\mathbf{R}), \check{G}(\mathbf{R}, \mathbf{p}, \varepsilon) \right] \right) \\ - \left[ \frac{1}{2m}\hat{\mathbf{A}}^2(\mathbf{R}) + \tilde{\Sigma}(\mathbf{R}, \mathbf{p}, \varepsilon) - \varepsilon\hat{\rho}_3, \check{G}(\mathbf{R}, \mathbf{p}, \varepsilon) \right] \\ - \frac{i}{4m} \left( \nabla_{\mathbf{R}} \left\{ \hat{\mathbf{A}}(\mathbf{R}), \check{G}(\mathbf{R}, \mathbf{p}, \varepsilon) \right\} + \left\{ \hat{\mathbf{A}}(\mathbf{R}), \nabla_{\mathbf{R}}\check{G}(\mathbf{R}, \mathbf{p}, \varepsilon) \right\} \right) = 0. \end{aligned} \quad (2.50)$$

Defining the covariant derivative,

$$\bar{\nabla}\check{G}(\mathbf{R}, \mathbf{p}, \varepsilon) := \nabla_{\mathbf{R}}\check{G}(\mathbf{R}, \mathbf{p}, \varepsilon) - i \left[ \hat{\mathbf{A}}(\mathbf{R}), \check{G}(\mathbf{R}, \mathbf{p}, \varepsilon) \right], \quad (2.51)$$

and dropping the function parameters for notational clarity, eq. (2.50) can be written

$$\frac{i}{m}\mathbf{p} \cdot \bar{\nabla}\check{G} - \left[ \frac{1}{2m}\hat{\mathbf{A}}^2 + \tilde{\Sigma} - \varepsilon\hat{\rho}_3, \check{G} \right] - \frac{i}{4m} \left( \nabla_{\mathbf{R}} \left\{ \hat{\mathbf{A}}, \check{G} \right\} + \left\{ \hat{\mathbf{A}}, \nabla_{\mathbf{R}}\check{G} \right\} \right) = 0 \quad (2.52)$$

### The Quasiclassical Approximation

In the quasiclassical approximation the Fermi wavelength,  $\lambda_F$ , is assumed much smaller than the other relevant physical length scales. The covariant derivative defines a characteristic length scale,  $L$ , over which the system changes in the center of mass coordinate  $\mathbf{R}$ . A formal way of such a definition is shown in definition 2.1.

**Definition 2.1.**  $L \in \mathbb{R}$  is the characteristic length scale over which the system changes if it is the greatest real number satisfying

$$L\|\bar{\nabla}F\| < \|F\| \quad (2.53)$$

for all physical quantities  $F$  of interest. Here  $\|\cdot\|$  is some norm on the relevant space of functions.

In the quasiclassical approximation,  $L \gg \lambda_F$ , and since in the quasiclassical approximation we are assuming the momentum relevant for describing the physical behaviour is at the Fermi surface, the momentum  $\mathbf{p}$  is of the order  $1/\lambda_F$ , so

$$\mathbf{p} \cdot \bar{\nabla}\check{G}$$

is of order  $1/(\lambda_FL)$ , while

$$\left[ \frac{1}{2m}\hat{\mathbf{A}}^2, \check{G} \right] - \frac{i}{4m} \left( \nabla_{\mathbf{R}} \left\{ \hat{\mathbf{A}}, \check{G} \right\} + \left\{ \hat{\mathbf{A}}, \nabla_{\mathbf{R}}\check{G} \right\} \right)$$

is of order  $1/L^2$  and is therefore negligible in the quasiclassical approximation.  $\nabla_{\mathbf{p}}$  is of the order  $\lambda_F$ , so the right hand side of eq. (2.46) corresponds to an expansion in  $\lambda_F/L$ , which justifies keeping only the zeroth order in the gradient expansion above.

An expression for the impurity averaged self energy  $\Sigma_{\text{imp}}$  in the self consistent Born approximation has been derived for the quasiclassical limit in [20, 30], and can be written

$$\Sigma_{\text{imp}}(\mathbf{R}, \mathbf{p}_F, \varepsilon) = -\frac{i}{2\tau} \check{g}_s(\mathbf{R}, \mathbf{p}_F, \varepsilon), \quad (2.54)$$

where  $\tau$  is the scattering time and

$$\check{g}_s(\mathbf{R}, T, \varepsilon) = \int \frac{d\Omega_p}{4\pi} \check{g}(\mathbf{R}, T, \mathbf{p}_F, \varepsilon) = \frac{i}{\pi N_0} \int \frac{d^3p}{(2\pi)^3} \check{G}(\mathbf{R}, T, \mathbf{p}, \varepsilon), \quad (2.55)$$

is the spherically symmetric part of the quasiclassical Green's function.

Finally, integrating eq. (2.52) with respect to energy and using the definition of the quasiclassical Green's function (2.5), we get the Eilenberg equation,

$$\frac{\mathbf{p}_F}{m} \cdot \bar{\nabla} \check{g} + \left[ \frac{1}{2\tau} \check{g}_s + i\Sigma - i\varepsilon \hat{\rho}_3, \check{g} \right] = 0, \quad (2.56)$$

where  $\mathbf{p}_F$  is the Fermi momentum. Equation (2.56) is simpler than the Gorkov equation (2.52) in that it has one less degree of freedom because the quasiclassical Green's function depend only on the direction of the momentum, not on the magnitude. By going from the Eilenberg equation to the Usadel equation in the final step of the derivation, we will get rid of the dependence on the direction of momentum as well. Thus since we have assumed the solution independent of  $T$ , the only degrees of freedom left will be  $\mathbf{R}$  and  $\varepsilon$ . To do this, we will consider dirty materials. First, however, we must address the question of normalization.

### Normalization

The Eilenberg equation (2.56) is homogeneous, which implies that if  $\check{g}$  is a solution, then so is  $c\check{g}$  for all scalars  $c$ . Hence, eq. (2.56) does not fully determine  $\check{g}$ . This indeterminacy is not present in the original Gorkov equations, eqs. (2.29) and (2.31), but came from the fact that the inhomogeneity was removed when subtracting eq. (2.31) from eq. (2.29). To find  $\check{g}$ , therefore, we must employ an additional normalization condition. The normalization condition typically used in the literature [5, 23, 31] is

$$\check{g}\check{g} = 1. \quad (2.57)$$

Remember that  $\check{g}$  is an  $8 \times 8$  matrix, and hence it is not a priori given that multiplying  $\check{g}$  by a scalar can result in an involutory matrix<sup>5</sup>. However, it can be explicitly shown by starting from the inhomogeneous Gorkov equations, as was done by Shelankov [32], that eq. (2.57) is the correct normalization condition. The derivation by Shalenkov will not be reproduced here, but can be found for instance in [20].

### The Dirty Limit

*Dirty materials* are those with a large number of impurities such that the scattering time,  $\tau$ , is small and the impurity scattering term dominates the Eilenberg equation (2.56). When  $\tau$  is small the particles will be frequently scattered, and this has an averaging effect on direction of particle propagation. Hence, it is reasonable to expand the quasiclassical Green's function in spherical harmonics and assume that the lowest order will dominate.

Following Usadel [24] we expand  $\check{g}$  in a  $s$ -wave and a  $p$ -wave,

$$\check{g}(\mathbf{R}, \mathbf{p}_F, \varepsilon) = \check{g}_s(\mathbf{R}, \varepsilon) + \mathbf{e}_F \cdot \check{\mathbf{g}}_p(\mathbf{R}, \varepsilon), \quad (2.58)$$

<sup>5</sup>An *involutory matrix* is a matrix that is its own inverse.

where  $\check{g}_s$  is the isotropic part and  $\mathbf{e}_F \cdot \check{\mathbf{g}}_p$  is the linearized anisotropy with respect to the transport direction,

$$\mathbf{e}_F := \frac{\mathbf{p}_F}{|\mathbf{p}_F|}. \quad (2.59)$$

The anisotropic part is assumed small and by neglecting second order terms in  $\check{\mathbf{g}}_p$ , the normalization condition (2.57) becomes

$$\check{g}_s \check{g}_s = 1, \quad \check{g}_s \check{\mathbf{g}}_p + \check{\mathbf{g}}_p \check{g}_s = \mathbf{0}. \quad (2.60)$$

Plugging eq. (2.58) into the Eilenberg equation (2.56) and performing an angular average in momentum space,  $\int d\Omega_p / (4\pi)$ ,

$$\frac{v_F}{3} \bar{\nabla} \cdot \check{\mathbf{g}}_p - i [\varepsilon \hat{\rho}_3 - \Sigma, \check{g}_s] = 0, \quad (2.61)$$

where  $v_F = |\mathbf{p}_F|/m$ .

By first multiplying the Eilenberg equation (2.56) with  $\mathbf{e}_F$  and then average over angles in momentum space,

$$v_F \bar{\nabla} \check{g}_s + \frac{1}{2\tau} [\check{g}_s, \check{\mathbf{g}}_p] = 0, \quad (2.62)$$

where I have used the assumption that the impurity scattering dominates the commutator and hence neglected the remaining terms. Multiplying eq. (2.62) from the left with  $\check{g}_s$  and using the normalization relation eq. (2.60),

$$v_F \check{g}_s \bar{\nabla} \check{g}_s = -\frac{1}{2\tau} (\check{g}_s \check{g}_s \check{\mathbf{g}}_p - \check{g}_s \check{\mathbf{g}}_p \check{g}_s) = -\frac{1}{2\tau} (\check{g}_s \check{g}_s \check{\mathbf{g}}_p + \check{g}_s \check{g}_s \check{\mathbf{g}}_p) = -\frac{1}{\tau} \check{\mathbf{g}}_p. \quad (2.63)$$

Plugging this into eq. (2.61), we finally get the Usadel equation,

$$D \bar{\nabla} \cdot (\check{g}_s \bar{\nabla} \check{g}_s) + i [\varepsilon \hat{\rho}_3 - \Sigma, \check{g}_s] = 0, \quad (2.64)$$

where

$$D := \frac{\tau v_F^2}{3} \quad (2.65)$$

is the diffusion coefficient.

In the BCS theory, superconductivity comes from an effective attractive interaction between electrons of opposite spin and momentum [33, 34]. The Hamiltonian can be written

$$H = H_0 + \int d^3r V(\mathbf{r}) \psi_{\uparrow}^{\dagger}(\mathbf{r}) \psi_{\downarrow}^{\dagger}(\mathbf{r}) \psi_{\downarrow}(\mathbf{r}) \psi_{\uparrow}(\mathbf{r}), \quad (2.66)$$

where  $H_0$  is given by eq. (2.34) and  $V < 0$ . In order to get it on the form of eq. (2.18) we can do a mean field approximation by defining

$$\Delta(\mathbf{r}) := V(\mathbf{r}) \langle \psi_{\downarrow}(\mathbf{r}) \psi_{\uparrow}(\mathbf{r}) \rangle. \quad (2.67)$$

Inserting this into the Hamiltonian, removing the resulting constant term and neglecting terms proportional to  $(\psi_{\downarrow}(\mathbf{r}) \psi_{\uparrow}(\mathbf{r}) - \langle \psi_{\downarrow}(\mathbf{r}) \psi_{\uparrow}(\mathbf{r}) \rangle)^2$ , I get

$$H = H_0 + \int d^3r \left( \Delta(\mathbf{r}) \psi_{\uparrow}^{\dagger}(\mathbf{r}) \psi_{\downarrow}^{\dagger}(\mathbf{r}) + \Delta^*(\mathbf{r}) \psi_{\downarrow}(\mathbf{r}) \psi_{\uparrow}(\mathbf{r}) \right), \quad (2.68)$$

which is of the form of eq. (2.18) with  $\gamma_{\uparrow\downarrow} = \Delta$ . Hence, the self energy in a conventional superconductor is

$$\Sigma = -\hat{\Delta}, \quad (2.69)$$

where

$$\hat{\Delta} := \begin{pmatrix} 0 & 0 & 0 & \Delta(\mathbf{r}) \\ 0 & 0 & -\Delta(\mathbf{r}) & 0 \\ 0 & \Delta^*(\mathbf{r}) & 0 & 0 \\ -\Delta^*(\mathbf{r}) & 0 & 0 & 0 \end{pmatrix}, \quad (2.70)$$

which concludes the derivation of the Usadel equation on the form it is used in this thesis.

### 2.2.2 Parametrization

When solving the Usadel equation numerically, we will use the Ricatti parametrization. By parametrizing  $\hat{g}^R$  in a way that takes advantage of the symmetries and normalization  $\tilde{g}\tilde{g} = \hat{1}$ , the equations can be rewritten to a set of fewer, unconstrained equations. In the Ricatti parametrization, the parameter is the  $2 \times 2$  matrix  $\gamma$  and the retarded Green's function is written

$$\hat{g}^R = \begin{pmatrix} N & 0 \\ 0 & -\tilde{N} \end{pmatrix} \begin{pmatrix} 1 + \gamma\tilde{\gamma} & 2\gamma \\ 2\tilde{\gamma} & 1 + \tilde{\gamma}\gamma \end{pmatrix}, \quad (2.71)$$

where  $N := (1 - \gamma\tilde{\gamma})^{-1}$  and tilde conjugation is  $\tilde{\gamma}(\varepsilon) = \gamma^*(-\varepsilon)$ . Inserting eq. (2.71) into eq. (2.7) I get the following equations for the Ricatti parameters:

$$\begin{aligned} \nabla^2 \gamma &= -2\nabla\gamma \cdot \tilde{N}\tilde{\gamma}\nabla\gamma - 2i\varepsilon\gamma - \Delta\sigma_2 + \gamma\Delta^*\sigma_2\gamma + 4e^2|\mathbf{A}|^2\gamma\tilde{N}(1 + \tilde{\gamma}\gamma) \\ &\quad + 2ie\mathbf{A} \cdot \left[ (1 + \gamma\tilde{\gamma})N\nabla\gamma + \nabla\gamma\tilde{N}(1 + \tilde{\gamma}\gamma) \right] + 2i\gamma e\nabla \cdot \mathbf{A}, \end{aligned} \quad (2.72a)$$

$$\begin{aligned} \nabla^2 \tilde{\gamma} &= -2\nabla\tilde{\gamma} \cdot N\gamma\nabla\tilde{\gamma} - 2i\varepsilon\tilde{\gamma} - \Delta^*\sigma_2^* + \tilde{\gamma}\Delta\sigma_2^*\tilde{\gamma} + 4e^2|\mathbf{A}|^2\tilde{\gamma}N(1 + \gamma\tilde{\gamma}) \\ &\quad - 2ie\mathbf{A} \cdot \left[ (1 + \tilde{\gamma}\gamma)\tilde{N}\nabla\tilde{\gamma} + \nabla\tilde{\gamma}N(1 + \gamma\tilde{\gamma}) \right] - 2i\tilde{\gamma}e\nabla \cdot \mathbf{A}. \end{aligned} \quad (2.72b)$$

### 2.2.3 Bulk BCS Solution

In the systems considered in this thesis superconductors will enter through boundary conditions. It is therefore necessary to know what the quasiclassical impurity-averaged Greens functions are in conventional superconductors. If the superconductors are assumed large in comparison to the center material, the Greens function will be the same as for a bulk superconductor. This is a commonly used approximation when the center material is a normal metal, and in chapters 3 and 4 I show why it is a reasonable approximation and that it is true also for a half-metal.

In a bulk superconductor all the derivatives in eq. (2.72) vanish and when  $\mathbf{A} = 0$  the equations decouple,

$$0 = -2i\varepsilon\gamma - \Delta\sigma_2 + \gamma\Delta^*\sigma_2\gamma, \quad (2.73a)$$

$$0 = -2i\varepsilon\tilde{\gamma} - \Delta^*\sigma_2^* + \tilde{\gamma}\Delta\sigma_2^*\tilde{\gamma}. \quad (2.73b)$$

Observe that  $\gamma$  must be written on the form  $\gamma = \text{antidiag}(b, -b)$  in order to solve eq. (2.73). Inserting this I get after some algebra that

$$b = \frac{\Delta}{\varepsilon \pm i\sqrt{|\Delta|^2 - \varepsilon^2}}. \quad (2.74)$$

To determine which of these solutions are correct one could insert them in the Gor'kov equations, which would involve a Fourier transform. The solution is

$$b = \begin{cases} \frac{\Delta}{\varepsilon + i\sqrt{|\Delta|^2 - \varepsilon^2}} & \text{if } |\varepsilon| < |\Delta|, \\ \frac{\Delta \text{sgn}(\varepsilon)}{|\varepsilon| + \sqrt{\varepsilon^2 - |\Delta|^2}} & \text{if } |\varepsilon| > |\Delta|, \end{cases} \quad (2.75)$$

as can be verified by inserting it in the Gor'kov equation and using that the retarded Green's function must vanish at negative relative times. Plugging this into eq. (2.71) yields

$$\hat{g}_{\text{BCS}} = \left[ \frac{\theta(\varepsilon^2 - |\Delta|^2)}{\sqrt{\varepsilon^2 - |\Delta|^2}} \text{sgn}(\varepsilon) - \frac{\theta(|\Delta|^2 - \varepsilon^2)}{\sqrt{|\Delta|^2 - \varepsilon^2}} i \right] (\varepsilon\hat{\rho}_3 + \hat{\Delta}). \quad (2.76)$$

### 2.2.4 Strongly Polarized Ferromagnets

Notice that the matrix structure of the Ricatti parameter in a bulk conventional superconductor is

$$\gamma = \begin{pmatrix} 0 & \gamma_{\uparrow\downarrow} \\ -\gamma_{\uparrow\downarrow} & 0 \end{pmatrix} \quad (2.77)$$

and the same is true for proximity systems involving only superconductors and normal metals, as will be showed in chapter 4. However, adding an exchange field, as would be necessary to capture the physics of a ferromagnet, would induce triplet correlations. Consequently, it would require considering all four elements of the Ricatti parameter,

$$\gamma = \begin{pmatrix} \gamma_{\uparrow\uparrow} & \gamma_{\uparrow\downarrow} \\ \gamma_{\downarrow\uparrow} & \gamma_{\downarrow\downarrow} \end{pmatrix}. \quad (2.78)$$

For the case of very strong ferromagnets, the exchange field is so large that the associated energy is not negligible compared to the Fermi energy [35]. This invalidates the assumption behind the quasiclassical treatment, stating that all energies should be small compared to the Fermi energy. The redemption comes from the realization that the spin-splitting in such system is so severe that there is effectively no interaction between different spin bands. We can then continue to use the quasiclassical theory if we, instead of including an exchange field, treat the spin-bands as non-interacting and with different diffusion constants,  $D_{\uparrow}$  and  $D_{\downarrow}$ . Doing this we must require that the off-diagonal elements of  $\gamma$  is zero, such that

$$\gamma = \begin{pmatrix} \gamma_{\uparrow\uparrow} & 0 \\ 0 & \gamma_{\downarrow\downarrow} \end{pmatrix}. \quad (2.79)$$

Inserting the two different diffusion constant into the Usadel equation gives [36]

$$D \left\{ \nabla^2 \gamma + 2 \nabla \gamma \cdot \tilde{N} \tilde{\gamma} \nabla \gamma - 2ie \mathbf{A} \cdot \left[ (1 + \gamma \tilde{\gamma}) N \nabla \gamma + \nabla \gamma \tilde{N} (1 + \tilde{\gamma} \gamma) \right] - 4e^2 |\mathbf{A}|^2 \gamma \tilde{N} (1 + \tilde{\gamma} \gamma) - 2i\gamma e \nabla \cdot \mathbf{A} \right\} = -2i\varepsilon \Pi \gamma, \quad (2.80)$$

and similarly for  $\tilde{\gamma}$ . Here,  $D = (D_{\uparrow} + D_{\downarrow})/2$  and

$$\Pi = \begin{pmatrix} 2/(1+p) & 0 \\ 0 & 2/(1-p) \end{pmatrix}, \quad (2.81)$$

where  $p = (D_{\uparrow} - D_{\downarrow})/(D_{\uparrow} + D_{\downarrow})$ . In a fully polarized (half-metallic) ferromagnet  $p = 1$ . Hence,  $\gamma_{\downarrow\downarrow} = 0$  and

$$\nabla^2 a + \frac{2\tilde{a} \nabla a \cdot \nabla a}{1 - a\tilde{a}} = \frac{4(1 + a\tilde{a})e \mathbf{A} \cdot (ae \mathbf{A} + i \nabla a)}{1 - a\tilde{a}} + 2iae \nabla \cdot \mathbf{A} - 2i\varepsilon a, \quad (2.82)$$

where I have made the equation dimensionless and set  $a \equiv \gamma_{\uparrow\uparrow}$ .

## 2.3 Observables

A range of physical observables can be extracted from the quasiclassical Green's function. In the following it will be useful to write

$$\hat{g}^R = \begin{pmatrix} g & f \\ -\tilde{f} & -\tilde{g} \end{pmatrix}. \quad (2.83)$$

### 2.3.1 Local Density of States

The local density of states for spin  $\sigma$  at energy  $\varepsilon$  and location  $\mathbf{r}$  can be written

$$N_\sigma(\varepsilon, \mathbf{r}) = N_0 \Re\{g_{\sigma\sigma}(\varepsilon, \mathbf{r})\}, \quad (2.84)$$

where  $N_0$  is the normal state density of state at the Fermi surface.

To derive eq. (2.84), we will use the assumption that the system is in thermal equilibrium, meaning that the density operator is given by the grand canonical ensemble. That is, the expectation value of some operator  $\mathcal{O}$  is

$$\langle \mathcal{O} \rangle = \frac{1}{Z} \sum_{n \in I} e^{-\beta \varepsilon_n} \langle n | \mathcal{O} | n \rangle, \quad (2.85)$$

where  $\{|n\rangle\}_{n \in I}$  and  $\{\varepsilon_n\}_{n \in I}$  are the eigenvectors and eigenvalues of the Hamiltonian in the grand canonical ensemble.<sup>6</sup> We assume that the Hamiltonian is a single-particle Hamiltonian. Single-particle Hamiltonians are separable in the single-particle operators, so their eigenvectors are tensor products of the single-particle eigenstates and the corresponding eigenvalues are the sum of the respective single-particle eigenvalues.

The local density of states is the number of single-particle states at a certain position and for a certain energy, that is,

$$N_\sigma(\mathbf{R}, \varepsilon) := \sum_{n \in J} |\langle \mathbf{R}, \sigma | n \rangle|^2 \delta(\varepsilon - \varepsilon_n). \quad (2.86)$$

where  $\{|n\rangle\}_{n \in J}$  and  $\{\varepsilon_n\}_{n \in J}$  are the eigenvectors and eigenvalues of the single-particle Hamiltonian.

We want to rewrite eq. (2.86) in terms of the retarded Greens function,<sup>7</sup>

$$G_{\sigma\sigma'}^{\mathbf{R}}(\mathbf{r}, t, \mathbf{r}', t') = -i\theta(t - t') \left\langle \left\{ \psi_\sigma(\mathbf{r}, t), \psi_{\sigma'}^\dagger(\mathbf{r}', t') \right\} \right\rangle. \quad (2.87)$$

Setting  $\sigma' = \sigma$ ,  $\mathbf{r}' = \mathbf{r}$  and assuming the Hamiltonian does not explicitly depend on time, we may write<sup>8</sup>

$$\begin{aligned} G_{\sigma\sigma}^{\mathbf{R}}(\mathbf{r}, t, \mathbf{r}, t') &= -i\theta(t - t') \left\langle e^{iH(t-t')} \psi_\sigma(\mathbf{r}, t) e^{-iH(t-t')} \psi_\sigma^\dagger(\mathbf{r}, t') + \psi_\sigma^\dagger(\mathbf{r}, t') e^{iH(t-t')} \psi_\sigma(\mathbf{r}, t) e^{-iH(t-t')} \right\rangle \\ &= -\frac{i}{Z} \theta(t - t') \sum_{n, m \in I} |\langle n | \psi_\sigma(\mathbf{r}, t') | m \rangle|^2 e^{-i(\varepsilon_m - \varepsilon_n)(t-t')} \left( e^{-\beta \varepsilon_n} + e^{-\beta \varepsilon_m} \right). \end{aligned} \quad (2.88)$$

In the last equality we inserted eq. (2.85) and the identity  $1 = \sum_{m \in I} |m\rangle \langle m|$ . Because we are considering equilibrium, the system is time-translationally invariant and the Green's function should only depend on the relative coordinate  $t - t'$ . We may therefore set  $t' = 0$  such that  $t$  becomes the relative coordinate. Fourier transforming in terms of the relative coordinate  $t$ , we get

$$\begin{aligned} G_{\sigma\sigma}^{\mathbf{R}}(\mathbf{r}, \varepsilon) &= \int dt e^{i\varepsilon t} \left[ -\frac{i}{Z} \theta(t) \sum_{n, m \in I} |\langle n | \psi_\sigma(\mathbf{r}, 0) | m \rangle|^2 e^{-i(\varepsilon_m - \varepsilon_n)t} \left( e^{-\beta \varepsilon_n} + e^{-\beta \varepsilon_m} \right) \right] \\ &= \lim_{\eta \rightarrow 0^+} \frac{1}{Z} \sum_{n, m \in I} \frac{|\langle n | \psi_\sigma(\mathbf{r}, 0) | m \rangle|^2}{\varepsilon - (\varepsilon_m - \varepsilon_n) + i\eta} \left( e^{-\beta \varepsilon_n} + e^{-\beta \varepsilon_m} \right). \end{aligned} \quad (2.89)$$

<sup>6</sup>“Hamiltonian in the grand canonical ensemble” means that the chemical potential is included. The eigenvalues of this Hamiltonian,  $\varepsilon_n$  is related to the “normal” Hamiltonian,  $E_n$  by  $\varepsilon_n = E_n - N\mu$ , where  $N$  is the number of particles and  $\mu$  is the chemical potential.

<sup>7</sup> Note that this Green's function is the upper left  $2 \times 2$  block of  $\hat{G}^{\mathbf{R}}$ .

<sup>8</sup>The fact that  $\psi_\sigma(\mathbf{r}, t) = e^{iH(t-t')} \psi_\sigma(\mathbf{r}, t') e^{-iH(t-t')}$  comes directly from solving the Heisenberg equation (2.17) under the assumption that the Hamiltonian  $H$  does not depend explicitly on time  $t$ .

Using the relation

$$\lim_{\eta \rightarrow 0^+} \frac{1}{\varepsilon - (\varepsilon_m - \varepsilon_n) + i\eta} = \mathcal{P} \left( \frac{1}{\varepsilon - (\varepsilon_m - \varepsilon_n)} \right) - i\pi \delta(\varepsilon - (\varepsilon_m - \varepsilon_n)) \quad (2.90)$$

we therefore get

$$\Im \{G_{\sigma\sigma}^{\text{R}}(\mathbf{r}, \varepsilon)\} = -\pi \frac{1}{Z} \sum_{n,m \in I} |\langle n | \psi_{\sigma}(\mathbf{r}, 0) | m \rangle|^2 \left( e^{-\beta\varepsilon_n} + e^{-\beta\varepsilon_m} \right) \delta(\varepsilon - (\varepsilon_m - \varepsilon_n)). \quad (2.91)$$

Next, using that

$$\psi_{\sigma}(\mathbf{r}, 0) = \sum_{k \in J} \langle \mathbf{r}, \sigma | k \rangle a_k, \quad (2.92)$$

we get that

$$\langle n | \psi_{\sigma}(\mathbf{r}, 0) | m \rangle = \sum_{k \in J} \langle \mathbf{r}, \sigma | k \rangle \langle n | a_k | m \rangle. \quad (2.93)$$

$a_k$  annihilates a single-particle eigenstate with energy  $\varepsilon_k$ , so the terms in eq. (2.93) are nonzero only if  $|n\rangle$  and  $|m\rangle$  differs by one particle in state  $|k\rangle$ , in which case  $\varepsilon_m - \varepsilon_n = \varepsilon_k$ .<sup>9</sup> That is,  $\langle n | a_k | m \rangle = 1$  only if  $|n\rangle$  does not have a particle in the state  $|k\rangle$  and  $|m\rangle$ , otherwise  $\langle n | a_k | m \rangle = 0$ . For each state  $|n\rangle$  that satisfies this, there is only one  $|m\rangle$  which gives a nonzero contribution. In other words, if  $\{|n\rangle\}_{n \in K}$  is the subset of  $\{|n\rangle\}_{n \in I}$  which does not include a particle in state  $|k\rangle$ ,

$$\Im \{G_{\sigma\sigma}^{\text{R}}(\mathbf{r}, \varepsilon)\} = -\pi \sum_{k \in J} |\langle \mathbf{r}, \sigma | k \rangle|^2 \frac{1}{Z} \overbrace{\sum_{n \in I \setminus K} e^{-\beta\varepsilon_n} (1 + e^{-\beta\varepsilon_k})}^{=Z} \delta(\varepsilon - \varepsilon_k) = -\pi N_{\sigma}(\mathbf{r}, \varepsilon). \quad (2.94)$$

To relate the density of states to the quasiclassical Green's function, we must Fourier transform also in terms of the relative spatial coordinates,

$$\begin{aligned} N_{\sigma}(\mathbf{R}, \varepsilon) &= -\frac{1}{\pi} \Im \{G_{\sigma\sigma}^{\text{R}}(\mathbf{R}, \mathbf{r} = 0, \varepsilon)\} = -\frac{1}{\pi} \Im \left\{ \int \frac{d^3p}{(2\pi)^3} e^{-i\mathbf{p}\cdot\mathbf{0}} G_{\sigma\sigma}^{\text{R}}(\mathbf{R}, \mathbf{p}, \varepsilon) \right\} \\ &= -\frac{1}{\pi} \Im \left\{ \frac{\pi N_0}{i} g_{s\sigma\sigma}^{\text{R}}(\mathbf{R}, \varepsilon) \right\} = N_0 \Re \{g_{s\sigma\sigma}^{\text{R}}(\mathbf{R}, \varepsilon)\}. \end{aligned} \quad (2.95)$$

In the penultimate equality I used the definition of the quasiclassical Green's function,

$$\check{g}(\mathbf{R}, T, \mathbf{p}_F, \varepsilon) = \frac{i}{\pi} \int d\xi_p \check{G}(\mathbf{R}, T, \mathbf{p}, \varepsilon), \quad (2.96)$$

and

$$\frac{d^3p}{(2\pi)^3} = \frac{d\Omega_p N_0}{4\pi} d\xi_p, \quad (2.97)$$

where  $\xi_p = \mathbf{p}^2/2m - \mu$ , with  $\mu$  being the chemical potential and  $d\Omega_p$  is the differential solid angle in momentum space and

$$N_0 = \frac{mp_F}{2\pi^2} \quad (2.98)$$

is the density of states per spin and per volume evaluated at the Fermi surface of a free electron gas.

From the previous computation of the quasiclassical retarded Green's in a bulk conventional superconductor we can with eq. (2.84) find an expression for the density of states averaged over

<sup>9</sup>In order to avoid confusion, I note here that  $\varepsilon_k$  is the eigenvalue of the single-particle operator while  $\varepsilon_n$  and  $\varepsilon_m$  are eigenvalues of the full Hamiltonian.



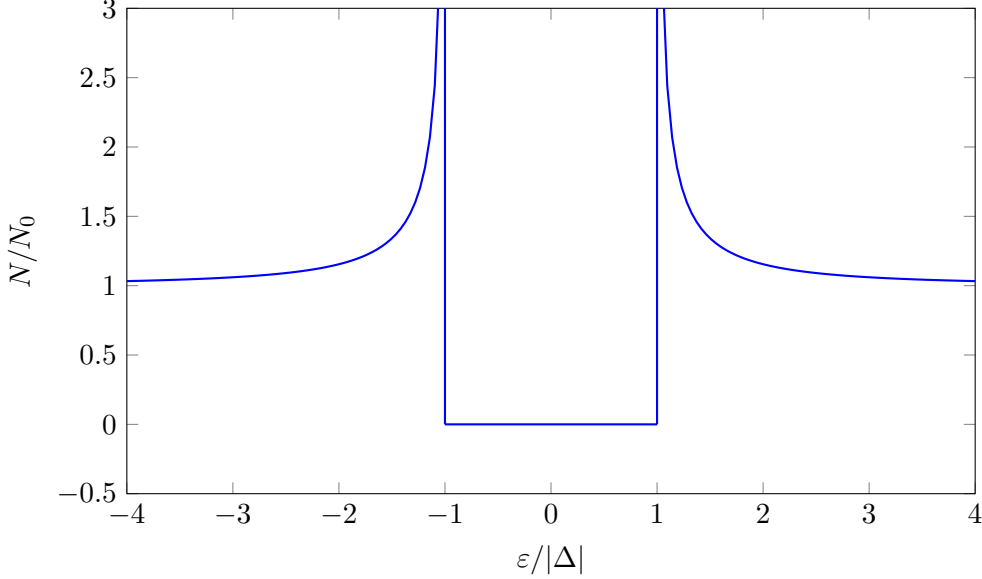


**Figure 2.1:** The density of states for a bulk superconductor.

spin in a bulk superconductor by taking the trace over the upper left block of  $\hat{g}_{\text{BCS}}$  and extracting the real part. This yields

$$N(\mathbf{r}, \varepsilon) = N_0 \frac{|\varepsilon|}{\sqrt{\varepsilon^2 - |\Delta|^2}} \theta(\varepsilon^2 - |\Delta|^2), \quad (2.99)$$

which is shown in figure 2.1. Observe that the density of states is independent of spin, so that  $N_\uparrow = N_\downarrow =: N$ , that  $\hat{\Delta}$  will not contribute in the upper left block, and that the real part is 0 when  $\varepsilon < |\Delta|$ .

### 2.3.2 Current

An expression for the charge current density is

$$\mathbf{j} = \frac{N_0 e D}{4} \int \text{Tr} (\hat{\rho}_3 [\check{g} \bar{\nabla} \check{g}]^{\text{K}}) d\varepsilon. \quad (2.100)$$

To derive eq. (2.100) we may start from the expression for the charge density in the second quantization formalism,

$$\rho(\mathbf{r}, t) = e \left\langle \psi^\dagger(\mathbf{r}, t) \hat{\rho}_3 \psi(\mathbf{r}, t) \right\rangle, \quad (2.101)$$

and use that the current density must satisfy the continuity equation,

$$\frac{\partial}{\partial t} \rho + \nabla \cdot \mathbf{j} = 0. \quad (2.102)$$

Here,  $\psi$  and  $\psi^\dagger$  are the Nambu bispinors defined in eq. (2.1) and  $\hat{\rho}_3$  comes from the fact that holes contribute with a charge  $-e = |e|$  to the charge density.

Applying the Heisenberg equation (2.17) and assuming the Hamiltonian is given by eq. (2.20), I get, using eqs. (2.22) and (2.25), that

$$\begin{aligned} \frac{\partial}{\partial t} \rho &= \frac{ie}{2m} \left\langle \left[ (-i\nabla + e\mathbf{A}\hat{\rho}_3)^2 \psi^\dagger \right] \hat{\rho}_3 \psi - \psi^\dagger \hat{\rho}_3 \left[ (-i\nabla - e\mathbf{A}\hat{\rho}_3)^2 \psi \right] \right\rangle \\ &= -\nabla \cdot \frac{ie}{2m} \left\langle \left[ (\nabla + ie\mathbf{A}\hat{\rho}_3) \psi^\dagger \right] \hat{\rho}_3 \psi - \psi^\dagger \hat{\rho}_3 \left[ (\nabla - ie\mathbf{A}\hat{\rho}_3) \psi \right] \right\rangle. \end{aligned} \quad (2.103)$$

Hence,

$$\mathbf{j} = \frac{ie}{2m} \left\langle \left[ (\nabla + ie\mathbf{A}\hat{\rho}_3)\psi^\dagger \right] \hat{\rho}_3\psi - \psi^\dagger \hat{\rho}_3 \left[ (\nabla - ie\mathbf{A}\hat{\rho}_3)\psi \right] \right\rangle \quad (2.104)$$

satisfies the continuity equation. This way of determining the charge current only specifies the current up to a field with zero divergence, of course, but we can argue that eq. (2.104) is indeed correct. We can relate the field operators  $\psi(\mathbf{r})$  and  $\psi^\dagger(\mathbf{r})$  to the operators which create and annihilate particles and holes with specific momentum states,  $\nu^\dagger(\mathbf{p})$  and  $\nu(\mathbf{p})$  [21],

$$\psi^\dagger(\mathbf{r}) = \frac{1}{\sqrt{V}} \sum_{\mathbf{p}} e^{-i\hat{\rho}_3\mathbf{p}\cdot\mathbf{r}} \nu^\dagger(\mathbf{p}), \quad \psi(\mathbf{r}) = \frac{1}{\sqrt{V}} \sum_{\mathbf{p}} e^{i\hat{\rho}_3\mathbf{p}\cdot\mathbf{r}} \nu(\mathbf{p}), \quad (2.105)$$

where  $V$  is the system volume and the sum goes over possible momenta. Inserting this in eq. (2.104) yields

$$\mathbf{j} = e \sum_{\mathbf{p}} \frac{(\mathbf{p} - e\mathbf{A})}{m} \frac{\langle \nu^\dagger(\mathbf{p})\nu(\mathbf{p}) \rangle}{V}, \quad (2.106)$$

which is exactly what we would expect from the classical expression  $\mathbf{j} = en\mathbf{v}$ , where  $n$  is the electron density and  $\mathbf{v}$  is velocity.

In order to relate eq. (2.104) to Green's functions, it is advantageous to extract the differential operators out of the expectation value. One way of doing this is to use different coordinates for the different field operators and then, after the differentiations are done, let the different coordinates approach the same value, that is

$$\mathbf{j}(\mathbf{R}) = \lim_{\mathbf{r}_1, \mathbf{r}_2 \rightarrow \mathbf{R}} \frac{ie}{2m} [\nabla_{\mathbf{r}_1} - \nabla_{\mathbf{r}_2} + 2ie\hat{\rho}_3\mathbf{A}(\mathbf{R})] \left\langle \psi^\dagger(\mathbf{r}_1, t) \hat{\rho}_3 \psi(\mathbf{r}_2, t) \right\rangle. \quad (2.107)$$

This procedure requires one word of caution. Taking the differential operators out of the expectation value is only possible as long as  $\mathbf{r}_1 \neq \mathbf{r}_2$ . Hence, while both  $\mathbf{r}_1$  and  $\mathbf{r}_2$  approach  $\mathbf{R}$ , they must do so without being equal. Since  $\mathbf{r}_1 \neq \mathbf{r}_2$ , we can use the anticommutation relations (2.19) to write

$$\left\langle \psi^\dagger(\mathbf{r}_1, t) \hat{\rho}_3 \psi(\mathbf{r}_2, t) \right\rangle = -\frac{i}{2} \text{Tr}[\hat{\rho}_3 \hat{G}^{\text{K}}(\mathbf{r}_1, t, \mathbf{r}_2, t)]. \quad (2.108)$$

Writing the Keldysh Green's function in terms of its Fourier transform in the relative coordinates yields

$$\begin{aligned} \mathbf{j}(\mathbf{R}) &= -\frac{e}{4\pi m} \int d\varepsilon \text{Tr} \left( \int \frac{d^3p}{(2\pi)^2} [i\mathbf{p} + ie\hat{\rho}_3\mathbf{A}(\mathbf{R})] \hat{\rho}_3 \hat{G}^{\text{K}}(\mathbf{R}, t, \mathbf{p}, \varepsilon) \right) \\ &= \frac{N_0 e D}{4} \int d\varepsilon \text{Tr} \{ (\check{g} \bar{\nabla} \check{g})^{\text{K}} \} + \frac{N_0 e^2}{4m} \int d\varepsilon \mathbf{A} \text{Tr} (\hat{g}^{\text{K}}), \end{aligned} \quad (2.109)$$

where in the last equality I used eq. (2.63). Now it remains only to show that the second integral does not contribute. Using eqs. (2.11) and (2.83), we see from the fact that  $\tanh(\varepsilon\beta/2)$  introduces an extra sign change under energy reversal that we can write

$$\hat{g}^{\text{K}} = \begin{pmatrix} g^{\text{K}} & f^{\text{K}} \\ \check{f}^{\text{K}} & \check{g}^{\text{K}} \end{pmatrix} \quad (2.110)$$

Hence,

$$\int d\varepsilon \mathbf{A} \text{Tr} (\hat{g}^{\text{K}}) = \mathbf{A} \int d\varepsilon \text{Tr} (g^{\text{K}} - g^{\text{K}*}) = 2i\Im \left\{ \int d\varepsilon \mathbf{A} \text{Tr} (g^{\text{K}}) \right\}. \quad (2.111)$$

As the contribution is imaginary it can not contribute to the current, and we are left with the anticipated result in eq. (2.100).

Using eqs. (2.11) and (2.83) and

$$\int \tilde{h}(\varepsilon) \tanh\left(\frac{\beta\varepsilon}{2}\right) d\varepsilon = - \int h^*(\varepsilon) \tanh\left(\frac{\beta\varepsilon}{2}\right) d\varepsilon, \quad (2.112)$$

eq. (2.100) can be rewritten

$$\mathbf{j} = \frac{N_0 e D}{2} \int \tanh\left(\frac{\beta\varepsilon}{2}\right) \text{Tr}\left(\text{Re}\left[\tilde{f}^\dagger \nabla f^\dagger - f \nabla \tilde{f}\right] + 2e\mathbf{A} \text{Im}\left[f \tilde{f} - \tilde{f}^\dagger f^\dagger\right]\right) d\varepsilon. \quad (2.113)$$

Deriving expressions for the spin currents can be done in a similar way by replacing the electron charge  $e$  in eq. (2.101) by the electron spin amplitude  $1/2$  and multiplying  $\hat{\rho}_3$  by the Pauli matrix corresponding to the spin direction in question. The same derivation as above will then give, for the spin currents in the  $x$ -,  $y$ - and  $z$ -direction, respectively,

$$\mathbf{j}_x^s = \frac{N_0 D}{8} \int \text{Tr}(\sigma_1 \hat{\rho}_3 [\check{g} \bar{\nabla} \check{g}]^K) d\varepsilon, \quad (2.114a)$$

$$\mathbf{j}_y^s = \frac{N_0 D}{8} \int \text{Tr}(\sigma_2 \hat{\rho}_3 [\check{g} \bar{\nabla} \check{g}]^K) d\varepsilon, \quad (2.114b)$$

$$\mathbf{j}_z^s = \frac{N_0 D}{8} \int \text{Tr}(\sigma_3 \hat{\rho}_3 [\check{g} \bar{\nabla} \check{g}]^K) d\varepsilon. \quad (2.114c)$$

For a half metal considered in chapter 3, the spin current in the direction of the spin-conducting band is proportional to the electric current while the remaining spin currents vanish. In the normal metal considered in chapter 4,  $\mathbf{j}_x^s = \mathbf{j}_y^s = \mathbf{j}_z^s = \mathbf{0}$ .

## 2.4 Cooper Pair Correlation Function

The anomalous Greens function,  $f$ , is central in characterizing superconducting order and hence the strength of the proximity effect. In the BCS theory, a superconductor is characterized by having a non-zero gap parameter

$$\Delta(\mathbf{r}) = V(\mathbf{r}) \langle \psi_\downarrow(\mathbf{r}, 0) \psi_\uparrow(\mathbf{r}, 0) \rangle \quad (2.115)$$

where  $V$  is the phonon-mediated attractive interaction potential.  $\Delta = 0$  outside a superconductor because  $V = 0$ , but we can still have  $\langle \psi_\downarrow(\mathbf{r}, 0) \psi_\uparrow(\mathbf{r}, 0) \rangle \neq 0$ , as is the case in normal proximity systems. Written in terms of Green's functions, the superconducting order parameter, or Cooper pair correlation function, reads

$$\langle \psi_\downarrow(\mathbf{r}, 0) \psi_\uparrow(\mathbf{r}, 0) \rangle = \frac{N_0}{8} \int_{-\infty}^{\infty} d\varepsilon (\hat{g}_{2,3}^K - \hat{g}_{1,4}^K). \quad (2.116)$$

In order to rewrite the Cooper pair correlation function in terms of the anomalous Green's function as given in eq. (2.83), we write  $f$  in terms of the spin-singlet correlation,  $f_s$ , and the triplet correlations  $f_\uparrow$ ,  $f_t$  and  $f_\downarrow$ ,

$$f = \begin{pmatrix} f_\uparrow & f_t + f_s \\ f_t - f_s & f_\downarrow \end{pmatrix}. \quad (2.117)$$

In a normal spin-singlet superconductor, all but  $f_s$  are zero, while in a half metal, only  $f_\uparrow$  is nonzero. With this, eq. (2.116) can be written

$$\Psi(\mathbf{r}) := \langle \psi_\downarrow(\mathbf{r}, 0) \psi_\uparrow(\mathbf{r}, 0) \rangle = \frac{N_0}{4} \int_{-\infty}^{\infty} d\varepsilon \{f_s(\mathbf{r}, \varepsilon) - f_s(\mathbf{r}, -\varepsilon)\} \tanh\left(\frac{\beta\varepsilon}{2}\right) \quad (2.118)$$

The analogous correlation function in diffusive half metals is

$$\langle \psi_{\uparrow}(\mathbf{r}, 0) \psi_{\uparrow}(\mathbf{r}, 0) \rangle = \frac{N_0}{4} \int_{-\infty}^{\infty} d\varepsilon \{f_{\uparrow}(\mathbf{r}, \varepsilon) + f_{\uparrow}(\mathbf{r}, -\varepsilon)\} \tanh\left(\frac{\beta\varepsilon}{2}\right) = 0, \quad (2.119)$$

so it does not work as an order parameter. One alternative which is often used in the Bogoliubov-deGennes formalism [37] is to keep a nonzero time difference between the field operators. That is,

$$\Psi_1(\mathbf{r}, t) := \langle \psi_{\uparrow}(\mathbf{r}, t) \psi_{\uparrow}(\mathbf{r}, 0) \rangle = \frac{N_0}{4} \int_{-\infty}^{\infty} d\varepsilon \{f_{\uparrow}(\mathbf{r}, \varepsilon) + f_{\uparrow}(\mathbf{r}, -\varepsilon)\} \tanh\left(\frac{\beta\varepsilon}{2}\right) e^{-i\varepsilon t}. \quad (2.120)$$

Another strategy sometimes used [38] is to make the order parameter even in time by differentiation. That is,

$$\Psi_2(\mathbf{r}) := \left. \frac{\partial \langle \psi_{\uparrow}(\mathbf{r}, t) \psi_{\uparrow}(\mathbf{r}, 0) \rangle}{\partial t} \right|_{t=0} = \frac{-iN_0}{4} \int_{-\infty}^{\infty} d\varepsilon \{f_{\uparrow}(\mathbf{r}, \varepsilon) + f_{\uparrow}(\mathbf{r}, -\varepsilon)\} \tanh\left(\frac{\beta\varepsilon}{2}\right) \varepsilon. \quad (2.121)$$

One characteristic of vortices is that their cores are non-superconducting, so it is important for our discussion to have an order parameter which can be used to identify vortices. It is not obvious that eqs. (2.120) and (2.121) works equally well to identify vortices. For instance, there are some times  $t$  for which the normal superconducting order parameter  $\langle \psi_{\downarrow}(\mathbf{r}, t) \psi_{\uparrow}(\mathbf{r}, 0) \rangle = 0$  even in a bulk superconductor because of the cancellations coming from the exponential in eq. (2.120). It could be that some locations have vanishing order parameters for some relative times  $t$  but not for others, which would mean that using the wrong order parameter could give the wrong impression of there being extra vortices. Vortices are associated with other observables as well, such as a circulating supercurrent, and comparing the position of roots of different order parameters with these observables can give a good indication of whether the order parameters work to identify the existence and location of vortices. This will be further discussed in chapter 3.

## 2.5 Numerics

In order to solve the Usadel equation numerically, I employ a finite element scheme. In this section I will briefly highlight how this procedure works, and then I will show how we can use a clever trick to numerically differentiate any function accurately. This trick has allowed me to write a program which can solve any nonlinear second order partial differential equation. This will be useful because the equations we want to solve differs when considering half-metals in two dimensions and normal metals in three dimensions.

### 2.5.1 Weak Formulation of Differential Equations

The first step in the finite element scheme is to write the equations on weak form. To illustrate how this works we will rewrite the following the set of differential equations:

$$\nabla^2 u(x) = F(x, u, \nabla u), \quad (2.122a)$$

$$\mathbf{e}_n \cdot \nabla u(x) \Big|_{x \in \partial\Omega} = B(x, u), \quad (2.122b)$$

where  $u$  is a function of  $x \in \Omega$ ,  $F$  and  $B$  are arbitrary functions,  $\partial\Omega$  is the boundary of  $\Omega$  and  $\mathbf{e}_n$  is a outward pointing normal vector. From eq. (2.122a) it is clear that

$$\int_{\Omega} dx (v \nabla^2 u - v F) = 0 \quad (2.123)$$

for all functions  $v$ . Using Green's first identity [26],

$$\int_{\Omega} dx v \nabla^2 u = \int_{\partial\Omega} dx v (\nabla u \cdot \mathbf{e}_n) - \int_{\Omega} dx \nabla v \cdot \nabla u = \int_{\partial\Omega} dx v B - \int_{\Omega} dx \nabla v \cdot \nabla u, \quad (2.124)$$

eq. (2.123) can be rewritten

$$\int_{\Omega} dx (\nabla v \cdot \nabla u + v F) - \int_{\partial\Omega} dx v B = 0. \quad (2.125)$$

Equation (2.125) is known as the *weak form* of eq. (2.122).

Any function  $u$  which satisfies eq. (2.122) must satisfy eq. (2.125) for all  $v$ , but the inverse is not true. That is, even if a function  $u$  satisfies eq. (2.125) for every function  $v$ , it is not necessarily true that it must also satisfy eq. (2.122). It could for instance be the case that the  $u$  is not twice differentiable. It is in this sense that eq. (2.125) is a weaker form than eq. (2.122).

## 2.5.2 The Finite Element Method

In the finite element method one looks for solution to eq. (2.125) of the form

$$u(x) = \sum_{i=1}^N \chi_i \varphi_i(x), \quad (2.126)$$

where  $\{\varphi_i\}_{i \in [1, \dots, N]}$  is a set of finitely many basis functions. The objective of the finite element method is to find the unknown coefficients  $\{\chi_i\}_{i \in [1, 2, \dots, N]}$ . It will in general not be possible to find a solution to eq. (2.122) on this form for any finite  $N$ , and this is the reason for introducing the weak formulation. In fact, it is necessary to use an even weaker form. Instead of requiring eq. (2.125) to hold for *every*  $v$ , we require only that it holds for all  $v \in \{\varphi_i\}_{i \in [1, 2, \dots, N]}$ . To find an approximate solution to eq. (2.122) in the finite element method, one solves the system

$$\int_{\Omega} dx \left\{ \sum_{i=1}^N (\chi_i \nabla \varphi_i \cdot \nabla \varphi_j) + \varphi_j F \right\} - \int_{\partial\Omega} dx \varphi_j B = 0, \quad \forall j \in \{1, 2, \dots, N\}, \quad (2.127)$$

which is a set of  $N$  equations for  $N$  unknowns. The Usadel equation, which is what we want to solve here, is itself a set of equations, and the way of converting a single differential equations to a set of algebraic equations generalizes to a set of coupled differential equations. For a set of  $k$  differential equations, convert each to the form eq. (2.127) and solve the resulting set of  $k \times N$  algebraic equations.

The name *finite element* comes from how the set of functions  $\{\varphi_i\}_{i \in [1, \dots, N]}$  is determined. First, the domain  $\Omega$  is divided up into cells, or *elements*. Then, each cell is assigned a set of nodes, and each node is assigned a function. Hence,  $N$  is equal to the number of nodes. The functions are such that they are nonzero only in the cells which are closest. That is, if a node is placed in the center of a cell, then the corresponding function is nonzero only in that cell. Similarly, if it is placed on the edge between two cells, then the function is nonzero only in those two cells. In this work we will work with two and three dimensional rectangular domains, so the cells can be chosen to be equally sized rectangular cuboids. However, one of the great advantages of the finite element method is that the cells need not be equal in size and can be chosen such that they fill rather complex shapes. Various kinds of cell types exists, but in this work I will use quadratic quadrilateral elements in the two-dimensional case and linear hexahedral elements in the three-dimensional case.

If the original differential equation (2.122) is linear, then the resulting set of algebraic equations (2.127) will also be linear, meaning that it can be written on the form  $A\mathbf{x} = \mathbf{b}$ . Solving can be done efficiently on a computer, especially if one can take advantage of symmetries of the matrix  $A$ . However, the Usadel equation is not linear, and to solve it we must use a method such as the Newton-Rhapon method.

### 2.5.3 The Newton-Rhapson Method

A strategy for solving nonlinear problems is to search for a solution as limit of an infinite sequence of solutions to linear problems [39]. Finding an approximate solution can then be done by performing the computation of only a finite number of steps in this sequence and terminate when the deviation from the true solution is sufficiently small. In this way, one can solve a difficult nonlinear problem by instead solving many easier linear problems. One approach to formulate a nonlinear problem as a sequence of linear problems is the so-called *Newton-Rhapson method*.

A nonlinear set of  $N$  equations, such as eq. (2.127), may be written

$$\mathbf{R}(\mathbf{u}) = \mathbf{0}, \quad (2.128)$$

where  $\mathbf{R}$  is a vector-valued function taking the vector  $\mathbf{u}$  as parameter. We assume  $\mathbf{u}$  solves eq. (2.128) and  $\mathbf{R}$  is differentiable in a neighborhood around  $\mathbf{u}$ . Further, assume  $\mathbf{u}_n$  is close to  $\mathbf{u}$  such that  $\mathbf{R}$  is differentiable also close to  $\mathbf{u}_n$ . Then,

$$\mathbf{R}(\mathbf{v}) \approx \mathbf{R}(\mathbf{u}_n) + J(\mathbf{u}_n)(\mathbf{v} - \mathbf{u}_n), \quad (2.129)$$

for  $\mathbf{v}$  close to  $\mathbf{u}_n$ . Here,  $J(\mathbf{u}_n)$  is the Jacobian of  $\mathbf{R}$  evaluated at  $\mathbf{u}_n$ . Solving eq. (2.129) for  $\mathbf{R}(\mathbf{v}) = \mathbf{0}$  yields

$$\mathbf{v} = \mathbf{u}_n - J^{-1}(\mathbf{u}_n)\mathbf{R}(\mathbf{u}_n). \quad (2.130)$$

Equation (2.129) is only approximate and therefore we typically have that  $\mathbf{v} \neq \mathbf{u}$ . However, as will be shown below,  $|\mathbf{v} - \mathbf{u}| < |\mathbf{u}_n - \mathbf{u}|$  in general. Hence,  $\mathbf{v}$  is a better approximation to  $\mathbf{u}$  than  $\mathbf{u}_n$ . Plugging  $\mathbf{v}$  into the right hand side of eq. (2.130) one gets an even better approximation to  $\mathbf{u}$ . This is the idea behind the Newton-Rhapson method. First, let  $\mathbf{u}_0$  be some initial guess. Subsequent iterations is then found by

$$\mathbf{u}_{n+1} = \mathbf{u}_n - J^{-1}(\mathbf{u}_n)\mathbf{R}(\mathbf{u}_n). \quad (2.131)$$

If this sequence converges and  $J(\mathbf{u}) \neq 0$ , then  $\lim_{n \rightarrow \infty} \mathbf{u}_n$  solves eq. (2.128). To verify this, set  $\mathbf{u}_{n+1} = \mathbf{u}_n$  in eq. (2.131).

The mathematical treatment of when and how fast the Newton-Rhapson method converges is covered by the *Newton-Kantorovich theorem* [40]. The Newton-Kantorovich theorem states that if the Jacobian is Lipschitz continuous and its inverse,  $J^{-1}$  exists and is bounded, the Newton-Rhapson method converges if the initial guess is sufficiently close to a zero of  $\mathbf{R}$ , and that the rate of convergence is quadratic [40]. I will not go into the details or proof of the Newton-Kantorovich theorem in the general case, which is formulated in terms of Banach spaces and Fréchet derivatives, but refer instead to [40–42] for discussion on the topic. A proof of the quadratic convergence for the specific situation of when  $\mathbf{R}$  is real or complex-valued and how the method can be implemented in the programming language Julia will be given in the remainder of this section.

Consider the vector-valued function  $\mathbf{R} : \mathbb{F}^N \rightarrow \mathbb{F}^N$  where  $\mathbb{F}$  is either the complex or real numbers. Let  $\mathbf{u}$  be a root of  $\mathbf{R}$ . That is,  $\mathbf{R}(\mathbf{u}) = \mathbf{0}$ . Further, consider  $\mathbf{u}_n \in \mathbb{F}^N$  and let

$$X := B_{|\mathbf{u} - \mathbf{u}_n|}(\mathbf{u}) \quad (2.132)$$

be the closed ball of radius  $|\mathbf{u} - \mathbf{u}_n|$  with center in  $\mathbf{u}$ .

Assume the Jacobian of  $\mathbf{R}$ ,  $J$ , is Lipschitz continuous in  $X$  with Lipschitz constant  $L$ , that is,  $\forall \mathbf{x}, \mathbf{y} \in X$ ,

$$\|J(\mathbf{x}) - J(\mathbf{y})\|_F \leq L|\mathbf{x} - \mathbf{y}|, \quad (2.133)$$

where  $\|\cdot\|_F$  is the Frobenius norm,

$$\|J(\mathbf{u})\|_F = \sqrt{\sum_{i,j=1}^N |J_{ij}(\mathbf{u})|^2}. \quad (2.134)$$

Assume further that the Jacobian is invertible in  $X$ , and that the inverse satisfies,  $\forall \mathbf{x} \in X$

$$\|J^{-1}(\mathbf{x})\|_F \leq \rho, \quad (2.135)$$

where  $\rho \in \mathbb{R}$ .

From the fundamental theorem of calculus,

$$-\mathbf{R}(\mathbf{u}_n) = \mathbf{R}(\mathbf{u}) - \mathbf{R}(\mathbf{u}_n) = \int_0^1 dt J(\mathbf{u}_n + t[\mathbf{u} - \mathbf{u}_n]) (\mathbf{u} - \mathbf{u}_n), \quad (2.136)$$

so

$$-\mathbf{R}(\mathbf{u}_n) - J(\mathbf{u}_n)(\mathbf{u} - \mathbf{u}_n) = \int_0^1 dt \{J(\mathbf{u}_n + t[\mathbf{u} - \mathbf{u}_n]) - J(\mathbf{u}_n)\} (\mathbf{u} - \mathbf{u}_n). \quad (2.137)$$

Multiplying from the left by  $J^{-1}(\mathbf{u}_n)$  and using eq. (2.131), we get

$$\mathbf{u}_{n+1} - \mathbf{u} = J^{-1}(\mathbf{u}_n) \int_0^1 dt \{J(\mathbf{u}_n + t[\mathbf{u} - \mathbf{u}_n]) - J(\mathbf{u}_n)\} (\mathbf{u} - \mathbf{u}_n). \quad (2.138)$$

Using eqs. (2.133) and (2.135),

$$\begin{aligned} |\mathbf{u}_{n+1} - \mathbf{u}| &= \left| J^{-1}(\mathbf{u}_n) \int_0^1 dt \{J(\mathbf{u}_n + t[\mathbf{u} - \mathbf{u}_n]) - J(\mathbf{u}_n)\} (\mathbf{u} - \mathbf{u}_n) \right| \\ &\leq \|J^{-1}(\mathbf{u}_n)\|_F \int_0^1 dt L |\mathbf{u}_n + t(\mathbf{u} - \mathbf{u}_n) - \mathbf{u}_n| |\mathbf{u} - \mathbf{u}_n| \\ &\leq \frac{L\rho}{2} |\mathbf{u} - \mathbf{u}_n|^2. \end{aligned} \quad (2.139)$$

Hence, if  $L\rho|\mathbf{u} - \mathbf{u}_n|/2 < 1$ , doing one iteration of the Newton-Rhapson method result in a better approximation for the solution,  $\mathbf{u}$ , and the convergence is quadratic. Moreover, since  $\mathbf{u}_{n+1}$  is also inside  $X$ , the same argument shows that the  $\mathbf{u}_{n+1}$  will be even closer to  $\mathbf{u}$ .

Whether or not the Newton-Rhapson method converge depend on how good the initial guess,  $\mathbf{u}_0$ , is as well as the properties of  $\mathbf{R}$ . For instance, if  $\mathbf{R}$  is linear, then  $J$  is constant and  $L = 0$ , so  $|\mathbf{u}_1 - \mathbf{u}| = 0$  regardless of the choice of  $\mathbf{u}_0$ .

In practice we do not determine bounds on  $L$  and  $\rho$  when using the Newton-Rhapson method. Instead, for each  $\mathbf{u}_n$  we calculate  $\mathbf{R}(\mathbf{u}_n)$  and terminate when  $|\mathbf{R}(\mathbf{u}_n)|$  is less than some threshold, in which case we take  $\mathbf{u}_n$  as the approximate solution for  $\mathbf{u}$ . Conversely, we throw an error if  $|\mathbf{R}(\mathbf{u})|$  or the number of iterations has reached an upper bound. An example of how this can be implemented numerically in the programming language Julia is shown in listing 2.1, and an example of how this is run to solve

$$\begin{pmatrix} \sqrt{u_1} - 2 \\ 3u_2 - u_1 \end{pmatrix} = \mathbf{0} \quad (2.140)$$

with  $\mathbf{u}_0 = (1, 1)$  is given in listing 2.2.

**Listing 2.1:** An implentation of the Newton-Rhapson method in Julia.

```

1 using LinearAlgebra
2 function NewtonRhapson(u0, R, J)
3     # Setting up parameters
4     N = length(u0)
5     newtonTol = 1e-8
6     newtonItr = -1
7     maxItr = 100
8     maxError = 1e8

```

```

9     u_n = u_0
10
11     while true; newtonItr += 1
12         # Computing new iteration
13         Res = R(u_n)
14         Jac = J(u_n)
15         u_n -= Jac\Res
16
17         # Checking termination conditions
18         normRes = norm(Res)
19         if normRes < newtonTol
20             break
21         elseif normRes > maxError
22             error("\nError threshold reached: Error ", normRes, " Aborting...\n")
23             break
24         elseif newtonItr > maxItr
25             error("\nMaximum Newton iterations reached at residual norm ", normRes, ". Aborting...\n")
26             break
27         end
28     end
29     return u_n, newtonItr
30 end

```

**Listing 2.2:** An example execution of the Newton-Rhapson method implemented in listing 2.1 used to find to solve  $(\sqrt{u_1} - 2, 3u_2 - u_1) = \mathbf{0}$ . The solution was correctly found after 4 iterations.

```

1 > julia
2 julia> include("filename.jl")
3 NewtonRhapson (generic function with 1 method)
4
5 julia> R(u) = [u[1]^2 - 2, 3*u[2] - u[1]]
6 R (generic function with 1 method)
7
8 julia> J(u) = [2*u[1] 0; -1 3]
9 J (generic function with 1 method)
10
11 julia> NewtonRhapson([1.0, 1.0], R, J)
12 ([1.4142135623730951, 0.47140452079103173], 4)
13
14 julia> [sqrt(2) , (1.0/3.0)*sqrt(2)] .- ans[1]
15 2-element Array{Float64,1}:
16  0.0
17 -5.551115123125783e-17

```

### 2.5.4 Forward Mode Automatic Differentiation

Solving a nonlinear problem such as the Usadel equation involves computing the Jacobian, therefore it is necessary to differentiate efficiently. For small problems, the analytical expression for the Jacobian can be efficiently evaluated directly. For larger systems, such as the Usadel equations, which in its most general form is a system of 8 complex-valued second order partial differential equations, the analytical expression for the Jacobian can become long and numerical differentiation can be advantageous. In this section we will use automatic differentiation [43] to produce a Julia function which, in only a few lines of code, computes the Jacobian of any function.

Forward mode automatic differentiation automatically computes the derivative of a function  $f(x)$  by passing a dual number as a parameter. This has some advantages over other numerical differentiation schemes such as finite difference methods and symbolic differentiation. Firstly, the result is exact, in contrast to finite difference which introduces discretization and truncation errors. Secondly, it only requires doing arithmetic, not symbolic manipulations, so it can be implemented efficiently [43] and works for complicated functions defined using structures not



easily translatable to symbols, such as while-loops.

Dual numbers is an extension of the real or complex numbers achieved by adding a nilpotent variable. For one-dimensional dual numbers, the nilpotent variable is the same as a one-dimensional Grassmann variable. That is,  $x$  is a dual number if it can be written

$$x = a + b\varepsilon, \quad \text{where } \varepsilon^2 = 0. \quad (2.141)$$

Here,  $a \in \mathbb{F}$  is the *principal* part<sup>10</sup> of  $x$  and  $b \equiv \text{dual}(x) \in \mathbb{F}$  is the *dual* part of  $x$ .  $\mathbb{F}$  is some field, which in this context is either the real numbers,  $\mathbb{R}$ , or the complex numbers,  $\mathbb{C}$ .

To understand how dual numbers can extract the derivative, we express an arbitrary function  $f(x)$  in terms of its Taylor series,

$$f(x) = \sum_{n=0}^{\infty} \frac{f^{(n)}(a)}{n!} (x - a)^n, \quad (2.142)$$

where  $f^{(n)}$  is the  $n$ 'th derivative of  $f$ . Let  $a, b \in \mathbb{F}$ , then

$$f(a + b\varepsilon) = \sum_{n=0}^{\infty} \frac{f^{(n)}(a)}{n!} (b\varepsilon)^n = f(a) + f'(a)b\varepsilon. \quad (2.143)$$

Setting  $b = 1$  we therefore get the derivative of  $f$  as the dual part.

As an example, consider  $f(x) = 1/x$ . To extract  $f'(x) = -1/x^2$ , we can evaluate  $f$  in  $x + \varepsilon$ , that is

$$\frac{1}{x + \varepsilon} = \frac{x - \varepsilon}{(x + \varepsilon)(x - \varepsilon)} = \frac{1}{x} - \frac{1}{x^2}\varepsilon,$$

and  $f'(x) = \text{dual}(f(x + \varepsilon)) = -1/x^2$ .

Extending this to the Jacobian of a function  $\mathbf{F} : \mathbb{F}^n \rightarrow \mathbb{F}^n$  where  $\mathbb{F}$  is either  $\mathbb{C}$  or  $\mathbb{R}$ , we get that

$$J_{ij} = \frac{\partial F_i}{\partial x_j} = \text{dual}(F_i(x_1, \dots, x_j + \varepsilon, \dots, x_n)) \quad (2.144)$$

We are now ready to implement a Julia function which uses automatic differentiation to determine the Jacobian of any function. Listing 2.3 shows an implementation of a function which uses the dual number implementation `DualNumbers.jl` which defines the dual number type and rules for how to add, subtract, multiply and divide dual numbers in Julia, as well as how to apply other functions, such as trigonometric functions [43]. Note that this function calculates the Jacobian of function as long as it does not call non-Julia code. Because of Julia's multiple dispatch it will automatically compile code for evaluating the function  $F$  for dual numbers. The only requirement is that  $F$  takes as input a number or array of the same type as  $x$ . That is, listing 2.3 works for both real and complex numbers and for arbitrary large vectors.

**Listing 2.3:** `autoJac!` determines the Jacobian of a function  $\mathbf{F}$  at  $\mathbf{x}$ , saving it to a preallocated matrix  $\mathbf{J}$ .

```

1 using DualNumbers
2 function autoJac!(J, F, x)
3     for i in 1:length(x)
4         X = Dual.(x)
5         X[i] += 1ε
6         J[:,i] = dualpart.(F(X))
7     end
8 end

```

<sup>10</sup> $a$  is called the *real* part of  $x$  in the literature, but that is confusing when talking about complex dual numbers, so in this thesis I call it the *principal* part.

### 2.5.5 Romberg Integration and Gaussian Quadratures

Numerical integration is important when solving finite element problems in general, as one must integrate over every cell. Efficient numerical integration is particularly important when solving the Usadel equation (2.7). This is because to extract quantities such as currents or the Cooper pair correlation function from the Green's function, one must integrate the solution over energy at every point in space. That is, one must evaluate an integral such as

$$I = \int d\varepsilon \begin{pmatrix} f_1(\varepsilon) \\ f_2(\varepsilon) \\ \vdots \\ f_N(\varepsilon) \end{pmatrix} \equiv \int d\varepsilon \mathbf{f}(\varepsilon), \quad (2.145)$$

where  $f_i$  is some function of the Green's function evaluated at some point  $\mathbf{r}_i$ .

In order to ensure that the numerical integration scheme gives the correct result within the desired accuracy, it is beneficial to have several different methods implemented for comparison. In this section, I will introduce two adaptive integration schemes, GK715 and Romberg integration, and implement them in Julia.

The most costly part of evaluating eq. (2.145) is the evaluation of  $f_i(\varepsilon)$  because it requires solving the Usadel equation, and as discussed above. It is therefore preferable to use a scheme which minimize the number of evaluations of  $f$ . Three features are preferable in this regard. Firstly, the integration scheme should be adaptive. An adaptive scheme is iterative and estimates the error while performing the integration. In this way, one avoids doing excess function evaluations when an adequate estimate has already been obtained. Of course, if a reasonable estimate for how many evaluations is needed can be obtained beforehand, it could be more efficient not to use an adaptive scheme. The second feature is that the integration scheme should be able to reuse function evaluations when iterating. Finally, the scheme should be of high order.

Numerical integration schemes approximate an integral by a linear combination of the function values at  $N$  points. That is,

$$\int_{-1}^1 dx \mathbf{f}(x) \approx \sum_{i=1}^N w_i \mathbf{f}(x_i). \quad (2.146)$$

The *weights*,  $\{w_i\}_{i \leq N}$ , and the *points*,  $\{x_i\}_{i \leq N}$ , differ for different schemes. If the interval is not  $(-1, 1)$  one can still use eq. (2.146) by first doing a substitution. That is,

$$\int_a^b dx \mathbf{f}(x) = \frac{b-a}{2} \int_{-1}^1 \mathbf{f} \left( \frac{b-a}{2}x + \frac{a+b}{2} \right) \approx \frac{b-a}{2} \sum_{i=1}^N w_i \mathbf{f} \left( \frac{b-a}{2}x_i + \frac{a+b}{2} \right). \quad (2.147)$$

In Newton-Cotes schemes, the points are chosen to be equidistant and the weight are chosen such that the approximation is exact for a polynomial of degree  $N - 1$  which interpolates the points [44]. Examples are the trapezoid rule ( $N = 2$ ), Simpson's rule ( $N = 3$ ) and Boole's rule ( $N = 5$ ). For Newton-Cotes methods it can be an advantage to use a method with  $N$  odd because, from the symmetry of the interval, odd polynomials do not contribute to the integral. Hence, Simpson's rule is in fact exact for polynomials of degree 3, even though it is only constructed from interpolating a polynomial of degree 2.

One way of using Newton-Cotes formulas adaptively is to what is known as the Romberg's method [45], which is an example of *Richardson extrapolation*. Richardson extrapolation is a method for accelerating the convergence of a sequence. Before going into Romberg's method, it is constructive to see how Richardson extrapolation works.

First, assume a sequence can be written in terms of some function

$$\{u_i\}_{i \in \mathbb{N}} = \{u(h_i)\}_{i \in \mathbb{N}}, \quad (2.148)$$

where  $u$  is some function such that  $u(0) = \tilde{u}$  and the sequence  $\{h_i\}_{i \in \mathbb{N}}$  with  $h \in \mathbb{R}$  is such that  $h_i \rightarrow 0$  as  $i \rightarrow \infty$ . Further, assume

$$u(h) = \tilde{u} + Ch^n + \mathcal{O}(h^{n+1}) \quad (2.149)$$

for some constant  $C$ . Now, let  $t \in \mathbb{R}$  be some number and define

$$R(h) := \frac{t^n u(h/t) - u(h)}{t^n - 1}. \quad (2.150)$$

then,

$$\begin{aligned} R(h) &= \frac{t^n \left[ \tilde{u} + C(h/t)^n + \mathcal{O}([h/t]^{n+1}) \right] - \tilde{u} - Ch^n - \mathcal{O}(h^{n+1})}{t^n - 1} \\ &= \tilde{u} + \underbrace{\frac{t^n \mathcal{O}([h/t]^{n+1}) - \mathcal{O}(h^{n+1})}{t^n - 1}}_{=\mathcal{O}(h^{n+1})}. \end{aligned} \quad (2.151)$$

Hence,  $\{R(h_i)\}_{i \in \mathbb{N}}$  is a sequence which converges faster than  $\{u(h_i)\}_{i \in \mathbb{N}}$  to  $\tilde{u}$ .

In Romberg's method,  $u_i$  is the numerical approximation to an integral obtained performing the trapezoid rule on  $2^i$  subintervals. Hence, if the integral is that on the left hand side of eq. (2.147),

$$h_i = \frac{1}{2^i} (b - a). \quad (2.152)$$

In Romberg's method,  $t = 2$ , such that

$$R(h_i) = \frac{4}{3}u(h_{i+1}) - \frac{1}{3}u(h_i). \quad (2.153)$$

Note how no new calculations of  $u$  is needed to compute  $R$ . This is, however, only the first iteration in Romberg's method, because now that the Richardson extrapolation is calculated, it is possible to do the same procedure again. Putting  $R(h_i)$  into the right hand side of eq. (2.150) increases the rate of convergence even further.

From eq. (2.153) one can see that in order to the  $i$ 'th term in the first extrapolated sequence requires  $i + 1$  terms in the first sequence. Similarly, one needs  $i + 1$  terms of the first extrapolated sequence to calculate the  $i$ 'th terms in the second extrapolated sequence. Having the calculated  $n$  terms of  $u$ , therefore, one may extrapolate using Richardson extrapolation  $n - 1$  times.

We are now ready to define the Romberg's method explicitly. This can be done inductively. Let  $n$  be the number of subintervals and  $m$  be the number of Richardson extrapolations, then

$$R(0, 0) = h_1 (f(b) - f(a)), \quad (2.154)$$

$$R(n, 0) = \frac{1}{2}R(n - 1, 0) + h_n \sum_{k=1}^{2^{n-1}} f(a + (2k - 1)h_n), \quad (2.155)$$

$$R(n, m) = \frac{1}{4^m - 1} [4^m R(n, m - 1) - R(n - 1, m - 1)]. \quad (2.156)$$

Note that all function evaluations are reused at every iteration of  $m$ .

The difference between  $R(n, m)$  and the integral it approximates is of order  $\mathcal{O}(h_n^{2m+2})$  [39]. Hence, an estimate for the absolute error of  $R(n, m - 1)$  can be obtained from  $R(n, m) - R(n, m - 1)$ . By continuing the iterations until  $R(n, m) - R(n, m - 1)$  is less than the tolerance wanted for the approximation, one can terminate the computation without doing unnecessarily many function evaluations.

An implementation of Romberg's method in Julia is shown in listing 2.4, and an example of how the implemented function can be used to integrate

$$\int_{-10}^{10} \begin{pmatrix} e^{-x^2} \\ \cos(x) \end{pmatrix} = \begin{pmatrix} \sqrt{\pi} \operatorname{erf}(10) \\ 2 \sin(10) \end{pmatrix} \quad (2.157)$$

numerically is shown in listing 2.5. `erf` is the error function.

**Listing 2.4:** *Implementation of Romberg's method in Julia.*

```

1 using Printf
2 function Romberg(func, start, stop, tol=1e-4, maxIter = 10)
3     n = 1
4     m = 1
5     h = (stop - start)/2.0
6     R_init = h.*(func(start) .+ func(stop))
7     R = Array{typeof(R_init)}(undef, maxIter, maxIter)
8     R[1, 1] = R_init
9     error = Inf
10    h *= 2.0
11    while error > tol
12        n += 1
13        m += 1
14        h /= 2.0
15        R[n, 1] = (0.5) .* R[n-1, 1]
16        for k ∈ 1:2^(n-2)
17            R[n, 1] = R[n, 1] .+ h.*func(start + (2k-1)*h)
18        end
19        for i ∈ 1:m-1
20            R[n, i+1] = (1.0/(4^i - 1.0)).*((4^i).*R[n, i] .- R[n-1, i])
21        end
22        error = max((map(x -> max(abs.(x)...), (R[n, m] .- R[n, m-1])))...))
23    end
24    return R[n, m]
25 end

```

**Listing 2.5:** *An example execution of Romberg's method implemented in listing 2.4 used to find to evaluate the integral in eq. (2.145). The solution was correctly found within the given tolerance of  $10^{-6}$  after 7 iterations.*

```

1 > julia
2 julia> using SpecialFunctions; include("filename.jl")
3 Romberg (generic function with 3 methods)
4
5 julia> f(x) = [exp(-x^2), cos(x)]
6 f (generic function with 1 method)
7
8 julia> Romberg(f, -10.0, 10.0, 1e-6)
9 2-element Array{Float64,1}:
10  1.7724520422287362
11 -1.0880422225974014
12
13 julia> ans .- [sqrt(π)*erf(10), 2*sin(10)]
14 2-element Array{Float64,1}:
15 -1.8086767796798853e-6
16 -8.186618050132211e-10

```

One important point worth noting is that, while it is true that  $R(n, 0)$ ,  $R(n, 1)$  and  $R(n, 2)$  are equivalent to Newton-Cotes rules (trapezoid rule, Simpson's rule and Boole's rule, respectively), it is not true that it is equivalent to Newton-Cotes formulas for higher  $m$ . The reason for why this is important is that it makes Romberg less susceptible to the so-called *Runge's phenomenon*. Runge's phenomenon, restricts the usefulness of high order Newton-Cotes formulas. It is the phenomenon that interpolating a high order polynomial through equidistant points tend to create

large oscillations near the end of the interval [46]. Another approach to circumvent Runge’s phenomenon is to instead use Gaussian quadrature rules.

Gaussian quadrature rules requires function evaluations which are not equally spaced, but instead chosen as the roots of a polynomial in an orthogonal set of polynomials [44]. The Gaussian quadrature rule I have implemented here uses the Legendre polynomials to choose weights and points. The advantage of doing this instead of a Newton-Cotes rules is that, in addition to not be susceptible to the Runge’s phenomenon, the approximation is exact for polynomials of degree  $2N - 1$ .

To implement an adaptive scheme from Gaussian quadrature, we will use two different schemes of different order, assume that the one of higher order is more accurate and estimate the error by the difference between the two schemes. It is preferable to choose the lower order scheme such that it can be computed from the same function evaluations as the higher order scheme. This was easily incorporated in the Romberg’s method because the points were equidistant, but in the Gaussian quadrature scheme this is not possible. That is, if we were to do this using purely Gaussian quadrature, it would require us to find two Legendre polynomials with common roots.

Kronrod [47] found in 1964 that by using the zeros of Stieltjes polynomials, one can add an additional  $n + 1$  points to a  $n$ -point Gaussian quadrature rule and get a scheme which is exact for polynomials of degree at most  $3n + 1$  [48]. That is, one can find a set of  $2n + 1$  points and corresponding weights such that the scheme is exact for polynomials of degree up to  $3n + 1$  and such that  $n$  points correspond to a Gaussian quadrature rule of order  $n$ .

In listing 2.6 I implement GK715 which uses a Gaussian quadrature rule with 7 points and the corresponding Kronrod rule with 15 points. The scheme goes as follows: First the points and weights are obtained from the *QuadGK* package in Julia. Second, the Gaussian and Kronrod quadratures are computed and the error is estimated as the difference between the two schemes. Finally, if the error is bigger than the requested tolerance, the interval is divided equally in two, and GK715 is called recursively in each interval with half the tolerance. An example of how GK715 can be used to evaluate the integral in eq. (2.145) is shown in listing 2.7.

One advantage of GK715 over Romberg’s method is that the recursive nature of GK715 allows it to adjust the number of required iterations locally, doing more function evaluations in the subintervals where the function is most difficult to integrate. Romberg’s method, on the other hand, splits every subinterval on each iteration. However, each time GK715 iterates it disregards the 15 previous function evaluations and requires 30 new ones. In contrast, Romberg’s method always reuses each function evaluation.

**Listing 2.6:** *Implementation of GK715 in Julia.*

```

1 using QuadGK, Printf
2 function GK715(func, start, stop, tol=1e-6, iter::Int = 0, maxIter::Int = 10)
3     x, w, wg = kronrod(7) # [quadpoints (kronrod)], [weights (kronrod)], [weights (gauss)]
4     x .*= (stop - start)/2.0
5     x0 = (start + stop)/2.0
6     x- = x0 .+ x[1:end-1]
7     x+ = x0 .+ (-).x[1:end-1] # note: from big x to small x
8     fx0 = func(x0)
9     fx = func.(x-) .+ func.(x+)
10    IK = fx0.*w[end] # Kronrod integral
11    IG = fx0.*wg[end] # Gaussian integral
12    for i ∈ 1:7
13        IK = IK .+ (fx[i].*w[i])
14    end
15    for i ∈ 1:3
16        IG = IG .+ (fx[2i].*wg[i])
17    end
18    IK = IK.*((stop - start)/2)
19    IG = IG.*((stop - start)/2)
20    error = max((map(x -> max(abs.(x)...), (IK .- IG))...))
21    if error > tol
22        if iter >= maxIter

```

```

23     @printf("Max num of iterations (%i) reached. Returning with error %g\n", maxIter, error)
24     return I^K
25     end
26     I^K = GK715(func, start, x_0, tol/2, iter+1) .+ GK715(func, x_0, stop, tol/2, iter+1)
27     end
28     return I^K
29 end

```

**Listing 2.7:** An example execution of GK715 implemented in listing 2.6 used to find to evaluate the integral in eq. (2.145). The solution was correctly found within the given tolerance of  $10^{-6}$  after 7 iterations.

```

1  julia> using SpecialFunctions; include("filename.jl")
2  GK715 (generic function with 4 methods)
3
4  julia> f(x) = [exp(-x^2), cos(x)]
5  f (generic function with 1 method)
6
7  julia> GK715(f, -10.0, 10.0, 1e-6)
8  2-element Array{Float64,1}:
9   1.772453850905516
10  -1.0880422217787404
11
12 julia> ans .- [sqrt(pi)*erf(10), 2*sin(10)]
13 2-element Array{Float64,1}:
14  2.220446049250313e-16
15 -8.881784197001252e-16

```

### 2.5.6 The Final Program

The theory presented in this chapter has been put together in the computer program showed in appendix C. From this theory it is clear that an important part of the resulting program is numerical differentiation and integration. Numerical differentiation is needed in order to compute the Jacobian needed for the Newton-Rhapson method and numerical integration is required in the finite element method when integrating over each cell. In the quasiclassical Green's function approach, numerical integration is needed in order to extract observables such as current densities and Cooper pair correlation functions. I have implemented forward mode automatic differentiation for the numerical differentiation and adaptive Gaussian quadrature schemes and the Romberg method for numerical integration. Gaussian quadratures are used to integrate over each cell and Romberg integration and GK715 are used to integrate over energy.

The final program is quite general in that it takes as input an arbitrary number of real or complex coupled nonlinear second order partial differential equations with Robin boundary conditions (boundary conditions of the form of eq. (2.122b)) in two or three dimensions. The shape is restricted to be rectangular because of how the elements are generated, but this restriction could be relaxed if the elements are created in a different way. I am considering two different systems in this work, and their parametrized Usadel equation and boundary conditions looks different. For this reason it is convenient to be able to specify the equations as the program is called. Additionally, specifying the equations on the user level makes the code versatile, and it is no additional work to include other effects such as spin-orbit coupling and exchange fields. What made this possible was the combination of multiple dispatch in the Julia Programming language [49] and forward-mode automatic differentiation [43], which allows for efficient evaluation of Jacobians for general vector-valued functions, as long as they are written in Julia.

---

# SUPERCONDUCTING VORTICES IN HALF-METALS

“ We have entered a new stage of studying new phases of matter previously out of our reach, and of merging the hitherto disparate fields of superconductivity and spintronics to a new research direction: super-spintronics. ”

MATTHIAS ESCHRIG, 2015

Since the discovery of the Meissner effect in 1933 by Meissner and Ochsenfeld [50], it has been known that superconductors expel magnetic fields from its interior. Nevertheless, a synergy between magnetic and superconducting order is possible at the interface between a superconductor and a ferromagnet. Interestingly, it is even possible for a half-metallic ferromagnet. The superconducting condensate in a normal superconductor consists of spin-singlet electron pairs, meaning that they have opposite spin and their combined wavefunction is odd in the interchange of these spins. Half-metals, on the other hand, are 100% spin-polarized, meaning that only one spin-band is conducting, and hence no spin-singlet Cooper pairs are possible. Nevertheless, supercurrents has been observed in half-metals [51].

Any supercurrent through half-metals are necessarily spin-polarized mediated by spin-triplet Cooper pairs of equal spin. This makes them especially interesting to study in order to understand the interplay between ferromagnetic and superconducting order. An understanding of spin-triplet superconducting order is of importance in the field of superconducting spintronics, which has as one of its goals to enable new types of devices utilizing spin-polarized supercurrents [4, 5]. This is now an active field of research and much experimental and theoretical work has recently been conducted in order to understand the behaviour of hybrid structures involving superconductors (S) and half metals (H) [9, 25, 36, 51–57].

A characterizing feature of Cooper pairs in diffusive half-metals is that they must be non-local in time. This follows from the Pauli exclusion principle. The wavefunction must be odd in the combined interchange of positions, time and spin. In the dirty limit we are assuming that the quasiclassical Green’s function is dominated by the s-wave component because the system, so the wavefunction is even in position. Consequently, the wavefunction is odd in either spin or time but not both. Conventional Cooper pairs are spin-singlet and therefore even in time. Cooper pairs in half-metallic ferromagnets, in contrast, are spin-triplet and hence odd in time.

The proximity effect in half-metals is more complicated than in normal SNS-junctions because it requires a mechanism which converts the spinless (singlet) Cooper pairs to spin-polarized (triplet) pairs. The theorized mechanism to produce such correlations involve spin mixing and spin-flip scattering at the interface [56]. Spin mixing introduces triplet correlations at the superconducting side, and spin-flip scattering mediates these correlations to the half-metallic side. What has allowed me to investigate SH-heterostructures in the presence of an external magnetic field is the recent derivation of general spin-active boundary conditions for the quasiclassical theory applied to diffusive systems [25, 36]. This means that it is possible to apply the quasiclassical Usadel

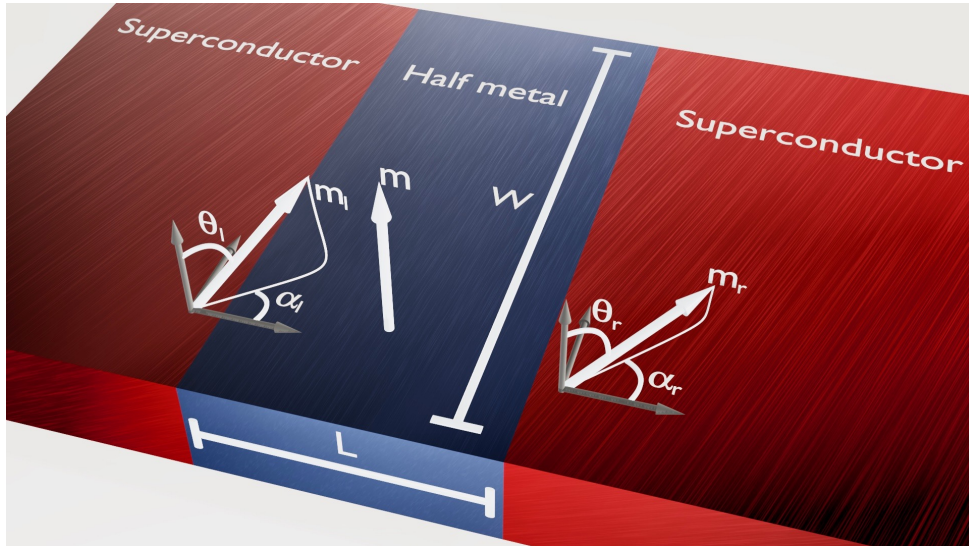


**Figure 3.1:** Sketch of a SHS junction.  $\mathbf{m}$  is the magnetization direction in the half-metal and  $\mathbf{m}_l$  and  $\mathbf{m}_r$  are the magnetization directions at the left and right interface, respectively.  $\theta_l$  and  $\theta_r$  are the associated polar angles and  $\alpha_l$  and  $\alpha_r$  are the associated azimuthal angles.  $L$  and  $W$  are the length and width of the half metal, respectively.

theory in such a way that the Cooper pair conversion mechanism described above is included.

One hitherto unsolved problem is whether superconducting quantum vortices will form in half metallic hybrid structures. These topological excitations can form when ordinary superconductors are exposed to a magnetic field. This is a basic characteristic of superconductivity, but yet little is known about if and how vortices appear in odd-frequency superconductors. Odd-frequency superconductivity has never been observed to arise spontaneously in a material, but the fact that purely odd-frequency superconducting correlations occur in SH-heterostructures gives us a way to determine if vortices can occur despite the complete absence of conventional superconducting correlations. To investigate this problem I apply the quasiclassical theory both analytically and numerically to a two-dimensional SHS-junction as depicted in figure 3.1 under a constant perpendicular magnetic field.

### 3.1 System

Chapter 2 introduced the Usadel equation (2.7). The system we consider here is shown in figure 3.1 and is a two-dimensional SHS-junction with length  $L$  and width  $W$ . That is,  $(x, y) \in [0, L] \times [-W/2, W/2]$  inside the half-metal. Superconductors are located at  $x < 0$  and  $x > L$  and have lengths which are large compared to  $L$ . The interfaces between the half-metal and superconductors are spin-active tunneling boundaries, meaning that they discriminate between particles of different spin. The magnetization of the half-metallic ferromagnet,  $\mathbf{m}$ , is taken to be along the  $z$ -axis. The direction of the magnetization of the interfaces,  $\mathbf{m}_l$  and  $\mathbf{m}_r$ , are kept arbitrary and we will look at how different choices for these angles affect the outcome. Crucially, we will see that the strength of the proximity effect in the half-metal is proportional to the in-plane component of the interfacial magnetization directions, meaning that in order to get superconducting correlations in the half-metal, at least one of the polar angles,  $\theta_l$  or  $\theta_r$ , must be nonzero. These effective interfacial magnetization directions can come from either artificially inserted thin ferromagnetic layers or from magnetic disorder at the interfaces [53]. That is, natural misalignment of magnetic dipoles arising from the conjunction of different atomic structures meeting at the interface can possibly lead to an effective magnetization direction at the interface which is not collinear with the magnetization direction of the half-metal. Finally,



the superconductors are assumed to be equal, such that the amplitude of the gap parameters  $\Delta_l$  and  $\Delta_r$  are equal, although the phases may differ.

### 3.1.1 Gauge Field

It is important to clearly state what gauge is being used when working with systems such as that presented here. The reason is that superconductivity spontaneously breaks the  $U(1)$  gauge symmetry. A consequence of this is that the superconducting order parameter and the electromagnetic vector potential are intimately connected. Changing the vector potential or the order parameter by themselves changes the physical situation. Hence, if one wants to use another gauge while preserving the physical situation, one must change both the vector potential and the order parameter simultaneously. As we will see, certain observables, such as the vortex location, will depend on the phase difference between the order parameters in the superconductors. However, because of the relation mentioned above, giving a relation between a physical observable and the superconducting phase difference is meaningless without also specifying what gauge is used.

The magnetic field considered here is constant and parallel to the  $z$ -axis in the half-metal and zero in the superconductors. That is,  $\mathbf{B} = -B\mathbf{e}_z[\theta(x) - \theta(x - L)]$ . We shall use the vector potential

$$Le\mathbf{A} = -n\pi\frac{y}{W}[\theta(x) - \theta(x - L)]\mathbf{e}_x, \quad (3.1)$$

where  $n = BLW/(\pi/|e|) = \Phi/\Phi_0$  is the total magnetic flux  $\Phi$  divided by the flux quantum  $\Phi_0 = \pi/|e|$ . Equation (3.1) has the advantage of being in the Coulomb-gauge inside the half-metal. Additionally, the fact that it is nonzero only in the  $x$ -direction will allow us to convert the Usadel equation to an ordinary differential equation in the wide junction limit described below. Finally, it is zero inside the superconductors, which allows for the superconducting phase to be constant.

## 3.2 Boundary conditions

The reason that superconductivity can exist in the half-metal in the first place is that superconducting correlation can leak through the interface with the superconductors. This phenomenon must in the quasiclassical theory be entirely captured by the boundary conditions, as the relevant length scales are too small to be treated quasiclassically. Boundary conditions are therefore of crucial importance for describing proximity effects in heterogenic structures.

The interface between a conventional superconductor and a diffusive half-metallic ferromagnetic is special because the superconducting correlations that exist in the superconductor, spin-singlet and even-frequency, are impossible in a half-metal. Hence, in order for any proximity effect in the half-metal there must be some mechanism that converts the Cooper pairs into spin-triplet odd-frequency Cooper pairs as they make their way into the half-metal. As mentioned above, the proposed mechanism involve spin mixing and spin-flip scattering at the interface [56]. Spin mixing introduces triplet correlations at the superconducting side, and spin-flip scattering mediates these correlations to the half-metallic side. Although this mechanism has been known since 2003, it took more than a decade before the relevant boundary conditions was developed for the diffusive limit [25]. These boundary conditions must distinguish between spins, and we therefore call them spin-active boundary conditions.

It is not immediately obvious that a general spin-active quasiclassical boundary condition is even possible. The quasiclassical Green's functions are typically discontinuous across boundaries, even if the microscopic Gor'kov Green's functions are not. Some information about the microscopic Green's function is lost when integrating over energy to produce the quasiclassical Green's function, and the quasiclassical treatment itself is not applicable at the boundary. Determining quasiclassical boundary conditions means to calculate the jump in the energy-integrated Green's function despite

not knowing the full microscopic Green's function. This difficult task has been proven possible, and in 2015 it was found for general spin-active boundaries between diffusive materials by Eschrig et al. [25].

The expressions for the boundary conditions in found in [25] was simplified in 2017 by Ouassou et al. [36], making them easier to implement and more efficient to compute. To second order in transmission probabilities and spin-mixing angles the boundary conditions are

$$\begin{aligned}
G_i L_i \mathbf{e}_n \cdot (\hat{g}_i \bar{\nabla} \hat{g}_i) &= \frac{G_0^i}{2} [\hat{g}_i, F(\hat{g}_j)] - \frac{iG_\varphi^i}{2} [\hat{g}_i, \hat{m}_i] + \frac{G_2^i}{8} F(\hat{g}_j) \hat{g}_i F(\hat{g}_j) \\
&+ \frac{G_{\varphi^2}^i}{8} [\hat{g}_i, \hat{m}_i \hat{g}_i \hat{m}_i] + \frac{iG_\chi^i}{8} [\hat{g}_i, F(\hat{g}_j) \hat{g}_i \hat{m}_i + \hat{m}_i \hat{g}_i F(\hat{g}_j)] \\
&+ \frac{iG_\chi^j}{8} [\hat{g}_i, F(\hat{g}_j \hat{m}_j \hat{g}_j - \hat{m}_j)], \tag{3.2}
\end{aligned}$$

where  $\mathbf{e}_n$  is the outward-pointing normal vector for region  $i$ ,  $G_i$  is the bulk conductance of material  $i$  and  $L_i$  is the length of material  $i$  in the direction of  $\mathbf{e}_n$ . For a half-metallic ferromagnet,

$$F(\hat{v}) = \hat{v} + \{\hat{v}, \hat{m}\} + \hat{m} \hat{v} \hat{m} \tag{3.3}$$

and  $\hat{m}_k = \text{diag}(\mathbf{m}_k \cdot \boldsymbol{\sigma}, \mathbf{m}_k \cdot \boldsymbol{\sigma}^*)$ . Here  $\boldsymbol{\sigma} = (\sigma_1, \sigma_2, \sigma_3)^\top$  is the vector of Pauli matrices and  $\mathbf{m}_k$  is a unit vector in the direction of the magnetization experienced by a particle being reflected in material  $k$ . Similarly,  $\hat{m} = \text{diag}(\mathbf{m} \cdot \boldsymbol{\sigma}, \mathbf{m} \cdot \boldsymbol{\sigma}^*)$  where  $\mathbf{m}$  is the unit vector in the direction of the magnetization being felt by a particle which is transmitted. The interface conductances are [36]

$$\begin{aligned}
G_0^i &= G_q \sum_{n=1}^N T_n^i, & G_\varphi^i &= 2G_q \sum_{n=1}^N \varphi_n^i, \\
G_2^i &= G_q \sum_{n=1}^N (T_n^i)^2, & G_\chi^i &= G_q \sum_{n=1}^N T_n^i \varphi_n^i, \\
G_{\varphi^2}^i &= 2G_q \sum_{n=1}^N (\varphi_n^i)^2, \tag{3.4}
\end{aligned}$$

where  $T_n^i$  and  $\varphi_n^i$  are respectively the transmission probability and spin mixing angle for tunneling channel  $n$  from material  $i$  to material  $j$ .  $G_q = e^2/\pi$  is the conductance quantum (remember,  $\hbar = 1$ ). The boundary condition across the boundaries with vacuum at  $y = \pm W/2$  is  $\mathbf{e}_n \cdot \bar{\nabla} \hat{g} = 0$ .

### 3.3 Superconducting Order Parameter

Looking at superconducting vortices in odd-frequency superconducting condensates naturally poses an interesting question regarding how to identify such vortices. Superconducting vortices are characterized by a root in the superconducting order parameter in its core and a phase winding of  $2\pi$  in the superconducting order parameter along a trajectory circulating the vortex. The superconducting order parameter,  $\langle \psi_\downarrow(\mathbf{r}, 0) \psi_\uparrow(\mathbf{r}, 0) \rangle$ , is normally used to identify vortices in conventional superconductors and normal proximity systems. However, as was mentioned in section 2.4, the analogous quantity in odd-frequency superconductors,  $\langle \psi_\uparrow(\mathbf{r}, 0) \psi_\uparrow(\mathbf{r}, 0) \rangle$ , is identically equal to zero.

What makes this an interesting challenge is that it is not obvious that other choices of order parameters work equally well. One type of order parameter which one could use, and which is often used in the Bogoliubov deGennes formalism [37], is to keep a nonzero time between the order parameters,

$$\Psi_1(\mathbf{r}, t) := \langle \psi_\uparrow(\mathbf{r}, t) \psi_\uparrow(\mathbf{r}, 0) \rangle. \tag{3.5}$$

However, it is not obvious that eq. (3.5) should work better than the analogous  $\langle \psi_{\downarrow}(\mathbf{r}, t) \psi_{\uparrow}(\mathbf{r}, 0) \rangle$  works in the normal case. Plugging in the bulk BCS solution I find that there are certain relative times  $t$  where this order parameter vanishes even for conventional superconductors. Additionally, using this order parameter in normal SNS-junctions, I find that there are sometimes additional roots with phase windings which are not present in the normal order parameter. Moreover, these additional roots do not correspond to circulating supercurrents and do not have cores where the density of states is equal to that of the normal state. Hence, these additional roots do not correspond to superconducting vortices, which means that  $\langle \psi_{\downarrow}(\mathbf{r}, t) \psi_{\uparrow}(\mathbf{r}, 0) \rangle$  can be misleading when used to identify vortices.

One possibility is that  $\Psi_1(\mathbf{r}, t)$  works better when  $t$  approaches 0. Alternatively, one can use the order parameter

$$\Psi_2(\mathbf{r}) := \left. \frac{\partial \langle \psi_{\uparrow}(\mathbf{r}, t) \psi_{\uparrow}(\mathbf{r}, 0) \rangle}{\partial t} \right|_{t=0}. \quad (3.6)$$

When it comes to locating vortices by the roots of an order parameter,  $\Psi_2(\mathbf{r})$  is equivalent to using  $\Psi_1(\mathbf{r}, t)$  with an infinitesimally small  $t$ , since  $\Psi_1(\mathbf{r}, t) \sim t\Psi_2(\mathbf{r})$  as  $t \rightarrow 0$ .

Numerically, it could be beneficial to simply use  $\Psi_1$  with a small value of  $t$  rather than  $\Psi_2$ . Written in terms of the anomalous Green's function  $f_{\uparrow}$ , the order parameters are

$$\Psi_1(\mathbf{r}, t) = \frac{-iN_0}{2} \int d\varepsilon f_{\uparrow}(\mathbf{r}, \varepsilon) \tanh\left(\frac{\beta\varepsilon}{2}\right) \sin(\varepsilon t) \quad (3.7)$$

and

$$\Psi_2(\mathbf{r}) = \frac{-iN_0}{2} \int d\varepsilon f_{\uparrow}(\mathbf{r}, \varepsilon) \tanh\left(\frac{\beta\varepsilon}{2}\right) \varepsilon. \quad (3.8)$$

The integrand in eq. (3.7) goes more quickly to 0 than the integrand in eq. (3.8) and numerically it is therefore expected to be easier to integrate as long as  $t$  is small.

In this chapter we will compare the location of the roots of these order parameters to the location of vortices as revealed by other observables in order to determine which order parameters work to locate superconducting vortices in odd-frequency superconducting condensates.

## 3.4 Analytics

### 3.4.1 Analytic Solution in the Superconductors

Before writing the boundary condition in the Ricatti parametrization, we must determine the solution in the superconductors. I shall show that it suffices to use the bulk solution

$$\hat{g}_{\text{BCS}} = \left[ \frac{\theta(\varepsilon^2 - |\Delta|^2)}{\sqrt{\varepsilon^2 - |\Delta|^2}} \text{sgn}(\varepsilon) - \frac{\theta(|\Delta|^2 - \varepsilon^2)}{\sqrt{|\Delta|^2 - \varepsilon^2}} i \right] (\varepsilon \hat{\rho}_3 + \hat{\Delta}), \quad (3.9)$$

when assuming that the superconductors are long compared to the half metal.

First, let

$$\hat{g} = \hat{g}_{\text{BCS}} + \delta\hat{g} \quad (3.10)$$

be the solution of the Usadel equation,

$$D_{\text{sc}} \nabla \cdot (\hat{g} \nabla \hat{g}) + i [\varepsilon \hat{\rho}_3 + \hat{\Delta}, \hat{g}] = 0 \quad (3.11)$$

in the superconductor at  $x < 0$ . This gives an equation for  $\delta\hat{g}$ ,

$$D_{\text{sc}} \nabla \cdot ([\hat{g}_{\text{BCS}} + \delta\hat{g}] \nabla \delta\hat{g}) + i [\varepsilon \hat{\rho}_3 + \hat{\Delta}, \delta\hat{g}] = 0, \quad (3.12)$$

where I have used that  $\hat{g}_{\text{BCS}}$  solves the eq. (3.11) for a bulk superconductor. Next, assume the inverse proximity effect to be weak, such that  $\delta\hat{g} \ll \hat{g}_{\text{BCS}}$ . Using that  $\hat{g}_{\text{BCS}}\hat{g}_{\text{BCS}} = 1$ , this yields

$$D_{\text{SC}}\nabla^2\delta\hat{g} + i\hat{g}_{\text{BCS}}\left[\varepsilon\hat{\rho}_3 + \hat{\Delta}, \delta\hat{g}\right] = 0. \quad (3.13)$$

$\hat{g}_{\text{BCS}} + \delta\hat{g}$  must also satisfy the normalization condition (2.10), so

$$(\hat{g}_{\text{BCS}} + \delta\hat{g})^2 = 1 \implies \{\hat{g}_{\text{BCS}}, \delta\hat{g}\} = 0. \quad (3.14)$$

Hence, using that  $[\varepsilon\hat{\rho}_3 + \hat{\Delta}, \hat{g}_{\text{BCS}}] = 0$ ,

$$\hat{g}_{\text{BCS}}\left[\varepsilon\hat{\rho}_3 + \hat{\Delta}, \delta\hat{g}\right] = (\varepsilon\hat{\rho}_3 + \hat{\Delta})\hat{g}_{\text{BCS}}\delta\hat{g} + \delta\hat{g}(\varepsilon\hat{\rho}_3 + \hat{\Delta})\hat{g}_{\text{BCS}} = \left\{\delta\hat{g}, (\varepsilon\hat{\rho}_3 + \hat{\Delta})\hat{g}_{\text{BCS}}\right\}. \quad (3.15)$$

Finally, from

$$\left(\varepsilon\hat{\rho}_3 + \hat{\Delta}\right)^2 = \varepsilon^2 - \Delta^2 \quad (3.16)$$

I get that  $\delta\hat{g}$  is an eigenvector of the Laplacian,

$$\nabla^2\delta\hat{g} = \lambda^2\delta\hat{g} \quad (3.17)$$

where

$$\lambda^2 = -\frac{2i}{D_{\text{SC}}}\left[\text{sgn}(\varepsilon)\sqrt{\varepsilon^2 - |\Delta|^2}\theta\left(\varepsilon^2 - |\Delta|^2\right) + i\sqrt{|\Delta|^2 - \varepsilon^2}\theta\left(|\Delta|^2 - \varepsilon^2\right)\right]. \quad (3.18)$$

We can choose the sign of  $\lambda$  to be such that  $\Re(\lambda) > 0$ .

Let  $L_{\text{SC}}$  be the length of the superconductor in multiples of the length of the half metal. Using the boundary condition

$$\nabla\delta\hat{g}|_{\mathbf{r}\in\Omega} = 0, \quad (3.19)$$

where  $\Omega$  is the boundary not interfacing the half metal, I get

$$\delta\hat{g}(\varepsilon, x, y) = C\left[e^{-\lambda|x|} - e^{-2\lambda L_{\text{SC}} + \lambda|x|}\right], \quad (3.20)$$

where  $C$  is some a function of  $y$  and  $\varepsilon$  to be determined by the final boundary condition. If the matrix current across this boundary is  $\hat{I}_{\text{SC}}$ , then

$$C = \frac{\hat{g}_{\text{BCS}}\hat{I}_{\text{SC}}}{\lambda G_{\text{SC}}L_{\text{SC}}(1 - e^{-2\lambda L_{\text{SC}}})}. \quad (3.21)$$

$\hat{I}_{\text{SC}}$  depends implicitly on  $L_{\text{SC}}$ , but only through terms which are second order or more in transmission probabilities and spin-mixing angles. Hence, the contribution from the correction to the Green's function in the superconductor scales inversely proportionally with the length of the superconductor to second order in transmission probabilities and spin-mixing angles. Assuming  $L_{\text{SC}} \gg L$  we are therefore justified in setting  $\delta\hat{g} = 0$ . The same calculation shows that we can use  $\hat{g}_{\text{BCS}}$  also in the superconductor at  $x > L$ .

### 3.4.2 Ricatti-Parametrized Equations

We are now in a position to write down the full set of equations for the half-metal. The dimensionless Usadel equations with the Ricatti were introduced in chapter 2 and are

$$\nabla^2 a + \frac{2\tilde{a}\nabla a \cdot \nabla a}{1 - a\tilde{a}} = \frac{4(1 + a\tilde{a})e\mathbf{A} \cdot (ae\mathbf{A} + i\nabla a)}{1 - a\tilde{a}} - 2i\varepsilon a, \quad (3.22a)$$

$$\nabla^2 \tilde{a} + \frac{2a\nabla \tilde{a} \cdot \nabla \tilde{a}}{1 - a\tilde{a}} = \frac{4(1 + a\tilde{a})e\mathbf{A} \cdot (\tilde{a}e\mathbf{A} - i\nabla a)}{1 - a\tilde{a}} - 2i\varepsilon a. \quad (3.22b)$$

Plugging in the Ricatti-parametrized bulk BCS Green's function in eq. (3.2) I get

$$G_{\text{HM}} \mathbf{e}_n \cdot \nabla a = 2iG_{\text{HM}} a \mathbf{e}_n \cdot \mathbf{A} e + 4G_0^{\text{HM}} BC a - G_2^{\text{HM}} B^2 C^2 a (a\tilde{a} + 3) + 2iG_{\chi}^{\text{SC}} BC^2 \left( b [m_1 - im_2] - \tilde{b} [m_1 + im_2] a^2 \right), \quad (3.23a)$$

$$G_{\text{HM}} \mathbf{e}_n \cdot \nabla \tilde{a} = -2iG_{\text{HM}} \tilde{a} \mathbf{e}_n \cdot \mathbf{A} e + 4G_0^{\text{HM}} BC \tilde{a} - G_2^{\text{HM}} B^2 C^2 (a\tilde{a} + 3) - 2iG_{\chi}^{\text{SC}} BC^2 \left( \tilde{b} [m_1 + im_2] - b [m_1 - im_2] \tilde{a}^2 \right), \quad (3.23b)$$

where  $B = b\tilde{b} - 1$ ,  $C = 1/(1 + b\tilde{b})$  and  $m_1$  and  $m_2$  are the  $x$ - and  $y$ -components of the effective magnetization direction at the boundary.  $b$  is the Ricatti parameter in the superconductor, that is

$$\gamma_{\text{sc}} = \begin{pmatrix} 0 & b \\ -b & 0 \end{pmatrix} = \begin{pmatrix} 0 & |b| \\ -|b| & 0 \end{pmatrix} e^{i\varphi}. \quad (3.24)$$

In the following we write

$$m_1 + im_2 = \sin \theta e^{i\alpha}, \quad (3.25)$$

with the angles  $\theta$  and  $\alpha$  as shown in figure 3.1. For the interfaces with vacuum,  $\mathbf{e}_n \cdot \nabla a = 0$

### 3.4.3 Analytic Solution

In order to solve these equations we must make some simplifying assumptions. If we assume the proximity to be weak, we can keep only terms which are linear in  $a$  and  $\tilde{a}$  and their gradients. In this case the Usadel equation (3.22a) decouples:

$$\nabla^2 a = 4\mathbf{A} \cdot (a\mathbf{A} + i\nabla a) - 2i\varepsilon a, \quad (3.26a)$$

$$\nabla^2 \tilde{a} = 4\mathbf{A} \cdot (\tilde{a}\mathbf{A} - i\nabla \tilde{a}) - 2i\varepsilon \tilde{a}. \quad (3.26b)$$

and so does the boundary conditions,

$$\mathbf{e}_n \cdot \nabla a = \left\{ 4 \frac{G_0^{\text{HM}}}{G_{\text{HM}}} BC - 3 \frac{G_2^{\text{HM}}}{G_{\text{HM}}} B^2 C^2 + 2i \mathbf{e}_n \cdot \mathbf{A} e \right\} a + 2i \frac{G_{\chi}^{\text{SC}}}{G_{\text{HM}}} BC^2 |b| \sin \theta e^{i(\varphi - \alpha)}, \quad (3.27a)$$

$$\mathbf{e}_n \cdot \nabla \tilde{a} = \left\{ 4 \frac{G_0^{\text{HM}}}{G_{\text{HM}}} BC - 3 \frac{G_2^{\text{HM}}}{G_{\text{HM}}} B^2 C^2 - 2i \mathbf{e}_n \cdot \mathbf{A} e \right\} \tilde{a} - 2i \frac{G_{\chi}^{\text{SC}}}{G_{\text{HM}}} BC^2 |\tilde{b}| \sin \theta e^{-i(\varphi - \alpha)}. \quad (3.27b)$$

Equation (3.26) can be further simplified in the so-called wide junction limit, where  $n/W \ll 1$ . If  $\mathbf{A} = 0$ , the solution of eq. (3.26) is constant in the  $y$ -direction. Assuming this is approximately true also for small  $\mathbf{A}$ , we neglect the term  $\partial_y^2 a$ . Equation (3.26) can now be solved exactly, as it is a second order ordinary differential equation with constant coefficients. The solution of eq. (3.26a) is

$$a = C_1 e^{(u+k)x} + C_2 e^{(u-k)x}, \quad (3.28)$$

where  $u = -2\pi i n y / W$ ,  $k = \sqrt{-2i\varepsilon}$  and  $C_1$  and  $C_2$  are independent of  $x$ .

Determining  $C_1$  and  $C_2$  requires the boundary conditions, which can be written

$$\left. \frac{\partial a}{\partial x} \right|_{x=0} = -c \sin \theta_l e^{i(\varphi_l - \alpha_l)} - (d - u) a, \quad (3.29a)$$

$$\left. \frac{\partial a}{\partial x} \right|_{x=1} = c \sin \theta_r e^{i(\varphi_r - \alpha_r)} + (d + u) a, \quad (3.29b)$$

where

$$c = 2i \frac{G_{\chi}^{\text{SC}}}{G_{\text{HM}}} BC^2 |b| \quad \text{and} \quad d = 4 \frac{G_0^{\text{HM}}}{G_{\text{HM}}} BC - 3 \frac{G_2^{\text{HM}}}{G_{\text{HM}}} B^2 C^2. \quad (3.30)$$

After some algebra, the solution can be written

$$a = \frac{ce^{i(\varphi_l - \alpha_l) + ux}}{(k-d)^2 e^k - (k+d)^2 e^{-k}} \left\{ (k-d) \left( \sin \theta_l e^{-k(1-x)} + \sin \theta_r e^{i\delta\varphi - u} e^{-kx} \right) \right. \\ \left. + (k+d) \left( \sin \theta_l e^{k(1-x)} + \sin \theta_r e^{i\delta\varphi - u} e^{kx} \right) \right\}, \quad (3.31)$$

where

$$\delta\varphi = \varphi_r - \alpha_r - \varphi_l + \alpha_l. \quad (3.32)$$

Note that the wide junction approximation is not applicable at small energies. This is because the solution will be slowly varying in the  $x$ -direction and therefore  $\partial_y^2 a$  is no longer negligible compared to  $\partial_x^2 a$ .

When  $\sin \theta_l = \sin \theta_r$ ,  $a$  vanishes at  $x = 1/2$  and

$$\frac{y}{W} = \frac{1}{n} \left( \frac{1}{2} + N - \frac{\varphi_r - \alpha_r - \varphi_l + \alpha_l}{2\pi} \right), \quad (3.33)$$

where  $N$  is any integer. This means that  $f_{\uparrow}$  and hence also the order parameters  $\Psi_1$  and  $\Psi_2$  vanishes at these points.  $a$  is holomorphic, so from Cauchy's argument principle [58] there is a  $2\pi$  phase winding in the order parameters around these points because the multiplicity of the roots are 1. These  $n$  roots<sup>1</sup> are the only ones for  $\Psi_2$ , but for  $\Psi_1$  there are relative times  $t$  for which additional roots exist. Since each vortex is associated with a quantum of magnetic flux,  $\Phi_0$ , there should be at most  $n$  vortices when the flux is  $n\Phi_0$ . This suggests that  $\Psi_1$  is less suited for finding vortices than  $\Psi_2$  if we identify vortices by the roots of the order parameter. Using  $\Psi_2$  suggests that when  $\sin \theta_l = \sin \theta_r$  and the magnetic flux is  $n\Phi_0$ , there will in the wide-junction limit be  $n$  vortices whose location is determined by the difference in the superconducting phases and the magnetization angles.

The situation is more complicated when  $\sin \theta_l \neq \sin \theta_r$ . In this case the roots of eq. (3.31) depend on  $\varepsilon$ , and I will leave the discussion for how this affects the order parameter to the numerical investigation. However, some insight can still be had from the analysis. Scaling  $\sin \theta$  in the boundary condition (3.27) is equivalent to scaling the conductance  $G_{\chi}^{\text{SC}}$ . That is, if  $\sin \theta_r < \sin \theta_l$ , the proximity effect should be weaker at the right side, meaning that the vortices should be pushed to the right. This is indeed what I find numerically.

## 3.5 Numerics

We now proceed to the numerical results in the full (non-linear) proximity effect regime. The parameters  $|\Delta| = 4\varepsilon_{\text{T}}$ ,  $G_{\text{HM}} = 3G_0^{\text{HM}}$ ,  $G_{\chi}^{\text{SC}} = 0.01G_0^{\text{HM}}$ ,  $G_2^{\text{HM}} = 0.002G_0^{\text{HM}}$ ,  $\sin \theta_l = 1$  and  $\varphi_l = \alpha_l = 0$  are set common for all the numerical calculations, but I obtain qualitatively similar results for other choices of the conductance parameters  $G_i^{\text{HM/SC}}$ . I include the effect of inelastic scattering by doing the substitution  $\varepsilon \rightarrow \varepsilon + i\delta$  where  $\delta = 0.001|\Delta|$  in order to avoid the divergence of  $\hat{g}_{\text{BCS}}$  at  $\varepsilon = |\Delta|$  [59].

### 3.5.1 Local Density of States

In the symmetric case ( $\sin \theta_r = 1.0$ ), we suspect from the analysis above that for all energies, the local density of states is equal to that of the normal state, that is  $N = N_0$ , in about  $n$  points along the line  $x = 0.5$ , where  $n$  is the number of magnetic flux quanta. Using the expression for the local density of states derived in section 2.3.1, and which is implemented numerically in appendix C, I find that this is indeed the case. Figure 3.2 shows the local density of states at

<sup>1</sup>Strictly speaking there not always exactly  $n$  roots. For instance, when  $n = 1$  and  $\delta\varphi = 0$  the order parameters vanish at  $y \pm W/2$ . Any nonzero value of  $\delta\varphi$  will result in a single vortex.

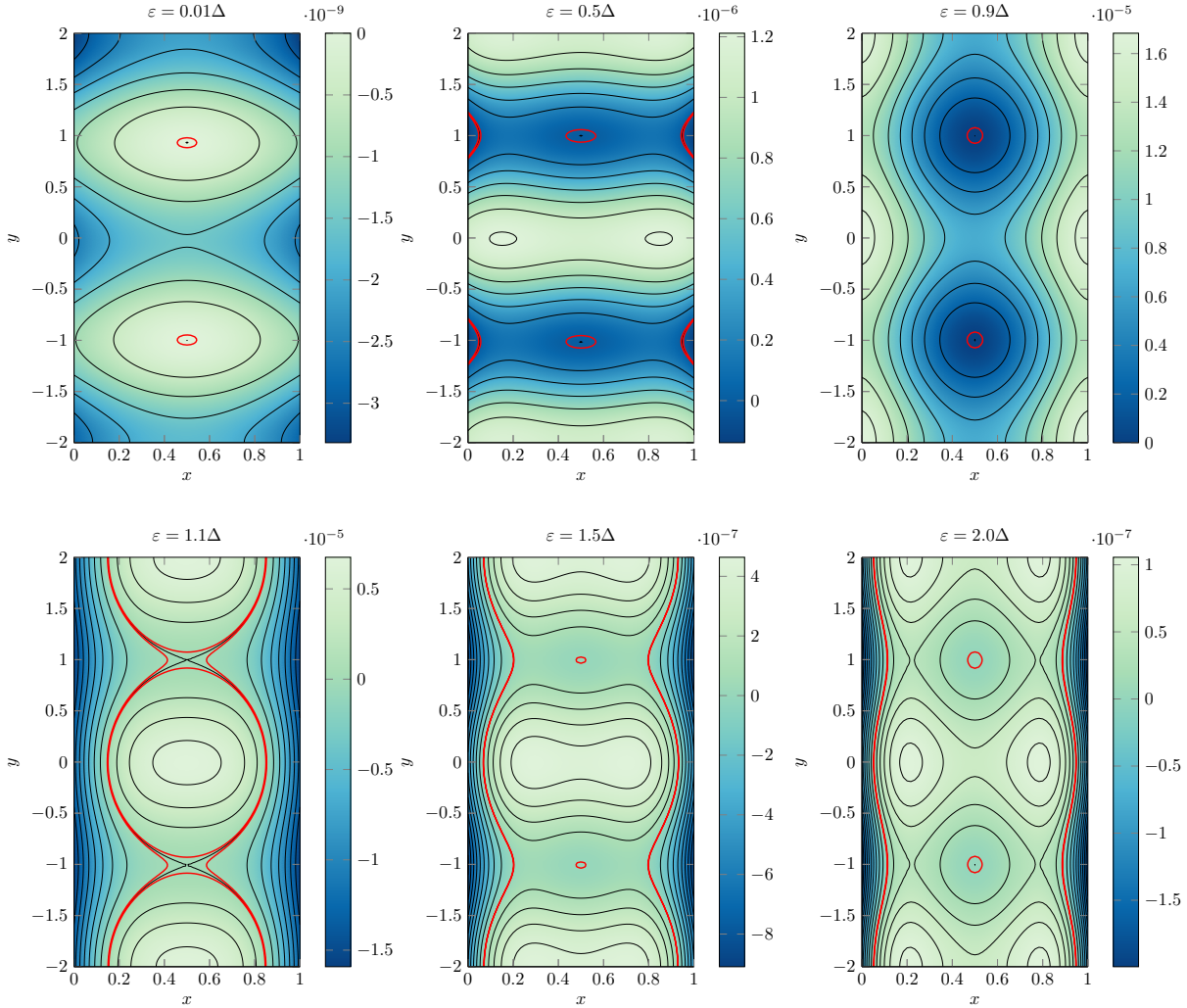


**Figure 3.2:** The normalized difference between the local density of states and the normal-state density of states,  $(N - N_0)/N_0$ , for various energies. Contour lines of constant values are added. These lines are red for the values close to zero, at  $\pm 0.01 \times S$ , where  $S$  is the number at the top of the respective colorbars. Here  $n = 2$ ,  $\varphi_r = \alpha_r = 0$  and  $\sin \theta_r = 1$ .

various energies for the symmetric case with  $n = 2$  with red lines close to where it is equal to the normal state density of states. We see that there are indeed 2 locations where the difference between the local density of states and the normal state density of states vanish for all energies, and that the locations of these points are exactly those predicted by the analysis.

The situation is slightly different for the asymmetric case ( $\sin \theta_r \neq 1$ ), as can be seen in figure 3.3. There is no longer a single point where  $N = N_0$  for all energies. Instead, the locations where  $N = N_0$  is slightly dependent on energy. For  $n = 2$ , as can be seen in figure 3.3, the location closest to  $x = 1/2$  where  $N = N_0$  occurs at  $y = \pm W/4$ , which is also the  $y$ -values where the vortices are in the symmetric case. The place closest to  $x = 1/2$  where  $N = N_0$  moves only slightly, but the general behaviour is to move towards the central line as the energy increases.

One could be led to believe that this energy-dependence on the position where  $N = N_0$  is a peculiarity only present in the special case of an SHS-junction, but that is not true. The same phenomenon occurs in normal SNS-junctions if the conductances at the interfaces are unequal, and the underlying reason is the same in that case. As mentioned above, changing  $\sin \theta$  is the same as changing the conductance  $G_\chi^{\text{sc}}$ . One does not even need a magnetic field to see this energy-dependence. In fact, removing the magnetic field will remove the  $y$ -dependence, and so make the explanation more intuitive. Because the phenomenon is the same for an asymmetric

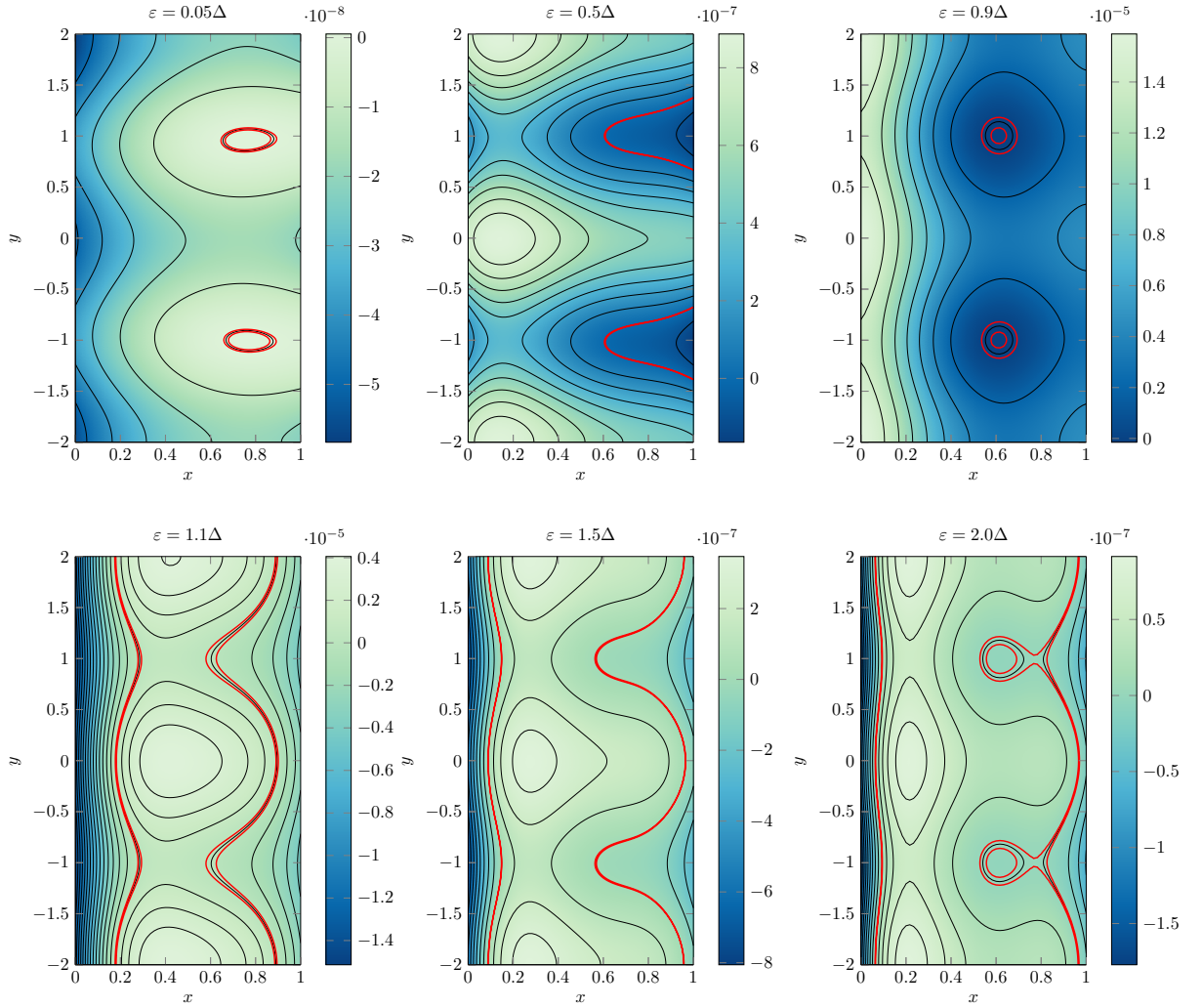


**Figure 3.3:** The normalized difference between the local density of states and the normal-state density of states,  $(N - N_0)/N_0$ , for various energies. Contour lines of constant values are added. These lines are red for the values close to zero, at  $\pm 0.01 \times S$ , where  $S$  is the number at the top of the respective colorbars. Here  $n = 2$ ,  $\varphi_r = \alpha_r = 0$  and  $\sin \theta_r = 0.5$ .



SNS-junction and the proximity effect in this case is more straight-forward, I will consider a SNS-junction in the following explanation.

Consider a SNS-junction with a superconducting phase difference of  $\pi$  and where the superconducting gap parameter in the two superconductors are equal. If the conductances across the two superconductors are equal, then the anomalous Green's function  $f$  vanish exactly midway between the superconductors for all energies. Consequently,  $N = N_0$  along this line for all energies. In a simplified model we can think of this as being because superconducting correlations leak in from the two boundaries and interfere destructively along the central line. This picture is what is suggested by the analytic solution in the weak proximity effect regime. The anomalous Green's function in the normal metal can in this regime be written<sup>2</sup>

$$f(x) = G_l e^{i\varphi_l} h(x) + G_r e^{i\varphi_r} h(L - x), \quad (3.34)$$

where  $G_l$  and  $G_r$  are the conductances across the boundaries with the left and right superconductors, respectively, and  $\varphi_l$  and  $\varphi_r$  are the superconducting phases in the left and right superconductors, respectively.  $L$  is the length of the normal metal. As the correlations propagate, they change in amplitude and phase in a manner given by the function  $h$ . Along  $x = L/2$  the contribution from the left superconductor is  $G_l e^{i\varphi_l} h(L/2)$  and the contribution from the right superconductor is  $G_r e^{i\varphi_r} h(L/2)$ . Thus, there is a complete destructive interference if  $G_l = G_r$  and  $\varphi_r - \varphi_l = \pm\pi$ .

If, on the other hand, the conductances differ, then numerically I find that there will still usually be a line where the anomalous Green's function vanish, but this line will be closer to the side where the conductance is smaller, and it will not be at the same location for all energies. The reason for why the anomalous Green's function no longer vanish midway between the superconductors is that the amplitude of the contributions from the different superconductors are no longer the same, so there is no longer complete destructive interference at  $x = L/2$ . To give a possible reason for why the destructive interference occur closer to the interface with the smaller conductance, consider only the amplitude. If we assume that there is destructive interference where the two amplitudes are equal and that the contributions from each superconductor diminish as a function of distance from the superconductors, then we can say two things. First, because the amplitude starts out smaller at the side where the conductance is the smallest, the destructive interference will occur on this half of the normal metal. Secondly, the destructive interference will occur closer to the central line the faster the decay is.

The last prediction fits well with what we observe. The destructive interference occur closer to  $x = L/2$  for higher energies, except for a jump at  $\varepsilon = \Delta$ , both for the SNS-case and for the SHS-case. From the theory of Andreev reflection we expect that the decay is faster for higher energies, at least as long as the energy is smaller than the superconducting energy gap [5]. The reason is the following. When a Cooper pair is transmitted from the superconductor into the normal metal, it must be converted into a pair of electrons whose energies are  $\mu + \varepsilon$  and  $\mu - \varepsilon$ , where  $\mu$  is the chemical potential and  $\varepsilon$  is some energy. This is because the energy of the Cooper pair is  $2\mu$ . Therefore, the higher the energy  $\varepsilon$ , the more different the wavelength of the two correlated electrons and the faster do they become decoherent.

This being said, the point where with  $y$ -value given by eq. (3.33) and  $N = N_0$  changes only very slightly with  $\varepsilon$ , at least as long as the asymmetry is moderate. A more noticeable difference between the symmetric and asymmetric case is that  $N = N_0$  in an isolated point for most energies in the symmetric case, while in the asymmetric case there is a larger elongated area where  $N$  is close to or equal to  $N_0$ . This feature is recognizable also in the supercurrents.

<sup>2</sup>See for instance [30].

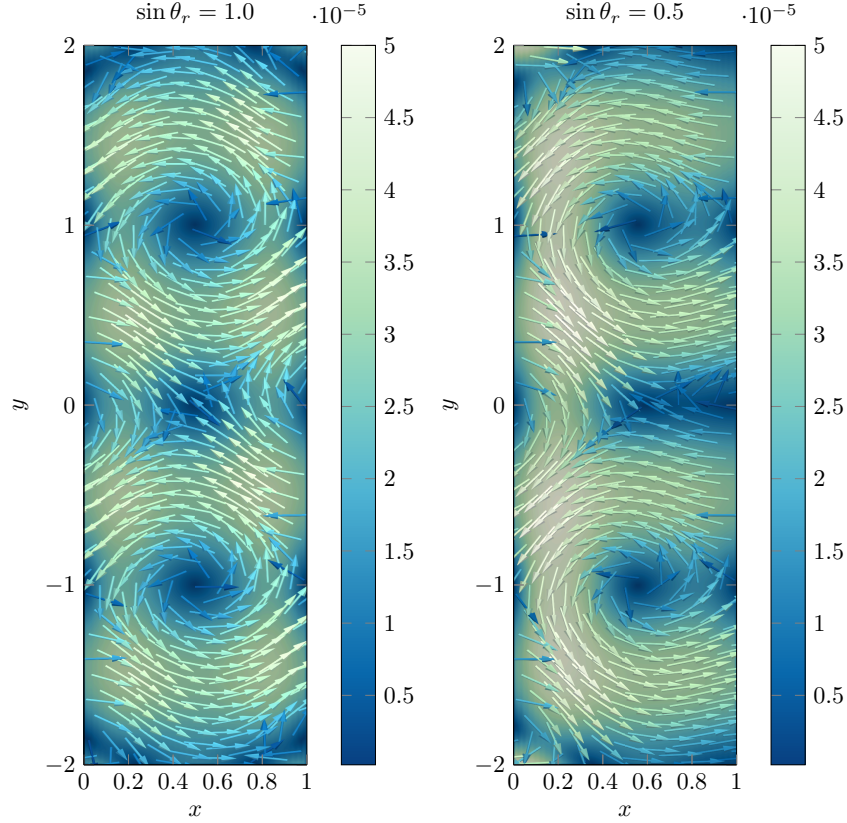


**Figure 3.4:** Amplitude and direction of the fully spin-polarized supercurrent  $\mathbf{j}$  for the symmetric case ( $\sin \theta_r = 1$ ) and the asymmetric case ( $\sin \theta_r \neq 1$ ). Here  $n = 2$  and  $\varphi_r = \alpha_r = 0$ . The values are given for the dimensionless supercurrent  $\mathbf{j} \times (L/N_0 e D \varepsilon_T)$ .

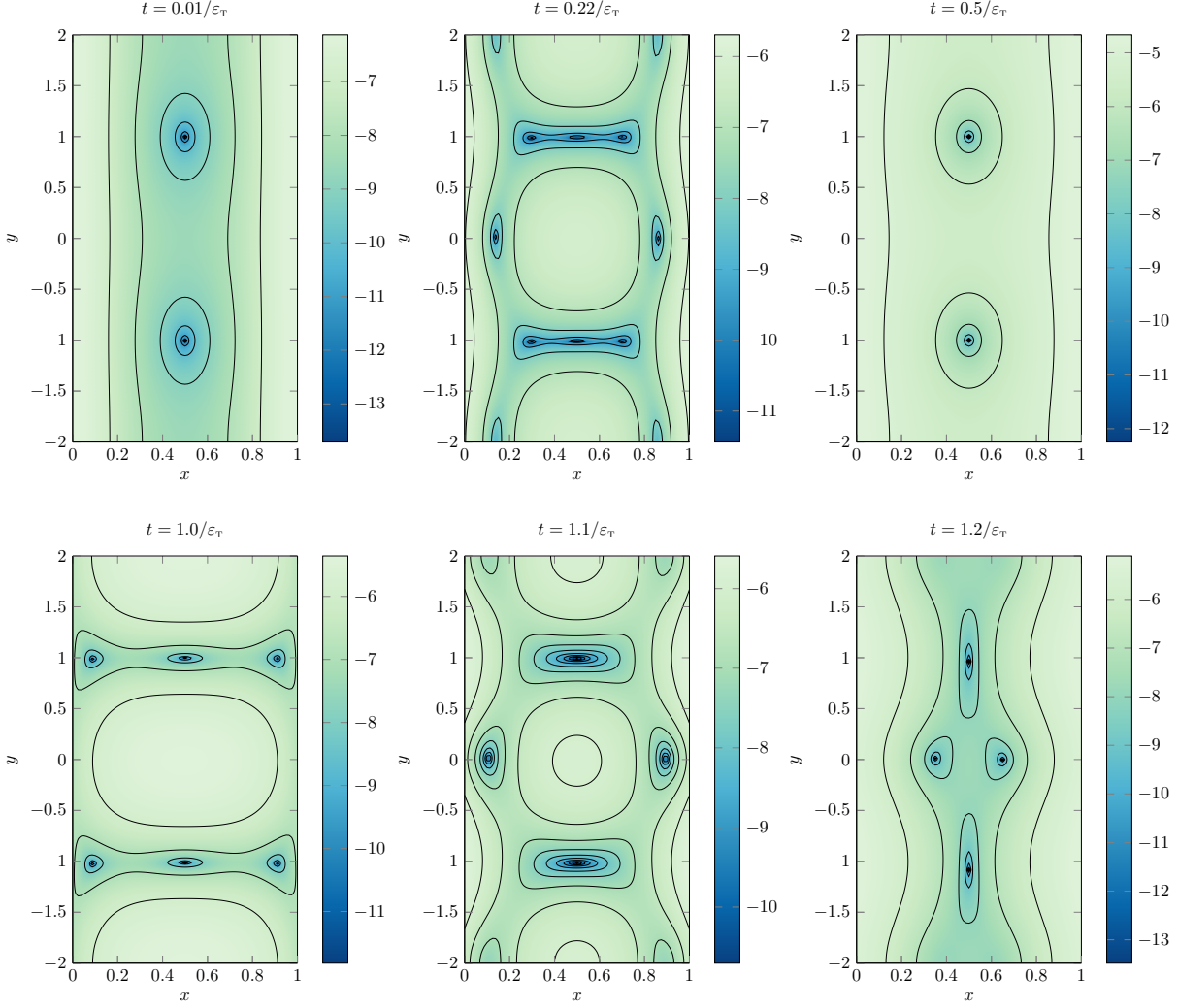
### 3.5.2 Supercurrent

Figure 3.4 shows the current amplitude and direction for the same two cases as was discussed in the previous section. That is, the symmetric case with  $n = 2$ ,  $\varphi_r = \alpha_r = 0$  and  $\sin \theta_r = 1$  and the asymmetric case with  $n = 2$ ,  $\varphi_r = \alpha_r = 0$  and  $\sin \theta_r = 0.5$ . In both cases there are exactly two points where the supercurrents vanish and where the supercurrent circles around. This indicates the existence of two superconducting vortices, which is in accordance with the analysis, local density of states and the fact that the system is experiencing two quanta of magnetic flux.

The  $y$ -value of the points with circulating supercurrents are the same as what is expected by the analysis, given by eq. (3.33). In the symmetric case these points are midway between the superconductors, i.e. at  $x = L/2$ , while in the asymmetric case they are moved slightly toward the side where  $\sin \theta$  is smaller. Hence, the vortex locations as given by the supercurrents agrees with the analysis as well as the results from the local density of states.

One feature of the asymmetric case worth noting is that the supercurrent is suppressed to the right of the vortex, which is towards the side where  $\sin \theta$  is smaller. This is in agreement with the fact that this region had a local density of states which was closer to the normal state value, as shown in section 3.5.1.

Finally, note that the currents are fully spin-polarized because the half-metal is fully spin-polarized. This is an important realization, as one goal of the field of superconducting spintronics is to be able manipulate spin-polarized supercurrents [5]. The topological nature of vortices means that they are stable, and using vortices as a means for transporting spin information has recently been proposed by coupling superconductors to magnetic insulators [15].



**Figure 3.5:** Plots of  $\log(|\Psi_1(\mathbf{r}, t)| \times 2/N_0\varepsilon_T)$  for various values of  $t$  in the symmetric case ( $\sin\theta_r = 1$ ) with  $n = 2$  and  $\varphi_r = \alpha_r = 0$ .

### 3.5.3 Cooper Pair Correlation Function

Investigating vortices in odd-frequency superconductors gives rise to the problem of choosing what order parameter to use. The Cooper pair correlation function which is normally used is not applicable as it is identically equal to zero. The two most obvious remaining choices are

$$\Psi_1(\mathbf{r}, t) := \langle \psi_\uparrow(\mathbf{r}, t) \psi_\uparrow(\mathbf{r}, 0) \rangle \quad (3.35)$$

and

$$\Psi_2(\mathbf{r}) := \left. \frac{\partial \langle \psi_\uparrow(\mathbf{r}, t) \psi_\uparrow(\mathbf{r}, 0) \rangle}{\partial t} \right|_{t=0}, \quad (3.36)$$

as mentioned above. From looking at the local density of states and the supercurrent we already know that we expect vortices and that their location should have  $y$ -value given by eq. (3.33) and be at  $x = L/2$  in the symmetric case and closer to the side where  $\sin\theta$  is smaller in the asymmetric case. Comparing the position of the roots of  $\Psi_1$  and  $\Psi_2$  with the position of the vortices as predicted by the local density of states and the supercurrent can be used to give an identification of how good the order parameters are as means to find vortices.

Figures 3.5 and 3.6 shows  $\Psi_1$  with various values of  $t$  for the two same cases which was shown in sections 3.5.1 and 3.5.2. Figure 3.5 shows the symmetric case with  $n = 2$ ,  $\varphi_r = \alpha_r = 0$  and

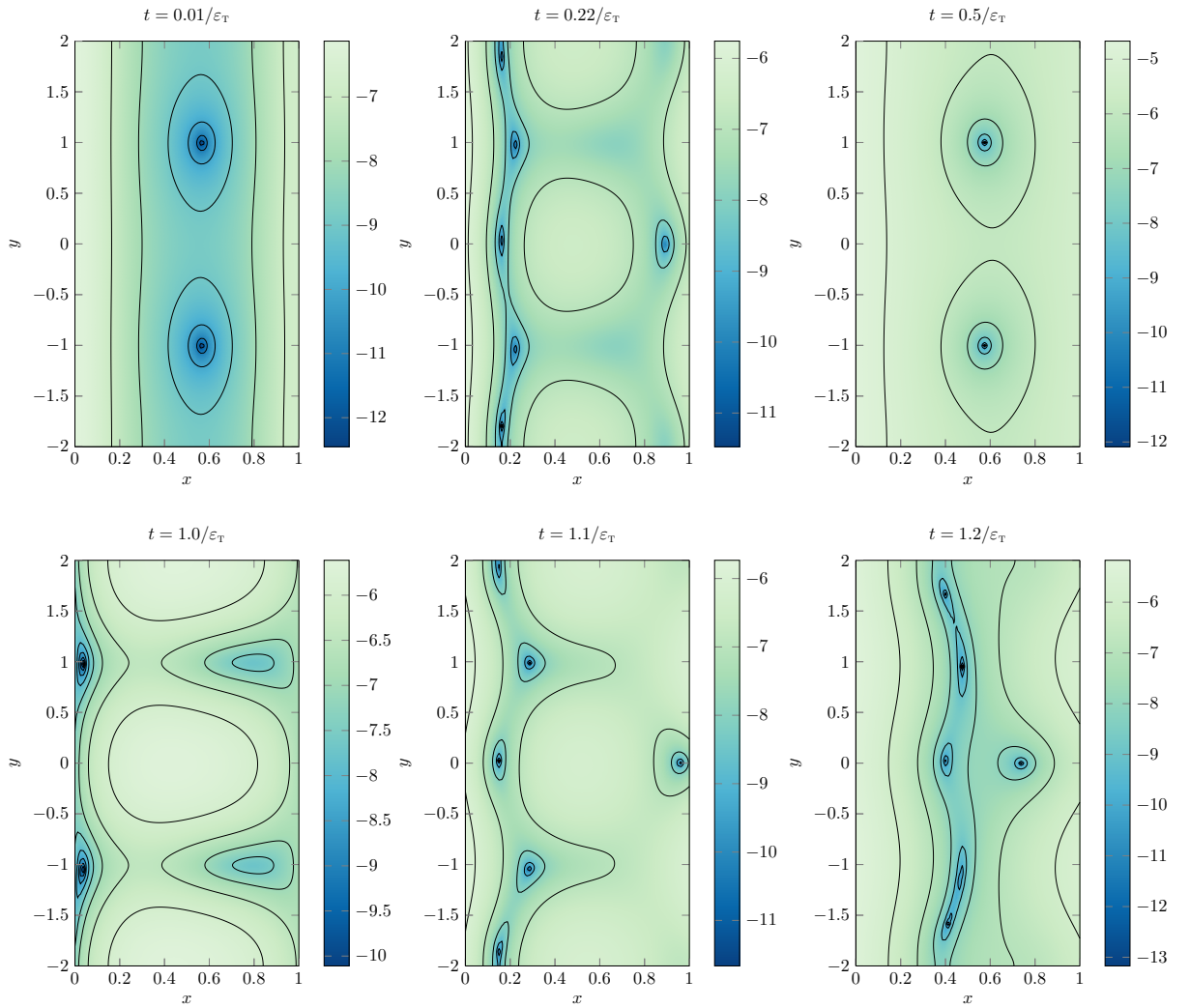


**Figure 3.6:** Plots of  $\log(|\Psi_1(\mathbf{r}, t)| \times 2/N_0\epsilon_T)$  for various values of  $t$  in the symmetric case ( $\sin\theta_r = 1$ ) with  $n = 2$  and  $\varphi_r = \alpha_r = 0$ .

$\sin \theta_r = 1$ , while figure 3.6 shows the asymmetric case with  $n = 2$ ,  $\varphi_r = \alpha_r = 0$  and  $\sin \theta_r = 0.5$ .  $\Psi_2(\mathbf{r})$  looks identical to  $\Psi_1(\mathbf{r}, 0.01/\varepsilon_T)$ , which is shown in the figures, but is a factor 100 larger in magnitude.  $\Psi_2$  is therefore not shown. In both cases, there are exactly two roots in  $\Psi_2$  and  $\Psi_1$  for small  $t$ , and the position are the same as those given for the vortices by the local density of states and supercurrent. Around these two roots are a phase winding of  $2\pi$ .

For larger values of  $t$ ,  $\Psi_1(\mathbf{r}, t)$  seems to be less suited for finding vortices. In the symmetric case there are additional roots which appear. These additional roots also has a corresponding phase winding of  $2\pi$ , but does not correspond to vortices when compared to the local density of states or supercurrent. The situation is even worse for large  $t$  in the asymmetric case. In addition to having extra roots, the original roots which correspond to vortices are either moved or not present. This is also the case for other choices of  $n$ ,  $\varphi_r$ ,  $\alpha_r$  and  $\sin \theta_r$ .

Thus, I conclude that using  $\Psi_2$  seems best suited as order parameter for the numerical investigation of quantum vortices in an purely odd-frequency superconducting condensate. Alternatively, one could use  $\Psi_1$  with  $\varepsilon_T t \ll 1$  which will give the same result since  $\Psi_1 \sim \Psi_2 t$  as  $t \rightarrow 0$ .

Figures 3.7 and 3.8 shows the phase of  $\Psi_2$ , in addition to the supercurrent and amplitude of  $\Psi_2$ , for a magnetic flux of  $4\Phi_0$  and with  $\sin \theta_r = 1$ ,  $\varphi_r = \alpha_r = 0$  and  $\sin \theta_r = 0.5$ ,  $\varphi_r - \alpha_r = \pi/2$ , respectively. Note that there is indeed a phase winding of  $2\pi$ , as mentioned above.

### 3.5.4 Vortex Position

So far we have seen only at the case with  $\varphi_r = \alpha_r = 0$ . Choosing a nonzero value for  $\varphi_r - \alpha_r$  moves the vortices along the  $y$ -axis, and the locations correspond to those predicted by the analysis and given in eq. (3.33) Figures 3.7 and 3.8 shows the amplitude and phase of  $\Psi_2$  as well as the supercurrent  $\mathbf{j}$  for a wide junction subjected to a magnetic flux of  $4\Phi_0$ , with  $\sin \theta_r = 1$ ,  $\varphi_r - \alpha_r = 0$  and  $\sin \theta_r = 0.5$ ,  $\varphi_r - \alpha_r = \pi/2$ , respectively. In figure 3.8 the vortices are shifted  $W/16$  down along the  $y$ -axis, which is exactly what is predicted by eq. (3.33). Note that also that the vortices are moved towards the side where  $\sin \theta$  is smaller also in figure 3.8.

The dependence of the vortex position on both  $\alpha$  and  $\theta$  suggests an experimental method to determine the effective magnetization angles describing disorder in the form of interfacial misaligned moments or artificially inserted misaligned magnetic layers in half-metallic hybrid structures. For a fixed value of the magnetic flux and phase difference  $\varphi_r - \varphi_l$  (which is tunable by the applied current), the  $y$ -coordinates of the vortices gives information about the azimuthal angles  $\alpha_l$  and  $\alpha_r$ , while the  $x$ -coordinates gives information about the polar angles  $\theta_l$  and  $\theta_r$ . This approach could possibly be easier than trying to measure the magnetization angles directly, especially if the non-collinear magnetization angle at the interface is produced by the natural misalignment of magnetic dipoles arising from the conjunction of different atomic structures at the interface.

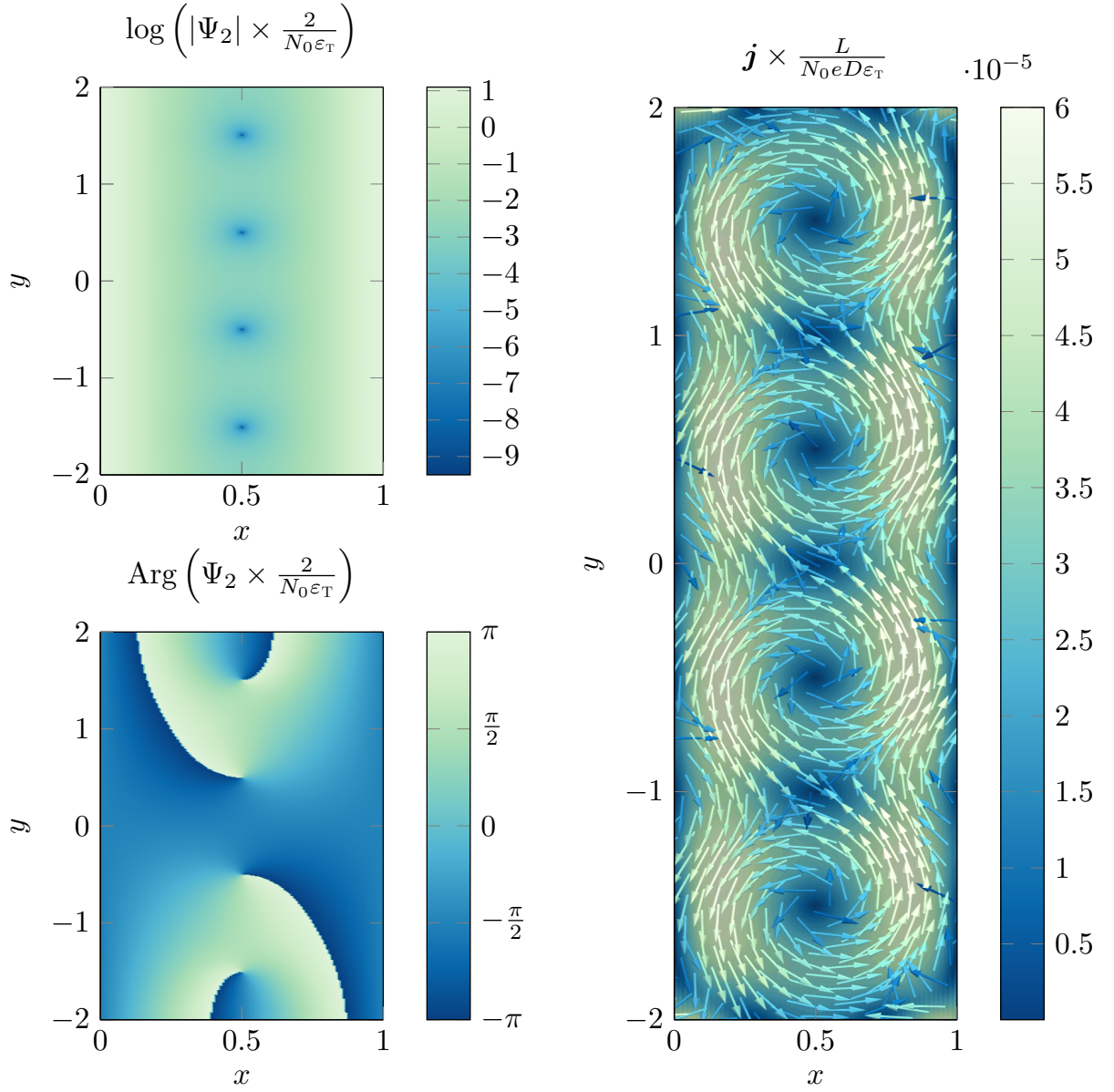


**Figure 3.7:** Amplitude and phase of the order parameter  $\Psi_2$  and amplitude and direction of the fully spin-polarized supercurrent  $\mathbf{j}$ . Here  $n = 4$ ,  $\varphi_r = \alpha_r = 0$  and  $\sin \theta_r = 1$ .



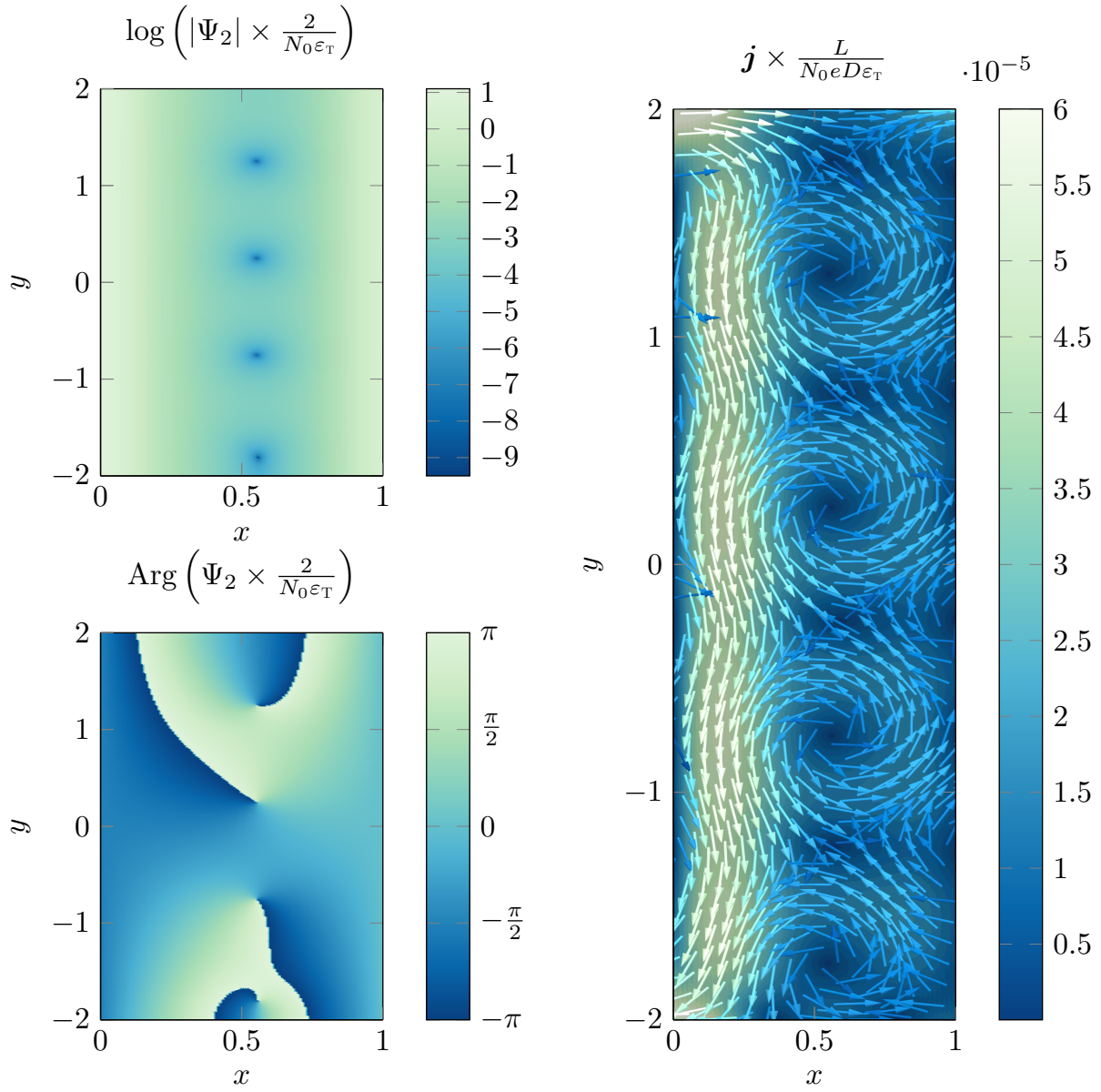


**Figure 3.8:** Amplitude and phase of the order parameter  $\Psi_2$  and amplitude and direction of the fully spin-polarized supercurrent  $\mathbf{j}$ . Here  $n = 4$ ,  $\varphi_r - \alpha_r = \pi/2$  and  $\sin \theta_r = 0.5$ .





---

# CONTROLLABLE VORTEX LOOPS IN SNS-JUNCTIONS

“Looking back at how this new field of topological quantum matter has developed since the initial discoveries in about 1980, I am struck by how important the use of stripped down “toy models” has been in discovering new physics.”

DUNCAN HALDANE, 2016

Superconducting vortices have a great influence on the properties and application of superconducting systems [13–15]. Even so, much is still yet to be discovered about these topological excitations. One aspect of superconducting vortices which are so far not verified by experiment is the formation of closed loop. The formation of superconducting vortex loops is topologically allowed, and has theoretically been predicted to form around strong magnetic inclusions inside the superconductor [16] or through vortex cutting and recombination [17, 18]. However, no observation of vortex loops in superconducting systems has been found to date. This is possibly because they are typically small in conventional superconductors and difficult to stabilize for an extended period of time [19].

Recently it has been shown that these obstacles can be overcome by considering superconducting condensates in proximity systems rather than in ordinary superconductors [18]. Berdiyrov et al. [18] achieved stable vortex loops in an SNS-junction by inserting physical superconducting barriers. The vortices would then be formed in the normal metal, initially as open lines, because of the applied magnetic field. Applying a current moves these vortex lines, and as they wrap around the cylindrical barriers they are cut and recombine into closed loops. Berdiyrov et al. provide suggestions for how these so-called Josephson vortex loops can be detected experimentally, including muon-spin rotation measurement [60] and changes of transport properties resulting from the vortex-loops. However, the radius of these vortex loops are fixed by the size of the nanostructured barriers.

Here I present a system which generate vortex loops with controllable radii. This means that one can tune the vortices such that they intersect the surface. Josephson vortices has recently been directly observed on surfaces by the use of scanning tunneling spectroscopy [61], which means that these vortex loops can be directly observed. The system considered is the three-dimensional SNS junction depicted in figure 4.1 with a current-carrying wire which creates the inhomogeneous magnetic field responsible for the vortex loops. In planar SNS-junctions with uniform applied magnetic field, changing the superconducting phase difference between the two superconductors shifts the vortex lines in the vertical direction [62]. As was revealed in chapter 3, this is also the case in planar SHS-junctions. For the system depicted in figure 4.1 we shall see that the corresponding effect on vortex loops in three dimensions is to change their size. Thus, these vortex loops are easily tunable.

Vortex loops in superconducting systems has previously been predicted using the phenomenological Ginzburg-Landau theory [16–18]. Here, in contrast, I use the microscopic Usadel theory.

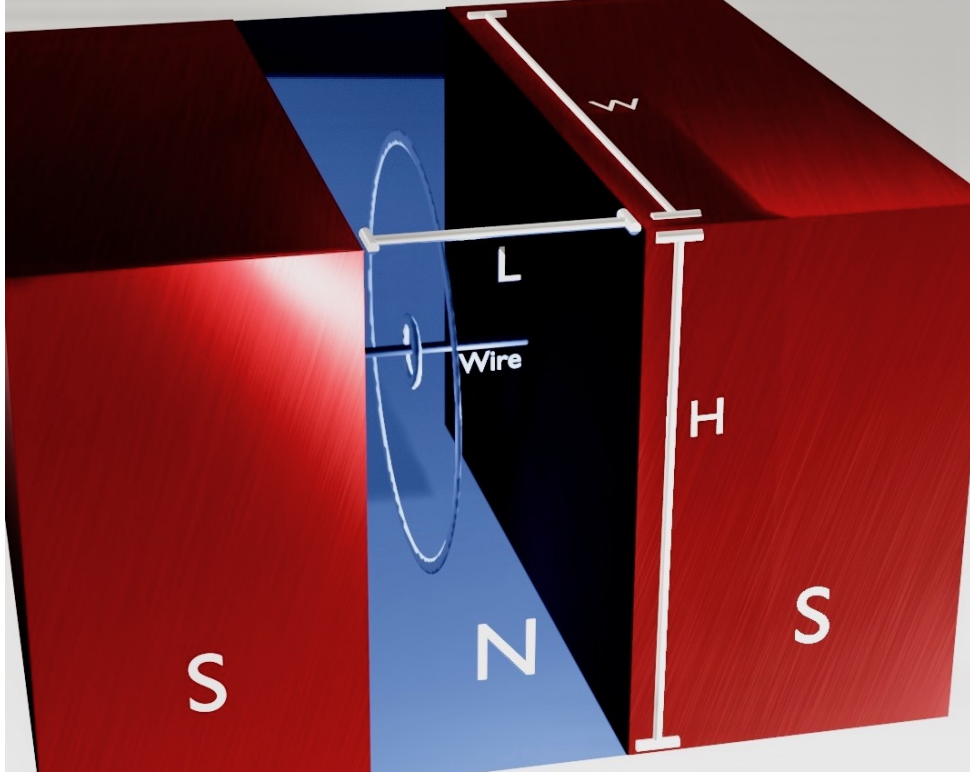


**Figure 4.1:** Sketch of a SNS junction with an insulating wire piercing it. The lengths of the normal metal in the  $x$ -,  $y$ - and  $z$ -direction are  $L$ ,  $H$  and  $W$ , respectively. Contours of the vortex loops are shown to indicate how the vortices form around the wire.

By showing that vortex loop formation occurs also in the microscopic theory, this result also gives valuable support to the earlier proposed mechanisms for superconducting vortex loops.

## 4.1 System

The system we will consider is shown in figure 4.1. A normal metal of length  $L$ , height  $H$  and width  $W$  is placed between two superconductors and pierced by a conducting and isolated wire. The domain of the normal metal will be  $[-L/2, L/2] \times [-H/2, H/2] \times [-W/2, W/2]$  and the superconductors are located at  $x < -L/2$  and  $x > L/2$ . The superconductors are assumed to be identical, meaning that quantities, such as the interface resistance, are identical. The superconducting gap parameters are identical in amplitude but may differ in phase. We will approximate this wire to be infinitely thin, meaning that it gives rise to a current density

$$\mathbf{J}(\mathbf{r}) = I\delta(y)\delta(z)\mathbf{e}_x, \quad (4.1)$$

where  $I$  is the total current running through the wire. The wire is assumed to be insulated so that the current does not leak out into the rest of the system. I will in section 4.6 discuss precisely how such an experimental setup can be realized.

### 4.1.1 Gauge field

Next, we determine the vector potential  $\mathbf{A}$ . As before, it is important to fully specify what gauge is being used, as the vector potential is intimately related to the superconducting phase difference.

The part of the wire which is inside the superconductor will be assumed screened and hence not contribute to the vector potential inside the normal metal. The magnetic field vanishes inside

the superconductors, and inside the normal metal we can use the effective current density

$$\mathbf{J}(\mathbf{r}) = I\delta(y)\delta(z) [\theta(x + L/2) - \theta(x - L/2)] \mathbf{e}_x. \quad (4.2)$$

With this current density, the Biot-Savart law gives that the magnetic field  $\mathbf{B}$  is

$$\begin{aligned} \mathbf{B} &= \frac{\mu}{4\pi} [\theta(x + L/2) - \theta(x - L/2)] \int \frac{\mathbf{J}(\mathbf{r}') \times (\mathbf{r} - \mathbf{r}')}{|\mathbf{r} - \mathbf{r}'|^3} d^3r' \\ &= \frac{\mu I}{4\pi\rho} \left( \frac{L/2 + x}{\sqrt{(L/2 + x)^2 + \rho^2}} + \frac{L/2 - x}{\sqrt{(L/2 - x)^2 + \rho^2}} \right) [\theta(x + L/2) - \theta(x - L/2)] \mathbf{e}_\varphi, \end{aligned} \quad (4.3)$$

where  $\mu$  is the permeability,  $\rho = \sqrt{y^2 + z^2}$  and  $\mathbf{e}_\varphi = (ye_z - ze_y)/\rho$ . Using that  $\mathbf{J} \parallel \mathbf{e}_x$  and

$$\frac{\mathbf{J}(\mathbf{r}') \times (\mathbf{r} - \mathbf{r}')}{|\mathbf{r} - \mathbf{r}'|^3} = \nabla \times \frac{\mathbf{J}(\mathbf{r}')}{|\mathbf{r} - \mathbf{r}'|}, \quad (4.4)$$

we see that a choice of  $\mathbf{A}$  which satisfies  $\mathbf{B} = \nabla \times \mathbf{A}$  is

$$\begin{aligned} \mathbf{A} &= \frac{\mu}{4\pi} [\theta(x + L/2) - \theta(x - L/2)] \int \frac{\mathbf{J}(\mathbf{r}')}{|\mathbf{r} - \mathbf{r}'|} d^3r' \\ &= \frac{\mu I}{4\pi} \ln \left( \frac{\sqrt{(L/2 - x)^2 + \rho^2} + L/2 - x}{\sqrt{(L/2 + x)^2 + \rho^2} - L/2 - x} \right) [\theta(x + L/2) - \theta(x - L/2)] \mathbf{e}_x. \end{aligned} \quad (4.5)$$

The vector potential gotten from the Biot-Savart law in the way done in eq. (4.11) usually satisfies  $\nabla \cdot \mathbf{A} = 0$ , but here

$$\nabla \cdot \mathbf{A} = \frac{\mu I}{4\pi} \left( \frac{1}{\sqrt{\rho^2 + (x + L/2)^2}} - \frac{1}{\sqrt{\rho^2 + (x - L/2)^2}} \right) [\theta(x + L/2) - \theta(x - L/2)]. \quad (4.6)$$

. The reason for this discrepancy is that our effective current density does not satisfy  $\nabla \cdot \mathbf{J} = 0$ . Taking the divergence of eq. (4.11) and using

$$\nabla \cdot \frac{1}{|\mathbf{r} - \mathbf{r}'|} = -\nabla_{\mathbf{r}'} \cdot \frac{1}{|\mathbf{r} - \mathbf{r}'|} \quad (4.7)$$

and partial integration I get

$$\nabla \cdot \mathbf{A} = \frac{\mu}{4\pi} [\theta(x + L/2) - \theta(x - L/2)] \int \frac{\nabla_{\mathbf{r}'} \cdot \mathbf{J}(\mathbf{r}')}{|\mathbf{r} - \mathbf{r}'|} d^3r', \quad (4.8)$$

which, by using from eq. (4.2) that

$$\nabla \cdot \mathbf{J} = I [\delta(x + L/2) - \delta(x - L/2)], \quad (4.9)$$

reproduces eq. (4.6).

Another consequence of using an effective current density that is not divergence free is that  $\nabla \times \mathbf{B} \neq \mu\mathbf{J}$ . Taking the curl of eq. (4.3) I get

$$\nabla \times \mathbf{B} = \mu\mathbf{J} + \frac{\mu}{4\pi} \nabla \int \frac{\nabla_{\mathbf{r}'} \cdot \mathbf{J}(\mathbf{r}')}{|\mathbf{r} - \mathbf{r}'|} d^3r'. \quad (4.10)$$

Using the effective current density (4.2) is in fact incompatible the Ampere's law. If  $\mathbf{B}$  were to satisfy Ampere's law, integrating  $\mathbf{B}$  along a closed loop would, through Stokes' theorem, be equal to  $\mu$  times the current which penetrates the surface enclosed by the closed loop. Depending on

how this surface is taken, this would mean that the magnetic field would be either equal to a  $\mathbf{0}$  or equal to the magnetic field of an infinitely long wire, neither of which would be correct.

In order to get a magnetic field which satisfies Ampere's law and a vector potential which is divergence free we would need to use a more sophisticated model for the screening currents close to where the wire enters the superconductors. However, the contribution from this screening current is expected to be negligible far away from these points, which is where we will do the analysis. This expectation is strengthened by the fact that it is only close to the points  $\mathbf{r} = (-L/2, 0, 0)$  and  $\mathbf{r} = (L/2, 0, 0)$  where the deviations from  $\nabla \times \mathbf{B} = \mu \mathbf{J}$  and  $\nabla \cdot \mathbf{A} = 0$  is significant. Therefore, adding the complications which comes from the screening current will not change any of the conclusions drawn in this chapter.

In order to simplify the analytical expressions we will write  $n := eL\mu I/4\pi^2$ , such that

$$eL\mathbf{A} = -n\pi \ln \left( \frac{\sqrt{(L/2 - x)^2 + \rho^2} + L/2 - x}{\sqrt{(L/2 + x)^2 + \rho^2} - L/2 - x} \right) \mathbf{e}_x. \quad (4.11)$$

## 4.2 Boundary Conditions

The Usadel equation in the normal metal does not make any reference to the superconducting gap parameter. Just as in the half-metallic case, it only enters the normal metal through the boundary conditions. Although deriving quasiclassical boundary conditions for diffusive systems is easier for normal spin-symmetric boundaries than for the spin-active boundaries needed in chapter 3, it is still complicated by the fact the quasiclassical assumption is invalid near the boundary.

A way to derive boundary conditions is to define an *isotropization zone* on either side of the boundary which extend far enough into the material to overlap with the *diffusive zone* where the quasiclassical region is satisfied. Then, one solves the full Gor'kov equations (2.35) in this region and connect this solution with the quasiclassical Green's function in the diffusive zone [25, 63]. After doing the explicit calculations one gets, in the spin-inactive case, the Nazarov boundary condition [64]. If the transmission coefficients are small, we can use the Kupriyanov-Lukichev boundary condition [65],

$$G_i L_i \mathbf{e}_n \cdot (\hat{g}_i \bar{\nabla} \hat{g}_i) = \frac{G_0^i}{2} [\hat{g}_i, \hat{g}_j]. \quad (4.12)$$

Note that eq. (4.12) could also have been arrived at from the more general boundary condition (3.2) used in chapter 3 by setting the spin-mixing angles and magnetization vectors equal to zero. As usual,  $\mathbf{e}_n \cdot \bar{\nabla} \hat{g} = 0$  across the boundaries with vacuum.

## 4.3 Analytics

### 4.3.1 Analytical Solution in the Superconductors

Calculating the quasiclassical impurity averaged Green's function in the superconductors can be done in a similar way as was done in section 3.4.1. That is, if we let

$$\hat{g} = \hat{g}_{\text{BCS}} + \delta \hat{g} \quad (4.13)$$

be the solution in the superconductor at  $x < -L/2$ , where

$$\hat{g}_{\text{BCS}} = \left[ \frac{\theta(\varepsilon^2 - |\Delta|^2)}{\sqrt{\varepsilon^2 - |\Delta|^2}} \text{sgn}(\varepsilon) - \frac{\theta(|\Delta|^2 - \varepsilon^2)}{\sqrt{|\Delta|^2 - \varepsilon^2}} i \right] (\varepsilon \hat{\rho}_3 + \hat{\Delta}), \quad (4.14)$$

is the bulk solution, then solving the Usadel equation in the same manner as in section 3.4.1 gives

$$\delta\hat{g}(\varepsilon, x, y, z) = C \left[ e^{-\lambda|x+L/2|} - e^{-2\lambda L_{\text{sc}} + \lambda|x+L/2|} \right], \quad (4.15)$$

where  $L_{\text{sc}}$  is the length of the superconductor in the  $x$ -direction,

$$\lambda^2 = -\frac{2i}{D_{\text{sc}}} \left[ \text{sgn}(\varepsilon) \sqrt{\varepsilon^2 - |\Delta|^2} \theta \left( \varepsilon^2 - |\Delta|^2 \right) + i \sqrt{|\Delta|^2 - \varepsilon^2} \theta \left( |\Delta|^2 - \varepsilon^2 \right) \right], \quad (4.16)$$

with  $\Re(\lambda) > 0$  and

$$C = \frac{G_0^{\text{sc}} \hat{g}_{\text{BCS}} [\hat{g}_{\text{BCS}} + \delta\hat{g}, \hat{g}_{\text{N}}]}{2\lambda G_{\text{sc}} L_{\text{sc}} (1 - e^{-2\lambda L_{\text{sc}}})}, \quad (4.17)$$

with  $\hat{g}_{\text{N}}$  being the solution in the normal metal. Thus, if we assume  $L_{\text{sc}} \gg L$ , we can neglect  $\delta\hat{g}$ .

### 4.3.2 Ricatti-Parametrized Equations

Because we can neglect the corrections to the bulk solution in the superconductors, the Ricatti parameter in the superconductors can be written

$$\gamma_{\text{sc}} = \begin{pmatrix} 0 & b \\ -b & 0 \end{pmatrix} = \begin{pmatrix} 0 & |b| \\ -|b| & 0 \end{pmatrix} e^{i\varphi}, \quad (4.18)$$

where  $b$  is given by eq. (2.73). Since the superconducting correlations in our system are spin-singlet, we may write  $\gamma_{\text{N}} = \text{antidiag}(a, -a)$ . Putting this into the Usadel equation and boundary condition yields

$$\nabla^2 a = \frac{2\tilde{a}\nabla a \cdot \nabla a}{1 + a\tilde{a}} + \frac{4(1 - a\tilde{a})e\mathbf{A} \cdot (ae\mathbf{A} + i\nabla a)}{1 + a\tilde{a}} + 2ie(\nabla \cdot \mathbf{A})a - 2i\varepsilon a, \quad (4.19a)$$

$$\nabla^2 \tilde{a} = \frac{2a\nabla \tilde{a} \cdot \nabla \tilde{a}}{1 + a\tilde{a}} + \frac{4(1 - a\tilde{a})e\mathbf{A} \cdot (\tilde{a}e\mathbf{A} - i\nabla \tilde{a})}{1 + a\tilde{a}} - 2e(\nabla \cdot \mathbf{A})\tilde{a} - 2i\varepsilon \tilde{a}, \quad (4.19b)$$

and

$$\mathbf{e}_n \cdot \nabla a = \frac{G_0^{\text{N}}(1 + a\tilde{b})(b - a)}{G_{\text{N}}(\tilde{b}\tilde{b} + 1)} + 2ia\mathbf{e}_n \cdot \mathbf{A}e, \quad (4.20a)$$

$$\mathbf{e}_n \cdot \nabla \tilde{a} = \frac{G_0^{\text{N}}(1 + \tilde{a}b)(\tilde{b} - \tilde{a})}{G_{\text{N}}(\tilde{b}\tilde{b} + 1)} - 2i\tilde{a}\mathbf{e}_n \cdot \mathbf{A}e \quad (4.20b)$$

respectively, where  $x, y$  and  $z$  is measured relative to  $L$  and energies are measured relative to the Thouless energy  $\varepsilon_{\text{T}} = D/L^2$ , such that the equations are dimensionless.

### 4.3.3 Analytical Solution

We can not solve the full Usadel equation analytically, and so must settle for an approximate solution valid only in certain limits. Moreover, in contrast to the situation in chapter 3, we will not even find a global solution valid for the whole domain, but will instead solve only for a subdomain far away from the wire.

In order to solve eqs. (4.19) and (4.20) we will assume that the proximity effect is weak and that the junction is wide, i.e.  $L \ll W, H$ . By assuming that the proximity effect is weak, we can linearize the equations, such that

$$\nabla^2 a = 4e\mathbf{A} \cdot (ae\mathbf{A} + i\nabla a) + 2e(\nabla \cdot \mathbf{A})a - 2i\varepsilon a, \quad (4.21a)$$

$$\nabla^2 \tilde{a} = 4e\mathbf{A} \cdot (\tilde{a}e\mathbf{A} - i\nabla \tilde{a}) + 2e(\nabla \cdot \mathbf{A})\tilde{a} - 2i\varepsilon \tilde{a}, \quad (4.21b)$$

and

$$\mathbf{e}_n \cdot \nabla a = \frac{G_0^N(b + a[b\tilde{b} - 1])}{G_N(b\tilde{b} + 1)} + 2ia\mathbf{e}_n \cdot \mathbf{A}e, \quad (4.22a)$$

$$\mathbf{e}_n \cdot \nabla \tilde{a} = \frac{G_0^N(\tilde{b} + \tilde{a}[b\tilde{b} - 1])}{G_N(b\tilde{b} + 1)} - 2i\tilde{a}\mathbf{e}_n \cdot \mathbf{A}e. \quad (4.22b)$$

In section 3.4 we could assume that  $a$  varies slowly with  $y$  throughout the domain because  $\mathbf{A}$  varied slowly with  $y$ . This does not work here, as  $\mathbf{A}$  changes rapidly when  $\rho \rightarrow 0$ . Thus, we can not get an ODE which is valid in all of  $\Omega$  by assuming that the junction is wide. Nevertheless, by restricting the analysis to regions where  $\rho \gg L$ , we can neglect  $\partial_y^2 a$  and  $\partial_z^2 a$ . We can simplify the calculations further by Taylor expanding the vector potential,

$$L\mathbf{e}\mathbf{A} = -n\pi\frac{L}{\rho}\mathbf{e}_x + \mathcal{O}(L^2/\rho^2)\mathbf{e}_x, \quad (4.23)$$

Thus, we get a solvable second order ordinary differential equation with solution

$$a = \frac{ce^{i(\varphi_l - \alpha_l) + u(x-0.5)}}{(k-d)^2 e^k - (k+d)^2 e^{-k}} \left\{ (k-d) \left( e^{k(x-0.5)} + e^{i\delta\varphi - u} e^{-k(x+0.5)} \right) \right. \\ \left. + (k+d) \left( e^{k(0.5-x)} + e^{i\delta\varphi - u} e^{k(x+0.5)} \right) \right\}, \quad (4.24)$$

where

$$\delta\varphi = \varphi_r - \varphi_l, \quad (4.25)$$

$$c = \frac{G_0^N|b|}{G_N(b\tilde{b} + 1)}, \quad d = \frac{G_0^N(b\tilde{b} - 1)}{G_N(b\tilde{b} + 1)}, \quad (4.26)$$

$$u = -2\pi inL/\rho \quad \text{and} \quad k = \sqrt{-2i\varepsilon}. \quad (4.27)$$

From eq. (4.24) I get that  $a$  vanishes when  $x = 0$  and

$$\frac{\rho}{L} = \frac{2n}{1 + 2N - \delta\varphi/\pi}, \quad (4.28)$$

where  $N$  is any integer. As was the case in the discussion in chapter 3, this implies that the superconducting order parameters is also zero. That is, there are loops of constant radii where the order parameter vanishes. Additionally, Cauchy's argument principle [58] implies that there is a  $2\pi$  phase winding in the order parameters around these loops, and hence we expect there to be a circulating supercurrent. One remarkable thing about eq. (4.28) is that the loops can be made arbitrary large by letting  $\delta\varphi$  approach  $\pi$ . Hence, the size of the largest vortex can always be tuned to touch the surface simply by changing  $\delta\varphi$ , making them directly detectable by methods which has already been successfully used to detect vortices.

#### 4.3.4 Vortex Loop Radii

When the superconducting phase difference is increased in normal SNS-junctions, and also in a SHS-junction, as we have seen in chapter 3, with constant applied magnetic field, the vortices respond by moving in unison in a certain direction. Here, I will give an argument for why it is natural that the corresponding behaviour for vortex loops is to shrink or grow.

Take the expression for the vortex position in the two-dimensional case with constant magnetic field, as was found in chapter 3,

$$\frac{y}{W} = \frac{1}{n} \left( \frac{1}{2} + N - \frac{\delta\varphi}{2\pi} \right). \quad (4.29)$$

When  $n > 0$ , increasing  $\delta\varphi$  will move the vortices *down*, that is to smaller  $y$ . Conversely, if  $n < 0$ , increasing  $\delta\varphi$  will move the vortices *up*, that is to larger  $y$ . The magnetic field going through two opposing points on the vortex loops are opposite in direction, meaning that it is as if  $n < 0$  at one side of the loop and  $n > 0$  at the opposite side. Hence, if increasing  $\delta\varphi$  moves the upper part of upwards, the lower part should simultaneously move downwards, increasing the size of the loop.

A more physical explanation for why changing the superconducting phase difference alters the position of superconducting vortices can be given in terms of the supercurrent related to the phase difference. Changing the superconducting phase difference changes the amount of current going between the superconductors. A current is also circulating around the vortices, and as a result the added current will be deflected by the circulating current in a direction transverse to the direction of the applied current. The deflection of the current around the vortex produces a reaction force on the vortex which pushes it in a direction transverse to the added current, much like how a spinning ball traversing through air is deflected through the Magnus effect. Unlike a spinning ball which is accelerating towards the side where the ball is moving in the same direction as the air, the vortex is pushed towards the side where the circulating current is moving against the applied current. This, of course, is because the current is mediated by negatively charged electrons moving oppositely to the current direction. For a more in-depth review of how vortices are affected by applied current, see for instance [66].<sup>1</sup> When the vortices are closed loops, the deflected current will either be all inwards or all outwards, and the resulting force on the vortex loop will either increase or decrease the radius.

The discussion above may indicate that the relationship between the radii of vortex loops and superconducting phase difference in proximity systems is a general feature and not specific to the system considered here. This could be important as it opens the possibility of controlling vortices in system that are less obviously controllable but easier to create in a laboratory. One possibility is to grow the normal metal around a magnetic dipole. The magnetic field from a dipole can, unlike the magnetic field from a wire, not be altered in strength. However, in our system the vortex can be made arbitrarily large regardless of field strength. Hence, it is possible that if the field from the magnetic dipole is strong enough to produce vortices, altering the superconducting phase difference could be a way to increase the size of the vortex to the point where it touches the surface and becomes directly observable.

## 4.4 Numerics

We now proceed to show numerical results in the full (non-linear) proximity effect regime. I have set the parameters  $|\Delta| = 4\varepsilon_T$ ,  $G_{NM} = 3G_0^{NM}$ ,  $W = H = 6L$  and  $\varphi_l = 0$  common for all the numerical calculations. The effect of inelastic scattering is included as before by doing the substitution  $\varepsilon \rightarrow \varepsilon + i\delta$  where  $\delta = 0.001|\Delta|$  in order to avoid the divergence of  $\hat{g}_{BCS}$  at  $\varepsilon = |\Delta|$  [59].

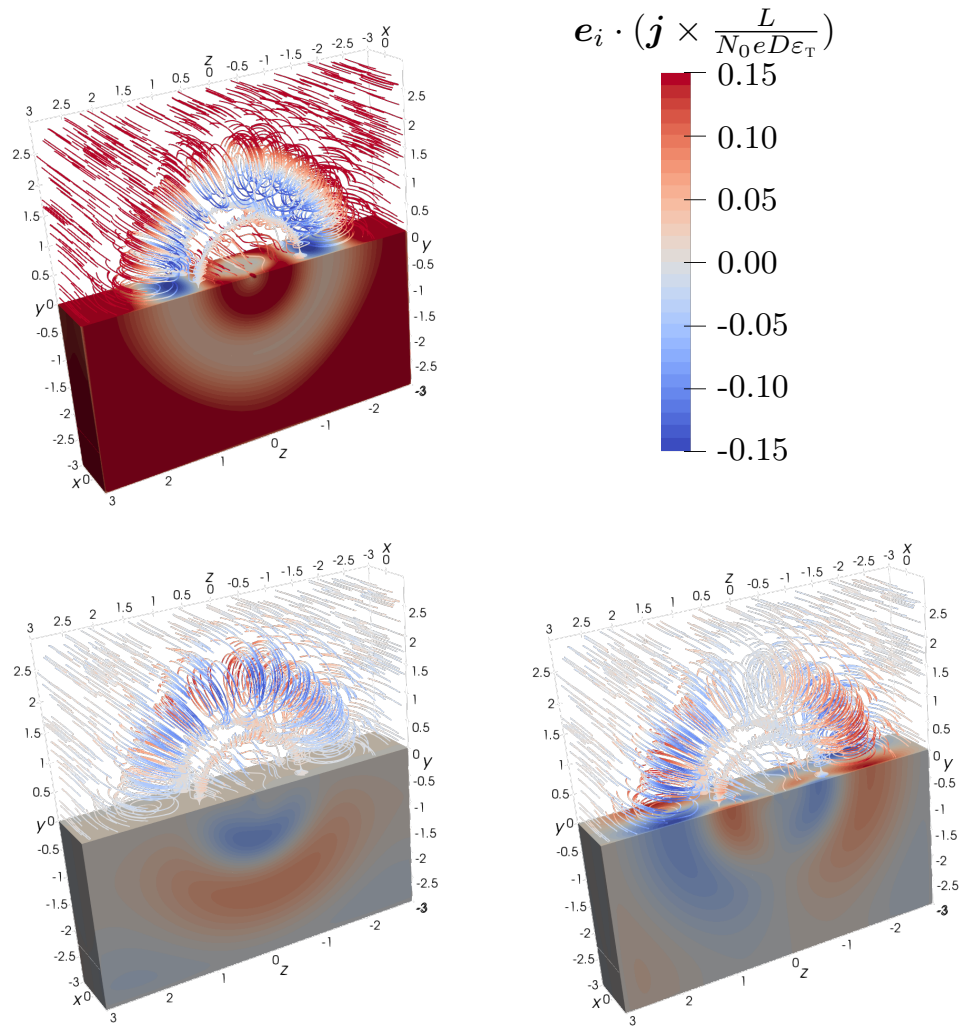
### 4.4.1 Supercurrent and Local Density of States

Figure 4.2 shows the supercurrent for  $n = 1$  and  $\varphi_r = 0$ . From the analysis we expect there to be a loop at around  $\rho = 2$  where the current circulates, and this is also what we observe from figure 4.2. As can be seen from the streamlines in figure 4.2, there is a tube of circulating current at around  $\rho = 2$ , indicating the existence of a superconducting vortex loop at that location.

One point which can be observed from figure 4.2 is that there is a net current in the  $x$ -direction, even at zero superconducting phase difference. This is a consequence of the gauge choice. Doing

---

<sup>1</sup>Incidentally, the fact that applied current moves vortices is one of the major reasons for why understanding the dynamics of vortices is of great technological interest. The movement of vortices have an associated energy cost. The existence of vortices is therefore a cause of resistance in superconductors, and in order to create high-performing superconductors it is advantageous to use a geometry where vortices are *pinned*, meaning that their movement is restricted [14].



**Figure 4.2:** Plot of the three different components of the supercurrent,  $\mathbf{e}_x \cdot \mathbf{j}$  (upper left),  $\mathbf{e}_y \cdot \mathbf{j}$  (lower left) and  $\mathbf{e}_z \cdot \mathbf{j}$  (lower right). The lower half shows the value of the current on the surface in color and the upper half shows streamlines of the current with the current strength indicated by the same color. Here  $n = 1$  and  $\varphi_r = 0$ .



the substitution  $e\mathbf{A} \rightarrow e\mathbf{A} + C[\theta(x + L/2) - \theta(x - L/2)]\mathbf{e}_x$  for some constant  $C$  is equivalent to doing the substitutions  $a \rightarrow ae^{-2iC(x+L/2)}$  and  $b_r \rightarrow be^{-2iCL}$ . This can be seen by observing that the Usadel equation (4.19) and the boundary conditions (4.20) are invariant under the transformations

$$e\mathbf{A} \mapsto e\mathbf{A} + \nabla\lambda(\mathbf{r}), \quad (4.30a)$$

$$a(\mathbf{r}, \varepsilon) \mapsto a(\mathbf{r}, \varepsilon)e^{2i\lambda(\mathbf{r})}, \quad (4.30b)$$

$$\tilde{a}(\mathbf{r}, \varepsilon) \mapsto \tilde{a}(\mathbf{r}, \varepsilon)e^{-2i\lambda(\mathbf{r})}, \quad (4.30c)$$

$$b(\mathbf{r}, \varepsilon) \mapsto b(\mathbf{r}, \varepsilon)e^{2i\lambda(\mathbf{r})}, \quad (4.30d)$$

$$\tilde{b}(\mathbf{r}, \varepsilon) \mapsto \tilde{b}(\mathbf{r}, \varepsilon)e^{-2i\lambda(\mathbf{r})}, \quad (4.30e)$$

where  $\lambda$  is some function of position  $\mathbf{r}$ .

It is also transparent that the Usadel equation must be invariant under the transformations eq. (4.30) by realizing that the anomalous Green's function  $f = 2N\gamma$  and the normal Green's function  $g = N(1 + \gamma\tilde{\gamma})$  are the expectation value of two field operators. The anomalous Green's function is the expectation value of two annihilation operators,  $f_{\sigma\sigma'} \propto \langle\{\psi_\sigma, \psi_{\sigma'}\}\rangle$  and should therefore transform like a charged particle with charge equal to twice that of an electron,  $2e$ , under a gauge transformation, just like how  $a$  transforms in eq. (4.30). The normal Green's function, on the other hand, should stay invariant under gauge transformations as it is composed of one creation operator and one annihilation operator. Since  $\gamma \propto a$  and  $\tilde{\gamma} \propto \tilde{a}$ , we obtain the correct transformation rules for  $f$  and  $g$  when  $a$  transforms as in eq. (4.30). This illustrates the point that specifying the superconducting gauge difference is meaningful only if the vector potential is also specified.

When the SNS-junction is studied in the laboratory, one must tune the phase difference indirectly through the applied current. In the two-dimensional case we used a gauge which correspond to no applied current when the phase difference is zero, and this is typically what has been used in the literature as well [67, 68]. Here, on the other hand, the situation is different and it is therefore perhaps especially important to stress that zero phase difference does not mean zero applied current when the vector potential is nonzero.

If the lines around which the supercurrent in figure 4.2 circulates are in fact superconducting vortices, this should be reflected also in the local density of states. Figures 4.3 and 4.4 shows the local density of states at energies  $\varepsilon = 0.5|\Delta|$  and  $\varepsilon = 1.5|\Delta|$  respectively, where  $\Delta$  is the superconducting gap parameter. In both figures 4.3 and 4.4 we see that the local density of states is indeed equal to the normal state density inside loops of radius around  $\rho = 2$ , which coincides with where we expect the vortex loop from looking at the supercurrent in figure 4.2.

#### 4.4.2 Cooper Pair Correlation Function

Figures 4.5 and 4.6 shows the amplitude and phase, respectively, of the Cooper pair correlation function. As can be seen from these figures there are indeed a vortex loop with radius  $\rho \approx 2$  where the superconducting correlation function vanishes and has a  $2\pi$  phase winding, in agreement with the supercurrent and local density of states shown in the previous section. There also seems to be a smaller vortex loop at a smaller radius which was more difficult to see from the supercurrent, as the supercurrent is weak so close to the wire where the magnetic field is strong. Figure 4.9 shows a contour plot of  $|\Psi|$ , together with the phase of  $\Psi$  and the circulating supercurrent  $\mathbf{j}$ , showing how circulating supercurrent, phase winding and vanishing order parameter are related.

Figures 4.7 and 4.8 shows how the vortex loops changes with superconducting phase difference,  $\varphi_r$ , and magnetic field strength,  $n$ , respectively. The radii of the largest vortices agrees well with the analytical expression (4.28). As can be seen from eq. (4.28), increasing  $\varphi_r$  can make the vortex radius arbitrary large, but will only change the number of vortices by at most one, as the size of each vortex increases continuously with  $\varphi_r$  and at  $\varphi_r = 2\pi$  the situation is the same as for

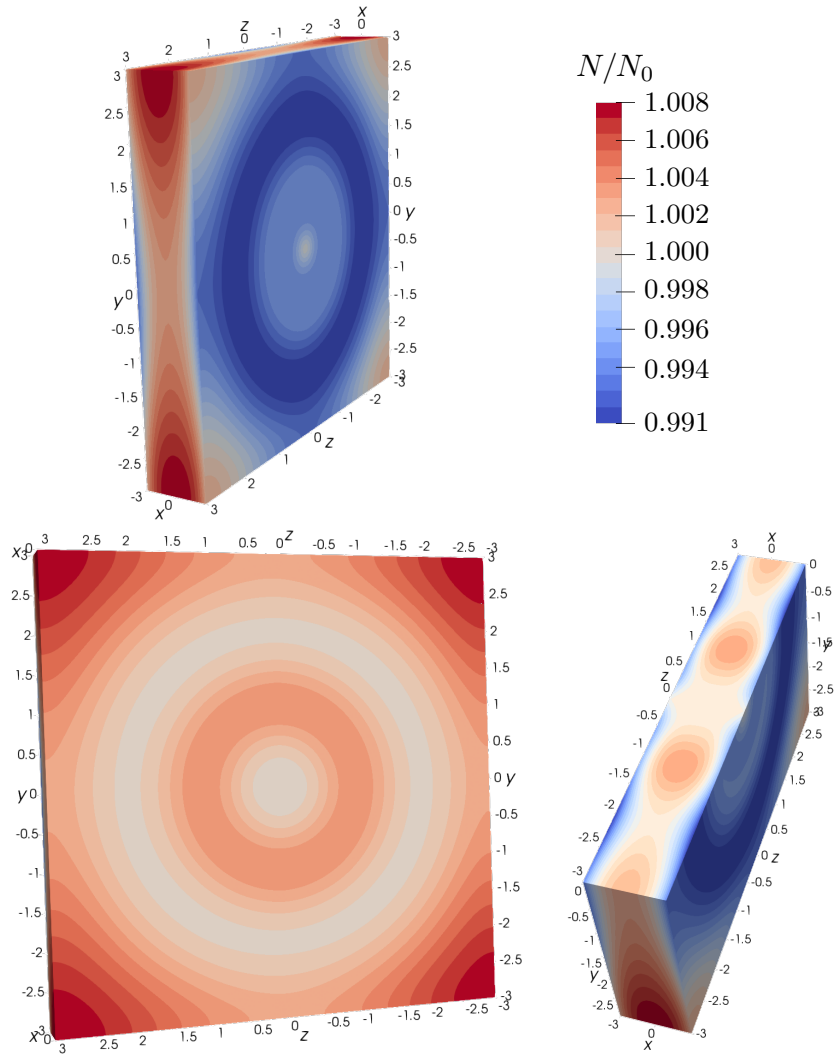


**Figure 4.3:** Local density of states  $N$  relative to the normal state density of states  $N_0$  at energy  $\varepsilon = 0.5|\Delta|$ , where  $\Delta$  is the superconducting gap parameter. Here  $n = 1$  and the superconducting phase difference is  $\varphi_r$ .

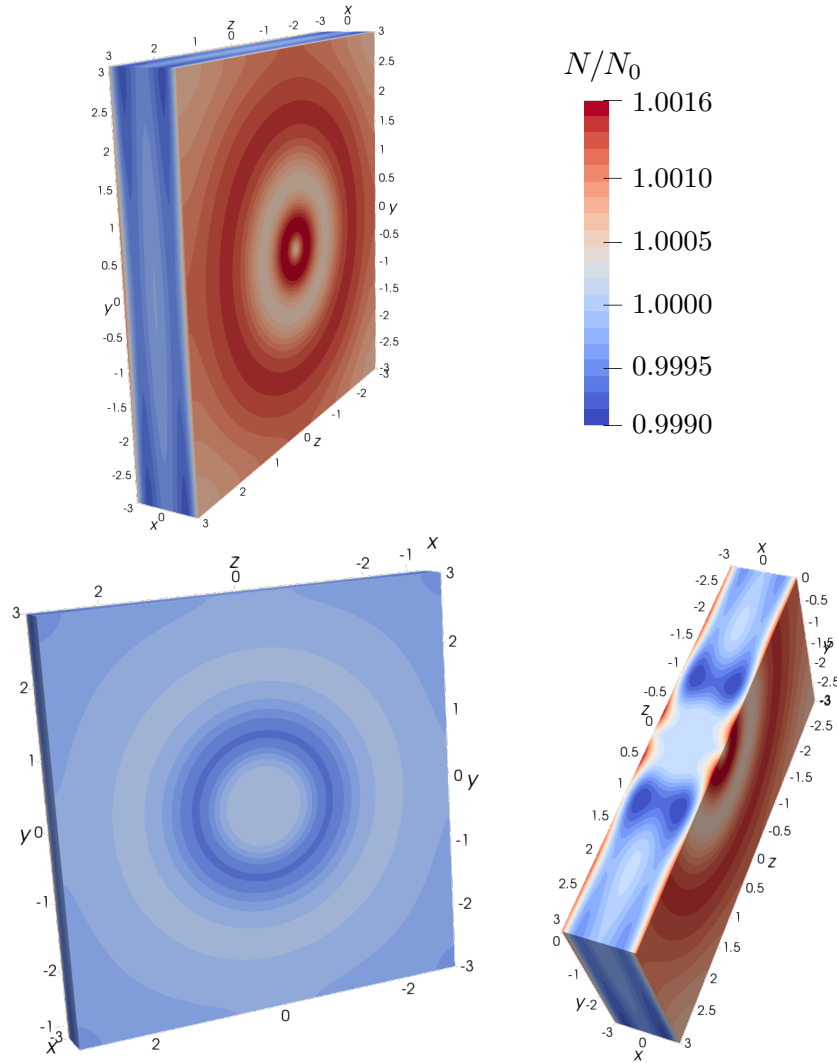


**Figure 4.4:** Local density of states  $N$  relative to the normal state density of states  $N_0$  at energy  $\varepsilon = 1.5|\Delta|$ , where  $\Delta$  is the superconducting gap parameter. Here  $n = 1$  and the superconducting phase difference is  $\varphi_r$ .

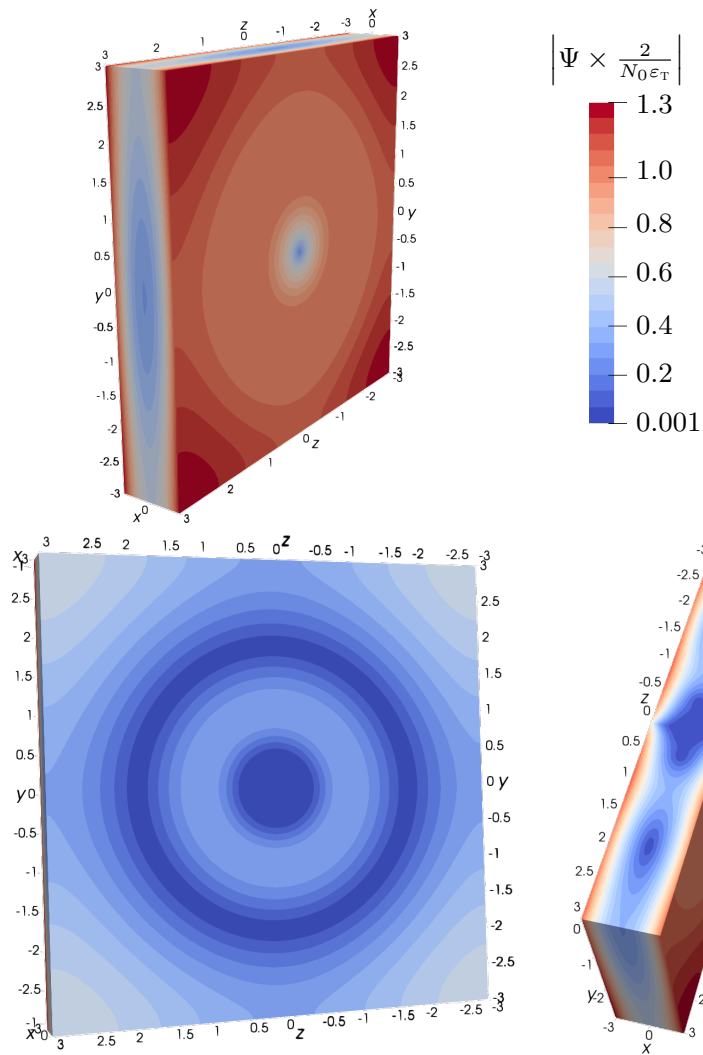


**Figure 4.5:** Amplitude of the superconducting order parameter  $\Psi$  for magnetic field strength  $n = 1$  and superconducting phase difference  $\varphi_r = 0$ .

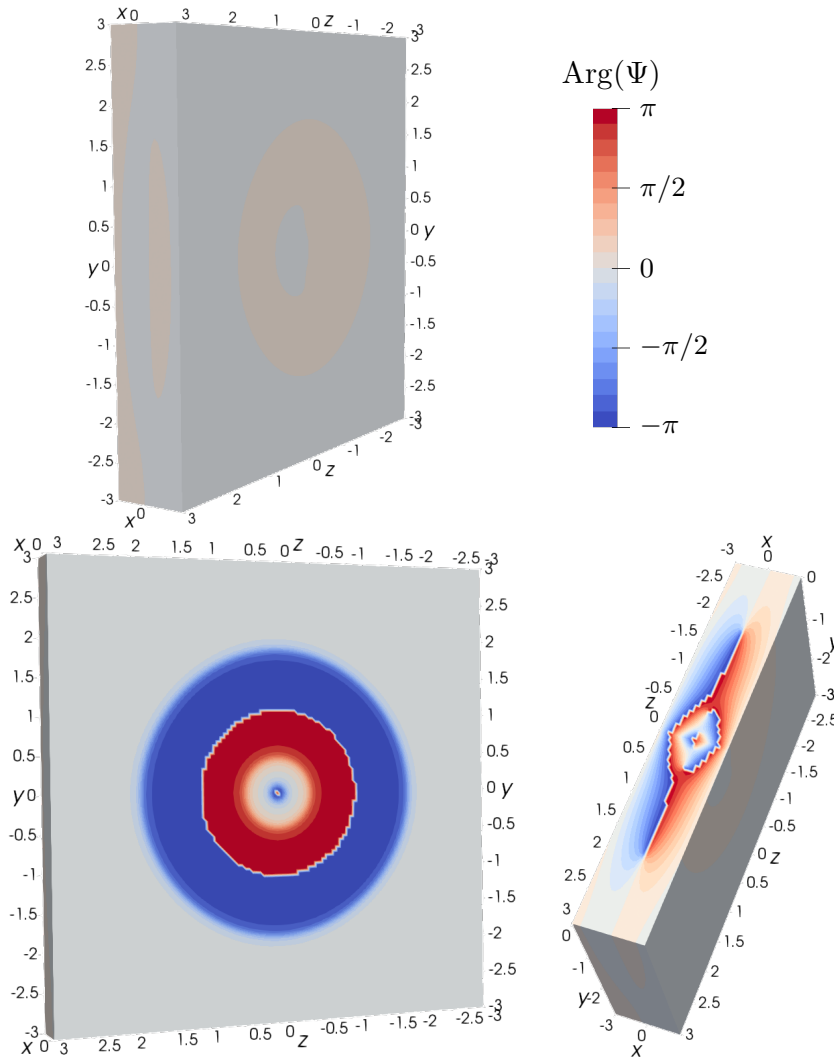


**Figure 4.6:** Amplitude of the superconducting order parameter  $\Psi$  for magnetic field strength  $n = 1$  and superconducting phase difference  $\varphi_r = 0$ .

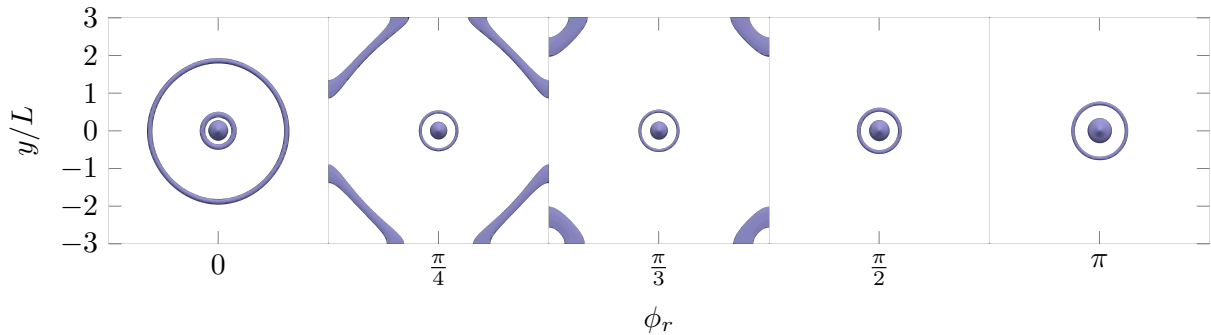


**Figure 4.7:** Contour plot of the amplitude of the superconducting order parameter  $\Psi$  for magnetic field strength  $n = 1$  and various values of the superconducting phase difference  $\varphi_r$ .

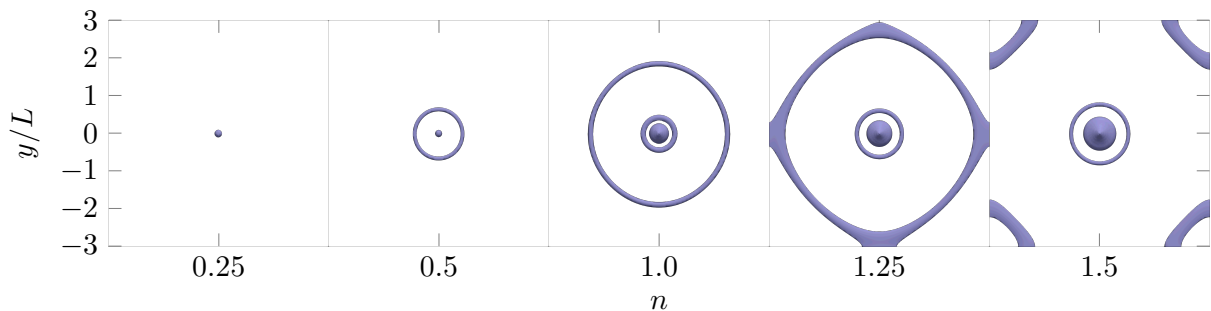


**Figure 4.8:** Contour plot of the amplitude of the superconducting order parameter  $\Psi$  for superconducting phase difference  $\varphi_r = 0$  and various values of magnetic field strength  $n$ .

$\varphi_r = 0$ . Hence, each vortex at  $\varphi_r = 0$  will take the position of the vortex above it when increasing  $\varphi_r$  to  $2\pi$ . At some interval there can be one less vortex if the outermost vortex escapes out of the system before a new one is created, or there can be one more if a new one is created before the outermost escapes, but changing  $\varphi_r$  will not change the number of vortices by more than one. Increasing  $n$ , on the other hand, also increase the number of vortices, as can be seen from figure 4.8, but the sizes grow only linearly with  $n$ . In conclusion, then, changing  $\varphi_r$  can make the vortices arbitrary large but can not change the number of vortices by more than one, and changing  $n$  will also change the number of vortices but the size will scale only linearly with  $n$ .

Note from figures 4.7 and 4.8 that as the vortex loops hit the surface, they curve so as to hit normally to the surface. This is because there should be no current component normal to the surface. If the vortices hit the surface at an angle, the circulating current would have to have a component normal to the surface. Thus, because the current at the surface must be tangential to that surface, the vortices must hit surfaces at right angles. This result of vortices hitting surfaces normally is consistent with previous results [16, 69].

## 4.5 Possible Model Improvements

As was mentioned in section 4.1.1, the effective current density from the nanowire used here has some limitations. The effective current density is that of an infinitely thin wire which is finite in length. This current density is not compatible with Ampere's law because it does not correspond to a complete physical current. The current is supposed to be steady, yet  $\nabla \cdot \mathbf{j} \neq 0$ . In reality, the screening currents in the superconductors will not simply fully cancel the magnetic field produced from the part of the wire which is inside the superconductors. They will produce their own fields, and while the main effect of this field is to cancel the field from the wire, close to where the wire enters the superconductors, which is where Ampere's law is broken, this cancellation will not be

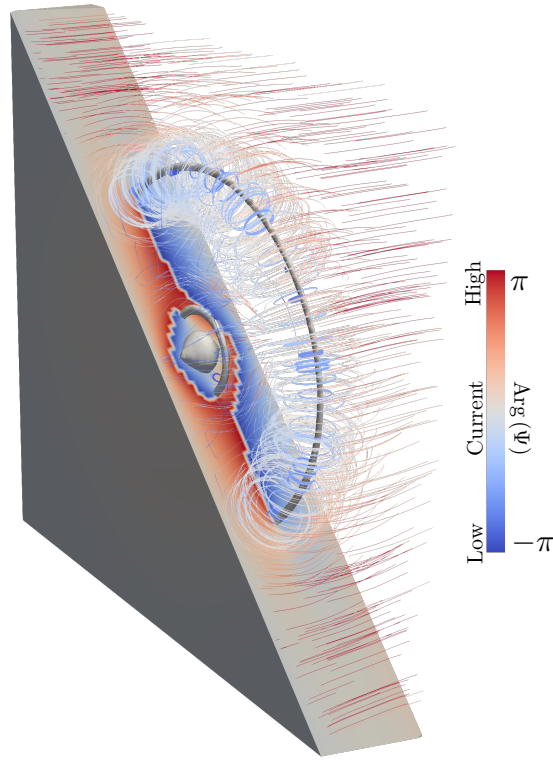


**Figure 4.9:** Plot of the phase of the superconducting order parameter  $\Psi$  on a surface of a diagonally cut part of the normal metal, contour plot of its amplitude,  $|\Psi|$ , and streamlines of the supercurrent  $\mathbf{j}$ . Here  $n = 1$  and  $\varphi_r = 0$ .

exact.

There are at least two possible ways to remedy the problem of screening currents. Firstly, one could develop some model for the screening currents. One possible way of doing this is to use the London equation,

$$\nabla^2 \mathbf{B} = \frac{1}{\lambda^2} \mathbf{B}, \quad (4.31)$$

where  $\lambda$  is the London penetration depth [33, 34]. Having found the magnetic field one can extract the current density by Ampere's law,

$$\mathbf{j} = \frac{1}{\mu_0} \nabla \times \mathbf{B}. \quad (4.32)$$

From this one can find the full magnetic field in the normal metal by combining the screening current and the current from the wire.

The other possibility is to solve the Usadel equation inside the superconductors as well as in the normal metal and do it self-consistently with Ampere's law. This would require significantly more computational power. Not only must the Usadel equation then be solved self-consistently with Ampere's equation, but it must be solved also self-consistently with the equation for the superconducting gap parameter  $\Delta$  which enters the Usadel equation in the superconductors. Both  $\Delta$  and  $\mathbf{j}$  would in this setup depend on the solution of the Usadel equation integrated over energy, so in order to solve the equations one would have to integrate the Usadel equation many times. This is because one would first have to make a guess for  $\mathbf{j}$  and  $\Delta$ , then solve the full Usadel equation with the boundary condition in both superconductors and in the normal metal for many different energies. These results would then have to be integrated at each position in space and combined in order to make new improved guesses for  $\mathbf{j}$  and  $\Delta$ . This scheme would have to be repeated until the self-consistency equations for  $\Delta$  and Ampere's law are satisfied within some

tolerance. Integrating the solution once already takes several days in the current implementation, and this scheme will be much more computationally intensive.

The two methods above will give a physically more correct solution, although the difference from the solution presented here is likely limited in space to the locations where the wires enter the superconductors, as this is where the screening currents are located. In this chapter we have specifically looked at the parts of the normal metal which is far away from this region. This is because this is the region which is most easily treated analytically and because this is the region which will determine when the vortex loops are observable on the surface. More importantly for the current discussion, however, it is because this is the region which is the least affected by the details of how the magnetic field from the wire is implemented. That is, doing the extra work of determining the details of how the currents induced in the superconductors screens the current from the wire will not significantly alter the solution far away from the wire. Hence, the analytical considerations presented here will remain largely unaffected and the existence and behaviour of the superconducting vortex loops will not change.

Another aspect which would improve the physicality of the setup presented here, but which impact is also restricted to small radii  $\rho$  is that the wire will not, in reality, be infinitely thin. In order to have a finite thickness of the wire, the finite element implementation would have to be changed. Instead of being a simple rectangular prism, the domain would have to have a cylindrically shaped hole. This would mean that the boundary conditions would have to be implemented at the resulting surface and the cells used in the finite element computation would have to be more complex. Although this would require some work in rewriting the program and adding the extra functionality associated with the more complicated cell structure, it would not lead to significantly more computationally intensive code.

## 4.6 Experimental Realization

Normal SNS junctions are created by vertically growing first a superconducting material such as niobium, then a normal metal such as copper and finally the same superconducting material. The layers are grown for instance by a sputter deposition technique such as direct current sputtering [70] or radio frequency sputtering [71]. The setup presented here adds an extra complication by requiring an isolated conducting nanowire to penetrate the system. One possible way to achieve this could be to first grow a vertical insulated nanowire and then grow the superconductor and normal metal around it in a layerwise fashion.

Growing a wire is more complicated than growing a plane because one must localize the growth to happen at the tip at the wire, even though most of the surface area will be on the sides. Nevertheless, growing vertical nanowires has successfully been done by methods such as the vapor-liquid-solid method [72–74] and template-directed synthesis [75]. The vapor-liquid-solid method works by using droplets of, for instance, gold which are a few angstroms in width to localize the growth [73], and template-directed synthesis works by having the wire grow inside a premade template which can later be removed [75]. The vapor-liquid-solid method has already been used to produce vertical surround-gate field-effect transistors with a precision exceeding what should be necessary for the system presented here [73].

Schmidt et al. [73] made nanowires using the vapor-liquid-solid method which were 40 nm in diameter and 400 nm in length. This should be on the same length scale as would be necessary for the system considered in this chapter. The superconducting energy gap of niobium is  $|\Delta| = 30.5 \times 10^{-4}$  eV [76], which is equivalent to about  $2.46 \text{ nm}^{-1}$  in natural units. The Fermi velocity and scattering time for copper are about  $3.70 \times 10^{-3}$  and  $10.8 \mu\text{m}$ , respectively [77]. From eq. (2.65) I get that the diffusion coefficient for copper is about  $D = 49.2 \text{ pm}^2$ . In the numerics I have used

$$|\Delta| = 4\varepsilon_{\text{T}} = \frac{4D}{L^2}, \quad (4.33)$$



so

$$L = 283 \text{ nm}, \quad (4.34)$$

which is on the same scale as what has been made with the vapor-liquid-solid method. Of course, other metals and superconductors could be used, giving different physical lengths corresponding to the values being used in the numerics here. Moreover, from the analysis it seems vortex loops would form also for other values of  $|\Delta|/\varepsilon_T$ . The calculation above is merely to show that the length scales used in this thesis is not unreasonable compared to what has already been experimentally achieved.



---

# CONCLUSION AND OUTLOOK

“*The interface is still the device*”

JOCHEN MANNHART, 2012

Nobel Laureate Kroemer [78] coined the phrase “the interface is the device” in the year 2000 specifically in the context of semiconductors. However, in the years since it has become clear that fascinating phenomena also arise when other types of materials are combined. For instance, combining two different types of oxide insulators can produce a layer which is highly conducting [79] and the combination of ferromagnetism and superconductivity can create superconducting correlations in the ferromagnet which are spin-triplet and non-local in time. The study of heterogenic mesoscopic structures offer opportunities for fundamental as well as applied research in various fields in physics, including quantum computation [1–3], spintronics [4, 5, 80, 81], interferometry [82, 83] and superconductivity [18, 84]. Still, much remains unknown and many problems remains unsolved. This thesis has had as its goal to shed light on two such problems. The first is regarding the formation of superconducting vortices in pure triplet-spin odd-frequency superconducting condensates and the latter is about the formation of vortex loops in superconducting systems.

Quantized vortices can form when ordinary superconductors are exposed to a magnetic field. Even though this is a basic characteristic of superconductivity, little is known about if and how vortices appear in odd-frequency superconductors. Odd-frequency superconductivity has never been observed to arise spontaneously in a material, but using the fact that purely odd-frequency superconducting correlations occur in SH-heterostructures we have seen in chapter 3 that superconducting vortices can occur despite the complete absence of conventional superconducting correlations. A circulating spin-supercurrent accompanies these vortices in addition to the usual charge supercurrent. Moreover, I have demonstrated that magnetic disorder at the interfaces of the half-metal add extra dynamics to the vortices. This insight offers a way to determine the effective interfacial misalignment angles describing the magnetic disorder, a quantity which previously has been difficult to determine experimentally.

There are certain circumstances under which the superconducting vortices are believed to form closed loops, such as in the inhomogeneous field from a magnetic inclusion [16] or through the process of vortex cutting and recombination [17, 18]. Nevertheless, superconducting vortex loops have so far avoided experimental detection. The second part of this thesis has focused on the exploration of a heterogenic structure which allows for controllable vortex loops. The magnetic field responsible for the vortex loops in this system is provided by a wire running through an otherwise normal SNS-junction. The amount of current running through this wire affect both the number and size of the vortices in a predictable way. Crucially, I find that there is an additional parameter which affect the vortex loop radius, namely the phase difference in the superconducting order parameters of the two superconductors. With these degrees of freedom the vortex loops can be manually controlled in the laboratory so as to hit the surface in predictable places. This would render the vortices easily detectable through means which has already been used to directly find

superconducting vortices on surfaces in other circumstances [61]. My finding indicates that the relationship between the superconducting phase difference and vortex loop radius is a general feature and not specific to the system considered here.

Both of the findings in this thesis is experimentally verifiable and both may serve as inspiration for further theoretical work. It is plausible that the relationship between the superconducting phase difference and vortex loop radius is a general feature of superconducting vortex loops in SNS-junctions, and not specific to the system considered here. This would mean that vortex loops from systems which are less complicated to create in the lab, but not obviously controllable, could still be controlled in the same way as what has been proposed in this thesis. One such system is a normal SNS-junction with a magnetic dipole inclusion. It would be of interest, then, to investigate a SNS-junction with a magnetic field coming from a magnetic dipole in the Usadel formalism and see if the superconducting phase difference could be used to control the vortex.

Having explored vortex formation in fully polarized ferromagnets, the next step could be to look at vortices in strongly, yet not fully, polarized ferromagnets. The coexistence of superconductivity and ferromagnets is believed to occur in several uranium compounds [85], but it is easier experimentally to look at superconductivity induced in otherwise normal ferromagnets through the proximity effect. A reason for why it would be of interest to explore vortex formation in such systems is that strongly polarized ferromagnetic systems could possibly host half-quantum vortices. That is, vortices for which the winding number is  $1/2$ , meaning that the superconducting phase changes by  $\pi$ , as opposed to the normal  $2\pi$ , along a trajectory around the vortex. Such half-quantum vortices are possible if there is a rotation of the vector  $\mathbf{d} = (f_{\downarrow} - f_{\uparrow}, -i(f_{\downarrow} + f_{\uparrow}), 2f_t)^{\top}$  in addition to the normal phase winding [86]. A rotation of  $\mathbf{d}$  is not possible in half-metals, but it could be possible in strongly polarized ferromagnets.

# BIBLIOGRAPHY

## References for Chapter 1: Introduction

- [1] C. Nayak et al. “Non-Abelian Anyons and Topological Quantum Computation”. In: *Rev. Mod. Phys.* 80 (3 2008), pp. 1083–1159. DOI: 10.1103/RevModPhys.80.1083 Cited on pages 1, 69.
- [2] T. W. Larsen et al. “Semiconductor-Nanowire-Based Superconducting Qubit”. In: *Physical Review Letters* 115 (12 2015), p. 127001. DOI: 10.1103/PhysRevLett.115.127001 Cited on pages 1, 69.
- [3] A. E. Antipov et al. “Effects of Gate-Induced Electric Fields on Semiconductor Majorana Nanowires”. In: *arXiv preprint arXiv:1801.02616* (2018) Cited on pages 1, 69.
- [4] J. Linder and J. W. Robinson. “Superconducting Spintronics”. In: *Nature Physics* 11.4 (2015), p. 307. DOI: 10.1038/nphys3242 Cited on pages 1, 33, 69.
- [5] M. Eschrig. “Spin-Polarized Supercurrents for Spintronics: A Review of Current Progress”. In: *Reports on Progress in Physics* 78.10 (2015), p. 104501. DOI: 10.1088/0034-4885/78/10/104501 Cited on pages 1, 13, 33, 43, 44, 69.
- [6] J. Bardeen, L. N. Cooper, and J. R. Schrieffer. “Theory of Superconductivity”. In: *Physical Review* 108 (5 1957), pp. 1175–1204. DOI: 10.1103/PhysRev.108.1175 Cited on page 1.
- [7] A. Andreev. “The Thermal Conductivity of the Intermediate State in Superconductors”. In: *Journal of Experimental and Theoretical Physics* 19 (1964), p. 1228 Cited on page 1.
- [8] B. Pannetier and H. Courtois. “Andreev Reflection and Proximity Effect”. In: *Journal of Low Temperature Physics* 118.5-6 (2000), pp. 599–615 Cited on page 1.
- [9] H. P. Dahal et al. “Wave Function for Odd-Frequency Superconductors”. In: *New Journal of Physics* 11.15pp (2009), p. 65005. DOI: 10.1088/1367-2630/11/6/065005 Cited on pages 1, 33.
- [10] P. Schoenherr et al. “Topological Domain Walls in Helimagnets”. In: *Nature Physics* 14.5 (2018), p. 465. DOI: 10.1038/s41567-018-0056-5 Cited on page 2.
- [11] J. Seidel. “Nanoelectronics Based on Topological Structures”. In: *Nature materials* 18.3 (2019), p. 188. DOI: 10.1038/s41563-019-0301-z Cited on page 2.
- [12] A. Gangui. “Topological Defects in Cosmology”. In: *arXiv preprint astro-ph/0110285* (2001) Cited on page 2.
- [13] W.-K. Kwok et al. “Vortices in High-Performance High-Temperature Superconductors”. In: *Reports on Progress in Physics* 79.11 (2016), p. 116501. DOI: 10.1088/0034-4885/79/11/116501 Cited on pages 2, 51.
- [14] B. I. Halperin, G. Refael, and E. Demler. “Resistance in Superconductors”. In: *International Journal of Modern Physics B* 24.20n21 (2010), pp. 4039–4080. DOI: 10.1142/S021797921005644X Cited on pages 2, 51, 57.

- [15] S. K. Kim, R. Myers, and Y. Tserkovnyak. “Nonlocal Spin Transport Mediated by a Vortex Liquid in Superconductors”. In: *Physical Review Letters* 121 (18 2018), p. 187203. DOI: 10.1103/PhysRevLett.121.187203 Cited on pages 2, 44, 51.
- [16] M. M. Doria et al. “Threefold Onset of Vortex Loops in Superconductors with a Magnetic Core”. In: *Epl* 79.4 (2007). DOI: 10.1209/0295-5075/79/47006 Cited on pages 2, 51, 64, 69.
- [17] A. Glatz et al. “Vortex Cutting in Superconductors”. In: *Physical Review B* 94.6 (2016). DOI: 10.1103/PhysRevB.94.064505 Cited on pages 2, 51, 69.
- [18] G. R. Berdiyrov et al. “Josephson Vortex Loops in Nanostructured Josephson Junctions”. In: *Scientific Reports* 8.1 (2018), p. 2733. DOI: 10.1038/s41598-018-21015-7 Cited on pages 2, 51, 69.
- [19] A. Schönenberger et al. “Strong Pinning and Plastic Deformations of the Vortex Lattice”. In: *Physical Review Letters* 77.22 (1996), pp. 4636–4639. DOI: 10.1103/PhysRevLett.77.4636 Cited on pages 2, 51.

## References for Chapter 2: Methodology

- [5] M. Eschrig. “Spin-Polarized Supercurrents for Spintronics: A Review of Current Progress”. In: *Reports on Progress in Physics* 78.10 (2015), p. 104501. DOI: 10.1088/0034-4885/78/10/104501 Cited on pages 1, 13, 33, 43, 44, 69.
- [20] J. Rammer. *Quantum field theory of non-equilibrium states*. Cambridge University Press, 2007 Cited on pages 5, 6, 13.
- [21] H. Bruus and K. Flensberg. *Many-body quantum theory in condensed matter physics: an introduction*. Oxford university press, 2004 Cited on pages 5, 7, 20.
- [22] V. Chandrasekhar. “Proximity-Coupled Systems: Quasiclassical Theory of Superconductivity”. In: *Superconductivity: Conventional and Unconventional Superconductors*. Ed. by K. H. Bennemann and J. B. Ketterson. Berlin, Heidelberg: Springer Berlin Heidelberg, 2008, pp. 279–313. ISBN: 978-3-540-73253-2. DOI: 10.1007/978-3-540-73253-2\_8 Cited on page 6.
- [23] W. Belzig et al. “Quasiclassical Green Function Approach to Mesoscopic Superconductivity”. In: *Superlattices and Microstructures* 25.5 (1999), pp. 1251–1288. DOI: 10.1006/spmi.1999.0710 Cited on pages 6, 13.
- [24] K. D. Usadel. “Generalized Diffusion Equation for Superconducting Alloys”. In: *Physical Review Letters* 25 (8 1970), pp. 507–509. DOI: 10.1103/PhysRevLett.25.507 Cited on pages 6, 13.
- [25] M. Eschrig et al. “General Boundary Conditions for Quasiclassical Theory of Superconductivity in the Diffusive Limit: Application to Strongly Spin-Polarized Systems”. In: *New Journal of Physics* 17.8 (2015). DOI: 10.1088/1367-2630/17/8/083037 Cited on pages 7, 33, 35, 36, 54.
- [26] D. Borthwick. *Introduction to Partial Differential Equations*. Universitext. Springer International Publishing, 2017. ISBN: 9783319489360 Cited on pages 7, 9, 23.
- [27] A. Barone and G. Paternò. *Physics and Applications of the Josephson Effect*. New York, NY: Wiley, 1982 Cited on page 7.
- [28] L. Gorkov. “On the Energy Spectrum of Superconductors”. In: *Journal of Experimental and Theoretical Physics* 7.505 (1958), p. 158 Cited on page 9.

- [29] G. Eilenberger. “Transformation of Gorkov’s Equation for Type II Superconductors Into Transport-Like Equations”. In: *Zeitschrift für Physik A Hadrons and Nuclei* 214.2 (1968), pp. 195–213. DOI: 10.1007/BF01379803 *Cited on page 9.*
- [30] E. H. Fyhn. “A Finite Element Approach to Solving the Usadel Equation in Multiple Dimensions”. NTNU, 2018 *Cited on pages 10, 11, 13, 43.*
- [31] U. Eckern and A. Schmid. “Quasiclassical Green’s Function in the BCS Pairing Theory”. In: *Journal of Low Temperature Physics* 45.1 (1981), pp. 137–166. DOI: 10.1007/BF00661147 *Cited on page 13.*
- [32] A. L. Shelankov. “On the Derivation of Quasiclassical Equations for Superconductors”. In: *Journal of Low Temperature Physics* 60.1 (1985), pp. 29–44. DOI: 10.1007/BF00681651 *Cited on page 13.*
- [33] K. Fossheim and A. Sudbø. *Superconductivity: physics and applications*. John Wiley & Sons, 2005 *Cited on pages 14, 65.*
- [34] M. Tinkham. *Introduction to superconductivity*. Courier Corporation, 2004 *Cited on pages 14, 65.*
- [35] P. Schlottmann. “Double-Exchange Mechanism for Cr<sub>2</sub>”. In: *Physical Review B* 67 (17 2003), p. 174419. DOI: 10.1103/PhysRevB.67.174419 *Cited on page 16.*
- [36] J. A. Ouassou et al. “Triplet Cooper Pairs Induced in Diffusive S-Wave Superconductors Interfaced With Strongly Spin-Polarized Magnetic Insulators or Half-Metallic Ferromagnets”. In: *Scientific Reports* 7.1 (2017), p. 1932. DOI: 10.1038/s41598-017-01330-1 *Cited on pages 16, 33, 36.*
- [37] K. Halterman, P. H. Barsic, and O. T. Valls. “Odd Triplet Pairing in Clean Superconductor/Ferromagnet Heterostructures”. In: *Physical Review Letters* 99.12 (2007), p. 127002. DOI: 10.1103/PhysRevLett.99.127002 *Cited on pages 22, 36.*
- [38] E. Abrahams et al. “Properties of Odd-Gap Superconductors”. In: *Physical Review B* 52.2 (1995), pp. 1271–1278. DOI: 10.1103/PhysRevB.52.1271 *Cited on page 22.*
- [39] R. Burden and J. Faires. *Numerical Analysis*. Brooks/Cole, Cengage Learning, 2011. ISBN: 9780538735643 *Cited on pages 24, 29.*
- [40] W. B. Gragg and R. A. Tapia. “Optimal Error Bounds for the Newton-Kantorovich Theorem”. In: *SIAM Journal on Numerical Analysis* 11.1 (1974), pp. 10–13 *Cited on page 24.*
- [41] J. M. Ortega. “The Newton-Kantorovich Theorem”. In: *The American Mathematical Monthly* 75.6 (1968), pp. 658–660 *Cited on page 24.*
- [42] R. A. Tapia. “The Kantorovich Theorem for Newton’s Method”. In: *The American Mathematical Monthly* 78.4 (1971), pp. 389–392 *Cited on page 24.*
- [43] J. Revels, M. Lubin, and T. Papamarkou. “Forward-Mode Automatic Differentiation in Julia”. In: *arXiv:1607.07892 [cs.MS]* (2016) *Cited on pages 26, 27, 32.*
- [44] T. Sauer. *Numerical Analysis: Pearson New International Edition*. Pearson Education Limited, 2013. ISBN: 9781292036748 *Cited on pages 28, 31.*
- [45] J. D. Sau, S. Tewari, and S. Das Sarma. “Experimental and Materials Considerations for the Topological Superconducting State in Electron- and Hole-Doped Semiconductors: Searching for Non-Abelian Majorana Modes in 1D Nanowires and 2D Heterostructures”. In: *Physical Review B* 85 (6 2012), p. 064512. DOI: 10.1103/PhysRevB.85.064512 *Cited on page 28.*
- [46] J. F. Epperson. “On the Runge Example”. In: *The American Mathematical Monthly* 94.4 (1987), pp. 329–341 *Cited on page 31.*

- [47] A. S. Kronrod. “Integration with Control of Accuracy”. In: *Doklady Akademii Nauk*. Vol. 154. 2. Russian Academy of Sciences. 1964, pp. 283–286 *Cited on page 31.*
- [48] D. Calvetti et al. “Computation of Gauss-Kronrod Quadrature Rules”. In: *Mathematics of Computation* 69.231 (2000), pp. 1035–1052 *Cited on page 31.*
- [49] J. Bezanson et al. “Julia: A Fresh Approach to Numerical Computing”. In: *SIAM Rev.* 59.1 (Jan. 2017), pp. 65–98. ISSN: 0036-1445. DOI: 10.1137/141000671 *Cited on page 32.*

## References for Chapter 3: Superconducting Vortices in Half-Metals

- [4] J. Linder and J. W. Robinson. “Superconducting Spintronics”. In: *Nature Physics* 11.4 (2015), p. 307. DOI: 10.1038/nphys3242 *Cited on pages 1, 33, 69.*
- [5] M. Eschrig. “Spin-Polarized Supercurrents for Spintronics: A Review of Current Progress”. In: *Reports on Progress in Physics* 78.10 (2015), p. 104501. DOI: 10.1088/0034-4885/78/10/104501 *Cited on pages 1, 13, 33, 43, 44, 69.*
- [9] H. P. Dahal et al. “Wave Function for Odd-Frequency Superconductors”. In: *New Journal of Physics* 11.15pp (2009), p. 65005. DOI: 10.1088/1367-2630/11/6/065005 *Cited on pages 1, 33.*
- [15] S. K. Kim, R. Myers, and Y. Tserkovnyak. “Nonlocal Spin Transport Mediated by a Vortex Liquid in Superconductors”. In: *Physical Review Letters* 121 (18 2018), p. 187203. DOI: 10.1103/PhysRevLett.121.187203 *Cited on pages 2, 44, 51.*
- [25] M. Eschrig et al. “General Boundary Conditions for Quasiclassical Theory of Superconductivity in the Diffusive Limit: Application to Strongly Spin-Polarized Systems”. In: *New Journal of Physics* 17.8 (2015). DOI: 10.1088/1367-2630/17/8/083037 *Cited on pages 7, 33, 35, 36, 54.*
- [30] E. H. Fyhn. “A Finite Element Approach to Solving the Usadel Equation in Multiple Dimensions”. NTNU, 2018 *Cited on pages 10, 11, 13, 43.*
- [36] J. A. Ouassou et al. “Triplet Cooper Pairs Induced in Diffusive S-Wave Superconductors Interfaced With Strongly Spin-Polarized Magnetic Insulators or Half-Metallic Ferromagnets”. In: *Scientific Reports* 7.1 (2017), p. 1932. DOI: 10.1038/s41598-017-01330-1 *Cited on pages 16, 33, 36.*
- [37] K. Halterman, P. H. Barsic, and O. T. Valls. “Odd Triplet Pairing in Clean Superconductor/Ferromagnet Heterostructures”. In: *Physical Review Letters* 99.12 (2007), p. 127002. DOI: 10.1103/PhysRevLett.99.127002 *Cited on pages 22, 36.*
- [50] W. Meissner and R. Ochsenfeld. “Ein neuer Effekt bei Eintritt der Supraleitfähigkeit”. In: *Naturwissenschaften* 21.44 (1933), pp. 787–788. DOI: 10.1007/BF01504252 *Cited on page 33.*
- [51] R. S. Keizer et al. “A Spin Triplet Supercurrent Through the Half-Metallic Ferromagnet CrO<sub>2</sub>”. In: *Nature* 439.7078 (2006), pp. 825–827. DOI: 10.1038/nature04499 *Cited on page 33.*
- [52] Y. Kalcheim et al. “Evidence for Anisotropic Triplet Superconductor Order Parameter in Half-Metallic Ferromagnetic La<sub>0.7</sub>Ca<sub>0.3</sub>Mn<sub>3</sub> Proximity Coupled to Superconducting Pr<sub>1.85</sub>Ce<sub>0.15</sub>CuO<sub>4</sub>”. In: *Physical Review B* 85.10 (Mar. 2012), p. 104504. DOI: 10.1103/PhysRevB.85.104504 *Cited on page 33.*
- [53] A. Singh et al. “Colossal Proximity Effect in a Superconducting Triplet Spin Valve Based on the Half-Metallic Ferromagnet CrO<sub>2</sub>”. In: *Physical Review X* 5.2 (2015), p. 021019. DOI: 10.1103/PhysRevX.5.021019. arXiv: 1410.4973v1 *Cited on pages 33, 34.*



- [54] V. Peña et al. “Coupling of Superconductors Through a Half-Metallic Ferromagnet: Evidence for a Long-Range Proximity Effect”. In: *Physical Review B* 69.22 (June 2004), p. 224502. DOI: 10.1103/PhysRevB.69.224502 *Cited on page 33.*
- [55] M. Eschrig et al. “Symmetries of Pairing Correlations in Superconductor-Ferromagnet Nanostructures”. In: *Journal of Low Temperature Physics* 147.3-4 (2007), pp. 457–476. DOI: 10.1007/s10909-007-9329-6 *Cited on page 33.*
- [56] M. Eschrig et al. “Theory of Half-Metal/Superconductor Heterostructures”. In: *Physical Review Letters* 90.13 (2003), p. 4. DOI: 10.1103/PhysRevLett.90.137003 *Cited on pages 33, 35.*
- [57] A. M. Black-Schaffer and A. V. Balatsky. “Odd-Frequency Superconducting Pairing in Multiband Superconductors”. In: *Physical Review B* 88.10 (Sept. 2013), p. 104514. DOI: 10.1103/PhysRevB.88.104514 *Cited on page 33.*
- [58] R. Churchill and J. Brown. *Complex Variables and Applications*. Churchill-Brown series. McGraw-Hill, 1990. ISBN: 9780070109056 *Cited on pages 40, 56.*
- [59] R. C. Dynes et al. “Tunneling Study of Superconductivity Near the Metal-Insulator Transition”. In: *Physical Review Letters* 53.25 (1984), pp. 2437–2440. DOI: 10.1103/PhysRevLett.53.2437 *Cited on pages 40, 57.*

## References for Chapter 4: Controllable Vortex Loops

- [13] W.-K. Kwok et al. “Vortices in High-Performance High-Temperature Superconductors”. In: *Reports on Progress in Physics* 79.11 (2016), p. 116501. DOI: 10.1088/0034-4885/79/11/116501 *Cited on pages 2, 51.*
- [14] B. I. Halperin, G. Refael, and E. Demler. “Resistance in Superconductors”. In: *International Journal of Modern Physics B* 24.20n21 (2010), pp. 4039–4080. DOI: 10.1142/S021797921005644X *Cited on pages 2, 51, 57.*
- [15] S. K. Kim, R. Myers, and Y. Tserkovnyak. “Nonlocal Spin Transport Mediated by a Vortex Liquid in Superconductors”. In: *Physical Review Letters* 121 (18 2018), p. 187203. DOI: 10.1103/PhysRevLett.121.187203 *Cited on pages 2, 44, 51.*
- [16] M. M. Doria et al. “Threefold Onset of Vortex Loops in Superconductors with a Magnetic Core”. In: *Epl* 79.4 (2007). DOI: 10.1209/0295-5075/79/47006 *Cited on pages 2, 51, 64, 69.*
- [17] A. Glatz et al. “Vortex Cutting in Superconductors”. In: *Physical Review B* 94.6 (2016). DOI: 10.1103/PhysRevB.94.064505 *Cited on pages 2, 51, 69.*
- [18] G. R. Berdiyrov et al. “Josephson Vortex Loops in Nanostructured Josephson Junctions”. In: *Scientific Reports* 8.1 (2018), p. 2733. DOI: 10.1038/s41598-018-21015-7 *Cited on pages 2, 51, 69.*
- [19] A. Schönemberger et al. “Strong Pinning and Plastic Deformations of the Vortex Lattice”. In: *Physical Review Letters* 77.22 (1996), pp. 4636–4639. DOI: 10.1103/PhysRevLett.77.4636 *Cited on pages 2, 51.*
- [25] M. Eschrig et al. “General Boundary Conditions for Quasiclassical Theory of Superconductivity in the Diffusive Limit: Application to Strongly Spin-Polarized Systems”. In: *New Journal of Physics* 17.8 (2015). DOI: 10.1088/1367-2630/17/8/083037 *Cited on pages 7, 33, 35, 36, 54.*
- [33] K. Fossheim and A. Sudbø. *Superconductivity: physics and applications*. John Wiley & Sons, 2005 *Cited on pages 14, 65.*
- [34] M. Tinkham. *Introduction to superconductivity*. Courier Corporation, 2004 *Cited on pages 14, 65.*

- [58] R. Churchill and J. Brown. *Complex Variables and Applications*. Churchill-Brown series. McGraw-Hill, 1990. ISBN: 9780070109056 *Cited on pages 40, 56.*
- [59] R. C. Dynes et al. “Tunneling Study of Superconductivity Near the Metal-Insulator Transition”. In: *Physical Review Letters* 53.25 (1984), pp. 2437–2440. DOI: 10.1103/PhysRevLett.53.2437 *Cited on pages 40, 57.*
- [60] I. Landau and H. Keller. “On the Interpretation of Muon-Spin-Rotation Experiments in the Mixed State of Type-II Superconductors”. In: *Physica C: Superconductivity* 466.1 (2007), pp. 131–141. DOI: <https://doi.org/10.1016/j.physc.2007.07.003> *Cited on page 51.*
- [61] V. S. Stolyarov et al. “Expansion of a Superconducting Vortex Core Into a Diffusive Metal”. In: *Nature communications* 9.1 (2018), p. 2277. DOI: 10.1038/s41467-018-04582-1 *Cited on pages 51, 70.*
- [62] J. Cuevas and F. Bergeret. “Magnetic Interference Patterns and Vortices in Diffusive SNS Junctions”. In: *Physical Review Letters* 99.21 (2007), p. 217002. DOI: 10.1103/PhysRevLett.99.217002 *Cited on page 51.*
- [63] A. Cottet et al. “Spin-Dependent Boundary Conditions for Isotropic Superconducting Green’s Functions”. In: *Physical Review B* 80 (18 2009), p. 184511. DOI: 10.1103/PhysRevB.80.184511 *Cited on page 54.*
- [64] Y. V. Nazarov. “Novel Circuit Theory of Andreev Reflection”. In: *Superlattices and microstructures* 25.5-6 (1999), pp. 1221–1231. DOI: 10.1006/spmi.1999.0738 *Cited on page 54.*
- [65] M. Y. Kuprianov and V. Lukichev. “Influence of Boundary Transparency on the Critical Current of Dirty SS’S structures”. In: *Journal of Experimental and Theoretical Physics* 94 (1988), p. 149 *Cited on page 54.*
- [66] E. B. Sonin. “Magnus Force in Superfluids and Superconductors”. In: *Physical Review B* 55 (1 1997), pp. 485–501. DOI: 10.1103/PhysRevB.55.485 *Cited on page 57.*
- [67] M. Amundsen and J. Linder. “General solution of 2D and 3D superconducting quasiclassical systems: coalescing vortices and nanoisland geometries”. In: *Scientific Reports* 6.1 (2016), p. 22765. DOI: 10.1038/srep22765 *Cited on page 59.*
- [68] F. S. Bergeret and J. C. Cuevas. “The Vortex State and Josephson Critical Current of a Diffusive SNS Junction”. In: *Journal of Low Temperature Physics* 153.5 (2008), pp. 304–324. DOI: 10.1007/s10909-008-9826-2 *Cited on page 59.*
- [69] A. R. de C. Romaguera, M. M. Doria, and F. M. Peeters. “Tilted Vortices in a Superconducting Mesoscopic Cylinder”. In: *Physical Review B* 75 (18 2007), p. 184525. DOI: 10.1103/PhysRevB.75.184525 *Cited on page 64.*
- [70] R. E. Miller et al. “Niobium Trilayer Josephson Tunnel Junctions with Ultrahigh Critical current densities”. In: *Applied Physics Letters* 63.10 (1993), pp. 1423–1425. DOI: 10.1063/1.109697 *Cited on page 66.*
- [71] V. M. Krasnov et al. “Josephson Properties of Nb/Cu Multilayers”. In: *Physical Review B* 49 (18 1994), pp. 12969–12974. DOI: 10.1103/PhysRevB.49.12969 *Cited on page 66.*
- [72] H. T. Ng et al. “Single Crystal Nanowire Vertical Surround-Gate Field-Effect Transistor”. In: *Nano Letters* 4.7 (2004), pp. 1247–1252. DOI: 10.1021/nl049461z *Cited on page 66.*
- [73] V. Schmidt et al. “Realization of a Silicon Nanowire Vertical Surround-Gate Field-Effect Transistor”. In: *Small* 2.1 (2006), pp. 85–88. DOI: 10.1002/smll.200500181 *Cited on page 66.*
- [74] K. Tomioka, M. Yoshimura, and T. Fukui. “A III–V Nanowire Channel on Silicon for High-Performance Vertical Transistors”. In: *Nature* 488.7410 (2012), p. 189. DOI: 10.1038/nature11293 *Cited on page 66.*

- [75] Y. Xia et al. “One-Dimensional Nanostructures: Synthesis, Characterization, and Applications”. In: *Advanced Materials* 15.5 (2003), pp. 353–389. DOI: 10.1002/adma.200390087 Cited on page 66.
- [76] C. Kittel et al. *Introduction to solid state physics*. Vol. 8. Wiley New York, 1976 Cited on page 66.
- [77] D. Gall. “Electron Mean Free Path in Elemental Metals”. In: *Journal of Applied Physics* 119.8 (2016), p. 085101. DOI: 10.1063/1.4942216 Cited on page 66.

## References for Chapter 5: Conclusion and Outlook

- [1] C. Nayak et al. “Non-Abelian Anyons and Topological Quantum Computation”. In: *Rev. Mod. Phys.* 80 (3 2008), pp. 1083–1159. DOI: 10.1103/RevModPhys.80.1083 Cited on pages 1, 69.
- [2] T. W. Larsen et al. “Semiconductor-Nanowire-Based Superconducting Qubit”. In: *Physical Review Letters* 115 (12 2015), p. 127001. DOI: 10.1103/PhysRevLett.115.127001 Cited on pages 1, 69.
- [3] A. E. Antipov et al. “Effects of Gate-Induced Electric Fields on Semiconductor Majorana Nanowires”. In: *arXiv preprint arXiv:1801.02616* (2018) Cited on pages 1, 69.
- [4] J. Linder and J. W. Robinson. “Superconducting Spintronics”. In: *Nature Physics* 11.4 (2015), p. 307. DOI: 10.1038/nphys3242 Cited on pages 1, 33, 69.
- [5] M. Eschrig. “Spin-Polarized Supercurrents for Spintronics: A Review of Current Progress”. In: *Reports on Progress in Physics* 78.10 (2015), p. 104501. DOI: 10.1088/0034-4885/78/10/104501 Cited on pages 1, 13, 33, 43, 44, 69.
- [16] M. M. Doria et al. “Threefold Onset of Vortex Loops in Superconductors with a Magnetic Core”. In: *Epl* 79.4 (2007). DOI: 10.1209/0295-5075/79/47006 Cited on pages 2, 51, 64, 69.
- [17] A. Glatz et al. “Vortex Cutting in Superconductors”. In: *Physical Review B* 94.6 (2016). DOI: 10.1103/PhysRevB.94.064505 Cited on pages 2, 51, 69.
- [18] G. R. Berdiyrov et al. “Josephson Vortex Loops in Nanostructured Josephson Junctions”. In: *Scientific Reports* 8.1 (2018), p. 2733. DOI: 10.1038/s41598-018-21015-7 Cited on pages 2, 51, 69.
- [61] V. S. Stolyarov et al. “Expansion of a Superconducting Vortex Core Into a Diffusive Metal”. In: *Nature communications* 9.1 (2018), p. 2277. DOI: 10.1038/s41467-018-04582-1 Cited on pages 51, 70.
- [78] H. Kroemer. *Nobel lecture - Quasi-Electric Fields and Band Offsets: Teaching Electrons New Tricks*. 2000 Cited on page 69.
- [79] H. Y. Hwang et al. “Emergent Phenomena at Oxide Interfaces”. In: *Nature materials* 11.2 (2012), p. 103. DOI: 10.1038/nmat3223 Cited on page 69.
- [80] S. A. Gulbrandsen and A. Brataas. “Spin Transfer and Spin Pumping in Disordered Normal Metal–Antiferromagnetic Insulator Systems”. In: *Physical Review B* 97 (5 2018), p. 054409. DOI: 10.1103/PhysRevB.97.054409 Cited on page 69.
- [81] R. Lebrun et al. “Tunable Long-Distance Spin Transport in a Crystalline Antiferromagnetic Iron Oxide”. In: *Nature* 561.7722 (2018), p. 222. DOI: 10.1038/s41586-018-0490-7 Cited on page 69.
- [82] R. C. Jaklevic et al. “Quantum Interference Effects in Josephson Tunneling”. In: *Physical Review Letters* 12 (7 1964), pp. 159–160. DOI: 10.1103/PhysRevLett.12.159 Cited on page 69.

- [83] M. Aprili. “The nanoSQUID Makes its Debut”. In: *Nature nanotechnology* 1.1 (2006), p. 15. DOI: 10.1038/nnano.2006.78 *Cited on page 69.*
- [84] H. G. Hugdal et al. “Magnon-Induced Superconductivity in a Topological Insulator Coupled to Ferromagnetic and Antiferromagnetic Insulators”. In: *Physical Review B* 97 (19 2018), p. 195438. DOI: 10.1103/PhysRevB.97.195438 *Cited on page 69.*
- [85] V. P. Mineev. “Superconductivity in Uranium Ferromagnets”. In: *Physics-Uspokhi* 60.2 (2017), pp. 121–148. DOI: 10.3367/ufne.2016.04.037771 *Cited on page 70.*
- [86] S. Autti et al. “Observation of Half-Quantum Vortices in Topological Superfluid  $^3\text{He}$ ”. In: *Physical Review Letters* (2016). DOI: 10.1103/PhysRevLett.117.255301 *Cited on page 70.*

Appendix A  
**PAPER I**



# Superconducting Vortices in Half-Metals

Eirik Holm Fyhn<sup>1</sup> and Jacob Linder<sup>1</sup>

<sup>1</sup>Center for Quantum Spintronics, Department of Physics, Norwegian University of Science and Technology, NO-7491 Trondheim, Norway

(Dated: April 16, 2019)

When the impurity mean free path is short, only spin-polarized Cooper pairs which are non-locally correlated in time may exist in a half-metallic ferromagnet. As a consequence, the half-metal acts as an odd-frequency superconducting condensate. We demonstrate both analytically and numerically that quantum vortices can emerge in half-metals despite the complete absence of conventional superconducting correlations. Because these metals are conducting in only one spin band, we show that a circulating spin supercurrent accompanies these vortices. Moreover, we demonstrate that magnetic disorder at the interfaces with the superconductor add extra dynamics to the vortices as compared to in a normal metal. This insight can be used to help determine the effective interfacial misalignment angles for the magnetization in hybrid structures. We also give a brief discussion regarding which superconducting order parameter to use for odd-frequency triplet Cooper pairs in the quasiclassical theory.

**Introduction:** New physical phenomena can emerge at the interface between materials with different quantum order. One such example is in systems combining ferromagnetism and superconductivity, where it is possible to generate Cooper pairs that are both spin-polarized and correlated non-locally in time. This has become the basis for the field of superconducting spintronics [1], which has as one of its goals to enable new types of devices utilizing spin-polarized supercurrents [2]. On a more fundamental level, it is of interest to consider the interplay between different types of spontaneous symmetry breaking in such hybrid structures, since symmetry breaking governs a wide range of physical phenomena, including mass differences of elementary particles and phase transitions.

Half-metallic ferromagnets are 100 % spin-polarized, meaning that only one spin-band is conducting. Any supercurrent flowing through such a material, as has been observed experimentally [3], is therefore necessarily spin-polarized. This makes them especially interesting to study in order to understand how superconductivity adapts to a fully polarized environment. Much experimental and theoretical work has recently been conducted in order to understand hybrid structures involving superconductors (S) and half-metals (H) [3–15].

One hitherto unsolved problem is whether superconducting quantum vortices can form in half-metallic materials. This is an unusual physical situation since the electrons are correlated exclusively non-locally in time, such that the half-metal in fact mimics a purely odd-frequency [16] superconducting state. Vortices have non-superconducting cores and a phase winding of an integer multiple of  $2\pi$  in the superconducting order parameter, leading to circulating supercurrents [17]. In addition to being interesting from a fundamental physics point of view, understanding the behaviour of vortices is useful on a practical level. Their motion is a source of non-zero electrical resistance [18], and recently it has been proposed that vortices can be used as a means for long-range spin transport [19].

It is known that vortices can form also inside normal metals that are in the proximity to a superconductor [20–23]. Cooper pairs can then leak into the normal metal through the process of Andreev reflection [24]. This is the key mechanism behind the proximity effect which consists of weak superconductivity observed in a material placed in contact with a superconductor.

The proximity effect in half-metals is more complicated

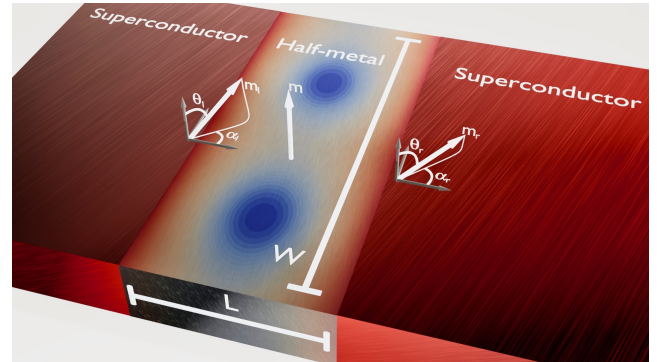


FIG. 1: Sketch of a SHS junction.  $\mathbf{m}$  is the magnetization direction in the half-metal and  $\mathbf{m}_l$  and  $\mathbf{m}_r$  are the magnetization directions at the left and right interface, respectively.  $\theta_l$  and  $\theta_r$  are the associated polar angles and  $\alpha_l$  and  $\alpha_r$  are the associated azimuthal angles.  $L$  and  $W$  are the length and width of the half-metal, respectively. The blue regions show the vortex cores where the DOS equals its normal-state value. Away from the cores, the DOS deviates from its normal-state value due to the superconducting proximity effect.

because it requires a mechanism which converts the spinless (singlet) Cooper pairs to spin-polarized (triplet) pairs. The theorized mechanism to produce such correlations involve spin mixing and spin-flip scattering at the interface [8]. Spin mixing introduces triplet correlations at the superconducting side, and spin-flip scattering mediates these correlations to the half-metallic side.

What allows us to investigate SH-heterostructures in the presence of an external magnetic field is the recent derivation of general spin-active boundary conditions for the quasiclassical theory applied to diffusive systems [9, 10]. This means that we can apply the quasiclassical Usadel theory in such a way that the Cooper pair conversion mechanism described above is included.

Here, we apply this theory both analytically and numerically to a two-dimensional SHS-junction as depicted in fig. 1 under a constant perpendicular magnetic field. We find that vortices indeed form in the purely triplet odd-frequency superconducting condensate existing in the half-metallic ferromagnet. Their

location depends not only on the superconducting phase difference, but also on the effective interfacial magnetization directions characterizing either magnetic disorder or artificially inserted thin ferromagnetic layers [5].

**Methodology:** The SHS junction depicted in fig. 1 can be treated in the quasiclassical formalism under the assumptions that the Fermi wavelength is much shorter than all other relevant length scales and so long as only one spin band is included in the half-metal. If in addition the system is diffusive, meaning that the scattering time is small, the isotropic part of the quasiclassical Green's function dominates and solves the Usadel equation [25–28],

$$D\bar{\nabla} \cdot (\check{g}\bar{\nabla}\check{g}) + i[\varepsilon\hat{\rho}_3, \check{g}] = 0. \quad (1)$$

Here,  $D$  is a diffusion constant,  $\hat{\rho}_3 = \text{diag}(1, 1, -1, -1)$  and the covariant derivative is  $\bar{\nabla}\check{g} = \nabla\check{g} - ie[\hat{\rho}_3\mathbf{A}, \check{g}]$ , where  $\mathbf{A}$  is the vector potential, and

$$\check{g} = \begin{pmatrix} \hat{g}^R & \hat{g}^K \\ 0 & \hat{g}^A \end{pmatrix} \quad (2)$$

is the quasiclassical impurity-averaged Green's function. In equilibrium, the components of the  $8 \times 8$  Green's function in eq. (2) are related by the identities  $\hat{g}^K = (\hat{g}^R - \hat{g}^A) \tanh(\varepsilon\beta/2)$  and  $\hat{g}^A = -\hat{\rho}_3\hat{g}^{R\dagger}\hat{\rho}_3$ , which means that in this case it is sufficient to solve for the retarded component  $\hat{g}^R$ . We use the vector potential  $e\mathbf{A} = -n\pi y/W[\theta(x) - \theta(x-L)]\mathbf{e}_x$ , where  $n = \Phi/\Phi_0$  is the number of flux quanta penetrating the half-metal and  $\mathbf{e}_x$  is the unit vector in the  $x$ -direction.

The quasiclassical formalism is not applicable across boundaries because the associated length scale is too short. The Usadel equation must therefore be solved in the half-metal and superconductors separately, and the solutions must be connected through boundary conditions, which can be written

$$G_i L_i \mathbf{e}_n \cdot (\hat{g}_i^R \bar{\nabla} \hat{g}_i^R) = \hat{I}(\hat{g}_i^R, \hat{g}_j^R), \quad (3)$$

where  $\mathbf{e}_n$  is the outward-pointing normal vector for region  $i$ ,  $G_i$  is the bulk conductance of material  $i$  and  $L_i$  is the length of material  $i$  in the direction of  $\mathbf{e}_n$ .  $\hat{I}(\hat{g}_i^R, \hat{g}_j^R)$  is the matrix current from material  $i$  to material  $j$ .

For the case of spin-active tunneling boundaries, the matrix current, to second order in transmission probabilities and spin-mixing angles, is [9, 10]

$$\begin{aligned} \hat{I} = & \frac{G_0^i}{2} [\hat{g}_i, F(\hat{g}_j)] - \frac{iG_\phi^i}{2} [\hat{g}_i, \hat{m}_i] + \frac{G_2^i}{8} F(\hat{g}_j) \hat{g}_i F(\hat{g}_j) \\ & + \frac{G_{\phi 2}^i}{8} [\hat{g}_i, \hat{m}_i \hat{g}_i \hat{m}_i] + \frac{iG_\chi^i}{8} [\hat{g}_i, F(\hat{g}_j) \hat{g}_i \hat{m}_i + \hat{m}_i \hat{g}_i F(\hat{g}_j)] \\ & + \frac{iG_\chi^j}{8} [\hat{g}_i, F(\hat{g}_j \hat{m}_j \hat{g}_j - \hat{m}_j)], \end{aligned} \quad (4)$$

where, for a half-metallic ferromagnet  $F(\hat{v}) = \hat{v} + \{\hat{v}, \hat{m}\} + \hat{m}\hat{v}\hat{m}$  and  $\hat{m}_k = \text{diag}(\mathbf{m}_k \cdot \boldsymbol{\sigma}, \mathbf{m}_k \cdot \boldsymbol{\sigma}^*)$ . Here  $\boldsymbol{\sigma} = (\sigma_1, \sigma_2, \sigma_3)^T$  is the vector of Pauli matrices and  $\mathbf{m}_k$  is a unit vector in the direction of the magnetization experienced by a particle being reflected in material  $k$ . Similarly,  $\hat{m} = \text{diag}(\mathbf{m} \cdot \boldsymbol{\sigma}, \mathbf{m} \cdot \boldsymbol{\sigma}^*)$  where  $\mathbf{m}$  is the unit vector in the direction of the magnetization being

felt by a particle which is transmitted. The expression for the various conductances,  $G_0, G_2, G_\chi, G_\phi$  and  $G_{\phi 2}$  can be found in [10]. For boundaries interfacing vacuum, the matrix current is  $\hat{I} = 0$ .

The Usadel equation can be made dimensionless by introducing the Thouless energy,  $\varepsilon_T := D/L^2$ , and measuring length scales relative to  $L$  and energies relative to  $\varepsilon_T$ .

In general, the Usadel equation has to be solved together with the Maxwell equation in a self-consistent manner. However, we are interested here in the case where the width  $W$  is smaller than the Josephson penetration depth. In this case one can ignore the screening of the magnetic field by the Josephson currents and the magnetic field is equal to the external one.

In the Ricatti parametrization [29] of  $\hat{g}^R$ , the parameter is the  $2 \times 2$  matrix  $\gamma$  and the retarded Green's function is written

$$\hat{g}^R = \begin{pmatrix} N & 0 \\ 0 & -\tilde{N} \end{pmatrix} \begin{pmatrix} 1 + \gamma\tilde{\gamma} & 2\gamma \\ 2\tilde{\gamma} & 1 + \tilde{\gamma}\gamma \end{pmatrix}, \quad (5)$$

where  $N := (1 - \gamma\tilde{\gamma})^{-1}$  and tilde conjugation is  $\tilde{\gamma}(\varepsilon) = \gamma^*(-\varepsilon)$ .

There is only one conducting spin band in a half-metal, and as a result  $\gamma$  has only one nonzero element,

$$\gamma_{\text{HM}} = \begin{pmatrix} a & 0 \\ 0 & 0 \end{pmatrix}. \quad (6)$$

Substituting this into eq. (1) we get that  $a$  solves the equation

$$\nabla^2 a + \frac{2\tilde{a}\nabla a \cdot \nabla a}{1 - a\tilde{a}} = \frac{4(1 + a\tilde{a})e\mathbf{A} \cdot (ae\mathbf{A} + i\nabla a)}{1 - a\tilde{a}} - 2i\varepsilon a, \quad (7)$$

The Ricatti parameter in the superconductors can be written as  $\gamma_{\text{sc}} = \text{antidiag}(b, -b)$ , where  $b$  is a function of  $\varepsilon$  and the superconducting gap parameter  $\Delta$ . Inserting this and eqs. (4) and (6) into eq. (3) we get

$$\begin{aligned} G_{\text{HM}} \mathbf{e}_n \cdot \nabla a = & 4G_0^{\text{HM}} B C a - G_2^{\text{HM}} B^2 C^2 a(a\tilde{a} + 3) \\ & + 2iG_\chi^{\text{sc}} B C^2 \sin \theta \left( b e^{-i\alpha} - \tilde{b} e^{i\alpha} a^2 \right) + 2iG_{\text{HM}} a \mathbf{e}_n \cdot \mathbf{A} e, \end{aligned} \quad (8)$$

where  $B = b\tilde{b} - 1$ ,  $C = 1/(1 + b\tilde{b})$  and  $\theta$  and  $\alpha$  are the angles for the magnetization directions on the superconducting side as shown in fig. 1. The corresponding equations for  $\tilde{a}$  and  $\mathbf{e}_n \cdot \nabla \tilde{a}$  is found by tilde conjugating eqs. (7) and (8).

*Supercurrent:* As mentioned initially, a vortex is accompanied by a circulating supercurrent. This can be extracted from the quasiclassical Green's function. In the following it will be useful to write

$$\hat{g}^R = \begin{pmatrix} g & f \\ -\tilde{f} & -\tilde{g} \end{pmatrix}. \quad (9)$$

In the half-metal,  $f$  has only one nonzero component,  $f_{\uparrow}$ .

Written in terms of the quasiclassical Green's function, the current density is [25]

$$\mathbf{j} = \frac{N_0 e D}{4} \int_{-\infty}^{\infty} \text{Tr} \left( \hat{\rho}_3 [\check{g}\bar{\nabla}\check{g}]^K \right) d\varepsilon. \quad (10)$$



Inserting eq. (9), using the relations  $\hat{g}^A = -\hat{\rho}_3 \hat{g}^{R^\dagger} \hat{\rho}_3$ ,  $\hat{g}^K = (\hat{g}^R - \hat{g}^A) \tanh(\varepsilon\beta/2)$ , eq. (10) can be rewritten

$$\mathbf{j} = \frac{N_0 e D}{2} \int_{-\infty}^{\infty} \tanh\left(\frac{\beta\varepsilon}{2}\right) \text{Tr}\left(\text{Re}\left[\tilde{f}^\dagger \nabla f^\dagger - f \nabla \tilde{f}\right] + 2eA \text{Im}\left[f \tilde{f} - \tilde{f}^\dagger f^\dagger\right]\right) d\varepsilon. \quad (11)$$

The spin current can be found by multiplying the matrix in the integrand of eq. (10) by the Pauli matrix corresponding to the appropriate spin direction before taking the trace. For a half-metal magnetized in the  $z$ -direction, the  $z$ -component of the spin supercurrent polarization is proportional to the electric current while the remaining spin current components vanish.

**Cooper Pair Correlation Function:** The Cooper pair correlation function in a diffusive half-metal must vanish at equal times due to the Pauli principle and is thus temporally non-local [16]. This naturally raises the question of how to define the superconducting order parameter. In a normal superconductor, the order parameter is  $\langle \psi_\uparrow(\mathbf{r}, 0) \psi_\downarrow(\mathbf{r}, 0) \rangle$  where  $\psi_\sigma(\mathbf{r}, t)$  is the field operator which destroys an electron with spin  $\sigma$  at position  $\mathbf{r}$  and time  $t$ . The same order parameter is used in a normal metal, but the analogous quantity for the half-metal,  $\langle \psi_\uparrow(\mathbf{r}, 0) \psi_\uparrow(\mathbf{r}, 0) \rangle$  is always zero.

One approach, which is often used in the Bogolioubov-de Gennes formalism [30], is to keep the relative time coordinate  $t$  finite between the field operators, that is

$$\Psi_1(\mathbf{r}, t) := \langle \psi_\uparrow(\mathbf{r}, t) \psi_\uparrow(\mathbf{r}, 0) \rangle = \frac{-iN_0}{2} \int_{-\infty}^{\infty} f_\uparrow(\mathbf{r}, \varepsilon) \tanh(\varepsilon\beta/2) \sin(\varepsilon t) d\varepsilon. \quad (12)$$

Another frequently used strategy [31] is to make the order parameter even in time by differentiation. This yields

$$\Psi_2(\mathbf{r}) := \left. \frac{\partial \Psi_1}{\partial t} \right|_{t=0} = \frac{-iN_0}{2} \int_{-\infty}^{\infty} \varepsilon f_\uparrow(\mathbf{r}, \varepsilon) \tanh(\varepsilon\beta/2) d\varepsilon. \quad (13)$$

Below, we shall compare these two possible choices for order parameter describing the odd-frequency superconducting condensate to see which of them that correctly captures the vortex behavior.

**Numerics:** The Usadel equation was solved numerically using a finite element scheme [32]. The program was written in Julia [33], Forward-mode automatic differentiation [34] was used to calculate the Jacobian and JuAFEM.jl [35] was used to iterate through the cells.

**Results and Discussion:** The Green's functions in the superconductors are needed through the boundary conditions. From solving the Usadel equation in the superconductors we find that the correction to the bulk solution  $\hat{g}_{\text{BCS}} = [\theta(|\varepsilon| - |\Delta|) \text{sgn}(\varepsilon) + \theta(|\Delta| - |\varepsilon|)] (\varepsilon \hat{\rho}_3 + \hat{\Delta}) / \sqrt{\varepsilon^2 - |\Delta|^2}$  is negligible in the limit  $L_{\text{sc}}/L \rightarrow \infty$  where  $L_{\text{sc}}$  is the length of the superconductors.

If we assume the proximity effect to be weak, we can keep only terms which are linear in  $a$ ,  $\tilde{a}$  and their gradients. In this case the Usadel equation (7) decouples:

$$\nabla^2 a = 4eA \cdot (aeA + i\nabla a) - 2iea. \quad (14)$$

Equation (14) can be further simplified in the so-called wide junction limit, where  $n/W \ll 1$ . If  $A = \mathbf{0}$ , the solution of eq. (14) is constant in the  $y$ -direction. Assuming this is approximately true also for small  $A$ , we neglect the term  $\partial_y^2 a$ . Equation (14) can now be solved exactly. Applying the linearized boundary conditions, the solution can be written on the form

$$a = h_1(x) \{\sin \theta_l h_2(1-x) + \sin \theta_r e^{i\Theta} h_2(x)\}, \quad (15)$$

where  $\Theta = \phi_r - \alpha_r - \phi_l + \alpha_l + 2\pi i n y / W$  and the functions  $h_1$  and  $h_2$  depend on  $\varepsilon$ ,  $\Delta$  and the conductances. Note that the wide junction approximation is not applicable at small energies.

When  $\sin \theta_l = \sin \theta_r$ ,  $a$  vanishes at  $x = 1/2$  and

$$\frac{y}{W} = \frac{1}{n} \left( \frac{1}{2} + N - \frac{\phi_r - \alpha_r - \phi_l + \alpha_l}{2\pi} \right), \quad (16)$$

where  $N$  is any integer. This means that  $f_\uparrow$  and hence also  $\Psi_1$  and  $\Psi_2$  vanishes at these points.  $a$  is holomorphic, so from Cauchy's argument principle [36] there is a  $2\pi$  phase winding in the order parameters around these points. These  $n$  roots are the only ones for  $\Psi_2$ , but for  $\Psi_1$  there are relative times  $t$  for which additional roots exist. Since each vortex is associated with a quantum of magnetic flux,  $\Phi_0$ , there should be at most  $n$  vortices when the flux is  $n\Phi_0$ . This suggests that  $\Psi_1$  is less suited for finding vortices than  $\Psi_2$  if we identify vortices by the roots of the order parameter. Using  $\Psi_2$  suggests that when  $\sin \theta_l = \sin \theta_r$  and the magnetic flux is  $n\Phi_0$ , there will in the wide-junction limit be  $n$  vortices whose location is determined by the difference in the superconducting phases and the magnetization angles.

The situation is more complicated when  $\sin \theta_l \neq \sin \theta_r$ . In this case the roots of eq. (15) depend on  $\varepsilon$ , and we will leave the discussion for how this affects the order parameter to the numerical investigation. However, some insight can still be had from the analysis. Scaling  $\sin \theta$  in the boundary condition (8) is equivalent to scaling the conductance  $G_\chi^{\text{sc}}$ . That is, if  $\sin \theta_r < \sin \theta_l$ , then the proximity effect is weaker at the right side, meaning that the vortices should be pushed to the right. This is indeed what we find numerically.

We now proceed to show numerical results in the full (non-linear) proximity effect regime. We have set the parameters  $|\Delta| = 4\varepsilon_T$ ,  $G_{\text{HM}} = 3G_0^{\text{HM}}$ ,  $G_\chi^{\text{sc}} = 0.01G_0^{\text{HM}}$ ,  $G_2^{\text{HM}} = 0.002G_0^{\text{HM}}$  and  $\phi_l = \alpha_l = 0$  common for all the numerical calculations. We obtain qualitatively similar results for other choices of the conductance parameters  $G_i^{\text{HM/sc}}$ . We include the effect of inelastic scattering by doing the substitution  $\varepsilon \rightarrow \varepsilon + i\delta$  where  $\delta = 0.001|\Delta|$  in order to avoid the divergence of  $\hat{g}_{\text{BCS}}$  at  $\varepsilon = |\Delta|$  [37].

Comparing the position of the roots of  $\Psi_1$  and  $\Psi_2$  with the circulating spin currents, we can see whether the order parameter gives a good indication of the existence and location of vortices. First we consider  $\sin \theta_l = \sin \theta_r$ . What we observe numerically is that  $\Psi_2$  gives the same location for vortices as the circulating current  $\mathbf{j}$  would suggest. Similarly, we have verified the  $\Psi_2$  vanish at the same points where the density of states (DOS) becomes equal to its normal-state value.  $\Psi_1$  vanish in the vortex cores, but also in additional points which depend on  $t$ .



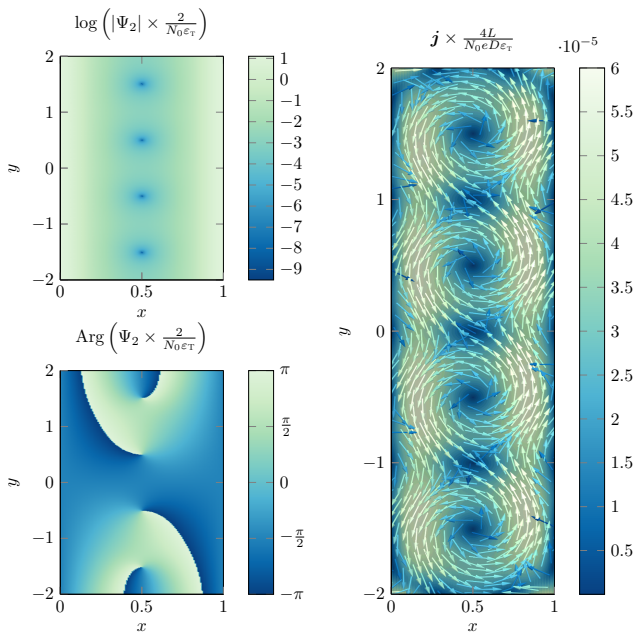


FIG. 2: Amplitude and phase of the order parameter  $\Psi_2$  and amplitude and direction of the fully spin-polarized supercurrent  $j$ . Here  $n = 4$ ,  $\phi_r = \alpha_r = 0$  and  $\sin \theta_r = 1$ .

There are also circulating currents around the locations where  $\Psi_2$  has a root and phase-winding when  $\sin \theta_l \neq \sin \theta_r$ . In the wide limit there are  $n$  vortices with locations slightly pushed to the side where  $\sin \theta$  is smaller. The DOS is still mostly equal to the normal-state value in the vortex core, but at some energies the location where the DOS is exactly equal to the normal-state is slightly different. We suggest that this effect stems from the fact that one superconducting interface is now closer to the vortex position than the other. Since the decay length of the superconducting correlations  $f_1$  inside the half-metal depends on  $\varepsilon$ , it is no longer possible for the correlations coming from each superconductor to interfere destructively at the same spatial point for all  $\varepsilon$  when this point is not equidistant from both interfaces. Consequently, the vortex core becomes more delocalized. Finally, in the asymmetric case  $\sin \theta_l \neq \sin \theta_r$ ,  $\Psi_1$  has the usual problem of having additional roots, but for some relative times the roots corresponding to the correct vortices are also either shifted or not present.

Thus, we conclude that using  $\Psi_2$  seems best suited as order parameter for the numerical investigation of quantum vortices in an purely odd-frequency superconducting condensate. Alternatively, one could use  $\Psi_1$  with  $\varepsilon_r t \ll 1$  which will give the same result since  $\Psi_1 \sim \Psi_2 t$  as  $t \rightarrow 0$ .

Figures 2 and 3 shows the amplitude and phase of  $\Psi_2$  as well as the supercurrent  $j$  for a wide junction subjected to a magnetic flux of  $4\Phi_0$ , with  $\sin \theta_r = 1$ ,  $\phi_r - \alpha_r = 0$  and  $\sin \theta_r = 0.5$ ,  $\phi_r - \alpha_r = \pi/2$ , respectively. Figures 2 and 3 shows that there are two vortices with fully spin-polarized supercurrent circulating them, and that their location has the  $y$ -coordinates given by eq. (16). In the non-symmetric case we see that the vortices are moved towards the side where  $\sin \theta$  is

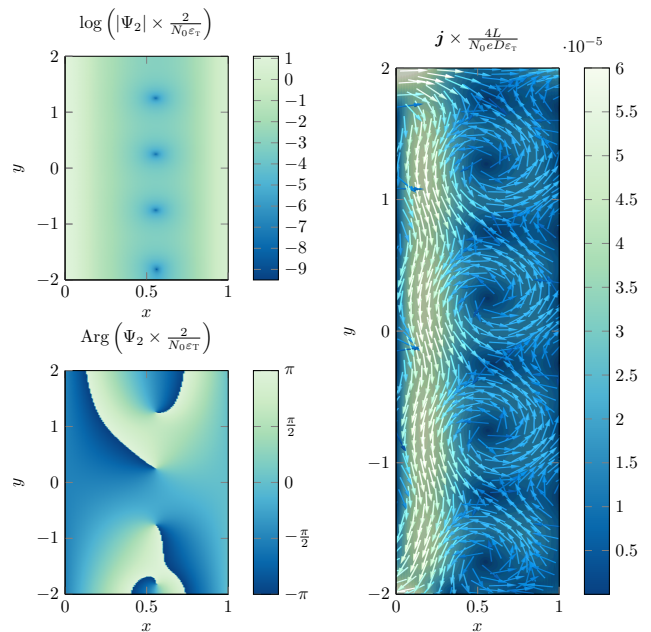


FIG. 3: Amplitude and phase of the order parameter  $\Psi_2$  and amplitude and direction of the fully spin-polarized supercurrent  $j$ . Here  $n = 4$ ,  $\phi_r - \alpha_r = \pi/2$  and  $\sin \theta_r = 0.5$ .

smaller, as expected from the analysis.

The dependence of the vortex position on both  $\alpha$  and  $\theta$  suggests an experimental method to determine the effective magnetization angles describing disorder in the form of interfacial misaligned moments or artificially inserted misaligned magnetic layers in half-metallic hybrid structures. For a fixed value of the magnetic flux and phase difference  $\phi_r - \phi_l$  (which is tunable by the applied current), the  $y$ -coordinates of the vortices gives information about the azimuthal angles  $\alpha_l$  and  $\alpha_r$ , while the  $x$ -coordinates gives information about the polar angles  $\theta_l$  and  $\theta_r$ . This approach could possibly be easier than trying to measure the magnetization angles directly. We suggest that this observation could be especially useful if the non-collinear magnetization angle at the interface is produced by the natural misalignment of magnetic dipoles arising from the conjunction of different atomic structures at the interface.

**Conclusion:** We have found both analytically and numerically that superconducting vortices occur also in the purely odd-frequency superconducting condensate that exists in proximized half-metallic ferromagnets. A fully polarized spin supercurrent is found to circulate each vortex core. The magnetization angles of the interfaces with the superconductor add extra dynamics to the vortices as compared to in a normal metal. We suggest that this insight can be used to help determine these angles in hybrid structures.

#### Acknowledgments

We thank M. Amundsen for helpful discussions. This work was supported by the Research Council of Norway through grant 240806, and its Centres of Excellence funding scheme grant 262633 “*QuSpin*”.

- 
- [1] J. Linder and J. W. A. Robinson, *Nat. Phys.* **11**, 307 (2015).
- [2] M. Eschrig, *Reports Prog. Phys.* **78** (2015).
- [3] R. S. Keizer, S. T. B. Goennenwein, T. M. Klapwijk, G. Miao, G. Xiao, and A. Gupta, *Nature* **439**, 825 (2006).
- [4] Y. Kalcheim, O. Millo, M. Egilmez, J. W. A. Robinson, and M. G. Blamire, *Phys. Rev. B* **85**, 104504 (2012).
- [5] A. Singh, S. Voltan, K. Lahabi, and J. Aarts, *Phys. Rev. X* **5**, 21019 (2015).
- [6] V. Peña, Z. Sefrioui, D. Arias, C. Leon, J. Santamaria, M. Varela, S. J. Pennycook, and J. L. Martinez, *Phys. Rev. B* **69**, 224502 (2004).
- [7] M. Eschrig, T. Löfwander, T. Champel, J. C. Cuevas, J. Kopu, and G. Schön, *J. Low Temp. Phys.* **147**, 457 (2007).
- [8] M. Eschrig, J. Kopu, J. C. Cuevas, and G. Schön, *Phys. Rev. Lett.* **90**, 4 (2003).
- [9] M. Eschrig, A. Cottet, W. Belzig, and J. Linder, *New J. Phys.* **17**, 83037 (2015).
- [10] J. A. Ouassou, A. Pal, M. Blamire, M. Eschrig, and J. Linder, *Sci. Rep.* **7**, 1932 (2017).
- [11] H. P. Dahal, E. Abrahams, D. Mozysky, Y. Tanaka, and A. V. Balatsky, *New J. Phys.* **11**, 65005 (2009).
- [12] C.-T. Wu and K. Halterman, *Phys. Rev. B* **98**, 054518 (2018).
- [13] S. Mironov and A. Buzdin, *Phys. Rev. B* **92**, 184506 (2015).
- [14] M. S. Anwar, F. Czeschka, M. Hesselberth, M. Porcu, and J. Aarts, *Phys. Rev. B* **82**, 100501 (2010).
- [15] Y. Asano, Y. Sawa, Y. Tanaka, and A. A. Golubov, *Phys. Rev. B* **76**, 224525 (2007).
- [16] J. Linder and A. V. Balatsky, [arXiv:1709.03986](https://arxiv.org/abs/1709.03986) (2017).
- [17] W. K. Kwok, U. Welp, A. Glatz, A. E. Koshelev, K. J. Kihlstrom, and G. W. Crabtree, *Reports Prog. Phys.* **79** (2016).
- [18] B. I. Halperin, G. Refael, and E. Demler, *Int. J. Mod. Phys. B* **24**, 4039 (2010).
- [19] S. K. Kim, R. Myers, and Y. Tserkovnyak, *Phys. Rev. Lett.* **121** (2018).
- [20] J. C. Cuevas and F. S. Bergeret, *Phys. Rev. Lett.* **99**, 217002 (2007).
- [21] F. S. Bergeret and J. C. Cuevas, *J. Low Temp. Phys.* **153**, 304 (2008).
- [22] M. Amundsen, J. A. Ouassou, and J. Linder, *Phys. Rev. Lett.* **120**, 207001 (2018).
- [23] V. S. Stolyarov, T. Cren, C. Brun, I. A. Golovchanskiy, O. V. Skryabina, D. I. Kasatonov, M. M. Khapaev, M. Y. Kupriyanov, A. A. Golubov, and D. Roditchev, *Nat. Commun.* **9** (2018).
- [24] B. Pannetier and H. Courtois, *J. low Temp. Phys.* **118**, 599 (2000).
- [25] W. Belzig, F. K. Wilhelm, C. Bruder, G. Schön, and A. D. Zaikin, *Superlattices Microstruct.* **25**, 1251 (1999).
- [26] V. Chandrasekhar, in *Phys. Supercond.* (Springer Berlin Heidelberg, Berlin, Heidelberg, 2004) pp. 55–110.
- [27] J. Rammer, *Quantum transport theory* (Westview, 2004) p. 521.
- [28] K. D. Usadel, *Phys. Rev. Lett.* **25**, 507 (1970).
- [29] N. Schopohl, [arXiv:cond-mat/9804064](https://arxiv.org/abs/cond-mat/9804064) (1998).
- [30] K. Halterman, P. H. Barsic, and O. T. Valls, *Phys. Rev. Lett.* **99**, 127002 (2007).
- [31] E. Abrahams, A. Balatsky, D. J. Scalapino, and J. R. Schrieffer, *Phys. Rev. B* **52**, 1271 (1995).
- [32] M. Amundsen and J. Linder, *Sci. Rep.* **6**, 22765 (2016).
- [33] J. Bezanson, A. Edelman, S. Karpinski, and V. B. Shah, *SIAM Rev.* **59**, 65 (2017).
- [34] J. Revels, M. Lubin, and T. Papamarkou, [arXiv:1607.07892](https://arxiv.org/abs/1607.07892) [cs.MS] (2016).
- [35] K. Carlsson, “Juafem.jl,” <https://github.com/KristofferC/JuAFEM.jl> (2019).
- [36] R. Churchill and J. Brown, *Complex variables and applications*, Churchill-Brown series (McGraw-Hill, 1990).
- [37] R. C. Dynes, J. P. Garno, G. B. Hertel, and T. P. Orlando, *Phys. Rev. Lett.* **53**, 2437 (1984).

Appendix B  
**PAPER II**



# Controllable Vortex Loops in Superconducting Proximity Systems

Eirik Holm Fyhn<sup>1</sup> and Jacob Linder<sup>1</sup>

<sup>1</sup>Center for Quantum Spintronics, Department of Physics, Norwegian University of Science and Technology, NO-7491 Trondheim, Norway

(Dated: June 7, 2019)

Superconducting vortex loops have so far avoided experimental detection despite being the focus of much theoretical work. We here propose a method of creating controllable vortex loops in the superconducting condensate arising in a normal metal through the proximity effect. We demonstrate both analytically and numerically that superconducting vortex loops emerge when the junction is pierced by a current-carrying insulated wire and give an analytical expression for their radii. The vortex loops can readily be tuned big enough to hit the sample surface, making them directly observable through scanning tunneling microscopy.

**Introduction:** Many key properties of physical systems are determined by topological defects such as dislocations in solids, domain walls in ferroics, vortices in superfluids, magnetic skyrmions in condensed matter systems and cosmic strings in quantum field theories. In superconductors, the topological entities are vortex lines of quantized magnetic flux. The topological nature of these vortices makes them stable, which is important for potential applications such as superconducting qubits [1–3], digital memory and long-range spin transport [4]. Vortices have non-superconducting cores and a phase winding of an integer multiple of  $2\pi$  in the superconducting order parameter, leading to circulating supercurrents [5].

The formation of superconducting vortex loops is topologically allowed, and has theoretically been predicted to form around strong magnetic inclusions inside the superconductor [6] or through vortex cutting and recombination [7, 8]. However, no observation of vortex loops in superconducting systems has been found to date. One challenging aspect is that vortex loops are typically small in conventional superconductors and difficult to stabilize for an extended period of time [9]. Recently it has been shown that vortex loops can be formed in proximity systems by inserting physical barriers, around which the vortices can wrap [8].

In this Letter, we present a way to create controllable vortices in mesoscopic proximity systems in a manner which makes them experimentally detectable through scanning tunneling microscopy. The system considered is a three-dimensional SNS junction pierced by a current-carrying wire which creates the inhomogeneous field responsible for the vortex loops. In planar SNS-junctions with uniform applied magnetic field, changing the superconducting phase difference between the two superconductors shifts the vortex lines in the vertical direction [10]. We here show that the corresponding effect on vortex loops in three dimensions is to change their size. Thus, these vortex loops are easily tunable. This makes it possible to make the vortices touch the surface, leaving distinct traces which are directly observable by scanning tunneling spectroscopy [11].

Vortex loops in superconducting systems has previously been predicted using the phenomenological Ginzburg-Landau theory [6–8]. Here we use a fully microscopic framework known as quasiclassical theory and solve the Usadel equation relevant for diffusive systems [12]. By showing that vortex loop formation occurs in a microscopic theory, we give valuable

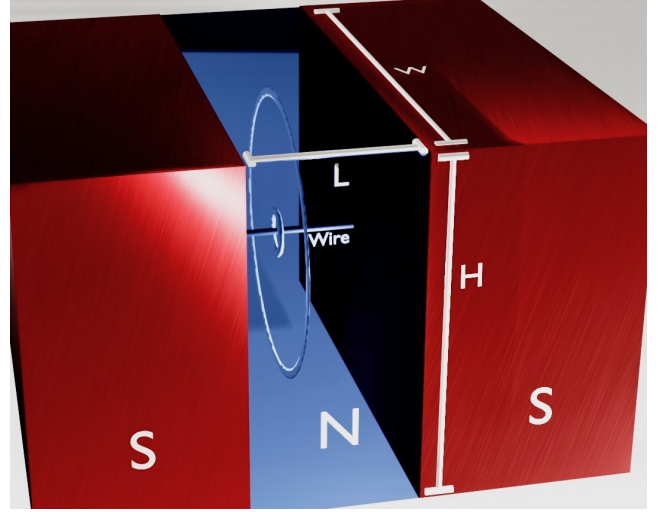


FIG. 1: Sketch of three-dimensional SNS junction considered in this Letter. The height, width and length are  $H$ ,  $W$  and  $L$ , respectively, and the junction is pierced by an insulated current-carrying wire. Contours of the superconducting vortex loops are shown at the location where they are found in our numerical simulations.

support to the earlier proposed mechanisms for superconducting vortex loops. Finally, we discuss how the proposed setup can be realized experimentally.

**Methodology:** In the Usadel theory, the system is described by a quasiclassical Green's function from which physical properties can be extracted. The SNS junction depicted in fig. 1 can be treated in the quasiclassical formalism under the assumptions that the Fermi wavelength is much shorter than all other relevant length scales. In thermal equilibrium it is sufficient to calculate the retarded Green's function,  $\hat{g}$ . If the system is diffusive, meaning that the scattering time is small, the isotropic part dominates and solves the Usadel equation [12–15],

$$D\bar{\nabla} \cdot (\hat{g}\bar{\nabla}\hat{g}) + i[\varepsilon\hat{\rho}_3, \hat{g}] = 0. \quad (1)$$

Here,  $D$  is a diffusion constant,  $\hat{\rho}_3 = \text{diag}(1, 1, -1, -1)$  and the covariant derivative is  $\bar{\nabla}\hat{g} = \nabla\hat{g} - ie[\hat{\rho}_3\mathbf{A}, \hat{g}]$ , where  $e = -|e|$  is the electron charge and  $\mathbf{A}$  is the vector potential. Finally,  $(x, y, z) \in [-L/2, L/2] \times [-W/2, W/2] \times [-H/2, H/2]$  in the normal metal.

The quasiclassical formalism is not applicable across boundaries because the associated length scale is too short. The Usadel equation must therefore be solved in the normal metal and superconductors separately, and the solutions must be connected through boundary conditions. If we assume a low-transparency interface, we may use the Kupriyanov-Lukichev boundary condition

$$\zeta_i L_i \mathbf{e}_n \cdot (\hat{g}_i \bar{\nabla} \hat{g}_i) = \frac{1}{2} [\hat{g}_i, \hat{g}_j], \quad (2)$$

where  $\mathbf{e}_n$  is the outward-pointing normal vector for region  $i$ ,  $\zeta_i$  is the ratio of the bulk and interface conductances of material  $i$  and  $L_i$  is the length of material  $i$  in the direction of  $\mathbf{e}_n$ . For the boundaries interfacing vacuum,  $\mathbf{e}_n \cdot \bar{\nabla} \hat{g} = 0$ .

Assuming that the superconductors are much larger than the normal metal, we can use the analytic bulk solution [16]  $\hat{g}_{\text{BCS}} = [\theta(|\varepsilon| - |\Delta|) \text{sgn}(\varepsilon) + \theta(|\Delta| - |\varepsilon|)] (\varepsilon \hat{\rho}_3 + \hat{\Delta}) / \sqrt{\varepsilon^2 - |\Delta|^2}$ . Here  $\hat{\Delta} = \text{antidiag}(\Delta, -\Delta, \Delta^*, -\Delta^*)$  where  $\Delta = |\Delta| e^{i\phi}$  is the superconducting gap parameter.

The Usadel equation can be made dimensionless by introducing the Thouless energy,  $\varepsilon_\tau := D/L^2$ , and measuring length scales relative to  $L$  and energies relative to  $\varepsilon_\tau$ .

In general, the Usadel equation has to be solved together with the Maxwell equation in a self-consistent manner. However, we are interested here in the case where the width  $W$  and height  $H$  is smaller than the Josephson penetration depth. In this case we can ignore the screening of the magnetic field by the Josephson currents and the magnetic field is equal to the external one [17]. The part of the wire which is inside the superconductor is assumed to be screened and hence not contribute to the vector potential inside the normal metal. From the remaining part of the wire, we get

$$e\mathbf{A} = -n\pi \log \left( \frac{\sqrt{(L/2 - x)^2 + r^2} + L/2 - x}{\sqrt{(L/2 + x)^2 + r^2} - L/2 - x} \right) \mathbf{e}_x, \quad (3)$$

where  $r = \sqrt{y^2 + z^2}$ ,  $\mathbf{e}_x$  is the unit vector in the  $x$ -direction and  $n = -e\mu I / 4\pi^2$  where  $I$  is the current and  $\mu$  is the permeability.

*The Riccati Parametrization:* In the Riccati parametrization [18] of  $\hat{g}^{\text{R}}$ , the parameter is the  $2 \times 2$  matrix  $\gamma$  and the retarded Green's function is written

$$\hat{g}^{\text{R}} = \begin{pmatrix} N & 0 \\ 0 & -\tilde{N} \end{pmatrix} \begin{pmatrix} 1 + \gamma \tilde{\gamma} & 2\gamma \\ 2\tilde{\gamma} & 1 + \tilde{\gamma} \gamma \end{pmatrix}, \quad (4)$$

where  $N := (1 - \gamma \tilde{\gamma})^{-1}$  and tilde conjugation is  $\tilde{\gamma}(\varepsilon) = \gamma^*(-\varepsilon)$ .

Since the superconducting correlations in our system are spin-singlet, we may write  $\gamma_{\text{N}} = \text{antidiag}(a, -a)$  and  $\gamma_{\text{BCS}} = \text{antidiag}(b, -b)$ . Substituting this into eqs. (1) and (2) we obtain the dimensionless equations

$$\nabla^2 a = \frac{2\tilde{a} \nabla a \cdot \nabla a}{1 + a\tilde{a}} + \frac{4(1 - a\tilde{a})e\mathbf{A} \cdot (ae\mathbf{A} + i\nabla a)}{1 + a\tilde{a}} + 2ie(\nabla \cdot \mathbf{A})a - 2i\varepsilon a, \quad (5)$$

and

$$\mathbf{e}_n \cdot \nabla a = \frac{(1 + a\tilde{b})(b - a)}{\zeta(b\tilde{b} + 1)} + 2iae_n \cdot \mathbf{A}e. \quad (6)$$

The corresponding equations for  $\tilde{a}$  and  $\mathbf{e}_n \cdot \nabla \tilde{a}$  is found by tilde conjugating eqs. (5) and (6).

*Observables:* As mentioned initially, a vortex is accompanied by a non-superconducting core and a circulating supercurrent. Both the superconducting order parameter and the supercurrent can be extracted from the quasiclassical Green's function. In the following it will be useful to write

$$\hat{g}^{\text{R}} = \begin{pmatrix} g & f \\ -\tilde{f} & -\tilde{g} \end{pmatrix}. \quad (7)$$

There are only singlet correlations in the SNS system, so  $f = \text{antidiag}(f_s, -f_s)$ .

Written in terms of the quasiclassical Green's function, the superconducting order parameter is

$$\Psi(\mathbf{r}) := \langle \psi_\uparrow(\mathbf{r}, 0) \psi_\downarrow(\mathbf{r}, 0) \rangle = \frac{N_0}{2} \int_{-\infty}^{\infty} f_s(\mathbf{r}, \varepsilon) \tanh(\varepsilon\beta/2) d\varepsilon. \quad (8)$$

where  $\psi_\sigma(\mathbf{r}, t)$  is the field operator which destroys an electron with spin  $\sigma$  at position  $\mathbf{r}$  and time  $t$ ,  $N_0$  is the normal state density of states and  $\beta = 1/k_B T$ .

The current density is [13]

$$\mathbf{j} = \frac{N_0 e D}{4} \int_{-\infty}^{\infty} \text{Tr} \left( \hat{\rho}_3 [\hat{g} \bar{\nabla} \hat{g}]^{\text{K}} \right) d\varepsilon. \quad (9)$$

Inserting eq. (7), using the relations  $\hat{g}^\Lambda = -\hat{\rho}_3 \hat{g}^{\text{R}\dagger} \hat{\rho}_3$ ,  $\hat{g}^{\text{K}} = (\hat{g}^{\text{R}} - \hat{g}^\Lambda) \tanh(\varepsilon\beta/2)$ , eq. (9) can be rewritten

$$\mathbf{j} = \frac{N_0 e D}{2} \int_{-\infty}^{\infty} \tanh \left( \frac{\beta\varepsilon}{2} \right) \text{Tr} \left( \text{Re} [ \tilde{f}^\dagger \nabla f^\dagger - f \nabla \tilde{f} ] + 2e\mathbf{A} \text{Im} [ f \tilde{f} - \tilde{f}^\dagger f^\dagger ] \right) d\varepsilon. \quad (10)$$

*Numerics:* The Usadel equation was solved numerically using a finite element scheme [19]. The program was written in Julia [20], Forward-mode automatic differentiation [21] was used to calculate the Jacobian and JuAFEM.jl [22] was used to iterate through the cells.

**Results and Discussion:** The non-linear Usadel equation does not have a general analytical solution, but it can be solved analytically in an approximate manner far away from the wire. If we assume the proximity effect to be weak, we can keep only terms which are linear in  $a$ ,  $\tilde{a}$  and their gradients. In this case the Usadel equation (5) decouples:

$$\nabla^2 a = 4e\mathbf{A} \cdot (ae\mathbf{A} + i\nabla a) + 2ie(\nabla \cdot \mathbf{A})a - 2i\varepsilon a. \quad (11)$$

Equation (11) can be further simplified when we only consider regions where  $r \gg L$ , with  $r = \sqrt{y^2 + z^2}$ . The solution of eq. (11) is constant in  $y$  and  $z$  when  $\mathbf{A} = \mathbf{0}$ , and by assuming this is also approximately true when  $|e\mathbf{A}| \ll 1$ , we assume that the terms  $\partial_y^2 a$  and  $\partial_z^2 a$  are negligible. Finally, we Taylor expand  $e\mathbf{A} = -n\pi/r + O(1/r^2)$  and keep only the first term. Equation (11) can now be solved exactly, and by applying the linearized boundary conditions the solution can be written on the form

$$a(x, y, z) = h_1(x, y, z) \{ h_2(1/2 - x) + e^{i\theta} h_2(1/2 + x) \}, \quad (12)$$



where

$$\Theta = \phi_r - \phi_l + 2\pi n/r \quad (13)$$

and the functions  $h_1$  and  $h_2$  depend on  $\varepsilon$ ,  $\Delta$  and  $\zeta$ . Note that the wide junction approximation is not applicable at small energies.

From eq. (12) we see that  $a$  vanishes at  $x = 0$  and

$$\frac{r}{L} = \frac{2n}{1 + 2N - \frac{\phi_r - \phi_l}{\pi}} \quad (14)$$

and  $N$  is any integer. This means that  $f$  and hence also  $\Psi$  vanish at these points.  $a$  is holomorphic, so from Cauchy's argument principle [23] there is a  $2\pi$  phase winding in the order parameters around these points. Equation (14) is our main analytical result as it predicts how the radius of the vortex loops depends on the tunable parameters of the system: the current through the wire and the applied phase difference. Although it was obtained using approximations, we demonstrate below that it matches the full numerical solution of the exact Usadel equation very well.

Note that the radius,  $r$ , of the largest vortex loop given eq. (14) can be made arbitrary large by letting  $\phi_r - \phi_l$  approach  $\pi$ . Thus, for a given sample size  $L \times W \times H$  and current  $I$ , there is a superconducting phase difference for which the vortex loop hits the surface and can be directly detected experimentally.

When the superconducting phase difference is increased in normal SNS-junctions the vortices respond to an increase in the superconducting phase difference by moving in unison in a certain direction [10]. If the direction of the external magnetic field is reversed, the vortices will move in the opposite direction when the phase difference is increased. The magnetic field going through two opposing points on the vortex loops are opposite in direction. Hence, if the upper part of the loop moves up, the lower part should move down, increasing the size of the loop. This may indicate that the relationship between the radii of vortex loops and superconducting phase difference in proximity systems is a general feature and not specific to the system considered here. This could be important as it opens the possibility of manipulating vortices in systems that are less obviously controllable than the one considered in the present manuscript while at the same time easier to design in the lab. For instance, one possibility is to grow the normal metal around a magnetic dipole. The magnetic field from a dipole can, unlike the magnetic field from a wire, not be altered in strength. Nevertheless, if the field is strong enough to produce vortices, altering the superconducting phase difference could be a way to increase the size of the vortex to the point where it touches the surface and becomes directly observable. This is consistent with the findings of ref. [6] who considered a magnetic dipole embedded in a single superconducting material.

We now proceed to show numerical results in the full (non-linear) proximity effect regime. We have set the parameters  $|\Delta| = 4\varepsilon_r$ ,  $G_{\text{NM}} = 3G_0^{\text{NM}}$ ,  $W = H = 6L$  and  $\phi_l = 0$  common for all the numerical calculations. We include the effect of inelastic scattering by doing the substitution  $\varepsilon \rightarrow \varepsilon + i\delta$  where  $\delta = 0.001|\Delta|$  in order to avoid the divergence of  $\hat{g}_{\text{BCS}}$  at  $\varepsilon = |\Delta|$  [24].

Numerically we find that vortex loops do indeed form at the locations predicted by the analysis. There are circular paths

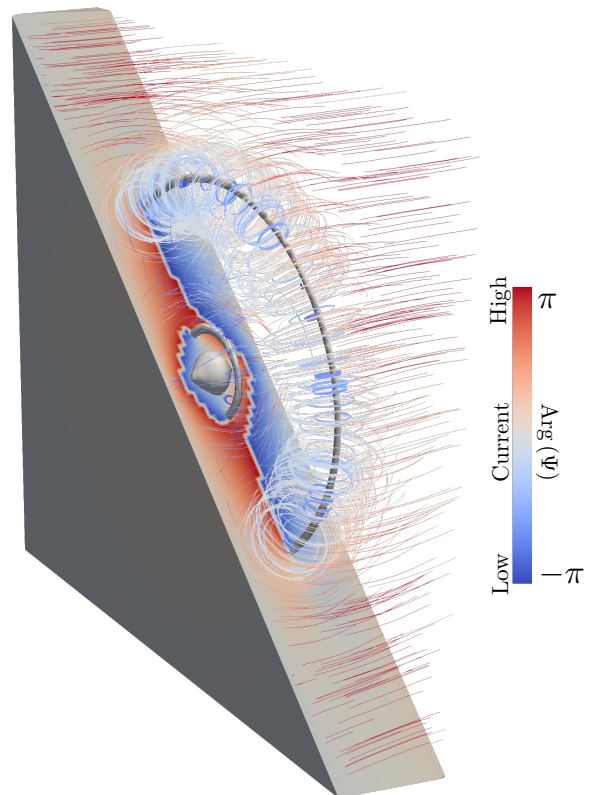


FIG. 2: Plot of the phase of the superconducting order parameter  $\Psi$  on the surface of a diagonally cut part of the normal metal, contour plot of its amplitude,  $|\Psi|$ , and streamlines of the supercurrent  $j$ . Here  $n = 1$  and  $\phi_r = 0$ .

around the origin where the superconducting order parameter vanish and the local density of states is equal to that of the normal state. Around these loops there are a circulating supercurrent and a phase winding in the order parameter of  $2\pi$ . Figure 2 shows a contour plot of  $|\Psi|$ , which shows the location of the vortices, together with the phase of  $\Psi$  and the circulating supercurrent  $j$ .

We find that the positions of the vortex loops match with eq. (14) for vortices with radius much larger than  $L$ , as predicted from the analysis. Figures 3 and 4 shows how the sizes of the vortex loops depend in superconducting phase difference  $\phi$  and magnetic field strength  $n$ , respectively. We find that increasing  $\phi$  can make the vortices arbitrary large, but does not increase the number of vortices. Increasing  $n$ , on the other hand, also increase the number of vortices, but the sizes grow only linearly with  $n$ . Note that as the vortex loops hit the surface, they curve so as to hit normally to the surface. This is because there should be no current component normal to the surface, and is consistent with previous results [6, 25].

The setup presented in this Letter can be realized experimentally by first growing a vertical insulated nanowire and then grow a superconductor, such as niobium, and a normal metal, such as copper, around it in a layerwise fashion. Growing a vertical wire has been done successfully by the vapor-liquid-solid method [26–28] and by template-directed synthesis [29]. The

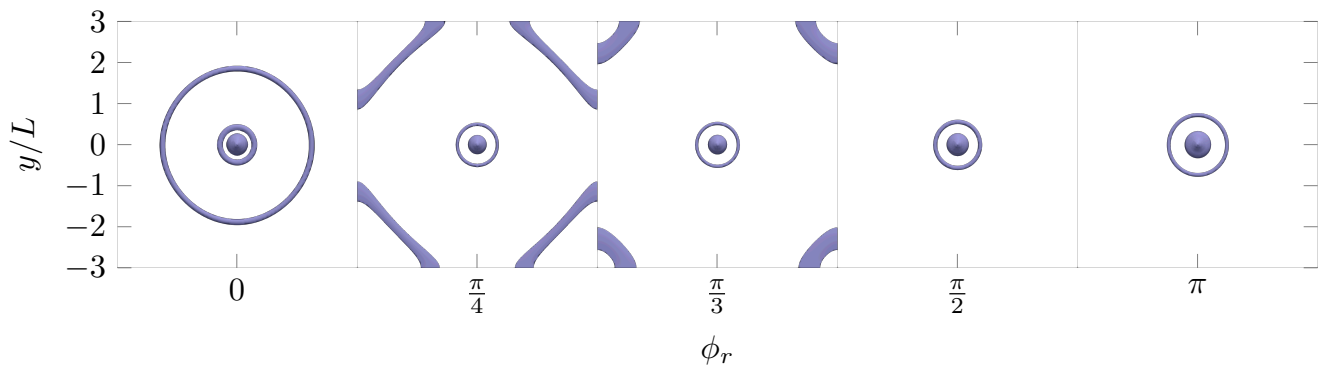


FIG. 3: Contour plot of the amplitude of the superconducting order parameter  $\Psi$  for magnetic field strength  $n = 1$  and various values of the superconducting phase difference  $\phi_r$ .

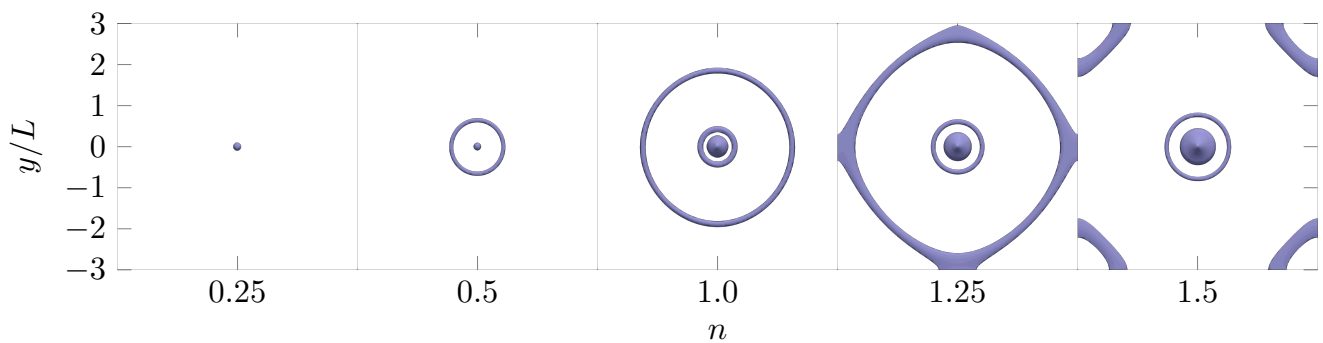


FIG. 4: Contour plot of the amplitude of the superconducting order parameter  $\Psi$  for superconducting phase difference  $\phi_r = 0$  and various values of magnetic field strength  $n$ .

vapor-liquid-solid method has already been used to produce vertical surround-gate field-effect transistors with a precision exceeding what should be necessary for the system presented here [27].

**Conclusion:** We have demonstrated that controllable superconducting vortex loops can emerge in a Josephson junction pierced by an insulated current-carrying wire. The size and number of vortices depend on the phase difference between the superconducting order parameter in the superconductors,  $\phi_r - \phi_l$ , as well as the strength of the magnetic field. Our findings suggest that even in systems where controlling the magnetic field strength is not an option, such as in system with a magnetic dipole inclusion, the superconducting phase gradient

causing a supercurrent flow can still be used to expand the vortex loops such that they hit the surface. This would make them directly detectable through scanning tunneling microscopy.

#### Acknowledgments

We thank M. Amundsen and V. Risinggård for helpful discussions. This work was supported by the Research Council of Norway through grant 240806, and its Centres of Excellence funding scheme grant 262633 “*QuSpin*”.

- 
- [1] K. G. Fedorov, A. V. Shcherbakova, M. J. Wolf, D. Beckmann, and A. V. Ustinov, *Phys. Rev. Lett.* **112**, 160502 (2014).  
 [2] M. H. Devoret and R. J. Schoelkopf, *Science* **339**, 1169 (2013).  
 [3] A. Herr, A. Fedorov, A. Shnirman, E. Il’ichev, and G. Schön, *Supercond. Sci. Technol.* **20**, 450 (2007).  
 [4] S. K. Kim, R. Myers, and Y. Tserkovnyak, *Phys. Rev. Lett.* **121** (2018), 10.1103/PhysRevLett.121.187203.  
 [5] W. K. Kwok, U. Welp, A. Glatz, A. E. Koshelev, K. J. Kihlstrom, and G. W. Crabtree, *Reports Prog. Phys.* **79** (2016), 10.1088/0034-4885/79/11/116501.  
 [6] Doria, M. M. and Romaguera, A. R. De C. and Milošević, M. V. and Peeters, F. M., *Epl* **79** (2007), 10.1209/0295-5075/79/47006.  
 [7] A. Glatz, V. K. Vlasko-Vlasov, W. K. Kwok, and G. W. Crabtree, *Phys. Rev. B* **94** (2016), 10.1103/PhysRevB.94.064505.  
 [8] G. R. Berdiyrov, M. V. Milošević, F. Kusmartsev, F. M. Peeters, and S. Savel’ev, *Sci. Rep.* **8**, 2733 (2018).  
 [9] A. Schönenberger, A. Larkin, E. Heeb, V. Geshkenbein, and G. Blatter, *Phys. Rev. Lett.* **77**, 4636 (1996).

- [10] J. C. Cuevas and F. S. Bergeret, *Phys. Rev. Lett.* **99**, 217002 (2007).
- [11] V. S. Stolyarov, T. Cren, C. Brun, I. A. Golovchanskiy, O. V. Skryabina, D. I. Kasatonov, M. M. Khapaev, M. Y. Kupriyanov, A. A. Golubov, and D. Roditchev, *Nat. Commun.* **9** (2018), 10.1038/s41467-018-04582-1.
- [12] K. D. Usadel, *Phys. Rev. Lett.* **25**, 507 (1970).
- [13] A. D. Zaikin, C. Bruder, W. Belzig, G. Schön, and F. K. Wilhelm, *Superlattices Microstruct.* **25**, 1251 (2002).
- [14] V. Chandrasekhar, in *Phys. Supercond.* (Springer Berlin Heidelberg, Berlin, Heidelberg, 2004) pp. 55–110.
- [15] J. Rammer, *Quantum transport theory* (Westview, 2004) p. 521.
- [16] M. Amundsen, J. A. Ouassou, and J. Linder, *Phys. Rev. Lett.* **120**, 207001 (2018).
- [17] A. Barone and G. Paternò, *Physics and applications of the Josephson effect* (Wiley, New York, NY, 1982).
- [18] N. Schopohl, [arXiv:cond-mat/9804064](https://arxiv.org/abs/cond-mat/9804064) (1998).
- [19] M. Amundsen and J. Linder, *Sci. Rep.* **6**, 22765 (2016).
- [20] J. Bezanson, A. Edelman, S. Karpinski, and V. B. Shah, *SIAM Rev.* **59**, 65 (2017).
- [21] J. Revels, M. Lubin, and T. Papamarkou, [arXiv:1607.07892](https://arxiv.org/abs/1607.07892) [cs.MS] (2016).
- [22] K. Carlsson, “Juafem.jl,” <https://github.com/KristofferC/JuAFEM.jl> (2019).
- [23] R. V. Churchill and J. W. Brown, *Complex variables and applications*, Churchill-Brown series (McGraw-Hill, 1990).
- [24] R. C. Dynes, J. P. Garno, G. B. Hertel, and T. P. Orlando, *Phys. Rev. Lett.* **53**, 2437 (1984).
- [25] A. R. de C. Romaguera, M. M. Doria, and F. M. Peeters, *Phys. Rev. B* **75**, 184525 (2007).
- [26] H. T. Ng, J. Han, T. Yamada, P. Nguyen, Y. P. Chen, and M. Meyyappan, *Nano Letters* **4**, 1247 (2004).
- [27] V. Schmidt, H. Riel, S. Senz, S. Karg, W. Riess, and U. Gösele, *Small* **2**, 85 (2006), <https://onlinelibrary.wiley.com/doi/pdf/10.1002/sml.200500181>.
- [28] K. Tomioka, M. Yoshimura, and T. Fukui, *Nature* **488**, 189 (2012).
- [29] Y. Xia, P. Yang, Y. Sun, Y. Wu, B. Mayers, B. Gates, Y. Yin, F. Kim, and H. Yan, *Advanced Materials* **15**, 353 (2003).



## C

## COMPUTER PROGRAM

**Listing C.1:** *The computer code for solving general systems of nonlinear equations in two and three dimensions.*

```

1  module ProjectTools
2  export solve2D, export2DVTK, Romberg, GK715, solve3D, export3DVTK, solveTrapezoid,
   export2DTrapezoidVTK, solve3DTrapezoid, export3DTrapezoidVTK
3
4  using LinearAlgebra, JuAFEM, SparseArrays, Printf, QuadGK, DualNumbers
5  using SparseArrays, ProgressMeter, BlockArrays, StaticArrays
6  using Distributed, IterativeSolvers, Preconditioners
7
8  # Solving nonlinear problems
9  function NewtonRhapson(u, J, R, JacRes!, showProgress::Bool=true)
10 # Setting up parameters
11 newtonTol = 1e-12
12 newtonItr = -1
13 maxItr = 100
14 maxError = 1e8
15
16 # Diagonal preconditioner
17 p = DiagonalPreconditioner(J)
18 if showProgress
19     prog = ProgressMeter.ProgressThresh(newtonTol, "Solving:")
20     ProgressMeter.update!(prog, Inf; showvalues=[(:iter, newtonItr)])
21 end
22
23 while true; newtonItr += 1
24     # Computing new iteration
25     JacRes!(J, R, u)
26     u -= bicgstabl(J, R)
27
28     normRes = norm(R)
29
30     if showProgress
31         ProgressMeter.update!(prog, normRes; showvalues=[(:iter, newtonItr)])
32     end
33
34     # Checking termination conditions
35     if normRes < newtonTol
36         break
37     elseif normRes > maxError
38         error("\nError threshold reached: Error ", normRes, " Aborting.\n")
39         break
40     elseif newtonItr > maxItr
41         error("\nMaximum Newton iterations reached at residual norm ", normRes, ". Aborting.\n")
42         break
43     end
44 end
45 return u
46 end
47 function autoJac!(J, F, x)
48     for i ∈ 1:length(x)
49         X = Dual.(x)
50         X[i] += 1ε
51         J[:,i] = dualpart.(F(X))
52     end

```

```

53 end
54
55 # Numerical integration
56 function Romberg(func, start, stop, tol=1e-4, maxIter = 10)
57 @printf("Starting Romberg integration on [%.2f, %.2f]\n", start, stop)
58 n = 1
59 m = 1
60 h = (stop - start)/2.0
61 R_init = h.*(func(start) .+ func(stop))
62 R = Array{typeof(R_init)}(undef, maxIter, maxIter)
63 R[1, 1] = R_init
64 error = Inf
65 h *= 2.0
66 N = length(vcat(R[1, 1]...))
67 while error > tol && n < maxIter
68   @printf("Iterating (m = %i). Error: %.3g (goal: %.3g)\n", m, error, tol)
69   n += 1
70   m += 1
71   h /= 2.0
72   R[n, 1] = (0.5) .* R[n-1, 1]
73   for k ∈ 1:2^(n-2)
74     R[n, 1] .+= h.*func(start + (2k-1)*h)
75   end
76   for i ∈ 1:m-1
77     R[n, i+1] = (1.0/(4^i - 1.0)).*((4^i).*R[n, i] .- R[n-1, i])
78   end
79   #= error = max((map(x -> max(abs.(x)...), (R[n, m] .- R[n, m-1])))...)=#
80   error = sum(map(x -> isnan(x) ? 0.0 : abs(x), vcat((R[n, m] .- R[n, m-1])...))) / N
81   println("Error: ", error)
82   if n == maxIter
83     println("Maximum number of iterations reached")
84   end
85 end
86 return R[n, m]
87 end
88 function GK715(func, start, stop, tol=1e-6, maxIter::Int = 10, iter::Int = 0)
89 @printf("Starting GK715 integration on [%.2f, %.2f]\n", start, stop)
90 x, w, wg = kronrod(7) # [quadpoints (kronrod)], [weights (kronrod)], [weights (gauss)]
91 x .*= (stop - start)/2
92 x_0 = (start + stop)/2
93 x^- = x_0 .+ x[1:end-1]
94 x^+ = x_0 .+ (-).x[1:end-1] # note: from big x to small x
95 fx_0 = func(x_0)
96 fx = func.(x^-) .+ func.(x^+)
97 I^K = fx_0.*w[end] # Kronrod integral
98 I^G = fx_0.*wg[end] # Gaussian integral
99 for i ∈ 1:7
100   I^K = I^K .+ (fx[i].*w[i])
101 end
102 for i ∈ 1:3
103   I^G = I^G .+ (fx[2i].*wg[i])
104 end
105 I^K = I^K.*((stop - start)/2)
106 I^G = I^G.*((stop - start)/2)
107 error = max((map(x -> max(abs.(x)...), (I^K .- I^G)))...)
108 if error > tol
109   if iter >= maxIter
110     @printf("Max num of iterations (%i) reached. Returning with error %g\n", maxIter, error)
111     return I^K
112   end
113   @printf("Splitting the interval [%.2g, %.2g]\nwith error %g (goal: %g).\n", start, stop, error,
114     tol)
115   I^K = GK715(func, start, x_0, tol/2, maxIter, iter+1) .+ GK715(func, x_0, stop, tol/2, maxIter,
116     iter+1)
117 end
118 return I^K
119 end
120 # Setting up 2D FEM
121 function create2DGrid(n::Int, width::Float64=1.0)
122   return generate_grid(QuadraticQuadrilateral, (n, Int(floor(n*width))), Vec{2}([0.0, -width/2]),
123     Vec{2}([1.0, width/2]))
124 end

```

```

123 function create2DValues()
124 # quadrature rules
125 quad_rule = QuadratureRule{2, RefCube}(4)
126 face_quad_rule = QuadratureRule{1, RefCube}(4)
127 # geometric interpolation
128 interpolation_geom = Lagrange{2, RefCube, 2}()
129 cellvalues = CellScalarValues(quad_rule, interpolation_geom)
130 facevalues = FaceScalarValues(face_quad_rule, interpolation_geom)
131
132 return cellvalues, facevalues
133 end
134 ## Calculating jacobian and residuals at once using automatic differentiation
135 function JacRes2D!(J::SparseMatrixCSC{T, Int64}, R::AbstractArray{T}, X::AbstractArray{T},
    cellvalues::CellScalarValues, facevalues::FaceScalarValues, grid::Grid, dh::DofHandler, F!, B_1
    !, B_r!, B_t!, B_b!) where {T}
136
137 fill!(J.nzval, 0.0) # Reset Jacobian
138 fill!(R, 0.0) # Reset residuals
139 q_points = getnquadpoints(cellvalues)
140 n_basefuncs = getnbasefunctions(cellvalues)
141 n = ndofs_per_cell(dh)
142 fDim = dh.field_dims[1]
143
144 eyeFDim = Matrix{T}(I, fDim, fDim) # fDimxfDim identity matrix
145 # Initialize element vectors
146  $\chi_e$  = zeros(T, fDim)
147  $\partial\chi_{e_x}$  = zeros(T, fDim)
148  $\partial\chi_{e_y}$  = zeros(T, fDim)
149 Fe_dual = zeros(Dual{T}, fDim)
150 Be_dual = zeros(Dual{T}, fDim)
151 Fe = zeros(T, fDim)
152 Be = zeros(T, fDim)
153  $\partial Fe_\chi$  = zeros(T, fDim, fDim)
154  $\partial Fe_\partial\chi_x$  = zeros(T, fDim, fDim)
155  $\partial Fe_\partial\chi_y$  = zeros(T, fDim, fDim)
156  $\partial Be_\chi$  = zeros(T, fDim, fDim)
157
158 # Spatial coordinates
159 r = zeros(Float64, 2)
160
161 Re = PseudoBlockArray(zeros(T, fDim*n_basefuncs), fDim*ones(Int, n_basefuncs))
162 Je = PseudoBlockArray(zeros(T, fDim*n_basefuncs, fDim*n_basefuncs), fDim*ones(Int, n_basefuncs),
    fDim*ones(Int, n_basefuncs))
163 Xe = PseudoBlockArray(zeros(T, fDim*n_basefuncs), fDim*ones(Int, n_basefuncs))
164
165 assembler = start_assemble(J, R)
166
167 @inbounds for cell in CellIterator(dh)
168 reinit!(cellvalues, cell)
169 global_dofs = celldofs(cell)
170 Xe[:] = X[global_dofs]
171 fill!(Re, 0.0)
172 fill!(Je, 0.0)
173 @inbounds for q_point in 1:q_points # The inbounds-macro removes boundchecking
174 fill!( $\chi_e$ , 0.0)
175 fill!( $\partial\chi_{e_x}$ , 0.0)
176 fill!( $\partial\chi_{e_y}$ , 0.0)
177 @inbounds for i in 1:n_basefuncs
178  $\varphi$  = shape_value(cellvalues, q_point, i)[1]
179  $\partial\varphi_x$  = shape_gradient(cellvalues, q_point, i)[1]
180  $\partial\varphi_y$  = shape_gradient(cellvalues, q_point, i)[2]
181 @inbounds for k in 1:fDim
182  $\chi_e[k]$  += Xe[BlockIndex(i, k)]* $\varphi$ 
183  $\partial\chi_{e_x}[k]$  += Xe[BlockIndex(i, k)]* $\partial\varphi_x$ 
184  $\partial\chi_{e_y}[k]$  += Xe[BlockIndex(i, k)]* $\partial\varphi_y$ 
185 end
186 end
187 r[:] = spatial_coordinate(cellvalues, q_point, cell.coords)
188 autoJac!( $\partial Fe_\chi$ ,  $\chi$ ->F!(Fe_dual,  $\chi$ ,  $\partial\chi_{e_x}$ ,  $\partial\chi_{e_y}$ , r),  $\chi_e$ )
189 autoJac!( $\partial Fe_\partial\chi_x$ ,  $\partial\chi_x$ ->F!(Fe_dual,  $\chi_e$ ,  $\partial\chi_x$ ,  $\partial\chi_{e_y}$ , r),  $\partial\chi_{e_x}$ )
190 autoJac!( $\partial Fe_\partial\chi_y$ ,  $\partial\chi_y$ ->F!(Fe_dual,  $\chi_e$ ,  $\partial\chi_{e_x}$ ,  $\partial\chi_y$ , r),  $\partial\chi_{e_y}$ )
191 Fe[:] = realpart.(Fe_dual)
192 d = getdetJdV(cellvalues, q_point)

```

```

193 @inbounds for i in 1:n_basefuncs
194     φ = shape_value(cellvalues, q_point, i)[1]
195     φ = shape_gradient(cellvalues, q_point, i)
196 @inbounds for j in 1:n_basefuncs
197     φ = shape_value(cellvalues, q_point, j)[1]
198     φ = shape_gradient(cellvalues, q_point, j)
199     Je[Block(i, j)] += d * (∂Fe_∂χ_x*(φ * φ [1]) + ∂Fe_∂χ_y*(φ * φ [2]) + ∂Fe_χ*(φ
200         *φ ) + eyefDim*( φ φ ))
201     Re[Block(i)] += d *(Fe*φ + ∂χe_x* φ [1] + ∂χe_y* φ [2])
202 end
203 end
204 @inbounds for face in 1:nfaces(cell)
205     if onboundary(cell, face)
206         reinit!(facevalues, cell, face)
207         @inbounds for q_point in 1:getnquadpoints(facevalues)
208             fill!(χe, 0.0)
209             @inbounds for i in 1:n_basefuncs
210                 φ = shape_value(facevalues, q_point, i)[1]
211                 @inbounds for k in 1:fDim
212                     χe[k] += Xe[BlockIndex(i, k)]*φ
213                 end
214             end
215             r[:] = spatial_coordinate(cellvalues, q_point, cell.coords)
216             if (cellid(cell), face) ∈ getfaceset(grid, "left")
217                 autoJac!(∂Be_χ, χ->B_l!(Be_dual, χ, r), χe)
218             elseif (cellid(cell), face) ∈ getfaceset(grid, "right")
219                 autoJac!(∂Be_χ, χ->B_r!(Be_dual, χ, r), χe)
220             elseif (cellid(cell), face) ∈ getfaceset(grid, "top")
221                 autoJac!(∂Be_χ, χ->B_t!(Be_dual, χ, r), χe)
222             elseif (cellid(cell), face) ∈ getfaceset(grid, "bottom")
223                 autoJac!(∂Be_χ, χ->B_b!(Be_dual, χ, r), χe)
224             end
225             Be[:] = realpart.(Be_dual)
226             d = getdetJdV(facevalues, q_point)
227             for i in 1:n_basefuncs
228                 φ = shape_value(facevalues, q_point, i)[1]
229                 for j in 1:n_basefuncs
230                     φ = shape_value(facevalues, q_point, j)[1]
231                     Je[Block(i, j)] -= ∂Be_χ*(φ *φ *d )
232                 end
233             Re[Block(i)] -= Be*(φ *d )
234         end
235     end
236 end
237 end
238 assemble!(assembler, global_dofs, Re, Je)
239 end
240 return J, R
241 end
242
243 # Setting up 3D FEM
244 function create3DGrid(n::Int, width::Float64=1.0, height::Float64=1.0)
245     return generate_grid(Hexahedron, (n, Int(floor(n*width)), Int(floor(n*height))), Vec{3}([-0.5, -
246         width/2.0, -height/2.0]), Vec{3}([0.5, width/2.0, height/2.0]))
247 end
248 function create3DValues()
249     # quadrature rules
250     quad_rule = QuadratureRule{3, RefCube}(4)
251     face_quad_rule = QuadratureRule{2, RefCube}(4)
252     # geometric interpolation
253     interpolation_geom = Lagrange{3, RefCube, 1}()
254     cellvalues = CellScalarValues(quad_rule, interpolation_geom)
255     facevalues = FaceScalarValues(face_quad_rule, interpolation_geom)
256
257     return cellvalues, facevalues
258 end
259 ## Calculating jacobian and residuals at once using automatic differentiation
260 function JacRes3D!(J::SparseMatrixCSC{T, Int64}, R::AbstractArray{T}, X::AbstractArray{T},
261     cellvalues::CellScalarValues, facevalues::FaceScalarValues, grid::Grid, dh::DofHandler, F!, B_l
262     !, B_r!, B_t!, B_b!, B_f!, B_ba!) where {T}
263     fill!(J.nzval, 0.0) # Reset Jacobian

```

```

262 fill!(R, 0.0) # Reset residuals
263 q_points = getnquadpoints(cellvalues)
264 n_basefuncs = getnbasefunctions(cellvalues)
265 n = ndofs_per_cell(dh)
266 fDim = dh.field_dims[1]
267
268 eyeDim = Matrix{T}(I, fDim, fDim) # fDimxfDim identity matrix
269 # Initialize element vectors
270  $\chi_e$  = zeros(T, fDim)
271  $\partial\chi_{e_x}$  = zeros(T, fDim)
272  $\partial\chi_{e_y}$  = zeros(T, fDim)
273  $\partial\chi_{e_z}$  = zeros(T, fDim)
274 Fe_dual = zeros(Dual{T}, fDim)
275 Be_dual = zeros(Dual{T}, fDim)
276 Fe = zeros(T, fDim)
277 Be = zeros(T, fDim)
278  $\partial Fe_\chi$  = zeros(T, fDim, fDim)
279  $\partial Fe_{\partial\chi_x}$  = zeros(T, fDim, fDim)
280  $\partial Fe_{\partial\chi_y}$  = zeros(T, fDim, fDim)
281  $\partial Fe_{\partial\chi_z}$  = zeros(T, fDim, fDim)
282  $\partial Be_\chi$  = zeros(T, fDim, fDim)
283
284 # Spatial coordinates
285 r = zeros(Float64, 3)
286
287 Re = PseudoBlockArray(zeros(T, fDim*n_basefuncs), fDim*ones(Int, n_basefuncs))
288 Je = PseudoBlockArray(zeros(T, fDim*n_basefuncs), fDim*ones(Int, n_basefuncs),
    fDim*ones(Int, n_basefuncs))
289 Xe = PseudoBlockArray(zeros(T, fDim*n_basefuncs), fDim*ones(Int, n_basefuncs))
290
291 assembler = start_assemble(J, R)
292
293 @inbounds for cell in CellIterator(dh)
294     reinit!(cellvalues, cell)
295     global_dofs = celldofs(cell)
296     Xe[:] = X[global_dofs]
297     fill!(Re, 0.0)
298     fill!(Je, 0.0)
299     @inbounds for q_point in 1:q_points # The inbounds-macro removes boundchecking
300         fill!( $\chi_e$ , 0.0)
301         fill!( $\partial\chi_{e_x}$ , 0.0)
302         fill!( $\partial\chi_{e_y}$ , 0.0)
303         fill!( $\partial\chi_{e_z}$ , 0.0)
304         @inbounds for i in 1:n_basefuncs
305              $\varphi$  = shape_value(cellvalues, q_point, i)[1]
306              $\varphi$  = shape_gradient(cellvalues, q_point, i)
307             @inbounds for k in 1:fDim
308                  $\chi_e[k] += Xe[\text{BlockIndex}(i, k)]*\varphi$ 
309                  $\partial\chi_{e_x}[k] += Xe[\text{BlockIndex}(i, k)]*\varphi$  [1]
310                  $\partial\chi_{e_y}[k] += Xe[\text{BlockIndex}(i, k)]*\varphi$  [2]
311                  $\partial\chi_{e_z}[k] += Xe[\text{BlockIndex}(i, k)]*\varphi$  [3]
312             end
313         end
314         r[:] = spatial_coordinate(cellvalues, q_point, cell.coords)
315         autoJac!( $\partial Fe_\chi$ ,  $\chi \rightarrow F!(Fe\_dual, \chi, \partial\chi_{e_x}, \partial\chi_{e_y}, \partial\chi_{e_z}, r)$ ,  $\chi_e$ )
316         autoJac!( $\partial Fe_{\partial\chi_x}$ ,  $\partial\chi_x \rightarrow F!(Fe\_dual, \chi_e, \partial\chi_x, \partial\chi_{e_y}, \partial\chi_{e_z}, r)$ ,  $\partial\chi_{e_x}$ )
317         autoJac!( $\partial Fe_{\partial\chi_y}$ ,  $\partial\chi_y \rightarrow F!(Fe\_dual, \chi_e, \partial\chi_{e_x}, \partial\chi_y, \partial\chi_{e_z}, r)$ ,  $\partial\chi_{e_y}$ )
318         autoJac!( $\partial Fe_{\partial\chi_z}$ ,  $\partial\chi_z \rightarrow F!(Fe\_dual, \chi_e, \partial\chi_{e_x}, \partial\chi_{e_y}, \partial\chi_z, r)$ ,  $\partial\chi_{e_z}$ )
319         Fe[:] = realpart.(Fe_dual)
320         d = getdetJdV(cellvalues, q_point)
321         @inbounds for i in 1:n_basefuncs
322              $\varphi$  = shape_value(cellvalues, q_point, i)[1]
323              $\varphi$  = shape_gradient(cellvalues, q_point, i)
324             @inbounds for j in 1:n_basefuncs
325                  $\varphi$  = shape_value(cellvalues, q_point, j)[1]
326                  $\varphi$  = shape_gradient(cellvalues, q_point, j)
327                 Je[Block(i, j)] += d * ( $\partial Fe_{\partial\chi_x}*(\varphi * \varphi$  [1]) +  $\partial Fe_{\partial\chi_y}*(\varphi * \varphi$  [2]) +  $\partial Fe_{\partial\chi_z}$ 
                    * ( $\varphi * \varphi$  [3]) +  $\partial Fe_\chi*(\varphi * \varphi)$  ) + eyeDim*( $\varphi$   $\varphi$  )
328             end
329             Re[Block(i)] += d * (Fe* $\varphi$  +  $\partial\chi_{e_x}*\varphi$  [1] +  $\partial\chi_{e_y}*\varphi$  [2] +  $\partial\chi_{e_z}*\varphi$  [3])
330         end
331     end
332 @inbounds for face in 1:nfaces(cell)

```

```

333     if onboundary(cell, face)
334         reinit!(facevalues, cell, face)
335         @inbounds for q_point in 1:getnquadpoints(facevalues)
336             fill!( $\chi^e$ , 0.0)
337             @inbounds for i in 1:n_basefuncs
338                  $\varphi$  = shape_value(facevalues, q_point, i)[1]
339                 @inbounds for k in 1:fDim
340                      $\chi^e[k] += X_e[\text{BlockIndex}(i, k)] * \varphi$ 
341                 end
342             end
343             r[:] = spatial_coordinate(cellvalues, q_point, cell.coords)
344             if (cellid(cell), face)  $\in$  getfaceset(grid, "left")
345                 autoJac!( $\partial \text{Be}_\chi$ ,  $\chi \rightarrow B_{l!}(\text{Be\_dual}, \chi, r)$ ,  $\chi^e$ )
346             elseif (cellid(cell), face)  $\in$  getfaceset(grid, "right")
347                 autoJac!( $\partial \text{Be}_\chi$ ,  $\chi \rightarrow B_{r!}(\text{Be\_dual}, \chi, r)$ ,  $\chi^e$ )
348             elseif (cellid(cell), face)  $\in$  getfaceset(grid, "top")
349                 autoJac!( $\partial \text{Be}_\chi$ ,  $\chi \rightarrow B_{t!}(\text{Be\_dual}, \chi, r)$ ,  $\chi^e$ )
350             elseif (cellid(cell), face)  $\in$  getfaceset(grid, "bottom")
351                 autoJac!( $\partial \text{Be}_\chi$ ,  $\chi \rightarrow B_{b!}(\text{Be\_dual}, \chi, r)$ ,  $\chi^e$ )
352             elseif (cellid(cell), face)  $\in$  getfaceset(grid, "front")
353                 autoJac!( $\partial \text{Be}_\chi$ ,  $\chi \rightarrow B_{f!}(\text{Be\_dual}, \chi, r)$ ,  $\chi^e$ )
354             elseif (cellid(cell), face)  $\in$  getfaceset(grid, "back")
355                 autoJac!( $\partial \text{Be}_\chi$ ,  $\chi \rightarrow B_{ba!}(\text{Be\_dual}, \chi, r)$ ,  $\chi^e$ )
356             end
357             Be[:] = realpart.(Be_dual)
358             d = getdetJdV(facevalues, q_point)
359             for i in 1:n_basefuncs
360                  $\varphi$  = shape_value(facevalues, q_point, i)[1]
361                 for j in 1:n_basefuncs
362                      $\varphi$  = shape_value(facevalues, q_point, j)[1]
363                     Je[Block(i, j)] -=  $\partial \text{Be}_\chi * (\varphi * \varphi * d)$ 
364                 end
365                 Re[Block(i)] -= Be*( $\varphi * d$ )
366             end
367         end
368     end
369     assemble!(assembler, global_dofs, Re, Je)
370 end
371 return J, R
372 end
373 end
374
375 # Solving 2DFEM
376 function solve2D(initGuess, N::Int, w::Float64, fDim::Int, F!, B_l!, B_r!, B_t!, B_b!, showProgress::Bool=true)
377
378     grid = create2DGrid(N, w)
379     cv, fv = create2DValues()
380     dh = createDofHandler(grid, fDim)
381
382     X = initGuess(ndofs(dh))
383     R = zeros(eltype(X), ndofs(dh))
384     J = convert(SparseMatrixCSC{eltype(X), Int64}, create_sparsity_pattern(dh))
385
386     JacRes!(J, R, X) = JacRes2D!(J, R, X, cv, fv, grid, dh, F!, B_l!, B_r!, B_t!, B_b!)
387
388     return NewtonRhapson(X, J, R, JacRes!, showProgress)
389 end
390 # Solving 3DFEM
391 function solve3D(initGuess, N::Int, w::Float64, h::Float64, fDim::Int, F!, B_l!, B_r!, B_t!, B_b!, B_f!, B_ba!, showProgress::Bool=true)
392
393     grid = create3DGrid(N, w, h)
394     cv, fv = create3DValues()
395     dh = createDofHandler(grid, fDim)
396
397     X = initGuess(ndofs(dh))
398     R = zeros(eltype(X), ndofs(dh))
399     J = convert(SparseMatrixCSC{eltype(X), Int64}, create_sparsity_pattern(dh))
400
401     JacRes!(J, R, X) = JacRes3D!(J, R, X, cv, fv, grid, dh, F!, B_l!, B_r!, B_t!, B_b!, B_f!, B_ba!)
402
403     return NewtonRhapson(X, J, R, JacRes!, showProgress)

```

```

404 end
405 function solve3DTrapezoid(initGuess, N::Int, wFront::Float64, wBack::Float64, h::Float64, fDim::Int,
    F!, B_l!, B_r!, B_t!, B_b!, B_f!, B_ba!, showProgress::Bool=true)
406
407     grid = create3DTrapezoidGrid(N, wFront, wBack, h)
408     cv, fv = create3DValues()
409     dh = createDofHandler(grid, fDim)
410
411     X = initGuess(ndofs(dh))
412     R = zeros(eltype(X), ndofs(dh))
413     J = convert(SparseMatrixCSC{eltype(X), Int64}, create_sparsity_pattern(dh))
414
415     JacRes!(J, R, X) = JacRes3D!(J, R, X, cv, fv, grid, dh, F!, B_l!, B_r!, B_t!, B_b!, B_f!, B_ba!)
416
417     return NewtonRhapson(X, J, R, JacRes!, showProgress)
418 end
419
420 # General FEM tools
421 function createDofHandler(grid, fDim::Int=1)
422     dh = DofHandler(grid)
423     push!(dh, :χ, fDim)
424     close!(dh)
425     return dh
426 end
427 function export2DVTK(filename::AbstractString, vals::Vector, u::Symbol, fieldDim::Int, N::Int, width
    ::Float64 = 1.0)
428     grid = create2DGrid(N, width)
429     dofh = DofHandler(grid)
430     push!(dofh, u, fieldDim)
431     close!(dofh)
432     vtk_grid(filename, dofh) do vtk
433         vtk_point_data(vtk, dofh, vals)
434     end
435 end
436
437 function export3DVTK(filename::AbstractString, vals::Vector, u::Symbol, fieldDim::Int, N::Int, width
    ::Float64 = 1.0, height::Float64=1.0)
438     grid = create3DGrid(N, width, height)
439     dofh = DofHandler(grid)
440     push!(dofh, u, fieldDim)
441     close!(dofh)
442     vtk_grid(filename, dofh) do vtk
443         vtk_point_data(vtk, dofh, vals)
444     end
445 end
446
447 # Tools for finding observables
448 function DOS_nm(X)
449     # Density of states for normal metal
450     n = div(length(X), 2)
451     dos = zeros(Float64, n)
452     for i ∈ 1:n
453         dos[i] = real((1 - X[2i - 1]*X[2i])/(1 + X[2i - 1]*X[2i]))
454     end
455     return dos
456 end
457 function DOS_hm(X)
458     # Density of states for half metal
459     n = div(length(X), 2)
460     dos = zeros(Float64, n)
461     for i ∈ 1:n
462         dos[i] = real((1 + X[2i - 1]*X[2i])/(1 - X[2i - 1]*X[2i]))
463     end
464     return dos
465 end
466 function currentMat_nm!(j, χ, ∂χ_x, ∂χ_y, vecPot, ε, β) # vecPot is an array, need only integrate
    positive energies
467     j[:] = 8.0*tanh(ε*β/2.0).*[
468         real((χ[1]*∂χ_x[2] - χ[2]*∂χ_x[1])/(1.0 + χ[1]*χ[2])^2) - 2.0*vecPot[1]
            *imag(χ[1]*χ[2]/(1.0 + χ[1]*χ[2])^2),
469         real((χ[1]*∂χ_y[2] - χ[2]*∂χ_y[1])/(1.0 + χ[1]*χ[2])^2) - 2.0*vecPot[2]
            *imag(χ[1]*χ[2]/(1.0 + χ[1]*χ[2])^2)
470     ]

```

```

471 end
472 function currentMat_hm!(j,  $\chi$ ,  $\partial\chi_x$ ,  $\partial\chi_y$ , vecPot,  $\varepsilon$ ,  $\beta$ ) # vecPot is an array
473     j[:] = -4.0*tanh( $\varepsilon*\beta/2.0$ ).*[
474         real(( $\chi[1]*\partial\chi_x[2] - \chi[2]*\partial\chi_x[1]$ )/(1.0 -  $\chi[1]*\chi[2]$ )^2) - 2.0*vecPot[1]
475         *imag( $\chi[1]*\chi[2]$ /(1.0 -  $\chi[1]*\chi[2]$ )^2),
476         real(( $\chi[1]*\partial\chi_y[2] - \chi[2]*\partial\chi_y[1]$ )/(1.0 -  $\chi[1]*\chi[2]$ )^2) - 2.0*vecPot[2]
477         *imag( $\chi[1]*\chi[2]$ /(1.0 -  $\chi[1]*\chi[2]$ )^2)
478     ]
479 end
480 function Current2D!(J::AbstractArray{Float64}, X::AbstractArray{T}, N, w, vecPot,  $\varepsilon$ ,  $\beta$ , currentMat!)
481     where {T}
482
483     fill!(J, 0.0)
484     grid = create2DGrid(N, w)
485     cellvalues, = create2DValues()
486     ip = Lagrange{2, RefCube, 2}()
487     dh = createDofHandler(grid, 2)
488
489     q_points = getnquadpoints(cellvalues)
490     n_basefuncs = getnbasefunctions(cellvalues)
491     n = ndofs_per_cell(dh)
492
493     # Initialize element vectors
494      $\chi_e$  = zeros(T, 2)
495      $\partial\chi_{e_x}$  = zeros(T, 2)
496      $\partial\chi_{e_y}$  = zeros(T, 2)
497     # Spatial coordinates
498     r = zeros(Float64, 2)
499     # Holder for current
500     je = zeros(Float64, 2)
501
502     Je = PseudoBlockArray(zeros(T, 2*n_basefuncs), 2*ones(Int, n_basefuncs))
503     Xe = PseudoBlockArray(zeros(T, 2*n_basefuncs), 2*ones(Int, n_basefuncs))
504
505     ref_coords = JuAFEM.reference_coordinates(ip)
506
507     @inbounds for cell in CellIterator(dh)
508         reinit!(cellvalues, cell)
509         global_dofs = celldofs(cell)
510         Xe[:] = X[global_dofs]
511         fill!(Je, 0.0)
512         @inbounds for (j, point) in enumerate(ref_coords)
513             fill!( $\chi_e$ , 0.0)
514             fill!( $\partial\chi_{e_x}$ , 0.0)
515             fill!( $\partial\chi_{e_y}$ , 0.0)
516             @inbounds for i in 1:n_basefuncs
517                  $\varphi$  = JuAFEM.value(ip, i, point)
518                  $\partial\varphi_x$ ,  $\partial\varphi_y$  = gradient( $\xi \rightarrow$  JuAFEM.value(ip, i,  $\xi$ ), point)
519                 @inbounds for k in 1:2
520                      $\chi_e[k] += Xe[\text{BlockIndex}(i, k)]*\varphi$ 
521                      $\partial\chi_{e_x}[k] += Xe[\text{BlockIndex}(i, k)]*\partial\varphi_x *N$ 
522                      $\partial\chi_{e_y}[k] += Xe[\text{BlockIndex}(i, k)]*\partial\varphi_y *N$ 
523                 end
524             end
525             r[:] = cell.coords[j]
526             currentMat!(je,  $\chi_e$ ,  $\partial\chi_{e_x}$ ,  $\partial\chi_{e_y}$ , vecPot(r),  $\varepsilon$ ,  $\beta$ )
527             if j  $\in$  (1, 2, 3, 4)
528                 Je[Block(j)] += je./4.0
529             elseif j  $\in$  (5, 6, 7, 8)
530                 Je[Block(j)] += je./2.0
531             elseif j == 9
532                 Je[Block(j)] += je
533             end
534         end
535         J[global_dofs] += Je
536     end
537     return J
538 end
539 function Current2D_nm!(J::AbstractArray{Float64}, X::AbstractArray{T}, N, w, vecPot,  $\varepsilon$ ,  $\beta$ ) where {T}
540     return Current2D!(J, X, N, w, vecPot,  $\varepsilon$ ,  $\beta$ , currentMat_nm!)
541 end
542 function Current2D_nm(X::AbstractArray{T}, N, w, vecPot,  $\varepsilon$ ,  $\beta$ ) where {T}
543     J = zeros(Float64, 2*div(length(X), 2))

```



```

541 fill!(J, 0.0)
542 return Current2D_nm!(J, X, N, w, vecPot, ε, β)
543 end
544 function Current2D_hm!(J::AbstractArray{Float64}, X::AbstractArray{T}, N, w, vecPot, ε, β) where {T}
545 return Current2D!(J, X, N, w, vecPot, ε, β, currentMat_hm!)
546 end
547 function Current2D_hm(X::AbstractArray{T}, N, w, vecPot, ε, β) where {T}
548 J = zeros(Float64, 2*div(length(X), 2))
549 fill!(J, 0.0)
550 return Current2D_hm!(J, X, N, w, vecPot, ε, β)
551 end
552
553
554 function currentMat3D_nm!(j, χ, ∂χ_x, ∂χ_y, ∂χ_z, vecPot, ε, β) # vecPot is an array, need only
    integrate positive energies
555 j[:] = 8.0*tanh(ε*β/2.0).*[
556     real((χ[1]*∂χ_x[2] - χ[2]*∂χ_x[1])/(1.0 + χ[1]*χ[2])^2) - 2.0*vecPot[1]
557     *imag(χ[1]*χ[2]/(1.0 + χ[1]*χ[2])^2),
558     real((χ[1]*∂χ_y[2] - χ[2]*∂χ_y[1])/(1.0 + χ[1]*χ[2])^2) - 2.0*vecPot[2]
559     *imag(χ[1]*χ[2]/(1.0 + χ[1]*χ[2])^2),
560     real((χ[1]*∂χ_z[2] - χ[2]*∂χ_z[1])/(1.0 + χ[1]*χ[2])^2) - 2.0*vecPot[3]
561     *imag(χ[1]*χ[2]/(1.0 + χ[1]*χ[2])^2)
562 ]
563 end
564 function Current3D!(J::AbstractArray{Float64}, X::AbstractArray{T}, N, w, h, vecPot, ε, β,
    currentMat!) where {T}
565
566 fill!(J, 0.0)
567 grid = create3DGrid(N, w, h)
568 cellvalues, = create3DValues()
569 ip = Lagrange{3, RefCube, 1}()
570 dh = createDofHandler(grid, 2)
571
572 q_points = getnquadpoints(cellvalues)
573 n_basefuncs = getnbasefunctions(cellvalues)
574 n = ndofs_per_cell(dh)
575
576 # Initialize element vectors
577 χe = zeros(T, 2)
578 ∂χe_x = zeros(T, 2)
579 ∂χe_y = zeros(T, 2)
580 ∂χe_z = zeros(T, 2)
581 # Spatial coordinates
582 r = zeros(Float64, 3)
583 # Holder for current
584 je = zeros(Float64, 3)
585
586 Je = PseudoBlockArray(zeros(T, 3*n_basefuncs), 3*ones(Int, n_basefuncs))
587 Xe = PseudoBlockArray(zeros(T, 2*n_basefuncs), 2*ones(Int, n_basefuncs))
588
589 ref_coords = JuAFEM.reference_coordinates(ip)
590
591 @inbounds for cell in CellIterator(dh)
592     reinit!(cellvalues, cell)
593     global_dofs = celldofs(cell)
594     Xe[:] = X[global_dofs]
595     fill!(Je, 0.0)
596     @inbounds for (j, point) in enumerate(ref_coords)
597         fill!(χe, 0.0)
598         fill!(∂χe_x, 0.0)
599         fill!(∂χe_y, 0.0)
600         fill!(∂χe_z, 0.0)
601         @inbounds for i in 1:n_basefuncs
602             φ = JuAFEM.value(ip, i, point)
603             ∂φ_x, ∂φ_y, ∂φ_z = gradient(ξ -> JuAFEM.value(ip, i, ξ), point)
604             @inbounds for k in 1:2
605                 χe[k] += Xe[BlockIndex(i, k)]*φ
606                 ∂χe_x[k] += Xe[BlockIndex(i, k)]*∂φ_x *N
607                 ∂χe_y[k] += Xe[BlockIndex(i, k)]*∂φ_y *N
608                 ∂χe_z[k] += Xe[BlockIndex(i, k)]*∂φ_z *N
609             end
610         end
611     end
612     r[:] = cell.coords[j]

```

```

609     currentMat!(je,  $\chi^e$ ,  $\partial\chi_{e-x}$ ,  $\partial\chi_{e-y}$ ,  $\partial\chi_{e-z}$ , vecPot(r),  $\epsilon$ ,  $\beta$ )
610     Je[Block(j)] += je ./ 4.0
611     end
612     blocks = [div(global_dofs[2i], 2) for i ∈ 1:div(length(global_dofs), 2)]
613     j_dofs = zeros(Int64, 3*length(blocks))
614     for (i, b) ∈ enumerate(blocks)
615         j_dofs[3i-2] = 3b-2
616         j_dofs[3i-1] = 3b-1
617         j_dofs[3i] = 3b
618     end
619     J[j_dofs] += Je
620     end
621     return J
622 end
623 function Current3D_nm!(J::AbstractArray{Float64}, X::AbstractArray{T}, N, w, h, vecPot,  $\epsilon$ ,  $\beta$ ) where
    {T}
624     return Current3D!(J, X, N, w, h, vecPot,  $\epsilon$ ,  $\beta$ , currentMat3D_nm!)
625 end
626 function Current3D_nm(X::AbstractArray{T}, N, w, h, vecPot,  $\epsilon$ ,  $\beta$ ) where {T}
627     J = zeros(Float64, 3*div(length(X), 2))
628     fill!(J, 0.0)
629     return Current3D_nm!(J, X, N, w, h, vecPot,  $\epsilon$ ,  $\beta$ )
630 end
631
632
633 function PairIntegrand_nm(X,  $\epsilon$ ,  $\beta$ )
634     n = div(length(X), 2)
635     integrand = zeros(Complex{Float64}, n)
636     for i ∈ 1:n
637         integrand[i] = (X[2i-1]/(1 + X[2i-1]*X[2i]) - conj(X[2i]/(1 + X[2i-1]*X[2i]))) * tanh( $\beta*\epsilon/2.0$ )
638     end
639     return integrand
640 end
641 function PairIntegrand_hm(X,  $\epsilon$ ,  $\beta$ )
642     n = div(length(X), 2)
643     integrand = zeros(Complex{Float64}, n)
644     for i ∈ 1:n
645         integrand[i] = -1.0im* $\epsilon*(X[2i-1]/(1 - X[2i-1]*X[2i]) + conj(X[2i]/(1 - X[2i-1]*X[2i]))) * tanh( $\beta*\epsilon/2.0$ )
646         #= integrand[i] = (X[2i-1]/(1 - X[2i-1]*X[2i]) - conj(X[2i]/(1 - X[2i-1]*X[2i]))) * tanh( $\beta*\epsilon/2.0$ )
647         =#
648     end
649     return integrand
650 end
651 function PairIntegrand_t_hm(X,  $\epsilon$ , t,  $\beta$ )
652     n = div(length(X), 2)
653     integrand = zeros(Complex{Float64}, n)
654     for i ∈ 1:n
655         integrand[i] = -1.0im* $\sin(\epsilon*t)*(X[2i-1]/(1 - X[2i-1]*X[2i]) + conj(X[2i]/(1 - X[2i-1]*X[2i]))) * tanh( $\beta*\epsilon/2.0$ )
656         #= integrand[i] = (X[2i-1]/(1 - X[2i-1]*X[2i]) - conj(X[2i]/(1 - X[2i-1]*X[2i]))) * tanh( $\beta*\epsilon/2.0$ )
657         =#
658     end
659     return integrand
660 end
661 function DivideAbsPhase(X)
662     n = length(X)
663     res = zeros(Float64, 2n)
664     for i ∈ 1:n
665         res[2i-1], res[2i] = abs(X[i]), angle(X[i])
666     end
667     return res
668 end
669 end$$ 
```

**Listing C.2:** An implementation of the code from listing C.1 to solve the Usadel equation in the half-metallic system from chapter 3.

```

1  include("../projectTools.jl")
2  using ProjectTools
3
4  b(E, Δ) = abs(real(E)) < abs(Δ) ? Δ/(E + 1im*√(Δ^2 - E^2 + 0im)) : sign(real(E))*Δ/(abs(E) + √(E^2 +
    0im - Δ^2))
5
6  function vecPot_x(r, n, w)
7      return -n*π*r[2]/w
8  end
9
10 function F!(F, χ, ∂χ_x, ∂χ_y, r, ε, n, w)
11     A = vecPot_x(r, n, w)
12     F[:] = [
13         2*χ[2]*(∂χ_x[1]^2 + ∂χ_y[1]^2)/(1.0 - χ[1]*χ[2]) + 4*A*(1 + χ[1]*χ[2])/(1 - χ[1]*χ[2])*(A
            *χ[1] + 1.0im*∂χ_x[1]) - 2.0im*ε*χ[1],
14         2*χ[1]*(∂χ_x[2]^2 + ∂χ_y[2]^2)/(1.0 - χ[1]*χ[2]) + 4*A*(1 + χ[1]*χ[2])/(1 - χ[1]*χ[2])*(A
            *χ[2] - 1.0im*∂χ_x[2]) - 2.0im*ε*χ[2]
15     ]
16     return F
17 end
18
19 function B!(B, χ, r, ζ, G_χ, G_φ, ε, Δ, φ, n, w, n_sc, mr)
20     # All Gs are measured relative to G_0
21     A = vecPot_x(r, n, w)
22     b_0 = b(ε, Δ)*exp(1.0im*φ)
23     b_tilde_0 = conj(b(-ε, Δ)*exp(1.0im*φ))
24     N = 1.0/(b_tilde_0*b_0 + 1.0)
25     M = b_tilde_0*b_0 - 1.0
26     B[:] = [
27         (4*N*M*χ[1] + 2.0im*G_χ*M*N*mr*(b_0 - χ[1]^2*b_tilde_0) - 2*(G_χ/G_φ)*M*M*N*χ[1]*(χ[1]*χ[2] +
            3.0))/ζ + n * 2.0im*A*χ[1],
28         (4*N*M*χ[2] - 2.0im*G_χ*M*N*mr*(b_0 - χ[2]^2*b_tilde_0) - 2*(G_χ/G_φ)*M*M*N*χ[2]*(χ[1]*χ[2] +
            3.0))/ζ - n * 2.0im*A*χ[2]
29     ]
30     return B
31 end
32 function B_vacuum!(B, χ, r, n::T, w::T, n_sc::T) where {T<:Float64}
33     B[:] = [
34         - n_sc * (2.0im*n*π*r[2]/w)*χ[1],
35         n_sc * (2.0im*n*π*r[2]/w)*χ[2]
36     ]
37     return B
38 end
39 function Neumann!(B, χ, r)
40     B[:] = 0.0 .* B
41 end
42
43 function initGuess(n)
44     return [0.0+0.0im for i ∈ 1:n]
45 end
46
47 function SingleSolve(N::Int, ε::Float64, l::Float64, width::Float64, φ::Float64, ζ::Float64, n::
    Float64, G_φ::Float64=10.0, showProgress::Bool = true, init=initGuess, mr=1.0)
48     # φ also includes the angle of the magnetization. That is, exp(iφ) = exp(iφ_sc)*(m_1 - im_2)
49     Δ = l*1
50     δ = Δ/1000.0
51     w = width/l # width in multiples of length
52     G_χ = 0.01
53     G_φ = 10.0
54     l_sc = 10.0 # length of SC compared to HM
55
56
57     Fe!(F, χ, ∂χ_x, ∂χ_y, r) = F!(F, χ, ∂χ_x, ∂χ_y, r, ε + 1.0im*δ, n, w)
58     Be_l!(B, χ, r) = B!(B, χ, r, ζ, G_χ, G_φ, ε + 1.0im*δ, Δ, 0.0, n, w, -1.0, 1.0)
59     Be_r!(B, χ, r) = B!(B, χ, r, ζ, G_χ, G_φ, ε + 1.0im*δ, Δ, φ, n, w, 1.0, mr)
60     Be_t!(B, χ, r) = Neumann!(B, χ, r)
61     Be_b!(B, χ, r) = Neumann!(B, χ, r)
62     X = solve2D(init, N, w, 2, Fe!, Be_l!, Be_r!, Be_t!, Be_b!, showProgress)
63     return X
64 end
65
66 function FindDOS(N::Int, ε::Float64, l::Float64, width::Float64, φ::Float64, ζ::Float64, n::Float64,

```

```

    G_φ::Float64=10.0, showProgress::Bool=true, filename::AbstractString="dos", save::Bool=true,
    init=initGuess, mr=1.0)
67 X = SingleSolve(N, ε, l, width, φ, ζ, n, G_φ, showProgress, init, mr)
68 dos = ProjectTools.DOS_hm(X)
69 if save
70     export2DVTK(string(filename, "_N", N, "_ε", ε, "_l", l, "_w", width, "_φ", φ, "_ζ", ζ, "_n", n),
        dos, :DOS, 1, N, width/l)
71 end
72 return dos, X
73 end
74
75 function FindDOSvE(N::Int, l::Float64, width::Float64, φ::Float64, ζ::Float64, n::Float64, G_φ::
    Float64=10.0, filename::AbstractString="DOSvE", ε_list=[0.4, 2.0, 3.6, 4.4, 6.0], mr=1.0)
76 εs = ε_list
77 println("solving for the following energies:")
78 for ε ∈ εs
79     print(ε, ", ")
80 end
81 println()
82 k = Int((2N+1)*(2*N*width/l + 1))
83 j = length(εs)
84 DOS = [zeros(Float64, k) for i ∈ 1:j]
85 init=initGuess
86 @showprogress 1 "Computing..." for (i, ε) ∈ enumerate(εs)
87     DOS[i], a = FindDOS(N, ε, l, width, φ, ζ, n, G_φ, false, filename, false, init, mr)
88     init = n -> a
89 end
90
91 dos = zeros(Float64, k*j)
92 dosNorm = zeros(Float64, k*j)
93 for i ∈ 1:k
94     dos[1+(i-1)*j:i*j] = [DOS[e][i] for e in 1:j]
95     dosNorm[1+(i-1)*j:i*j] = [abs(1.0 - DOS[e][i]) for e in 1:j]
96 end
97
98 export2DVTK(string(filename, "_N", N, "_l", l, "_w", width/l, "_φ", φ, "_ζ", ζ, "_n", n, "_Gφ", G_
    φ), dos, :dos, j, N, width/l)
99 export2DVTK(string(filename, "DiffFrom1_N", N, "_l", l, "_w", width/l, "_φ", φ, "_ζ", ζ, "_n", n,
    "_Gφ", G_φ), dosNorm, :dos, j, N, width/l)
100
101 end
102
103 function FindPairCorrelation(N::Int, l::Float64, width::Float64, φ::Float64, ζ::Float64, n::Float64,
    G_φ::Float64=10.0, filename::AbstractString="pairCorrelation", mr=1.0, tol=1e-7)
104
105 Δ = l*1
106 β = 1000.0/Δ
107 w = width/l # width in multiples of length
108
109 # Intervals
110 ints = [[0.0001 0.5*Δ], [0.5*Δ, 0.99*Δ], [1.01*Δ, 2.0*Δ], [2.0*Δ, 10.0*Δ]]
111
112 println("Finding initial guesses")
113 guessLocs = [(x[1] + x[2])/2.0 for x in ints]
114 guessProcs = [@spawn SingleSolve(N, ε, l, width, φ, ζ, n, G_φ, false, initGuess, mr) for ε in
    guessLocs]
115 guesses = [fetch(guessProc) for guessProc in guessProcs]
116
117 funcs = [ε -> ProjectTools.PairIntegrand_hm(SingleSolve(N, ε, l, width, φ, ζ, n, G_φ, false, k ->
    guess, mr), ε, β) for guess in guesses]
118
119 println("Starting integration")
120 = @distributed (+) for (f, i) ∈ collect(zip(funcs, ints))
121     ProjectTools.Romberg(f, i[1], i[2])
122 end
123
124 export2DVTK(string(filename, "_N", N, "_l", l, "_w", w, "_φ", φ, "_ζ", ζ, "_n", n, "_Gφ", G_φ),
    ProjectTools.DivideAbsPhase( , : , 2, N, w)
125
126 return
127 end
128
129 function FindCurrent(N::Int, l::Float64, width::Float64, φ::Float64, ζ::Float64, n::Float64, G_φ::

```

```

130   Float64=10.0, filename::AbstractString="current", mr=1.0, tol=1e-7)
131    $\Delta$  = 1*1
132    $\beta$  = 1000.0/ $\Delta$ 
133   w = width/l # width in multiples of length
134
135   # Intervals
136   ints = [[0.0001 0.5* $\Delta$ ], [0.5* $\Delta$ , 0.99* $\Delta$ ], [1.01* $\Delta$ , 2.0* $\Delta$ ], [2.0* $\Delta$ , 10.0* $\Delta$ ]]
137
138   println("Finding initial guesses")
139   guessLocs = [(i[1] + i[2])/2.0 for i in ints]
140   guessProcs = [@spawn SingleSolve(N,  $\epsilon$ , 1, width,  $\varphi$ ,  $\zeta$ , n, G_ $\varphi$ , false, initGuess, mr) for  $\epsilon$  in
141     guessLocs]
142   guesses = [fetch(guessProc) for guessProc in guessProcs]
143
144   vecPot(r) = [vecPot_x(r, n, width/l), 0.0]
145
146   funcs = [ $\epsilon$  -> ProjectTools.Current2D_hm(SingleSolve(N,  $\epsilon$ , 1, width,  $\varphi$ ,  $\zeta$ , n, G_ $\varphi$ , false, x ->
147     guess, mr), N, width/l, vecPot,  $\epsilon$ ,  $\beta$ ) for guess in guesses]
148
149   println("Starting integration")
150   j = @distributed (+) for (f, i) in collect(zip(funcs, ints))
151     ProjectTools.Romberg(f, i[1], i[2], tol)
152   end
153
154   export2DVTK(string(filename, "_N", N, "_l", l, "_w", width, "_ $\varphi$ ",  $\varphi$ , "_ $\zeta$ ",  $\zeta$ , "_n", n, "_G $\varphi$ ", G_ $\varphi$ )
155     , j, :j, 2, N, w)
156
157   # Find both current and paircorrelation
158   function FindCurrentAndPair(N::Int, l::Float64, width::Float64,  $\varphi$ ::Float64,  $\zeta$ ::Float64, n::Float64,
159     G_ $\varphi$ ::Float64=10.0, mr = 1.0, tol=1e-7)
160      $\Delta$  = 1*1
161      $\beta$  = 1000.0/ $\Delta$ 
162     w = width/l # width in multiples of length
163
164     # Intervals
165     ints = [[0.0001 0.5* $\Delta$ ], [0.5* $\Delta$ , 0.99* $\Delta$ ], [1.01* $\Delta$ , 2.0* $\Delta$ ], [2.0* $\Delta$ , 20.0* $\Delta$ ], [20.0* $\Delta$ , 100.0* $\Delta$ ]]
166
167     println("Finding initial guesses")
168     guessLocs = [(x[1] + x[2])/2.0 for x in ints]
169     guessProcs = [@spawn SingleSolve(N,  $\epsilon$ , 1, width,  $\varphi$ ,  $\zeta$ , n, G_ $\varphi$ , false, initGuess, mr) for  $\epsilon$  in
170       guessLocs]
171     guesses = [fetch(guessProc) for guessProc in guessProcs]
172
173     vecPot(r) = [vecPot_x(r, n, width/l), 0.0]
174
175     function func_template( $\epsilon$ , init)
176       a = SingleSolve(N,  $\epsilon$ , 1, width,  $\varphi$ ,  $\zeta$ , n, G_ $\varphi$ , false, k -> init, mr)
177       return [ProjectTools.PairIntegrand_hm(a,  $\epsilon$ ,  $\beta$ ),
178         ProjectTools.Current2D_hm(a, N, width/l, vecPot,  $\epsilon$ ,  $\beta$ )]
179     end
180
181     funcs = [ $\epsilon$  -> func_template( $\epsilon$ , guess) for guess in guesses]
182
183     println("Starting integration")
184     = @distributed (+) for (f, i) in collect(zip(funcs, ints))
185       ProjectTools.Romberg(f, i[1], i[2], tol)
186     end
187
188     export2DVTK(string("PairCorr_HM", "_N", N, "_l", l, "_w", w, "_ $\varphi$ ",  $\varphi$ , "_ $\zeta$ ",  $\zeta$ , "_n", n, "_G $\varphi$ ", G_ $\varphi$ )
189       , ProjectTools.DivideAbsPhase( [1]), : , 2, N, w)
190     export2DVTK(string("Current_HM", "_N", N, "_l", l, "_w", w, "_ $\varphi$ ",  $\varphi$ , "_ $\zeta$ ",  $\zeta$ , "_n", n, "_G $\varphi$ ", G_ $\varphi$ )
191       , [2], :j, 2, N, w)
192
193     return
194   end
195
196   function FindPairAtTs(N::Int, l::Float64, width::Float64,  $\varphi$ ::Float64,  $\zeta$ ::Float64, n::Float64, t_list
197     ::AbstractArray, G_ $\varphi$ ::Float64=10.0, mr = 1.0, tol=1e-7)

```

```

194  $\Delta = 1*1$ 
195  $\beta = 1000.0/\Delta$ 
196  $w = \text{width}/1$  # width in multiples of length
197
198
199 # Intervals
200 ints = [[0.0001 0.5* $\Delta$ ], [0.5* $\Delta$ , 0.999* $\Delta$ ], [1.001* $\Delta$ , 2.0* $\Delta$ ], [2.0* $\Delta$ , 20.0* $\Delta$ ], [20.0* $\Delta$ , 100.0* $\Delta$ ]]
201
202 println("Finding initial guesses")
203 guessLocs = [(x[1] + x[2])/2.0 for x in ints]
204 guessProcs = [@spawn SingleSolve(N,  $\epsilon$ , 1, width,  $\varphi$ ,  $\zeta$ , n, G_ $\varphi$ , false, initGuess, mr) for  $\epsilon$  in
    guessLocs]
205 guesses = [fetch(guessProc) for guessProc in guessProcs]
206
207 vecPot(r) = [vecPot_x(r, n, width/1), 0.0]
208  $\# = J = \text{zeros}(\text{Float64}, \text{div}(\text{length}(\text{guesses}[1]), 2)) = \#$ 
209
210 function func_template( $\epsilon$ , init)
211     a = SingleSolve(N,  $\epsilon$ , 1, width,  $\varphi$ ,  $\zeta$ , n, G_ $\varphi$ , false, k -> init, mr)
212     return [[ProjectTools.PairIntegrand_t_hm(a,  $\epsilon$ , t,  $\beta$ ) for t  $\in$  t_list]...,
213             ProjectTools.PairIntegrand_hm(a,  $\epsilon$ ,  $\beta$ ),
214             ProjectTools.Current2D_hm(a, N, w, vecPot,  $\epsilon$ ,  $\beta$ )]
215 end
216
217 funcs = [ $\epsilon$  -> func_template( $\epsilon$ , guess) for guess in guesses]
218
219 println("Starting integration")
220 = @distributed (+) for (f, i)  $\in$  collect(zip(funcs, ints))
221     ProjectTools.Romberg(f, i[1], i[2], tol)
222 end
223
224 j = length(t_list)
225 k = Int((2N+1)*(2*N*w + 1))
226 pairs = zeros(Float64, 2*j*k)
227 for i  $\in$  1:k
228     pairs[1+(i-1)*2j:2*i*j-j] = [abs.( [t][i] ) for t in 1:j]
229     pairs[1+(i-1)*2j+j:2*i*j] = [angle.( [t][i] ) for t in 1:j]
230 end
231
232 export2DVTK(string("TPairCorr_HM", string(t_list), "_N", N, "_1", 1, "_w", w, "_ $\varphi$ ",  $\varphi$ , "_ $\zeta$ ",  $\zeta$ , "
    "_n", n, "_G $\varphi$ ", G_ $\varphi$ , "_mr", mr), pairs, : , 2*j, N, w)
233 export2DVTK(string("PairCorr_HM", "_N", N, "_1", 1, "_w", w, "_ $\varphi$ ",  $\varphi$ , "_ $\zeta$ ",  $\zeta$ , "_n", n, "_G $\varphi$ ", G_ $\varphi$ ,
    "_mr", mr), ProjectTools.DivideAbsPhase( [end-1]), : , 2, N, w)
234 export2DVTK(string("Current_HM", "_N", N, "_1", 1, "_w", w, "_ $\varphi$ ",  $\varphi$ , "_ $\zeta$ ",  $\zeta$ , "_n", n, "_G $\varphi$ ", G_ $\varphi$ ,
    "_mr", mr), [end], :j, 2, N, w)
235
236 return
237 end
238 function FindPairAtTsGK715(N::Int, l::Float64, width::Float64,  $\varphi$ ::Float64,  $\zeta$ ::Float64, n::Float64,
    t_list::AbstractArray, G_ $\varphi$ ::Float64=10.0, mr = 1.0, tol::Float64=1e-4, maxIter=3)
239
240  $\Delta = 1*1$ 
241  $\beta = 1000.0/\Delta$ 
242  $w = \text{width}/1$  # width in multiples of length
243
244
245 # Intervals
246 ints = [[0.0001 0.25* $\Delta$ ], [0.25* $\Delta$ , 0.5* $\Delta$ ], [0.5* $\Delta$ , 0.75* $\Delta$ ], [0.75* $\Delta$ , 0.999* $\Delta$ ], [1.001* $\Delta$ , 1.25* $\Delta$ ], [
    1.25* $\Delta$ , 1.5* $\Delta$ ], [1.5* $\Delta$ , 1.75* $\Delta$ ], [1.75* $\Delta$ , 2.0* $\Delta$ ], [2.0* $\Delta$ , 5.0* $\Delta$ ], [5.0* $\Delta$ , 20.0* $\Delta$ ], [20.0* $\Delta$ ,
    100.0* $\Delta$ ]]
247
248 println("Finding initial guesses")
249 guessLocs = [(x[1] + x[2])/2.0 for x in ints]
250 guessProcs = [@spawn SingleSolve(N,  $\epsilon$ , 1, width,  $\varphi$ ,  $\zeta$ , n, G_ $\varphi$ , false, initGuess, mr) for  $\epsilon$  in
    guessLocs]
251 guesses = [fetch(guessProc) for guessProc in guessProcs]
252
253 vecPot(r) = [vecPot_x(r, n, width/1), 0.0]
254  $\# = J = \text{zeros}(\text{Float64}, \text{div}(\text{length}(\text{guesses}[1]), 2)) = \#$ 
255
256 function func_template( $\epsilon$ , init)
257     a = SingleSolve(N,  $\epsilon$ , 1, width,  $\varphi$ ,  $\zeta$ , n, G_ $\varphi$ , false, k -> init, mr)
258     return [[ProjectTools.PairIntegrand_t_hm(a,  $\epsilon$ , t,  $\beta$ ) for t  $\in$  t_list]...,

```

```

259     ProjectTools.PairIntegrand_hm(a, ε, β),
260     ProjectTools.Current2D_hm(a, N, w, vecPot, ε, β)]
261 end
262
263 funcs = [ε -> func_template(ε, guess) for guess in guesses]
264
265 println("Starting integration")
266     = @distributed(+) for (f, i) ∈ collect(zip(funcs, ints))
267     ProjectTools.GK715(f, i[1], i[2], tol, maxIter)
268 end
269
270 j = length(t_list)
271 k = Int((2N+1)*(2*N*w + 1))
272 pairs = zeros(Float64, 2*j*k)
273 for i ∈ 1:k
274     pairs[1+(i-1)*2j:2*i*j-j] = [abs.( [t][i]) for t in 1:j]
275     pairs[1+(i-1)*2j+j:2*i*j] = [angle.( [t][i]) for t in 1:j]
276 end
277
278 export2DVTK(string("GKTPairCorr_HM", string(t_list), "_N", N, "_l", l, "_w", w, "_φ", φ, "_ζ", ζ,
279     "_n", n, "_Gφ", G_φ, "_mr", mr), pairs, : , 2*j, N, w)
280 export2DVTK(string("GKPairCorr_HM", "_N", N, "_l", l, "_w", w, "_φ", φ, "_ζ", ζ, "_n", n, "_Gφ",
281     G_φ, "_mr", mr), ProjectTools.DivideAbsPhase( [end-1]), : , 2, N, w)
282 export2DVTK(string("GKCurrent_HM", "_N", N, "_l", l, "_w", w, "_φ", φ, "_ζ", ζ, "_n", n, "_Gφ", G_
283     φ, "_mr", mr), [end], :j, 2, N, w)
284
285 return
286 end

```

**Listing C.3:** An implementation of the code from listing C.1 to solve the Usadel equation in the three-dimensional system from chapter 4.

```

1  include("../projectTools.jl")
2  using .ProjectTools
3
4  b(E, Δ) = abs(real(E)) < abs(Δ) ? Δ/(E + 1im*√(Δ^2 - E^2 + 0im)) : sign(real(E))*Δ/(abs(E) + √(E^2 +
5      0im - Δ^2))
6
7  function vecPot_x(r, n) # n = e I/4π * L, but L=1.0
8      ρ = r[2]^2 + r[3]^2
9      if ρ < 0.000000001
10         ρ = 0.000000001
11     end
12     return -n*π * log((sqrt((0.5 - r[1])^2 + ρ ) + 0.5 - r[1])/(sqrt((0.5 + r[1])^2 + ρ ) - 0.5 - r[
13         1]))
14 end
15
16 function divVecPot_x(r, n) # n = e I/4π * L, but L=1.0
17     ρ = r[2]^2 + r[3]^2
18     if ρ < 0.000000001
19         ρ = 0.000000001
20     end
21     return -n*π * (1.0/sqrt(ρ + (r[1] + 0.5)^2) - 1.0/sqrt(ρ + (r[1] - 0.5)^2))
22 end
23
24 function F!(F, χ, ∂χ_x, ∂χ_y, ∂χ_z, r, ε, δ, n)
25     A = vecPot_x(r, n)
26     dA = divVecPot_x(r, n)
27     F[:] = [
28         2*χ[2]*(∂χ_x[1]^2 + ∂χ_y[1]^2 + ∂χ_z[1]^2)/(1.0 + χ[1]*χ[2]) + 4*A*(1 - χ[1]*χ[2])/(1 + χ
29             [1]*χ[2])*(A*χ[1] + 1.0im*∂χ_x[1]) + 2*(δ - 1.0im*ε)*χ[1] + 2.0im*dA*χ[1],
30         2*χ[1]*(∂χ_x[2]^2 + ∂χ_y[2]^2 + ∂χ_z[2]^2)/(1.0 + χ[1]*χ[2]) + 4*A*(1 - χ[1]*χ[2])/(1 + χ
31             [1]*χ[2])*(A*χ[2] - 1.0im*∂χ_x[2]) + 2*(δ - 1.0im*ε)*χ[2] - 2.0im*dA*χ[2]
32     ]
33     return F
34 end
35
36 function B!(B, χ, r, ζ, ε, δ, Δ, φ, n, n )
37     b_0 = b(ε + 1.0im*δ, Δ)*exp(1.0im*φ)
38     b̃_0 = conj(b(-ε - 1.0im*δ, Δ)*exp(1.0im*φ))
39     A = vecPot_x(r, n)

```

```

35 B[:] = [
36     (1.0/(ζ*(1.0 + b0*b̃0))*(1.0 + χ[1]*b̃0)*(b0 - χ[1]) + n *2.0im*A*χ[1],
37     (1.0/(ζ*(1.0 + b0*b̃0))*(1.0 + χ[2]*b̃0)*(b̃0 - χ[2]) - n *2.0im*A*χ[2]
38 ]
39 return B
40 end
41
42 function Neumann!(B, χ, r)
43     B[:] = 0.0 .* B
44 end
45
46 function initGuess(n)
47     return [0.00001+0.0im for i ∈ 1:n]
48 end
49
50 function SingleSolve(N::Int, ε::Float64, l::Float64, width::Float64, height::Float64, φ::Float64, ζ::
    Float64, n::Float64, showProgress::Bool = true, guess=initGuess)
51     Δ = l*1
52     δ = Δ/1000.0
53     w = width/l # width in multiples of length
54     h = height/l # height in multiples of length
55
56     Fe!(F, χ, ∂χ-x, ∂χ-y, ∂χ-z, r) = F!(F, χ, ∂χ-x, ∂χ-y, ∂χ-z, r, ε, δ, n)
57     Be_l!(B, χ, r) = B!(B, χ, r, ζ, ε, δ, Δ, 0.0, n, -1.0)
58     Be_r!(B, χ, r) = B!(B, χ, r, ζ, ε, δ, Δ, φ, n, 1.0)
59     X = solve3D(guess, N, w, h, 2, Fe!, Be_l!, Be_r!, Neumann!, Neumann!, Neumann!, Neumann!,
        showProgress)
60     return X
61 end
62
63 function FindDOS(N::Int, ε::Float64, l::Float64, width::Float64, height::Float64, φ::Float64, ζ::
    Float64, n::Float64, filename::AbstractString="dos3DWire", save::Bool=true)
64     X = SingleSolve(N, ε, l, width, height, φ, ζ, n, true)
65     dos = ProjectTools.DOS_nm(X)
66     if save
67         export3DVTK(string(filename, "_w",width/l, "_h", height/l, "_φ", φ, "_ζ", ζ, "ε", ε, "_n", n),
            dos, :DOS, 1, N, width/l, height/l)
68     end
69     return X, dos
70 end
71
72 function FindPairCorrelation(N::Int, l::Float64, width::Float64, height::Float64, φ::Float64, ζ::
    Float64, n::Float64, maxIter=4, tol::Float64=1e-4, fileprename::AbstractString="pairCorrelation
    ")
73     Δ = l*1
74     β = 1000.0/Δ
75     w = width/l
76     h = height/l
77
78     # Intervals
79     ints = [[0.0001 0.5*Δ], [0.5*Δ, 0.99*Δ], [1.01*Δ, 2.0*Δ], [2.0*Δ, 10.0*Δ]]
80
81     println("Finding initial guesses")
82     guessLocs = [(i[1] + i[2])/2.0 for i in ints]
83     guessProcs = [@spawn SingleSolve(N, ε, l, width, height, φ, ζ, n, false) for ε in guessLocs]
84     guesses = [fetch(guessProc) for guessProc in guessProcs]
85
86     funcs = [ε -> ProjectTools.PairIntegrand_nm(SingleSolve(N, ε, l, width, height, φ, ζ, n, false, x
        -> guess), ε, β) for guess in guesses]
87
88     println("Starting integration")
89     = @distributed (+) for (f, i) ∈ collect(zip(funcs, ints))
90         ProjectTools.Romberg(f, i[1], i[2], tol, maxIter)
91     end
92
93     export3DVTK(string(fileprename, "PairCorr_NM_3D", "_N", N, "_l", l, "_w", w, "_h", h, "_φ", φ, "_ζ
        ", ζ, "_n", n), ProjectTools.DivideAbsPhase( ), : , 2, N, w, h)
94
95     return
96 end
97
98 # Current
99 function FindCurrent(N::Int, l::Float64, width::Float64, height::Float64, φ::Float64, ζ::Float64, n:

```



```

:Float64, filename::AbstractString="current")
100
101  $\Delta = 1*1$ 
102  $\beta = 1000.0/\Delta$ 
103  $w = \text{width}/1$  # width in multiples of length
104  $h = \text{height}/1$ 
105
106 # Intervals
107 ints = [[0.0001 0.5* $\Delta$ ], [0.5* $\Delta$ , 0.9999* $\Delta$ ], [1.0001* $\Delta$ , 2.0* $\Delta$ ], [2.0* $\Delta$ , 10.0* $\Delta$ ]]
108
109 println("Finding initial guesses")
110 guessLocs = [(i[1] + i[2])/2.0 for i in ints]
111 guessProcs = [@spawn SingleSolve(N,  $\epsilon$ , 1, width, height,  $\varphi$ ,  $\zeta$ , n, false) for  $\epsilon$  in guessLocs]
112 guesses = [fetch(guessProc) for guessProc in guessProcs]
113
114 vecPot(r) = [vecPot_x(r, n), 0.0, 0.0]
115
116 funcs = [ $\epsilon \rightarrow$  ProjectTools.Current3D_nm(SingleSolve(N,  $\epsilon$ , 1, width, height,  $\varphi$ ,  $\zeta$ , n, false, x  $\rightarrow$ 
guess), N, w, h, vecPot,  $\epsilon$ ,  $\beta$ ) for guess in guesses]
117
118 println("Starting integration")
119 j = @distributed (+) for (f, i)  $\in$  collect(zip(funcs, ints))
ProjectTools.Romberg(f, i[1], i[2])
120
121 end
122
123 export3DVTK(string(filename, "_N", N, "_l", l, "_w", width/1, "_h", height/1, "_ $\varphi$ ",  $\varphi$ , "_ $\zeta$ ",  $\zeta$ , "_n", n), j, :j, 3, N, w, h)
124
125 return j
126 end
127
128 # Find both current and paircorrelation
129 function FindCurrentAndPair(N::Int, l::Float64, width::Float64, height::Float64,  $\varphi$ ::Float64,  $\zeta$ ::
Float64, n::Float64, maxIter=4, tol::Float64=1e-4, filename::AbstractString="")
130
131  $\Delta = 1*1$ 
132  $\beta = 1000.0/\Delta$ 
133  $w = \text{width}/1$  # width in multiples of length
134  $h = \text{height}/1$ 
135
136 # Intervals
137 ints = [[0.0001, 0.5* $\Delta$ ], [0.5* $\Delta$ , 0.99* $\Delta$ ], [1.01* $\Delta$ , 2.0* $\Delta$ ], [2.0* $\Delta$ , 10.0* $\Delta$ ]]
138
139 println("Finding initial guesses")
140 guessLocs = [(x[1] + x[2])/2.0 for x in ints]
141 guessProcs = [@spawn SingleSolve(N,  $\epsilon$ , 1, width, height,  $\varphi$ ,  $\zeta$ , n, false) for  $\epsilon$  in guessLocs]
142 guesses = [fetch(guessProc) for guessProc in guessProcs]
143
144 vecPot(r) = [vecPot_x(r, n), 0.0, 0.0]
145
146 function func_template( $\epsilon$ , guess)
147 a = SingleSolve(N,  $\epsilon$ , 1, width, height,  $\varphi$ ,  $\zeta$ , n, false, guess)
148 return [ProjectTools.PairIntegrand_nm(a,  $\epsilon$ ,  $\beta$ ),
ProjectTools.Current3D_nm(a, N, w, h, vecPot,  $\epsilon$ ,  $\beta$ )]
149
150 end
151
152 funcs = [ $\epsilon \rightarrow$  func_template( $\epsilon$ , guess) for guess in guesses]
153
154 println("Starting integration")
155 = @distributed (+) for (f, i)  $\in$  collect(zip(funcs, ints))
ProjectTools.Romberg(f, i[1], i[2], tol, maxIter)
156
157 end
158
159 export3DVTK(string(filename, "PairCorr_NM_3D", "_N", N, "_l", l, "_w", w, "_h", h, "_ $\varphi$ ",  $\varphi$ , "_ $\zeta$ ",  $\zeta$ , "_n", n), ProjectTools.DivideAbsPhase([1]), : , 2, N, w, h)
160 export3DVTK(string(filename, "Current_NM_3D", "_N", N, "_l", l, "_w", w, "_h", h, "_ $\varphi$ ",  $\varphi$ , "_ $\zeta$ ",  $\zeta$ , "_n", n), [2], :j, 3, N, w, h)
161
162 return
163 end

```



